UNIVERSITEIT ANTWERPEN
Faculteit Wetenschappen
Departement Fysica

Characteristic length scales and vortex interactions in two-component superconducting systems

---

Karakteristieke lengte schalen en vortex interacties in tweecomponent supergeleidende systemen

Proefschrift voorgelegd tot het behalen van de graad van doctor in de Wetenschappen: fysica aan de Universiteit Antwerpen te verdedigen door

Lucia Komendová

Promotor
Prof. Dr. Milorad Milošević

Antwerpen
5 December, 2013

Members of the Jury:

Chairman
Prof. Dr. Staf Van Tendeloo, University of Antwerp, Belgium

Supervisor
Prof. Dr. Milorad Milošević, University of Antwerp, Belgium

Members
Prof. Dr. Jörg Schmalian, Karlsruhe Institute of Technology, Germany
Prof. Dr. Tristan Cren, Institut des NanoSciences de Paris, France
Prof. Dr. Sabine Van Doorslaer, University of Antwerp, Belgium
Prof. Dr. Jacques Tempère, University of Antwerp, Belgium
Prof. Dr. Wim Magnus, IMEC and University of Antwerp, Belgium

Contact Information

Lucia Komendova
G.U. 209
Groenenborgerlaan 171
2020 Antwerpen
Belgium
Lucia.Komendova@gmail.com

Acknowledgement

I would like to thank all of those people who were staying by my side during the last couple of years. The foremost person I would like to thank is my promotor Milorad Milošević who lead me through all stages of the research and was always there when I did not know how to deal with something. He has a really marvelous ability to see potentially interesting problems from far ahead and then also the patience all the time it takes to finally see the answers to the original questions. I greatly benefitted from his experience also when preparing for conferences and other scientific meetings, and when writing and publishing the results of our work. I would also like to thank Arkady Shanenko to whom I can always come with no matter how dummy question for his enormous insight into physics and a nice view on the world. This first paragraph would not be complete without thanking the head of our group Prof. Francois Peeters, for his success in bringing so many talented people to work together. I would also like to thank Dr. Lara Benfatto, who was my host for my two months research stay in Rome at University La Sapienza.

There were many other people very important for me as sort of examples worthy to follow, among those I would like to mention in particular Bart Partoens, Jacques Tempère, Jonas Reijniers, Alexander Hernandez-Nieves, Rolando Saniz, Peter Samuely, Tomáš Blažek, Richard Hlubina, Goran Karapetrov, Oskar Vafek and Denis Kochan. This brings me smoothly to my closer age equals such as Andrey Chaves, Yajiang Chen, Edith Cristina Euan Diaz, Ben Xu, Roeland Geurts, Massoud, Mohamed, Nga Nguyen, Natalia and all the other PhD students in our group and at the University of Antwerp who taught me a lot and were also a very enjoyable company. I would like to thank especially William, Hamilton, Diego and Seyda for being such nice officemates and also to guys for trying to teach me to dance in a proper Latin-American way, to guys with whom I played football the first year for tolerating an almost useless player and trying hard to get me involved, to Andrey Kapra for the badminton games and introduction to body-building, to girls and guys from the molecular biology lab in particular Agnieszka, Daria

and Nora and then to Elena Telkova, Ivana Planojević and Sarah Vantorre for all the ladies nights out.

I would like to thank to Nikolas not only for his technical support, but also for his inexhaustible good humor and to our secretary Hilde who is one amazingly efficient and incredibly nice person.

Also I would like to thank my family and friends in Slovakia, for staying in touch and staying close despite the distance. In particular I would like to thank my dearest friends Palo, Inka, Tomáš, Lukáš, Monika, Martin and Ivka, for they are always there for me, whether it is to chat out my worries or to find a free bed for me on a short notice.

Last but not least, I would like to thank to my dearest friends in here, Jozef, Stephan, Slaviša, Marko and Dean, who were my daily source of fun and encouragement especially at the lunch time, and Pinaki who kept me company over the internet.

I hope you know that you are important for me (also if I did not put your name here explicitly) and this work would not be possible without you too.

Finally I thank the FWO for a travel grant and Academia Belgica in Rome for enjoyable stay at their premises.

Contents

Preface

The research topic of my PhD studies was the vortex matter in the two-gap superconductors. I studied these materials mainly in the framework of Ginzburg-Landau theory. During the first year of my PhD I was mostly directly solving full two-gap Ginzburg-Landau equations. I also reviewed the published literature in order to determine the appropriate numerical parameters for the magnesium diboride, which is the most common two-gap superconductor and also it was demonstrated to show the so-called *Type-1.5 superconductivity*, i. e., unusual stripe vortex patterns [1].

I began the investigations from two-gap superconducting thin films, as this seemed to be the simplest geometry. However, it turned out that the most interesting effects are found if the bands are of different superconducting type, i.e. one type-I, the other type-II, which is impossible to realize for the very thin films with the magnesium diboride parameters. Namely, if the thickness of the film is comparable to the penetration depth, the effective Ginzburg-Landau parameter for the type-I band changes effectively to the type-II. As a result, only the well-known type-II like behavior is realized and the vortices form regular Abrikosov lattice. To overcome this restriction we modified the program in order to compute the vortex states for arbitrary thickness of the sample and also for the special case of the bulk limit, which corresponds theoretically to the infinitely thick sample. We focused on the influence of the parameters of the model on the particular vortex states, and studied the effects of changing the Ginzburg-Landau parameter of the bands, the ratio of the respective coherence lengths, and the Josephson coupling within bands. More importantly, we also determined how the particular vortex state would evolve with increasing the temperature, where we found that the intervortex distances are growing. As a result, the Abrikosov vortex lattice found in a thin sample dissolves when the sample is made thicker, as one band changes from the effective type-II to the type-I behavior. Along this path, we have observed a gradual transition from the regular triangular lattice through the stripe phase to the laminar phase. These results are in principle experimentally verifiable.

Together with Andrey Chaves (Universidade Federal do Ceará, Fortaleza, Brazil) we made a short summary of the conditions for the existence of non-monotonic (type-1.5) vortex-vortex interactions in two-gap superconductors within Ginzburg-Landau theory. This manuscript has been published in Phys. Rev. B and is included in this thesis as Chapter 4. Then in July 2010 several important new papers about two-gap superconductivity became available on preprint server arxiv. Perhaps the most important one was the one by Kogan and Schmalian [2]. The authors found an inconsistency within the standardly used Ginzburg-Landau theory for two-gap superconductors and have proven that it mixes terms of different order in the expansion parameter $\tau = 1 - T/T_c$ (relative distance from the critical temperature). They concluded that it is necessary to remove the higher order terms. This correcting approach led them to conclusion that even in two-gap superconductors there is only a single Ginzburg-Landau parameter κ and single magnetic penetration depth and coherence length for both bands together, thus there is no space for the type-1.5 superconductivity. This conclusion is however limited in validity to very close vicinity of the critical temperature, as was shown later in paper by A. Shanenko *et al.* [3]. There the Ginzburg-Landau theory has been derived from the microscopic BCS theory with greatest care to include all the higher order terms, though only for the situation with zero applied magnetic field. We used this theory to calculate the healing lengths of the two individual bands, which we indeed found to be different, contrary to the belief of Kogan *et al.* This paper was also published in Phys. Rev. B and forms the core of Chapter 5. To further elucidate the relationship between the predictions of the extended Ginzburg-Landau theory and the standard two-gap Ginzburg-Landau theory, we investigated in detail their predictions for a specific multigap superconductor LiFeAs and these comparisons are discussed later in the same chapter.

We also wanted to estimate the validity region of the Ginzburg-Landau type theories for two-band superconductors by the direct comparison with the results of a *microscopic* theory, namely the Bogoliubov-de Gennes formalism. The calculations in the microscopic theory were done by Yajiang Chen, then also a PhD student in our group. We found an unexpected peak in the coherence length of the weak band as a function of temperature. We investigated this effect further and found that it finds place when the coupling between bands is very weak (but still attainable in real two-band superconductors). The explanation of the effect is as follows: If the interband coupling was completely turned off, this weak-band coherence length would be in fact diverging at T_{c2}, the bare critical temperature of the weak band. However, when the coupling is finite, this divergence does not completely disappear, but remains in a "shadowed" form of a peak. This automatically enhances

the disparity between two bands length scales, a necessary though not sufficient condition for the appearance of nonmonotonic intervortex interaction. Finally, the fact that the amplitude of the weak band becomes small at T_{c2} allowed us to construct an analytic approach valid at this temperature in the limit of vanishing interband coupling. The results of our investigation were published in Physical Review Letters and are reproduced here in Chapter 6.

Finally we investigated a bilayer structure made of two different single-gap superconductors, which we expected to show very similar phenomenology as a two-gap superconductor, however much more easily tunable. The theoretical description which we used is a variant of the famous Lawrence-Doniach model for high-temperature cuprates emphasizing the layered aspect of the structure. We found that there is indeed a mid-range intervortex attraction present and that this in combination with the long-range $1/r$ repulsion stemming from the interaction of stray magnetic fields of the vortices leads to myriads of possible vortex structures forming soft-matter-like gels, glasses, chain-like structures and other intriguing patterns. These results are published in Physical Review B and are also included in this thesis as Chapter 7.

Chapter 1

Introduction to superconductivity

In the following sections I will go shortly through all the basic information necessary to understand the rest of my thesis. However, my goal is not to be comprehensive, since many excellent books exist which provide more complete survey of the physics of superconductors at the introductory level. The interested reader is therefore referred to for example Introduction to superconductivity *by Michael Tinkham or P. G. de Gennes's* Superconductivity of metals and alloys*.*

1.1 History of superconductivity

Superconductivity was discovered in 1911 in the laboratory of Heike Kammerlingh Onnes in Leiden, The Netherlands. Onnes was the first in the world to develop a technique to liquefy helium few years earlier and that enabled experiments at temperatures around 4.2 Kelvin. Onnes and coworkers used such experiments to see the temperature behavior of the resistivity of metals when cooled towards the absolute zero. Surprisingly, they found that the resistivity of their mercury (Hg) sample dropped abruptly to unmeasurable values, i.e., became effectively zero at low temperatures. Therefore the first defining property of the superconductor is the *perfect DC conductivity* below the critical temperature T_c, which motivated also the name of the phenomenon. In 1933 another important property of superconductors was discovered - the *perfect diamagnetism* - meaning that the superconductor completely expels the applied magnetic field from its interior. This property

is called the Meissner-Ochsenfeld effect, after its discoverers.

The assumption of the coherent superconducting condensate, together with general electromagnetic arguments and the Meissner-Ochsenfeld effect, led the London brothers to a first theoretical description of superconductivity in 1935. For decades the full quantum-mechanical understanding of superconductivity lagged behind the experiments, but finally a breakthrough was achieved in 1950 [4] when the Ginzburg-Landau theory was proposed on phenomenological grounds, starting from the general Landau theory of second-order phase transitions as we shall see in more detail in Sec. 1.3. Few years later a microscopic theory was developed by Bardeen, Cooper and Schrieffer [5], hence called BCS theory after the initials of its founders. Bardeen, Cooper and Schriefer found that the appearance of superconductivity is accompanied by formation of Cooper pairs, sort of loosely bound two-electron molecules. The attractive interaction needed to bind the electrons was found to originate in the electron-phonon interaction. The Cooper pairs are no longer described by the fermionic statistics and as bosons they can occupy a single coherent quantum state described by a macroscopic wave function Ψ. We shall sketch the main points of the BCS theory in Sec. 1.5. Importantly, two years after the BCS theory was published it was shown by Gor'kov [6] that the originally phenomenological Ginzburg-Landau theory can be in fact rigorously derived from the BCS theory and its coefficients can be therefore related to the microscopic material parameters such as the Fermi velocity v_F and density of states at the Fermi level $N(0)$.

Another important leap forward was made by Abrikosov in 1957 [7], who found that the Ginzburg-Landau equations allow the existence of superconductors with negative energy cost of superconductor-normal metal (S-N) interface. He named this new class the *type-II superconductors*, materials creating as much S-N interface as possible, which in turn leads to magnetic flux penetration in the sample in the smallest quantum-mechanically allowed units - flux quanta $\Phi_0 = \frac{hc}{2e}$.[1] Every single line of the magnetic flux has supercurrents circulating around it which screen the magnetic field and prevent it from spreading to the rest of the sample. These circulating supercurrents are the reason why this magnetic structure was named a *vortex*. Due to the negative surface energy, vortices repel at all distances and as a consequence typically form a regular triangular lattice (called Abrikosov lattice). In the opposite case of the *type-I superconductors* with positive energy cost of forming interfaces, if the magnetic field is too large and cannot be screened completely anymore, the flux penetrates the sample in the form of macro-

[1] Throughout the text the formulas are given in CGS units as usual in the field of superconductivity.

scopic normal domains. The normal domains in type-I superconductors can be circular, laminar or a combination thereof. Their actual shape in a particular sample depends on the shape of the sample, the material itself and its purity, but also on the history. For example the domain structure is different for increasing magnetic field as compared to the structure for decreasing magnetic field, as depicted in Fig. 1.1 from Ref. [8].

In the course of the 20th century thousands of materials were found to be superconducting, even though mostly with a very low critical temperature. After decades of slow progress it was widely believed that the superconductivity will remain in the helium temperatures. The term "helium temperatures" refers to temperatures accessible with no other liquefied gas except rather rare and expensive helium. However, in 1986 a new family of *cuprate superconductors* was discovered in Zürich by Bednorz and Müller [9] with the critical temperatures eventually rising up to about 150 K. The main building block of the cuprate superconductors are tetragonal copper-oxygen planes. This discovery triggered a massive wave of research activity aimed to understand the physical mechanisms behind this *high-temperature* superconductivity, because it was understood early that pairing due to the electron-phonon coupling is insufficient to provide such high T_c. Despite the efforts the pairing mechanism is to date not convincingly understood; several competing theories exist, none of them emerging as a clear winner. There is however a body of experimental evidence for d-wave gap function, i.e., unlike in the conventional s-wave superconductors the pairing interaction does not open the gap in the excitation spectrum around the whole Fermi surface, but instead there are *nodes*, points at the Fermi surface where the gap is zero. This causes very different behavior of various physical quantities, e.g., the specific heat does not disappear exponentially as temperature approaches absolute zero.

The timeline of the most important new superconductors as they were discovered and their critical temperature are shown in Fig. 1.2.

1.2 The London equations

Let us attempt to describe the interaction of the superconductor with the external magnetic field in simple terms. The field is assumed to be small enough to not modify the density of superconducting electrons n_s, which is assumed to be independent of position.

The free energy of the superconductor can be written as

$$E = \int F_s d^3r + E_{\text{kin}} + E_{\text{mag}}, \tag{1.1}$$

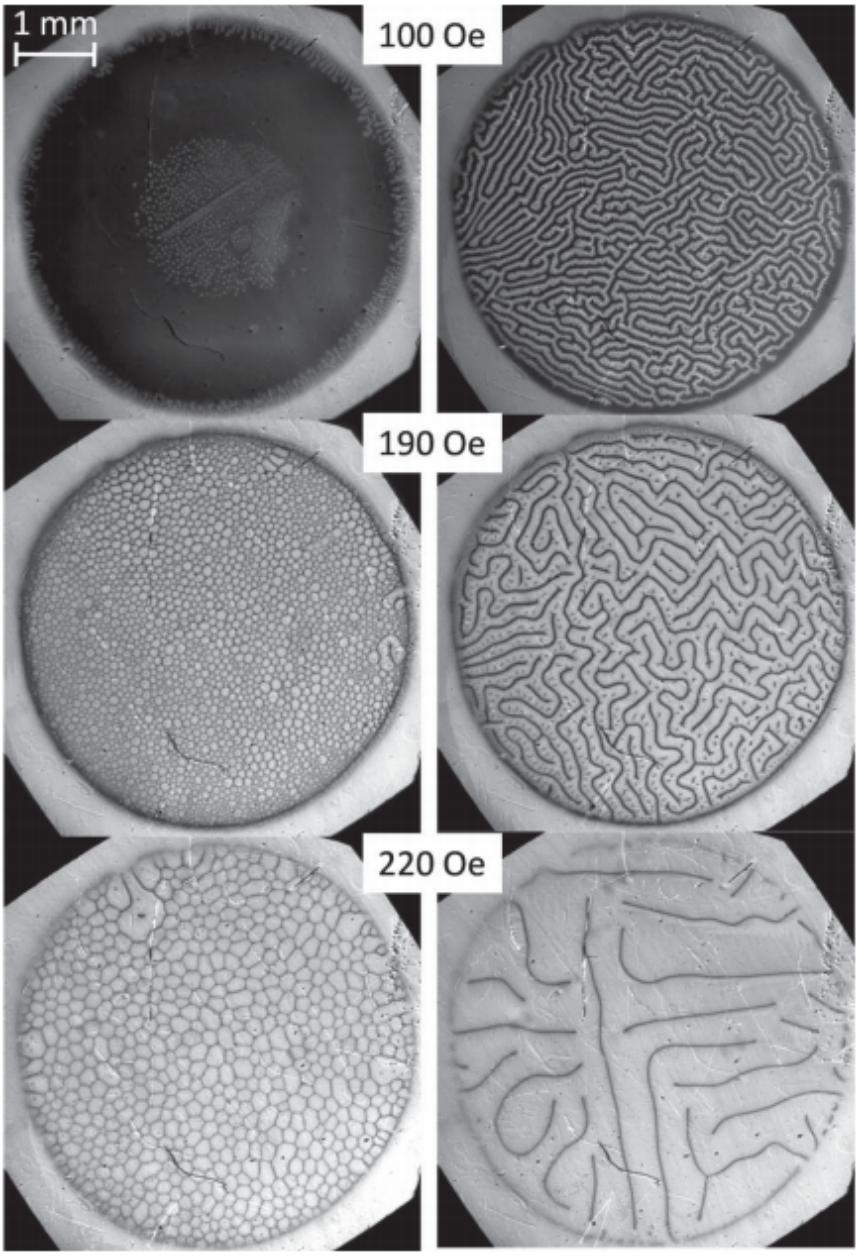

Figure 1.1: Structure of the intermediate (between superconducting and normal metal) state in a disc-shaped Pb single crystal at 5 K obtained by the magneto-optical technique. Light color is normal state, dark superconducting state. Left column: increasing magnetic field after cooling in the zero field. Right column: decreasing field. From Ref. [8].

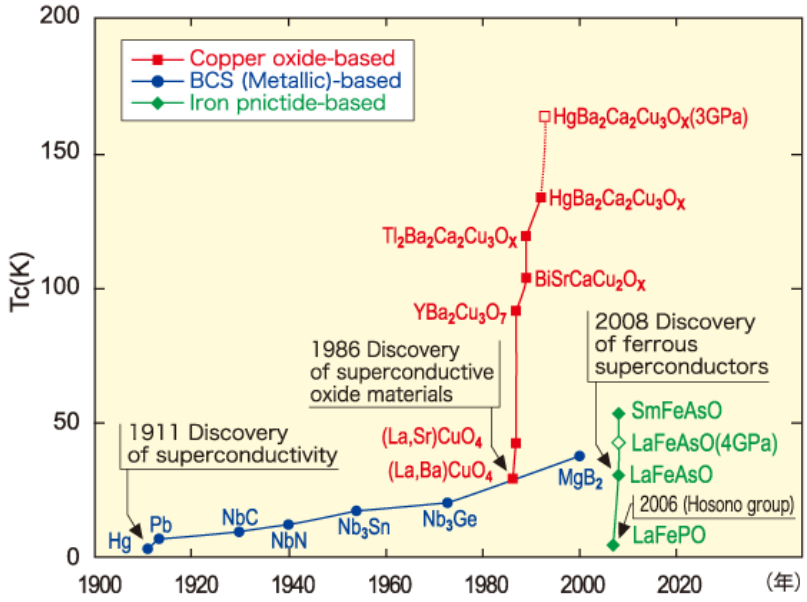

Figure 1.2: The most important superconductors displayed according to their year of discovery and critical temperature. Open symbols indicate materials under pressure. From Ref. [10].

where F_s is the superconducting energy density, E_{kin} the kinetic energy of the electric currents, and $E_{\text{mag}} = \int \mathbf{h}^2/8\pi\, d^3r$ the energy of the magnetic field $\mathbf{h}$.[2] Visualizing the supercurrent as a flow of superconducting electrons of number density n_s (per unit volume), charge e and mass m (free electron charge and mass) moving with the superfluid velocity $\mathbf{v}_s(\mathbf{r})$, one can calculate the supercurrent density as

$$\mathbf{j}_s = n_s e \mathbf{v}_s(\mathbf{r}). \tag{1.2}$$

The total kinetic energy of such flow of particles is then

$$E_{kin} = \int d^3r \frac{1}{2} n_s m v_s^2. \tag{1.3}$$

Moreover, the currents must obey the Maxwell equation:

$$\nabla \times \mathbf{h} = \frac{4\pi}{c} \mathbf{j}_s. \tag{1.4}$$

Substituting this information into Eq. (1.1) we obtain

$$E = E_0 + \frac{1}{8\pi} \int \left[\mathbf{h}^2 + \lambda_L^2 |\nabla \times \mathbf{h}|^2\right] d^3r, \tag{1.5}$$

where we denoted $E_0 = \int F_s d^3r$ and the *London penetration depth* λ_L is defined as

$$\lambda_L = \left[\frac{mc^2}{4\pi n_s e^2}\right]^{1/2}. \tag{1.6}$$

Now we look for the configuration of the local magnetic field $\mathbf{h}(\mathbf{r})$ which minimizes the above energy, by searching for a variational fixed point of energy E with respect to small variation of the $\delta\mathbf{h}(\mathbf{r})$:

$$\begin{aligned} \delta E = \frac{1}{4\pi} \int [\mathbf{h} \cdot \delta\mathbf{h} + \lambda_L^2 (\nabla \times \mathbf{h}) \cdot (\nabla \times \delta\mathbf{h})] d^3r = \\ \frac{1}{4\pi} \int [\mathbf{h} + \lambda_L^2 (\nabla \times \nabla \times \mathbf{h})] \cdot \delta\mathbf{h}\, d^3r, \end{aligned} \tag{1.7}$$

where the final expression has been obtained by integration by parts. For δE to be zero (stationarity condition), we must have

$$\mathbf{h} + \lambda_L^2 (\nabla \times \nabla \times \mathbf{h}) = 0. \tag{1.8}$$

[2] We follow here the notation of Tinkham [11] to denote by $\mathbf{h} = \nabla \times \mathbf{A}$ the value of magnetic flux density on the microscopic scale, reserving $\mathbf{B}$ for the macroscopic average value. $\mathbf{A}$ is the magnetic vector potential.

Additional use of the vectorial identity $\nabla \times \nabla \times \mathbf{h} = \nabla(\nabla \cdot \mathbf{h}) - \nabla^2\mathbf{h}$ and the Maxwell equation $\nabla \cdot \mathbf{h} = 0$ finally leads us to:

$$\mathbf{h}/\lambda_L^2 = \nabla^2\mathbf{h}, \tag{1.9}$$

where $\nabla^2 = \frac{\partial^2}{\partial x^2} + \frac{\partial^2}{\partial y^2} + \frac{\partial^2}{\partial z^2}$ is the Laplace operator. This equation was first derived by brothers Fritz and Heinz London, and together with the Maxwell equation (1.4), it allows one to calculate the spatial distribution of the magnetic fields and currents.

The simplest situation to consider is having a semi-infinite superconductor filling the half-space $x > 0$, with applied homogeneous external field H_a parallel to the surface, where we want to calculate the field profile inside the superconductor. It is trivial to see that the appropriate solution of Eq. (1.9) is $h(x) = H_a e^{-x/\lambda_L}$, meaning that **the magnetic field decays inside a superconductor with a characteristic length scale given by the London penetration depth** λ_L.

1.3 The Ginzburg-Landau (GL) theory

To describe phenomenologically the second-order phase transitions with temperature Landau introduced the idea of the *order parameter*, a quantity which will be zero for the ground state above T_c and acquires non-zero value below T_c. In the case of superconductivity, the order parameter proposed by Ginzburg and Landau was the wave function of the superconducting condensate $\Psi(\mathbf{r}) = |\Psi(\mathbf{r})|e^{i\varphi(\mathbf{r})}$, where $|\Psi(\mathbf{r})|^2$ represents the local density of the Cooper pairs, i.e., half of the density of superconducting electrons n_s. If $\Psi(\mathbf{r})$ is small and varies slowly in space, one can expand the free energy density as the polynomial of the order parameter and its gradients

$$f_s = f_{n0} + \alpha|\Psi|^2 + \frac{\beta}{2}|\Psi|^4 + \frac{1}{2m^*}\left|\left(\frac{\hbar}{i}\nabla - \frac{2e}{hc}\mathbf{A}\right)\Psi\right|^2 + \frac{\mathbf{h}^2}{8\pi}, \tag{1.10}$$

where $m^* = 2m$ is the mass of the Cooper pair, $\mathbf{A}$ is the magnetic vector potential and the expansion coefficients α and β will be discussed later. In the absence of the superconductivity, i.e., for $\Psi(\mathbf{r}) = 0$, the free energy Eq. (1.10) reduces to the free energy density of the normal state $f_{n0} + \mathbf{h}^2/8\pi$, where $f_{n0}(T) = f_{n0}(0) - \frac{1}{2}\gamma T^2$ and γ is the electronic specific heat coefficient, also known as the Sommerfeld constant. The free energy density due to superconductivity in the simplest case of no fields and gradients is

$$f_s - f_n = \alpha|\Psi|^2 + \frac{\beta}{2}|\Psi|^4, \tag{1.11}$$

which can be identified with the first two terms in the series expansion in $|\Psi|^2$. Apparently, Ψ itself cannot appear in the expansion, because it is a complex quantity while the free energy is real, and neither can its real part because the result may not be sensitive to the global phase of Ψ. Finally, the odd powers of $|\Psi|$ are excluded because they are not analytic at $\Psi = 0$, i.e., their derivative is not well defined there. In general, higher order terms, e.g., one proportional to $|\Psi|^6$ are possible, but are not necessary provided $|\Psi|$ is small, e.g., for temperatures close to the critical temperature. Therefore, if we stay with the two leading order terms, we see that, for the theory to be of any use, β must be positive, because otherwise the energy is not bounded from below, i.e., arbitrarily low energy could be achieved which is unphysical. On the other hand, both $\alpha > 0$ and $\alpha < 0$ are possible, and correspond to respective situations where energy minimum occurs for $|\Psi| = 0$ (normal metallic state with no superconducting condensate above T_c), or for $|\Psi| = \Psi_\infty = \sqrt{-\frac{\alpha}{\beta}}$ (in the superconducting state below T_c). The notation Ψ_∞ is introduced because this is the equilibrium value of the order parameter far inside the superconductor, i.e., in the bulk. From the above we see that α must change sign exactly at T_c, therefore its leading-order temperature dependence can be written as $\alpha(T) = -a(1 - T/T_c)$ with $a > 0$. Finally, we should explain the physical meaning of the term in free energy density comprising fields and gradients. This becomes clearer when the complex field $\Psi(\mathbf{r}) = |\Psi(\mathbf{r})|e^{i\varphi(\mathbf{r})}$ is understood via two independent real fields: amplitude $|\Psi(\mathbf{r})|$ and phase $\varphi(\mathbf{r})$. Then the free energy contribution from the fields and gradients can be written as

$$\frac{1}{2m^*}\left[\hbar^2(\nabla|\Psi|)^2 + \left(\hbar\nabla\varphi - \frac{2e\mathbf{A}}{c}\right)^2 |\Psi|^2\right], \tag{1.12}$$

so we see that first term accounts for the energy cost of having gradients in the amplitude of the order parameter, while the second term is the kinetic energy of the superconducting electrons $n_s(\frac{1}{2}mv_s^2)$, since one can identify $\hbar\nabla\varphi - \frac{2e\mathbf{A}}{c} = m^*\mathbf{v}_s = 2m\mathbf{v}_s$ and $|\Psi|^2 = n_s/2$ (the density of the superconducting electrons n_s is twice the density of the Cooper pairs $|\Psi|^2$).

1.3.1 Ginzburg-Landau equations

The total free energy of the superconductor is given by the volume integral of the free energy density, $F = \int f dV$. Since the free energy density is a functional of $\Psi(\mathbf{r})$ and $\mathbf{A}(\mathbf{r})$, in order to find which configuration of $\Psi(\mathbf{r})$ and $\mathbf{A}(\mathbf{r})$ gives a minimum of the free energy, one needs to evaluate the necessary

conditions $\frac{\delta F}{\delta \Psi^*} = 0$ and $\frac{\delta F}{\delta \mathbf{A}} = 0$. This leads to the *Ginzburg-Landau equations*:

$$\alpha\Psi + \beta|\Psi|^2\Psi + \frac{1}{2m^*}\left(\frac{\hbar}{i}\nabla - \frac{2e}{c}\mathbf{A}\right)^2\Psi = 0, \tag{1.13}$$

$$\mathbf{j} = \frac{c}{4\pi}\nabla \times \mathbf{h} = \frac{e\hbar}{m^* i}(\Psi^*\nabla\Psi - \Psi\nabla\Psi^*) - \frac{4e^2}{m^* c}|\Psi|^2\mathbf{A}. \tag{1.14}$$

The expression (1.14) is actually the standard quantum-mechanical formula for the current of particles with mass m^*, charge $2e$ and wave function $\Psi(\mathbf{r})$. The first Ginzburg-Landau equation resembles the Schrödinger equation for the above-mentioned particles with the energy eigenvalue $-\alpha$. However, unlike the Schrödinger equation it has an additional nonlinear term $\beta|\Psi|^2\Psi$. This term acts as a repulsive potential of Ψ on itself and tends to favor the configurations of Ψ maximally spread out in space.

Appropriate boundary conditions for Ginzburg-Landau equations are obtained during their derivation as [11]

$$\left(\frac{\hbar}{i}\nabla - \frac{2e}{c}\mathbf{A}\right)\Psi\Big|_n = 0, \tag{1.15}$$

corresponding to no current passing through the surface, or, more generally [12]

$$\left(\frac{\hbar}{i}\nabla - \frac{2e}{c}\mathbf{A}\right)\Psi\Big|_n = \frac{i\hbar}{b}\Psi, \tag{1.16}$$

where b would be close to zero for an interface with a magnetic material, infinity for an insulator, have some finite positive value for a metal, or negative for a contact to a superconductor with higher T_c.

1.3.2 Characteristic length scales

Let us now understand the basic behavior of Ψ prescribed by the Eq. (1.13). If $\mathbf{A} = 0$, all the coefficients in the differential equation are real, therefore we can look for a real function Ψ, for simplicity only dependent on x-coordinate (1D case). As seen before, in the absence of the gradients the solution of

$$\alpha\Psi + \beta|\Psi|^2\Psi + \frac{\hbar^2}{2m^*}\frac{d^2\Psi}{dx^2} = 0 \tag{1.17}$$

is just Ψ_∞. Let us therefore consider a normalized wave function $f = \Psi/\Psi_\infty$, so that the Ginzburg-Landau equation becomes

$$\frac{\hbar^2}{2m^*|\alpha|}\frac{d^2 f}{dx^2} + f - f^3 = 0. \tag{1.18}$$

From the dimensional analysis we see that the prefactor of the first term has dimensions of length squared. We thus introduce a length scale $\xi(T)$, known as the *Ginzburg-Landau coherence length*,

$$\xi^2(T) = \frac{\hbar^2}{2m^*|\alpha(T)|}. \tag{1.19}$$

Since $\alpha \propto \tau = 1 - T/T_c$, the temperature dependence of ξ must be $\tau^{-1/2}$. The equation (1.18) now reads

$$\xi^2(T)\frac{d^2f}{dx^2} + f - f^3 = 0. \tag{1.20}$$

For boundary conditions $f(0) = 0$ and $f'(x \to \infty) = 0$ this equation has an analytic solution $f = \tanh(x/\sqrt{2}\xi)$. This means that **the wave function Ψ changes over characteristic distance of the order of the coherence length** $\xi(T)$, sometimes in literature also referred to as the *healing length*.

1.3.3 Ginzburg-Landau parameter κ

The Ginzburg-Landau parameter κ is defined as ratio of the magnetic field penetration depth and the Ginzburg-Landau coherence length

$$\kappa = \lambda/\xi. \tag{1.21}$$

Since the temperature dependence of both characteristic lengths is the same within the GL theory, κ is typically considered a material constant with negligible temperature dependence. We shall see that the behavior of superconductors in the applied magnetic field is very different depending on whether their κ is less or more than $1/\sqrt{2}$.

1.3.4 Type-I superconductors

Type-I superconductors are the ones with $\kappa < \frac{1}{\sqrt{2}}$. Most of the superconducting elements are type-I superconductors. Examples include aluminium, lead, mercury, tin and many others.

Any superconductor stops being superconducting for a sufficiently high applied field. The field at which the energy cost of screening the magnetic field becomes equal to the energy gain from forming a condensate is called the *thermodynamic critical field* H_c. According to this definition we have

$$\frac{H_c^2}{8\pi} = f_n(T) - f_s(T), \tag{1.22}$$

where $f_n(T)$ and $f_s(T)$ are the Helmholtz free energy densities in the normal respectively superconducting state.[3] It can be shown that the normal phase and the superconducting phase have equal thermodynamic potential G (and therefore can coexist) only at applied field $H_a = H_c$. This is true for the samples with zero demagnetizing factors, i.e., for long, thin cylinder or sheet **parallel** to the applied magnetic field. For these geometries the field everywhere along the surface is just equal to the applied field. For other geometries the field at some points on the surface will exceed the applied field. For this reason the type-I superconductors with nontrivial geometry (nonzero demagnetization factor, e.g. spherical sample) will exhibit the *intermediate state*. This means that for applied magnetic fields below and close to the thermodynamic critical field H_c the superconductor cannot be fully in the normal state, but also cannot be superconducting in its whole volume. Therefore the resulting state is a **mix of macroscopic normal and superconducting domains**, as shown in Fig. 1.1.

Since the normal metal (N) and superconducting (S) regions coexist, we can calculate the *domain wall energy*, i.e., the energy per unit area of the SN interface. We will see that this energy is positive for type-I superconductors, therefore the SN interfaces are minimized.

To calculate the domain wall energy, we need to first solve the Ginzburg-Landau equations and find the profile of the magnetic field $\mathbf{B}$ and of the order parameter Ψ going from the vacuum (at $x \to -\infty$), where $H = H_a = H_c$ and $\Psi = 0$ to the bulk of the superconductor (for $x \to \infty$), where $H = 0$ and $\Psi = \Psi_\infty$. Then we insert this solution into the GL free energy density functional and integrate across the interface. By definition when $H_a = H_c$ the energy of purely superconducting state and purely normal state are equal, therefore any excess energy with respect to this value is solely due to the SN interface.

In this case the quantity fixed is the magnetic field H, and we need to use the thermodynamic potential G. We calculate the SN interface energy γ

[3]The Helmholtz free energy F is appropriate thermodynamic potential for the case when $\mathbf{B}$ is constant, i.e., there is no induced electromagnetic field. The thermodynamic potential $G = F - \int d^3r \frac{\mathbf{B}\cdot\mathbf{H}}{4\pi}$ needs to be used in case the magnetic field $\mathbf{H}$ is fixed (i.e., we maintain constant current through the material).

as:

$$\gamma = \int_{-\infty}^{\infty} (g_{sH} - f_{s0}) dx = \int_{-\infty}^{\infty} \left(f_{sH} - \frac{hH_c}{4\pi} - f_{s0} \right) dx \tag{1.23}$$

$$= \int_{-\infty}^{\infty} \left[\alpha |\Psi|^2 + \frac{\beta}{2} |\Psi|^4 + \frac{1}{2m^*} \left| \left(\frac{\hbar \nabla}{i} - \frac{2e\mathbf{A}}{c} \right) \Psi \right|^2 + \frac{(h - H_c)^2}{8\pi} \right] dx. \tag{1.24}$$

The last term is obtained by summing $\mathbf{h}^2/8\pi$ from the Helmholtz energy with $-hH_c/4\pi$ for the transformation to thermodynamic potential G, and $H_c^2/8\pi$ for $f_{n0} - f_{s0}$. We can simplify this because we know that we are dealing with the solution of the Ginzburg-Landau equations, so they must also be satisfied. Therefore we take the first GL equation (1.13), multiply it by Ψ^* and integrate from $-\infty$ to ∞ (the derivative term is integrated by parts), to get

$$0 = \int_{-\infty}^{\infty} \left[\alpha |\Psi|^2 + \beta |\Psi|^4 + \frac{1}{2m^*} \left| \left(\frac{\hbar \nabla}{i} - \frac{2e\mathbf{A}}{c} \right) \Psi \right|^2 \right] dx. \tag{1.25}$$

As a consequence, our expression for the surface energy simplifies to

$$\gamma = \int_{-\infty}^{\infty} \left[-\frac{\beta}{2} |\Psi|^4 + \frac{(h - H_c)^2}{8\pi} \right]. \tag{1.26}$$

This clearly shows how the surface energy is determined by the balance of the negative condensation energy (first term) and the positive energy cost of screening the magnetic field (second term). Quantitative results can only be obtained numerically (for tabulated values see Ref. [13]), but in general one finds that γ is approximately proportional to $\xi - \lambda$. Therefore, for type-I superconductors where $\lambda \ll \xi$ the surface energy is positive, while in the opposite case the surface energy is negative and qualitatively new physics arises. The precise boundary between these two regimes lies at $\kappa = 1/\sqrt{2}$.

1.3.5 Type-II superconductors

Type-II superconductors have $\kappa > \frac{1}{\sqrt{2}}$. Most of the alloys and compounds which show superconductivity belong to this category, as do all high-T_c superconductors.

In the type-II superconductors the normal metal-superconductor interface energy is negative, which results in the magnetic domains splitting to the smallest possible units. This process is only limited by the quantization of

the magnetic flux in units of Φ_0. Therefore in type-II superconductors the flux can pass through the sample in the form of quantized vortices, each of them carrying the flux Φ_0. Strictly speaking it is not the magnetic flux itself which is quantized, but the *fluxoid* Φ' associated with each hole or normal region passing through the superconductor,

$$\Phi' = \Phi + \frac{4\pi}{c} \oint \lambda^2 \mathbf{j}_S \cdot d\mathbf{s}. \tag{1.27}$$

The field value at which the energy of the superconductor without any vortex is the same as that of the superconductor with one vortex is the *lower critical field* H_{c1}. At this field the magnetic field starts to penetrate the superconductor. On the other hand, if the field is so high that the vortex cores begin to overlap, the entire material becomes normal. That field is called the *upper critical field* H_{c2} and is given by $H_{c2}(T) = \Phi_0/(2\pi\xi^2)$.

Between the two critical fields the vortices are present in the type-II superconductor and they form a regular triangular Abrikosov lattice due to the fact that their mutual interactions are purely repulsive. Apart from the effects of strong pinning by the defects of the underlying crystal structure or by the artificially introduced pinning centers the vortices in superconductors are thus expected to form a periodic structure.

A vortex consists of a normal core with radius ξ surrounded by a layer of screening supercurrents extending to distance λ. The neighboring vortices normally repel due to the Lorentz force exerted by the supercurrent of one vortex on the magnetic flux of the other ($\mathbf{F} = \mathbf{j} \times \mathbf{\Phi_0}$).

The vortex profile can be calculated in the London model, which assumes $\xi \to 0$, i. e., point-like vortex core. The finite size of the vortex core is accounted for in the Clem model (1975), where at low fields (otherwise vortices overlap) the magnetic field of the vortex is:

$$\mathbf{B}(r) = \frac{\Phi_0}{2\pi\lambda\xi_v} \frac{K_0((r^2 + \xi_v^2)^{1/2}/\lambda)}{K_1(\xi_v/\lambda)}, \tag{1.28}$$

with K_0 and K_1 the modified Bessel functions.

Additionally when interpreting the interactions between the vortices in the experiments one should be aware of the effects of the sample boundary (surface barrier to vortex entry (Bean and Livingston 1964)), Meissner belt, geometrical barrier and finally the mesoscopic effects, when sample size becomes comparable to ξ.

1.3.6 Superconductors at the type-I/type-II crossover

At this place it is appropriate to recall that the picture of two strongly contrasting types of superconductivity strictly divided by $\kappa = 1/\sqrt{2}$, as pre-

sented in the previous two sections, is actually oversimplified. Already in 1970's it was observed that type-I to type-II transition occurs at finite interval of $\kappa \approx 1/\sqrt{2}$. From the available literature let us particularly discuss the experimental work by Auer and Ullmaier [14]. They studied the samples of TaN, tuned from pure Tantalum which is a type-I superconductor with $\kappa = 0.355$ by addition of Nitrogen impurities through $\kappa \approx 1/\sqrt{2}$ till $\kappa = 1.535$. They demonstrated (see Fig. 1.3) that between pure type-I and pure type-II (there called type-II/2) there exists a region of type-II/1 superconductivity, with a particular magnetic response. Namely, in this regime the magnetization shows a finite jump at H_{c1}, as shown in Fig. 1.4. This behavior is due to the long-range attraction between vortices which causes them to penetrate the sample immediately in higher density than prescribed by the Abrikosov lattice constant at H_{c1}. For further examples one is referred to E. H. Brandt and Das [15] and the classic book by Huebener [16].

From the theoretical point of view, $\kappa = 1/\sqrt{2}$ is the Bogomol'nyi point of the GL theory [17]. It has an infinite number of degenerate solutions for the superconducting state, as each vorticity has the same energy there. Within Ginzburg-Landau theory, κ is temperature independent and therefore it predicts $\kappa = 1/\sqrt{2}$ as universal dividing value at all temperatures, regardless of whether one considers the sign of the normal metal-superconductor interface energy, $H_c = H_{c1}$, $H_c = H_{c2}$ or the long-range vortex asymptotics. However if one uses microscopic theory for that consideration, one gets corrections to this behavior - more in agreement with the actual experimental observations [18].

1.4 The Lawrence-Doniach model for layered superconductors

The Lawrence-Doniach model [19] can be understood as a modification of the anisotropic Ginzburg-Landau theory for the extremely anisotropic (layered) materials, where the discrete superconducting layers are only weakly coupled in the perpendicular direction. It is widely applied to the high-T_c cuprate superconductors as it is able to capture their highly anisotropic behavior which in some cases even becomes effectively two-dimensional (as expected from a stack of decoupled superconducting film planes). We will refer to this model in Chapter 7, where we will use its modification to study a superconducting bilayer composed of two single-band superconductors.

In the Lawrence-Doniach model the layered superconductors are viewed as a stacked array of two-dimensional superconductors. Within each layer

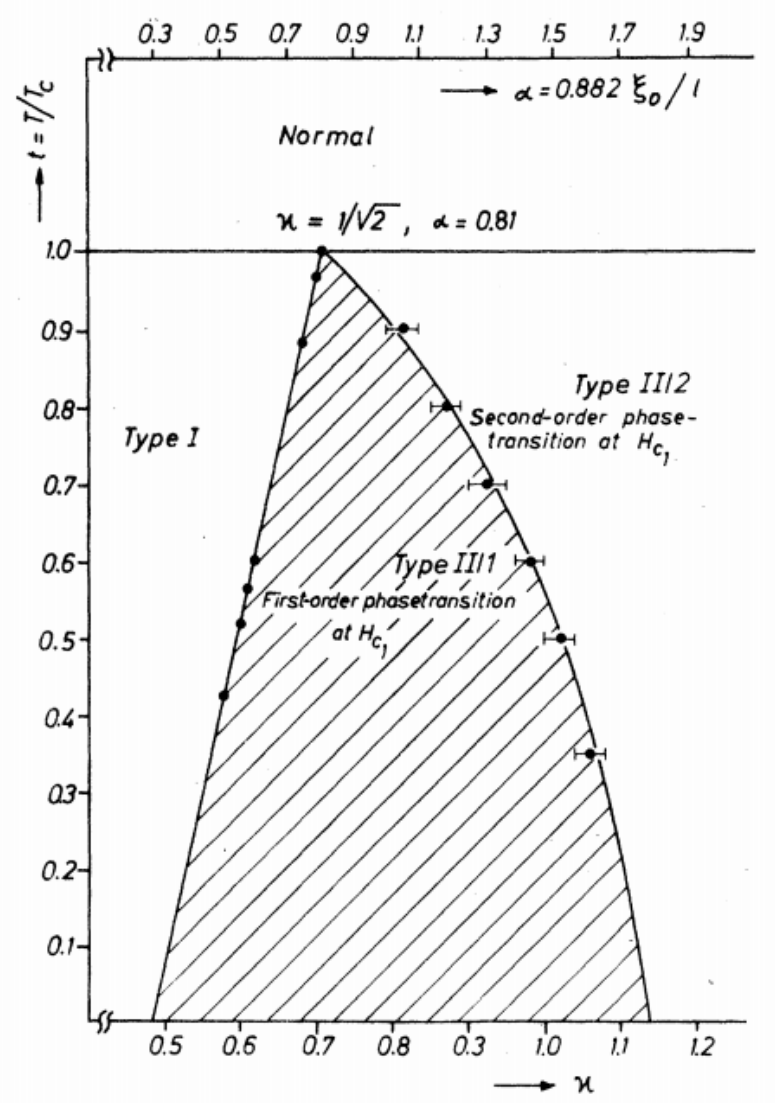

Figure 1.3: Phase diagram of the magnetic behavior for the TaN system. Both the Ginzburg-Landau parameter κ (lower abscissa) and the impurity parameter α (upper abscissa) are proportional to the amount of dissolved nitrogen. From Ref. [14].

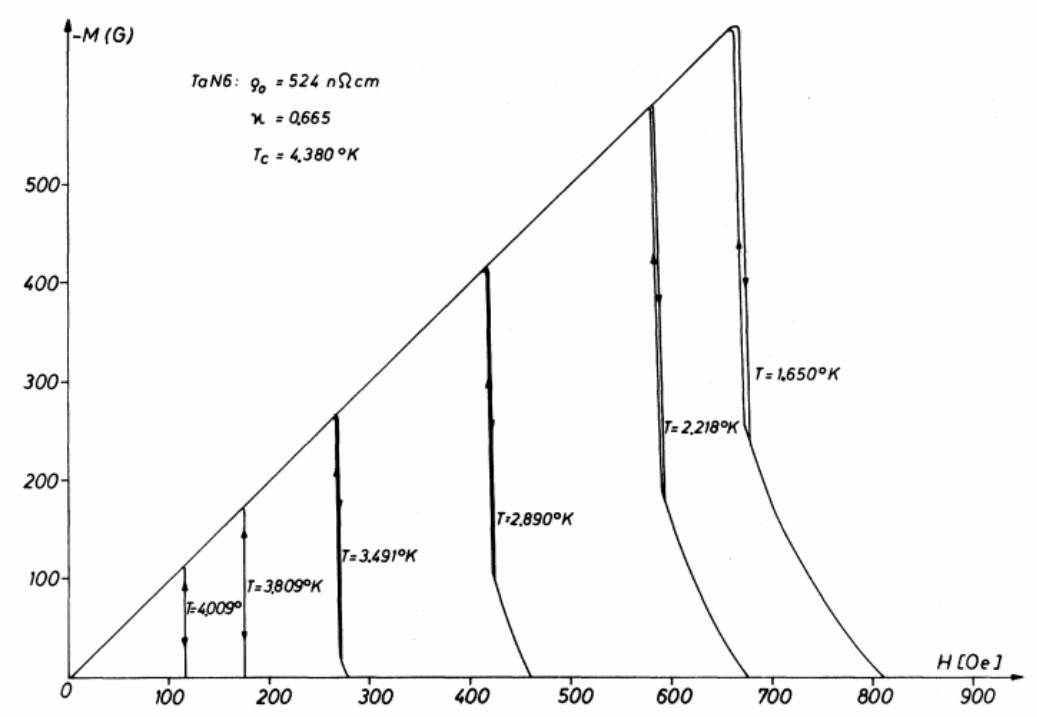

Figure 1.4: Magnetization curves for TaN sample with $\kappa = 0.665$, exhibiting the type-I behavior at the higher temperatures, and type-II/1 behavior at the lower temperatures. In the latter, the magnetization shows a discontinuity at H_{c1}, i.e., first order transition to the intermediate state. From Ref. [14].

the GL order parameter $\Psi_n(x, y)$ is a 2D function. The layers are coupled together by Josephson tunneling between adjacent layers. When the superconducting coherence length ξ is much larger than the distance between the layers, as is for example always the case close to T_c, the effective behavior is three-dimensional and the Lawrence-Doniach model gives essentially the same results as the anisotropic Ginzburg-Landau theory. If the coherence length is insufficient to "bridge" the layers, the effective behavior becomes two-dimensional. Let us take the layers to be in the ab plane, while the perpendicular direction will be denoted c as usual in crystallography. The Cartesian coordinates x and y then lie in the ab plane, while the z axis is along the c direction. The perpendicular distance between the layers is denoted by s. Then in the absence of the magnetic field we can write the free energy of the Lawrence-Doniach model as

$$F = \sum_n s \int \Big[\alpha|\Psi_n|^2 + \frac{1}{2}\beta|\Psi_n|^4 + \frac{\hbar^2}{2m_{ab}}\left(\left|\frac{\partial\Psi_n}{\partial x}\right|^2 + \left|\frac{\partial\Psi_n}{\partial y}\right|^2\right) + \frac{\hbar^2}{2m_c s^2}\left|\Psi_n - \Psi_{n-1}\right|^2\Big] dS, \tag{1.29}$$

where the sum runs over the layers and the integral is over the area of each layer. At this point we have only introduced different effective masses m_{ab} and m_c to describe different modes of charge transport within each layer and between neighboring layers and discretized the derivative along the z-direction. The reason to call the last term Josephson coupling becomes clear if we write $\Psi = |\Psi_n|e^{i\varphi_n}$ and assume that the amplitude of the order parameter $|\Psi_n|$ is the same same in all layers. Then that term becomes simply

$$\frac{\hbar^2}{m_c s^2}\left|\Psi_n\right|^2\left[1 - \cos(\varphi_n - \varphi_{n-1})\right], \tag{1.30}$$

and is seen to have the same form as the Josephson energy. If we minimize variationally the Lawrence-Doniach free energy Eq. (1.29) with respect to Ψ_n^* we get the LD equation for Ψ_n

$$\alpha\Psi_n + \beta|\Psi_n|^2\Psi_n - \frac{\hbar^2}{2m_{ab}}\left(\frac{\partial^2}{\partial x^2} + \frac{\partial^2}{\partial y^2}\right)\Psi_n - \frac{\hbar^2}{2m_c s^2}(\Psi_{n+1} - 2\Psi_n + \Psi_{n-1}) = 0, \tag{1.31}$$

where in the last term we recognize the discrete second derivative. With the inclusion of magnetic field i.e. non-zero vector potential $\mathbf{A}$ we would have

$$\alpha\Psi_n + \beta|\Psi_n|^2\Psi_n - \frac{\hbar^2}{2m_{ab}}(\nabla - i\frac{2e}{\hbar c}\mathbf{A})^2\Psi_n - \frac{\hbar^2}{2m_c s^2}(\Psi_{n+1}e^{-2ieA_z s/\hbar c} - 2\Psi_n + \Psi_{n-1}e^{2ieA_z s/\hbar c}) = 0. \tag{1.32}$$

In the m_{ab} term the gradient operator ∇ and $\mathbf{A}$ are two-dimensional vectors in the xy plane.

We recover the anisotropic GL theory if the variation of Ψ along the z direction is smooth enough so that we can replace $(\Psi_n - \Psi_{n+1})/s$ with $\partial\Psi/\partial z$. For example Eq. (1.32) becomes

$$\alpha\Psi + \beta|\Psi|^2\Psi - \frac{\hbar^2}{2}(\nabla - i\frac{2e}{\hbar c}\mathbf{A})\left(\frac{1}{m}\right)(\nabla - i\frac{2e}{\hbar c}\mathbf{A})\Psi = 0, \tag{1.33}$$

where $1/m$ is the reciprocal mass tensor i.e. $\mathrm{diag}(1/m_{ab}, 1/m_{ab}, 1/m_c)$.

1.5 The BCS theory

In the last two sections of this chapter we turn our attention to the microscopic theories of superconductivity, namely the Bardeen-Cooper-Schrieffer (BCS) theory and the Bogoliubov-de Gennes theory. We will later employ the two-gap version of these theories in Chapter 6 to study the gap amplitudes and the vortex size as a function of temperature.

The conjecture by Fröhlich that it is the interaction between phonons and electrons which is responsible for superconductivity dates back to 1950, when also the *isotope effect* was discovered.[4] The isotope effect is the observation that the superconducting samples made of a different isotope of the same chemical element have a different critical temperature, roughly following $T_c \propto M^{-1/2}$, where M is the mass of the relevant ion. When a compound does show isotope effect, it is a strong indication that the superconductivity is mediated by the lattice vibrations, i. e. phonons, whose characteristic frequency (and therefore also energy) $\omega_{\mathbf{q}}$ is also proportional to $M^{-1/2}$.

The interaction between electrons mediated by phonons can be effectively attractive for the electrons with energies within the small energy window around the Fermi energy E_F despite the ever-present Coulomb repulsion.[5] For the case of the phonon-mediated interaction, this energy window is the Debye energy $\hbar\omega_D$. This is the typical energy scale of the phonons present in the material and can be about 0.03 eV - 0.1 eV (few hundreds of Kelvin).

It was Cooper who realized that with no matter how small attractive interaction between electrons the Fermi sea becomes unstable with respect

[4] It was long believed that these two events happened independently, but it recently appeared that Fröhlich, himself a theorist, might have been aware of the early experimental data on the isotope effect [20].

[5] The derivation of this result can be found in the lecture notes by Piers Coleman [21], section on Interacting electrons and phonons and the chapter on the BCS theory, in the lecture notes by Timm Carsten [22] and in various textbooks on superconductivity.

to creation of bound states of two electrons in the time-reversed states $|\mathbf{k},\uparrow\rangle$ and $|-\mathbf{k},\downarrow\rangle$, so called *Cooper pairs*. One can then guess that the new ground state of the system would be a superposition of states built up from these pairs, which is captured in the following ansatz

$$|\Psi_{BCS}\rangle = \prod_{\mathbf{k}} (u_{\mathbf{k}}^* + v_{\mathbf{k}}^* c_{\mathbf{k}\uparrow}^\dagger c_{-\mathbf{k},\downarrow}^\dagger)|0\rangle, \tag{1.34}$$

where $|0\rangle$ is the true vacuum i.e. state without any electrons and $u_{\mathbf{k}}$ and $v_{\mathbf{k}}$ are complex coefficients characterizing the probability that the specific Cooper pair state is unoccupied or occupied. We demand the BCS wave function to be normalized: $\langle\Psi_{BCS}|\Psi_{BCS}\rangle = 1$:

$$\begin{aligned}
\langle\Psi_{BCS}|\Psi_{BCS}\rangle &= \prod_{\mathbf{k}} \langle 0|(u_{\mathbf{k}} + v_{\mathbf{k}} c_{-\mathbf{k},\downarrow} c_{\mathbf{k}\uparrow})(u_{\mathbf{k}}^* + v_{\mathbf{k}}^* c_{\mathbf{k}\uparrow}^\dagger c_{-\mathbf{k},\downarrow}^\dagger)|0\rangle \\
&= \prod_{\mathbf{k}} \langle 0||u_{\mathbf{k}}|^2 + |v_{\mathbf{k}}|^2 c_{-\mathbf{k},\downarrow} c_{\mathbf{k}\uparrow} c_{\mathbf{k}\uparrow}^\dagger c_{-\mathbf{k},\downarrow}^\dagger|0\rangle \\
&= \prod_{\mathbf{k}} \langle 0||u_{\mathbf{k}}|^2 + |v_{\mathbf{k}}|^2 c_{-\mathbf{k},\downarrow} (1 - c_{\mathbf{k}\uparrow}^\dagger c_{\mathbf{k}\uparrow}) c_{-\mathbf{k},\downarrow}^\dagger|0\rangle \\
&= \prod_{\mathbf{k}} (|u_{\mathbf{k}}|^2 + |v_{\mathbf{k}}|^2) \stackrel{!}{=} 1.
\end{aligned} \tag{1.35}$$

Therefore it is sufficient to require

$$|u_{\mathbf{k}}|^2 + |v_{\mathbf{k}}|^2 = 1 \tag{1.36}$$

individually for each $\mathbf{k}$ for the BCS wave function $|\Psi_{BCS}\rangle$ to be normalized (any other choice would select some special values of $\mathbf{k}$).

It is important to note that the wave function $|\Psi_{BCS}\rangle$ is a combination of states with different number of Cooper pairs, ranging from zero Cooper pairs to all electrons paired. The average number of particles in the condensate is

$$\begin{aligned}
\langle N\rangle &= \sum_{\mathbf{k}\sigma} \langle\Psi_{BCS}|c_{\mathbf{k}\sigma}^\dagger c_{\mathbf{k}\sigma}|\Psi_{BCS}\rangle \\
&= \sum_{\mathbf{k}} \langle 0|(u_{\mathbf{k}} + v_{\mathbf{k}} c_{-\mathbf{k},\downarrow} c_{\mathbf{k}\uparrow})(c_{\mathbf{k}\uparrow}^\dagger c_{\mathbf{k}\uparrow} + c_{-\mathbf{k},\downarrow}^\dagger c_{-\mathbf{k},\downarrow})(u_{\mathbf{k}}^* + v_{\mathbf{k}}^* c_{\mathbf{k}\uparrow}^\dagger c_{-\mathbf{k},\downarrow}^\dagger)|0\rangle \\
&= 2\sum_{\mathbf{k}} |v_{\mathbf{k}}|^2 = \frac{2\Omega}{(2\pi)^3} \int d\mathbf{k}\, |v_{\mathbf{k}}|^2,
\end{aligned} \tag{1.37}$$

which scales as a system volume Ω. On the other hand, the variance of the particle number $\sqrt{\langle (N - \langle N\rangle)^2\rangle} = \sqrt{\langle N^2\rangle - \langle N\rangle^2}$ is only proportional

to $\sqrt{\Omega}$. Since for any macroscopic system $\Omega \gg \sqrt{\Omega}$, the typical number of particles described by the BCS wave function is a well-defined quantity.

The BCS theory models the attraction between the electrons in the following way:

$$V_{\mathbf{k}\mathbf{k}'} = \begin{cases} -V & \text{if } |\xi_{\mathbf{k}}| < \omega_D \text{ and } |\xi_{\mathbf{k}'}| < \omega_D \\ 0 & \text{otherwise ,} \end{cases} \tag{1.38}$$

neglecting the repulsive part of the interaction. Then the many-body Hamiltonian is

$$\hat{H} = \sum_{\mathbf{k},\sigma} \xi_{\mathbf{k}} c^{\dagger}_{\mathbf{k}\sigma} c_{\mathbf{k}\sigma} - \frac{1}{\Omega} \sum_{\mathbf{k},\mathbf{k}'} V_{\mathbf{k}\mathbf{k}'} c^{\dagger}_{\mathbf{k}\uparrow} c^{\dagger}_{-\mathbf{k}\downarrow} c_{-\mathbf{k}'\downarrow} c_{\mathbf{k}'\uparrow} + \text{h.c.}, \tag{1.39}$$

where

$$\xi_{\mathbf{k}} = \frac{\hbar^2 \mathbf{k}^2}{2m} - \mu \tag{1.40}$$

is the kinetic energy of the electrons measured with respect to the chemical potential μ, here written in the parabolic band approximation. The chemical potential is present because the wave function (1.34) does not describe a state with the fixed number of particles, therefore we need to work in the grand-canonical ensemble. In the Hamiltonian (1.39) we only included the scattering of Cooper pairs from the state $(\mathbf{k}' \uparrow, -\mathbf{k}' \downarrow,)$ to $(\mathbf{k} \uparrow, -\mathbf{k} \downarrow)$. This is firstly because Cooper pairs formed by electrons with opposite spin will have lower energy due to the Pauli exclusion principle.[6] Secondly, provided that the Fermi surface is spherical, the scattering of Cooper pairs from the state $(\mathbf{k}', -\mathbf{k}')$ to $(\mathbf{k}, -\mathbf{k})$ has the largest "phase-space" available from all $(\mathbf{k}' + \mathbf{Q}, -\mathbf{k}') \rightarrow (\mathbf{k} + \mathbf{Q}, -\mathbf{k})$ possibilities.[7]

The next step is to find the coefficients $u_{\mathbf{k}}$ and $v_{\mathbf{k}}$ which would minimize the ground state energy $E_s = \langle \Psi_{BCS} | \hat{H} | \Psi_{BCS} \rangle$. Using Eqs. (1.34) and (1.39),

[6] There are however few exceptional materials such as Sr_2RuO_4, ^{3}He, where the pairing occurs between the fermions with the same spin (so-called triplet superconductivity/superfluidity).

[7] Non-zero Cooper-pair center-of-mass momentum $\mathbf{Q}$ can be favorable for Fermi surfaces possessing a non-trivial nesting vector i.e. some (nearly) parallel portions of Fermi surface. This is much more likely to occur in one- or two-dimensional systems and in multiband materials. Such pairing is then called the *FFLO state* (after Fulde, Ferrel, Larkin and Ovchinnikov) or the *Cooper-pair density wave*, but it has yet to be convincingly experimentally observed. Interesting theoretical studies exploring the FFLO state in multiband superconductors are e. g. Refs. [23, 24].

one finds:

$$E_s = \langle \Psi_{BCS}| \sum_{\mathbf{k},\sigma} \xi_{\mathbf{k}} c^\dagger_{\mathbf{k}\sigma} c_{\mathbf{k}\sigma} - \frac{1}{\Omega} \sum_{\mathbf{k},\mathbf{k}'} V_{\mathbf{k}\mathbf{k}'} c^\dagger_{\mathbf{k}\uparrow} c^\dagger_{-\mathbf{k}\downarrow} c_{-\mathbf{k}'\downarrow} c_{\mathbf{k}'\uparrow} + \text{h.c.} |\Psi_{BCS}\rangle$$
$$= 2 \sum_{\mathbf{k}} \xi_{\mathbf{k}} |v_{\mathbf{k}}|^2 - \frac{1}{\Omega} \sum_{\mathbf{k},\mathbf{k}'} (V_{\mathbf{k}\mathbf{k}'} u_{\mathbf{k}'} v_{\mathbf{k}} v^*_{\mathbf{k}'} u^*_{\mathbf{k}} + \text{c.c.}), \tag{1.41}$$

where the sums are restricted to electrons in the Debye window around the Fermi energy. The contribution of the interaction term can be seen from the physical term it describes: we started from the occupied Cooper pair state $(\mathbf{k}', -\mathbf{k}')$ and empty $(\mathbf{k}, -\mathbf{k})$ and we ended in occupied $(\mathbf{k}, -\mathbf{k})$, but empty $(\mathbf{k}', -\mathbf{k}')$. The occupied Cooper pair gives a factor of v, the empty u, with the corresponding momentum index. Finally the starting states are complex conjugated.

Now, taking $u_{\mathbf{k}}$ and $v_{\mathbf{k}}$ real,[8] the normalization condition (1.36) is automatically satisfied by the following parametrization:

$$u_{\mathbf{k}} = \sin(\theta_{\mathbf{k}}), \tag{1.42}$$
$$v_{\mathbf{k}} = \cos(\theta_{\mathbf{k}}). \tag{1.43}$$

Then we have

$$E_s = \sum_{\mathbf{k}} 2\xi_{\mathbf{k}} \cos^2 \theta_{\mathbf{k}} - \frac{1}{2\Omega} \sum_{\mathbf{k}\mathbf{k}'} V_{\mathbf{k}\mathbf{k}'} \sin 2\theta_{\mathbf{k}} \sin 2\theta_{\mathbf{k}'}, \tag{1.44}$$

which is minimal when:

$$\tan(2\theta_{\mathbf{k}}) = -\Delta_{\mathbf{k}}/\xi_{\mathbf{k}}, \tag{1.45}$$

where

$$\Delta_{\mathbf{k}} = \frac{1}{2\Omega} \sum_{\mathbf{k}'} V_{\mathbf{k}\mathbf{k}'} \sin(2\theta_{\mathbf{k}'}) = \frac{1}{\Omega} \sum_{\mathbf{k}'} V_{\mathbf{k}\mathbf{k}'} u_{\mathbf{k}'} v^*_{\mathbf{k}'}. \tag{1.46}$$

In the last equation the complex form of u and v has been recovered on the basis of Eq. (1.41).

We employ the trigonometric identities $\cos(\arctan x) = 1/\sqrt{1+x^2}$ and $\cos(2x) = 2\cos^2 x - 1$ to find

$$v_{\mathbf{k}} = \frac{\Delta^*_{\mathbf{k}}}{|\Delta_{\mathbf{k}}|} \sqrt{\frac{1}{2}(1 - \frac{\xi_{\mathbf{k}}}{E_{\mathbf{k}}})}, , \tag{1.47}$$
$$u_{\mathbf{k}} = \sqrt{\frac{1}{2}(1 + \frac{\xi_{\mathbf{k}}}{E_{\mathbf{k}}})}, \tag{1.48}$$

[8] This is not necessary, but it simplifies the calculation. We can take one of them real, because there is a global phase associated to $|\Psi_{BCS}\rangle$ and the remaining phase can be for the moment absorbed into the phase of $V_{\mathbf{k}\mathbf{k}'}$, if needed.

where

$$E_{\mathbf{k}} = \sqrt{\Delta_{\mathbf{k}}^2 + \xi_{\mathbf{k}}^2}, \tag{1.49}$$

and the complex phase of v was recovered from Eq. (1.46), while u has been chosen to be real.

Finally we insert the coefficients u and v from Eqs. (1.47) into Eq. (1.46) to get the celebrated *BCS gap equation* (so far at $T = 0$):

$$\Delta_{\mathbf{k}} = \frac{1}{\Omega} \sum_{\mathbf{k}'} V_{\mathbf{k}\mathbf{k}'} \frac{\Delta_{\mathbf{k}'}}{2E_{\mathbf{k}'}}. \tag{1.50}$$

The finite temperature version of Eq. (1.50) is

$$\Delta_{\mathbf{k}} = \frac{1}{\Omega} \sum_{\mathbf{k}'} V_{\mathbf{k}\mathbf{k}'} \frac{\Delta_{\mathbf{k}'}}{2E_{\mathbf{k}'}} \tanh(\frac{E_{\mathbf{k}'}}{2T}), \tag{1.51}$$

and can be derived in the more general way through treating the BCS Hamiltonian in the mean-field manner, thereby making it quadratic, using the Bogoliubov transformation to diagonalize it, and identifying new excitations - bogoliubons - as noninteracting fermions.

For the model BCS interaction $V_{\mathbf{k}\mathbf{k}'}$ (Eq. (1.38)) which is isotropic, the quantity $\Delta_{\mathbf{k}}$ is actually $\mathbf{k}$-independent, $\Delta_{\mathbf{k}} = \Delta$.

1.6 The Bogoliubov-de Gennes equations

The Bogoliubov-de Gennes (BdG) theory allows one to consider superconducting condensate and excitations (as in the BCS theory), but now in a spatially dependent situation, for example in the presence of impurities or vortices. We will solve the two-band BdG equations numerically in Chapter 6 to find the temperature dependence of the vortex core size in the two-band superconductors, in the interesting limit of vanishing interband coupling.

BdG equations are a generalization of Hartree-Fock equations for the case of superconductivity. They consist of two Schrödinger-like equations coupled by a pair potential $\Delta(\mathbf{r})$ (also called order parameter). The BdG equations should be solved self-consistently with the expressions for the Hartree-Fock potential $U(\mathbf{r})$ and the order parameter. In this thesis I only present the basic equations following de Gennes's book [12]. The details of numerical implementation of the BdG equations can be found in the PhD thesis of Yajiang Chen [25].

Bogoliubov-de Gennes equations We first rewrite the Hamiltonian of an interacting electron system in terms of field operators $\hat{\Psi}(\mathbf{r}\alpha)$,

$$\hat{H} = \hat{H}_0 + \hat{H}_1, \tag{1.52}$$

$$\hat{H}_0 = \int d\mathbf{r} \sum_{\alpha} \hat{\Psi}^\dagger(\mathbf{r}\alpha) H_e(\mathbf{r}) \hat{\Psi}(\mathbf{r}\alpha), \tag{1.53}$$

$$\hat{H}_1 = -\frac{1}{2} V \int d\mathbf{r} \sum_{\alpha\beta} \hat{\Psi}^\dagger(\mathbf{r}\alpha) \hat{\Psi}^\dagger(\mathbf{r}\beta) \hat{\Psi}(\mathbf{r}\beta) \hat{\Psi}(\mathbf{r}\alpha), \tag{1.54}$$

where α and β denote spin and

$$H_e(\mathbf{r}) = \frac{1}{2m_e}(-i\hbar\nabla - \frac{e\mathbf{A}}{c})^2 + U_0(\mathbf{r}) - \mu, \tag{1.55}$$

where $\mathbf{A}$ is the vector potential of the external magnetic field and μ the chemical potential. We do not take into account that the electron spins could be flipped due to the magnetic field. U_0 is an arbitrary spin-independent external potential. Furthermore, the interaction between electrons V has been modeled by a simple spin-independent contact potential $V(\mathbf{r}, \mathbf{r}') = V\delta(\mathbf{r}-\mathbf{r}')$.

The field operators are defined through the expansion in terms of electron creation and annihilation operators $c^\dagger_{\mathbf{k}\alpha}$ and $c_{\mathbf{k}\alpha}$ using some complete set of single-electron wave functions $w_{\mathbf{k}}(\mathbf{r})$ as follows:[9]

$$\hat{\Psi}(\mathbf{r}\alpha) = \sum_{\mathbf{k}} w_{\mathbf{k}}(\mathbf{r}) c_{\mathbf{k}\alpha}, \tag{1.56}$$

$$\hat{\Psi}^\dagger(\mathbf{r}\alpha) = \sum_{\mathbf{k}} w^*_{\mathbf{k}}(\mathbf{r}) c^\dagger_{\mathbf{k}\alpha}. \tag{1.57}$$

They satisfy the anticommutation rules

$$[\hat{\Psi}(\mathbf{r}\alpha), \hat{\Psi}^\dagger(\mathbf{r}'\beta)]_+ = \delta_{\alpha\beta}\delta(\mathbf{r}-\mathbf{r}'), \tag{1.58}$$

$$[\hat{\Psi}(\mathbf{r}\alpha), \hat{\Psi}(\mathbf{r}'\beta)]_+ = 0, \tag{1.59}$$

$$[\hat{\Psi}^\dagger(\mathbf{r}\alpha), \hat{\Psi}^\dagger(\mathbf{r}'\beta)]_+ = 0. \tag{1.60}$$

Now we want to replace the interaction term $V\hat{\Psi}^\dagger\hat{\Psi}^\dagger\hat{\Psi}\hat{\Psi}$ by the sum of terms such as $V\langle\hat{\Psi}^\dagger\hat{\Psi}^\dagger\rangle\hat{\Psi}\hat{\Psi}$. We try the effective Hamiltonian of the form

$$\hat{H}_{\text{eff}} = \int d\mathbf{r}\{\sum_{\alpha}[\hat{\Psi}^\dagger(\mathbf{r}\alpha) H_e(\mathbf{r}) \hat{\Psi}(\mathbf{r}\alpha) + U(\mathbf{r})\hat{\Psi}^\dagger(\mathbf{r}\alpha)\hat{\Psi}(\mathbf{r}\alpha)] + \Delta(\mathbf{r})\hat{\Psi}^\dagger(\mathbf{r}\uparrow)\hat{\Psi}^\dagger(\mathbf{r}\downarrow) + \Delta^*(\mathbf{r})\hat{\Psi}(\mathbf{r}\downarrow)\hat{\Psi}(\mathbf{r}\uparrow)\}. \tag{1.61}$$

[9] They must satisfy $\sum_{\mathbf{k}} w^*_{\mathbf{k}}(\mathbf{r}) w_{\mathbf{k}}(\mathbf{r}') = \delta(\mathbf{r}-\mathbf{r}')$. One possible choice are the plane waves $w_{\mathbf{k}}(\mathbf{r}) = e^{i\mathbf{k}\cdot\mathbf{r}}$.

The first term represents the kinetic energy of the electrons, the second is the Hartree-Fock energy, and the last two terms arise due to the formation of the Cooper pairs.

Disregarding for the moment that we do not know the precise form of $U(\mathbf{r})$ and $\Delta(\mathbf{r})$, the effective Hamiltonian is quadratic and as such it can be diagonalized by some linear combination of the original field operators (the Bogoliubov-Valatin transformation):

$$\hat{\Psi}^\dagger(\mathbf{r}\uparrow) = \sum_n [u_n^*(\mathbf{r})\gamma_{n\uparrow}^\dagger - v_n(\mathbf{r})\gamma_{n\downarrow}], \tag{1.62}$$

$$\hat{\Psi}^\dagger(\mathbf{r}\downarrow) = \sum_n [u_n^*(\mathbf{r})\gamma_{n\downarrow}^\dagger + v_n(\mathbf{r})\gamma_{n\uparrow}], \tag{1.63}$$

and

$$\hat{\Psi}(\mathbf{r}\uparrow) = \sum_n [u_n(\mathbf{r})\gamma_{n\uparrow} - v_n^*(\mathbf{r})\gamma_{n\downarrow}^\dagger], \tag{1.64}$$

$$\hat{\Psi}(\mathbf{r}\downarrow) = \sum_n [u_n(\mathbf{r})\gamma_{n\downarrow} + v_n^*(\mathbf{r})\gamma_{n\uparrow}^\dagger]. \tag{1.65}$$

The physical meaning of, for example, the first transformation is that the state with spin up can be created either by adding a particle with spin up or by removing a particle with spin down (creating a hole). Therefore $u_n(\mathbf{r})$ and $v_n(\mathbf{r})$ are called particle-like and hole-like wave functions respectively. New operators $\gamma_{n\sigma}$ and $\gamma_{n\sigma}^\dagger$ must be fermionic,

$$[\gamma_{n\alpha}, \gamma_{m\beta}^\dagger]_+ = \delta_{\alpha\beta}\delta_{nm}, \tag{1.66}$$

$$[\gamma_{n\alpha}, \gamma_{m\beta}]_+ = 0, \tag{1.67}$$

and also it must hold

$$\sum_n u_n^*(\mathbf{r})u_n(\mathbf{r}') + v_n(\mathbf{r})v_n^*(\mathbf{r}') = \delta(\mathbf{r}-\mathbf{r}') \tag{1.68}$$

so that the anticommutation relations for $\hat{\Psi}$'s are satisfied. We want the new γ operators to diagonalize the effective Hamiltonian of the excitations above the ground state:

$$\hat{H}_{\text{eff}} = \sum_{n\alpha} E_n \gamma_{n\alpha}^\dagger \gamma_{n\alpha}, \tag{1.69}$$

where E_g is the energy of the ground state and E_n is the energy of the quasiparticles created by $\gamma_{n\alpha}^\dagger$ and destroyed by $\gamma_{n\alpha}$. This can be reformulated as:

$$[\hat{H_{\text{eff}}}, \gamma_{n\alpha}] = -E_n\gamma_{n\alpha}, \tag{1.70}$$

$$[\hat{H_{\text{eff}}}, \gamma_{n\alpha}^\dagger] = E_n\gamma_{n\alpha}^\dagger. \tag{1.71}$$

We confront these relations with the commutators of $\hat{H}_{\text{eff}}$ with the field operators:

$$[\hat{\Psi}(\mathbf{r}\uparrow), \hat{H}_{\text{eff}}] = [H_e(\mathbf{r}) + U(\mathbf{r})]\hat{\Psi}(\mathbf{r}\uparrow) + \Delta(\mathbf{r})\hat{\Psi}^\dagger(\mathbf{r}\downarrow), \tag{1.72}$$

$$[\hat{\Psi}(\mathbf{r}\downarrow), \hat{H}_{\text{eff}}] = [H_e(\mathbf{r}) + U(\mathbf{r})]\hat{\Psi}(\mathbf{r}\downarrow) - \Delta(\mathbf{r})\hat{\Psi}^\dagger(\mathbf{r}\uparrow). \tag{1.73}$$

By comparing the coefficients of operators $\gamma_{n\alpha}$ and $\gamma^\dagger_{n\alpha}$ when we evaluate $[\hat{\Psi}(\mathbf{r}\downarrow), \hat{H}_{\text{eff}}]$, we get the *Bogoliubov-de Gennes equations*:

$$\begin{pmatrix} H_e(\mathbf{r}) + U(\mathbf{r}) & \Delta(\mathbf{r}) \\ \Delta^*(\mathbf{r}) & -H_e^*(\mathbf{r}) - U(\mathbf{r}) \end{pmatrix} \begin{pmatrix} u_n(\mathbf{r}) \\ v_n(\mathbf{r}) \end{pmatrix} = E_n \begin{pmatrix} u_n(\mathbf{r}) \\ v_n(\mathbf{r}) \end{pmatrix}. \tag{1.74}$$

Self-consistency conditions Demanding that the effective Hamiltonian and the original Hamiltonian be stationary for the same wave functions, the self-consistency equations are found to be [12, 26]:

$$U(\mathbf{r}) = -V\langle\hat{\Psi}^\dagger(\mathbf{r}\uparrow)\hat{\Psi}(\mathbf{r}\uparrow)\rangle = -V\langle\hat{\Psi}^\dagger(\mathbf{r}\downarrow)\hat{\Psi}(\mathbf{r}\downarrow)\rangle, \tag{1.75}$$

$$\Delta(\mathbf{r}) = -V\langle\hat{\Psi}(\mathbf{r}\downarrow)\hat{\Psi}(\mathbf{r}\uparrow)\rangle = V\langle\hat{\Psi}(\mathbf{r}\uparrow)\hat{\Psi}(\mathbf{r}\downarrow)\rangle. \tag{1.76}$$

We now rewrite the above in terms of γ-operators and then evaluate the thermal averages using the Fermi-Dirac distribution (since they are free fermions):

$$\langle\gamma^\dagger_{n\alpha}\gamma_{m\beta}\rangle = \delta_{nm}\delta_{\alpha\beta}f^{(n)}_{FD} \tag{1.77}$$

$$\langle\gamma_{n\alpha}\gamma_{m\beta}\rangle = 0, \tag{1.78}$$

where the Fermi-Dirac distribution is

$$f^{(n)}_{FD} = \frac{1}{e^{E_n/k_BT} + 1}. \tag{1.79}$$

Then we have

$$U(\mathbf{r}) = -V\sum_n [|u_n(\mathbf{r})|^2 f^{(n)}_{FD} + |v_n(\mathbf{r})|^2(1 - f^{(n)}_{FD})], \tag{1.80}$$

$$\Delta(\mathbf{r}) = V\sum_n u_n(\mathbf{r})v_n^*(\mathbf{r})(1 - 2f^{(n)}_{FD}). \tag{1.81}$$

Note that the summation in the expression for $U(\mathbf{r})$ goes over all electronic states, while the one in $\Delta(\mathbf{r})$ term is limited to the states in the Debye window $|\xi_n| < \hbar\omega_D$ where

$$\xi_n = \int d\mathbf{r}\{u_n^*(\mathbf{r})[H_e(\mathbf{r}) + U(\mathbf{r})]u_n(\mathbf{r}) + v_n^*(\mathbf{r})[H_e(\mathbf{r}) + U(\mathbf{r})]v_n(\mathbf{r})\} \tag{1.82}$$

is the original single particle energy plus the Hartree-Fock energy. If there is external magnetic field, the single electron Hamiltonian H_e should nevertheless be taken as if $\mathbf{A} = 0$. Finally the chemical potential is also determined self-consistently in order to get the correct density of electrons

$$n_e = \frac{2}{\Omega} \int d\mathbf{r} \sum_n [|u_n(\mathbf{r})|^2 f_n + |v_n(\mathbf{r})|^2 (1 - f_n)]. \tag{1.83}$$

Chapter 2

Two-gap superconductivity

2.1 Multi-gap superconductors

The superconducting electrons often originate from multiple bands crossing the Fermi surface. The amplitude of the superconducting gap for these bands is in general not the same. If these amplitudes differ to the extent that the overall behavior seen in experiments is no longer well-described within the single gap picture, we classify the material as a multi-gap superconductor. The experimental evidence for such relatively unusual situation is seen for example in the results of electronic specific heat measurements $c_v(T)$, in the heat current experiments, in the behavior of the second critical field $H_{c2}(T)$ and in the density of states determined by STM. We will discuss these experiments more in the following sections.

In the 2001 the story of the two-gap superconductors, the topic of this thesis, gained momentum with the discovery of the phonon-mediated superconductor magnesium diboride MgB_2 with critical temperature of 39 K. The MgB_2 crystal structure, band structure and gap values distribution as a function of energy are displayed in Fig. 2.1. It was not the first multigap superconductor, however it was the first one with very clearly observable multiple gaps and its discovery lead to great development in the theory of the multigap systems.

In 2008 another large family of iron-based superconductors was discovered and while they do not (so far) reach the critical temperatures of the cuprates, they are clearly not explained by exclusively phonon-mediated mechanism. They are composed of iron-pnictide layers typically intercalated with other elements, see Fig. 2.2. Despite their layered structure, their properties are less anisotropic than those of cuprates. There are always multiple bands crossing the Fermi surface. Most often the bands are quite regular cylinders,

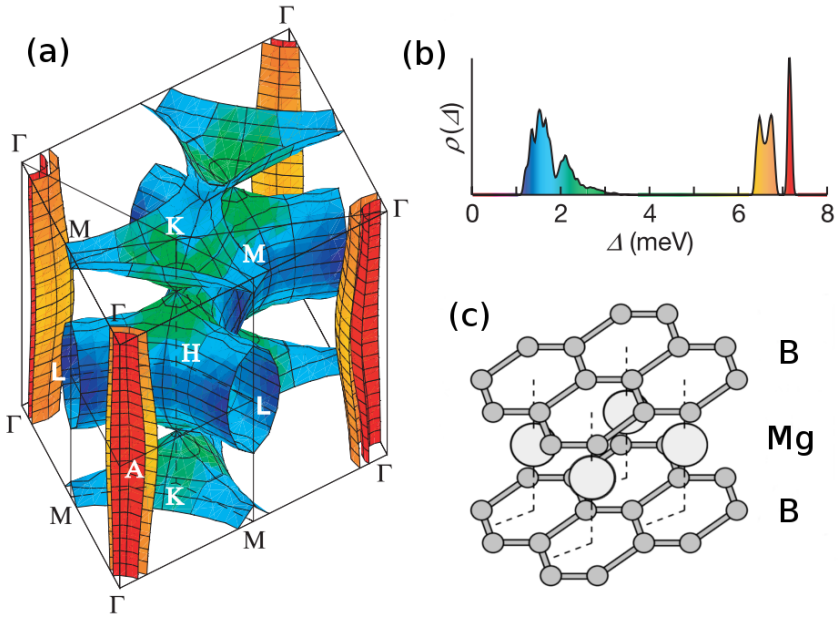

Figure 2.1: (a) The band structure, (b) the gap values distribution as a function of energy and (c) the crystal structure of magnesium diboride, a two-gap superconductor with critical temperature of 39 K. From Ref. [27].

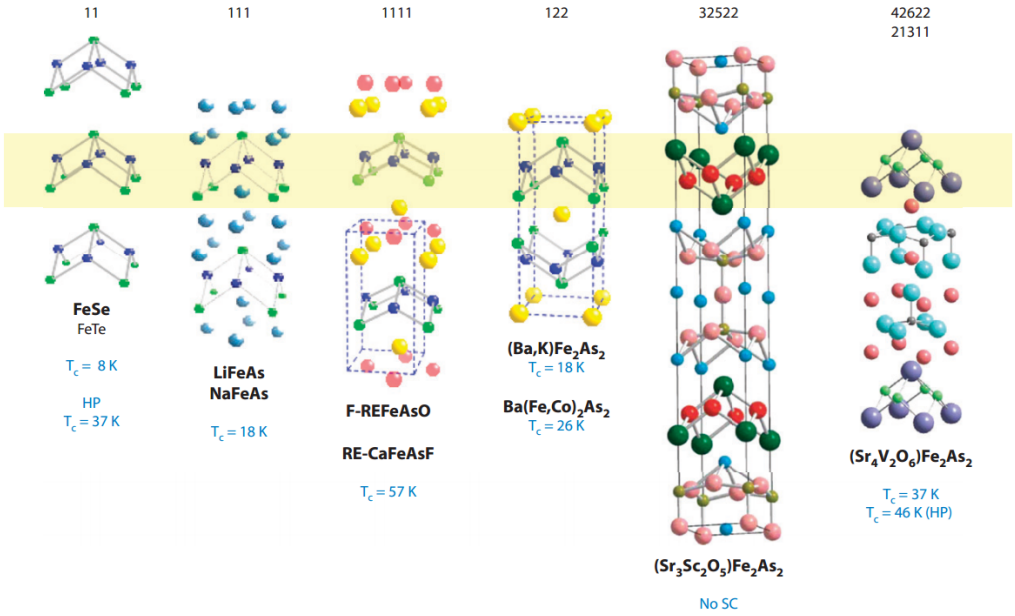

Figure 2.2: The crystal structure of five so-far discovered families of iron-based superconductors and one potential candidate structure. T_c is the maximum critical temperature achieved in the particular family, HP stands for high pressure. From Ref. [28].

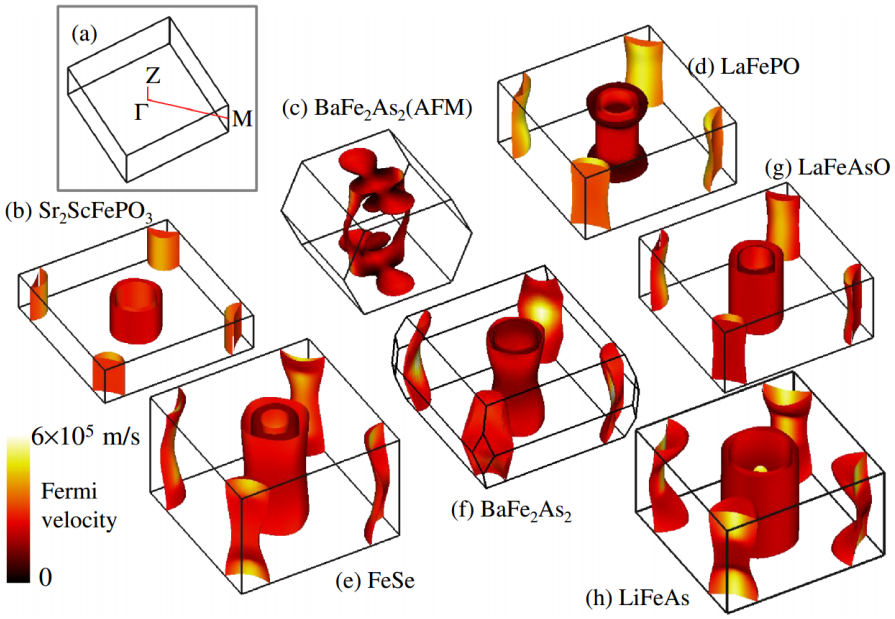

Figure 2.3: The band structure of selected iron-based superconductors (with the exception of panel (c) which shows antiferromagnetic parent compound $BaFe_2As_2$). From Ref. [29].

with different portions of the Fermi surface well nested as depicted in Fig. 2.3. In some materials the dispersion along the z axis (warping) becomes significant, though the basic cylindrical topology is preserved. Yet some other ($Ba_{1-x}K_xFe_2As_2$, KFe_2As_2 [30]) have Fermi surface sheets at the corner of the Brillouin zone shaped as a four-bladed propeller, preventing the nesting completely.

2.2 Experimental signatures of two-gap superconductivity

Experimental probes which are especially well suited to study superconductors (multigap or otherwise) can be roughly divided into four big groups:

1. Bulk probes - magnetization, transport, heat capacity, magnetic penetration depth;

2. Direct vortex imaging - Bitter decoration, magneto-optical imaging, scanning SQUID microscopy, scanning Hall probe microscopy, transmission electron microscopy;

3. Scattering experiments - Neutron scattering, muon spin rotation (determining the **k**-space structure, i.e., periodicity of the vortex lattice);

4. Tunneling of quasiparticles or Cooper pairs - ARPES, STM, STS - gap size, Point-contact spectroscopy, Josephson effect ...

In this section we will exemplify some experimental results obtained with these techniques on multiband superconductors. Signatures of two-gap superconductivity can be found, e.g., in the density of states measured by STM (MgB_2, LiFeAs), in the superfluid density, or in the Little-Parks effect. Since this thesis studies predominantly the physics of vortices in two-gap superconductors, we will devote a separate section to the discussion of the vortex imaging techniques.

2.3 Vortex matter in two-band superconductors

The vortex matter is experimentally studied with direct vortex imaging techniques. Experiments sensitive directly to the vortex magnetic field and with sufficient spatial resolution to resolve individual vortices are:

- Bitter decoration,
- magneto-optical imaging,
- scanning SQUID microscopy,
- scanning Hall probe microscopy,
- transmission electron microscopy (TEM).

Additionally, *scanning tunneling microscopy* (STM) can also resolve individual vortices, but it is sensitive to local density of states and through it to local gap function $|\Delta(\mathbf{r})|$, rather than $\mathbf{B}(\mathbf{r})$. For each of the techniques there is a trade-off between field sensitivity (or more generally signal-to-noise ratio) and spatial resolution. Another practical issue is the time required to get a single image frame.

Bitter decoration The Bitter decoration is a mature technique with spatial resolution of about 80 nm, and rather poor sensitivity. It provides no other information besides the vortex positions. The sample must be cleaned before repeating the experiment. It is used in small applied fields $H < 10$

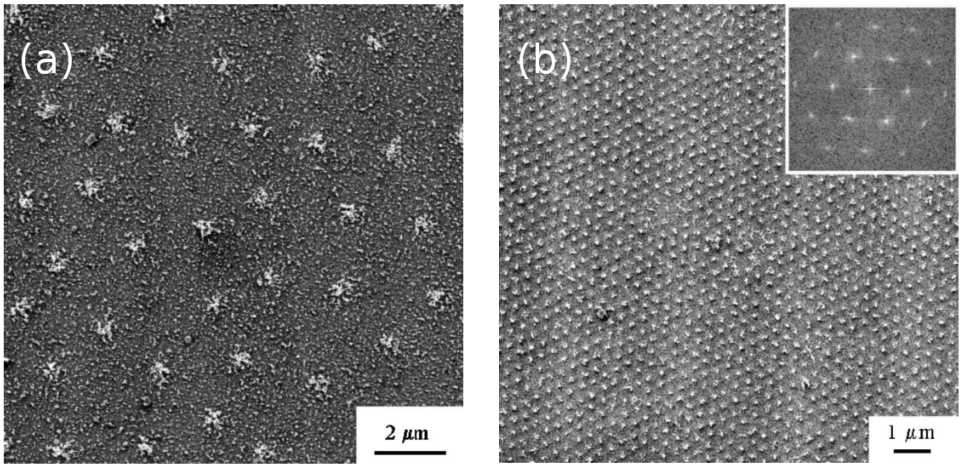

Figure 2.4: The vortices in MgB_2 imaged by Bitter decoration technique. (a) Small field B $\approx$ 4.4 G, $T \approx 6$ K, (b) At 200 Oe. From Ref. [32].

mT. The pinning forces increase on cooling, therefore vortices get stuck at their positions at some temperature T^* in between T_c and the chamber base temperature. T^* may be as high as 0.8 - 0.9 T_c [31]. Therefore the imaged vortex positions may not correspond to the ground state at the base temperature, which is a known caveat of the Bitter decoration technique. The images of vortices in MgB_2 obtained by Bitter decoration are shown in Fig. 2.4 and Fig. 2.5. The earlier data by Vinnikov *et al.* show regular Abrikosov lattice at higher field 200 Oe, and some signatures of slight disorder at lower field. The later data by Moshchalkov *et al.* showed very inhomogeneous vortex distribution with pronounced stripes with higher vortex density and depleted regions between them. This unusual behavior has been explained in terms of the presence of long-range attraction between vortices. It was named "Type-1.5 superconductivity" because it was proposed to be originating from the interplay between type-I superconductivity in the π-band of MgB_2 and type-II superconductivity in the σ-band. It should be noted that it is not clear whether the π-band indeed bears type-I superconductivity and even if it did the behavior of two coupled bands (the effective (coupled) GL parameter κ and bands' healing lengths) is related to their individual properties in a nontrivial manner, as we shall discuss in the Chapter 4 and the Chapter 5.

Magneto-optical imaging This is another relatively old technique, with strength in high imaging speed; therefore it can access magnetic flux dynamics. One typically uses yttrium iron garnet or EuSe films as these materials change their optical properties most strongly under the applied magnetic

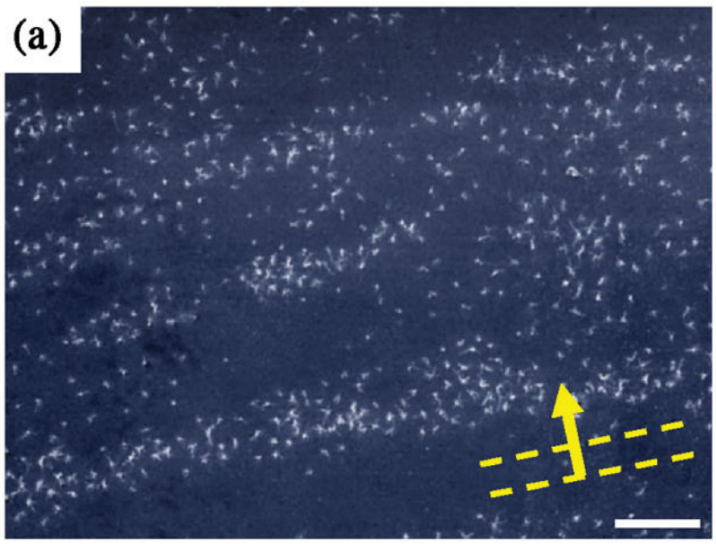

Figure 2.5: The vortices in MgB_2 imaged by Bitter decoration technique at $H = 5$ Oe. The scale bar corresponds to 10 μm. From Ref. [1].

field. This technique is limited by its spatial resolution. Only a few groups have achieved single-vortex resolution, therefore it is mostly used to study type-I superconductors (example shown in Fig. 1.1) and for phenomena occurring close to H_c.

Scanning SQUID microscopy This is one of the techniques with the highest sensitivity. Spatial resolution is mainly limited by microfabrication capabilities, however recently nano SQUID on tip has been fabricated [33], which suggests that in the nearest future images of much higher quality will be available. The technique is based on the fact that the critical current of the SQUID device depends on the flux Φ_a passing through it as $I_c^{SQUID} = 2I_c|\cos(\pi\Phi_a/\Phi_0)|$. The results of the SQUID microscopy on the "type-1.5" crystal from Ref. [34] are reproduced in Fig. 2.6. Significant clustering is visible, though the exact vortex positions had to be obtained by fitting because the resolution was not sufficiently high.

Scanning Hall probe microscopy This technique typically uses Hall probes made of the semiconductor heterostructure $GaAs/Al_{0.3}Ga_{0.7}As$. It provides a nice compromise between spatial resolution of about 200 nm and sensitivity 100 nT·Hz$^{-1/2}$. It is not good for measuring absolute values of local magnetic induction due to presence of the variable offset voltage between measurements. However, the sensitivity to relative changes is very good,

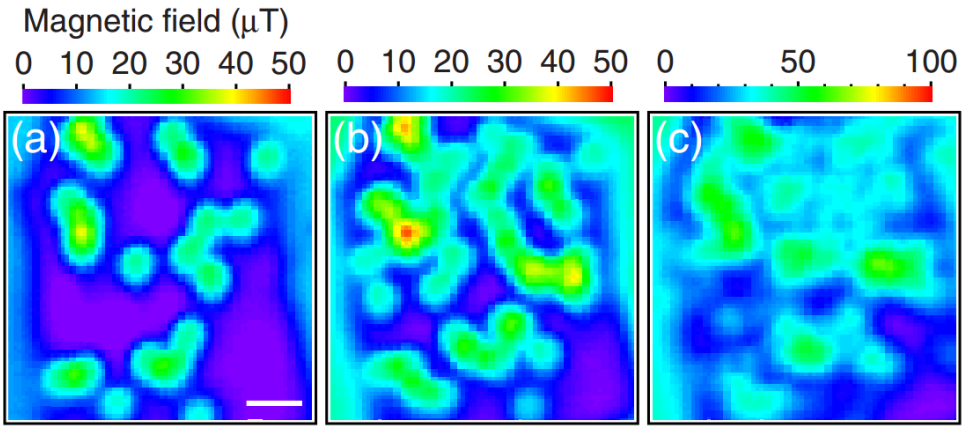

Figure 2.6: Scanning SQUID microscope images of vortices at (a) 10 μT, (b) 20 μT, and (c) 50μT for a MgB_2 single crystal. A scale bar corresponds to 10 μm. From Ref. [34].

which makes it ideal for imaging. Very interesting images of MgB_2 showing vortices forming chains were obtained by Gutierrez *et al.* [35], see Fig. 2.7.

Transmission electron microscopy (TEM) This technique requires very thin sample sections for enabling the electrons to cross the sample. For superconductors [cryo-Lorentz transmission electron microscopy (cryo-LTEM)] it started to gain importance only recently as it has been implemented in Cambridge [36, 37] and Lausanne [38] and used to image vortices in MgB_2.

Scanning tunneling microscopy (STM) For reviews see, e.g., Ref. [39–41]. Figure 2.8 shows STM images of vortices in MgB_2 from Ref. [42].

Hanaguri *et al.* [43] imaged vortices in LiFeAs with unprecedented resolution and were able not only to image the vortex lattice (Fig. 2.9), but also to study the size of the vortex as a function of temperature (Fig. 2.10).

Song *et al.* [44] argued that the dopant clustering, electronic inhomogeneity and disordered vortex lattice *in iron-pnictides* are caused by dopant ionic size mismatch. This could explain why $Ba_{0.6}K_{0.4}Fe_2As_2$ [45] displays a regular Abrikosov lattice, while the closely related $BaFe_{1.8}Co_{0.2}As_2$ [46] (see Fig. 2.11) and $Sr_{0.75}K_0.25Fe_2As_2$ [44] display only short-range hexagonal order, lost at larger distances.

To conclude this section, let us discuss how it might be possible to reconcile the different vortex imaging experiments on MgB_2. We do this with the help of Fig. 2.12 (taken from Ref. [35]), which gives the nearest neighbor distance $d_{vv}(B)$ summarized from different experiments on the con-

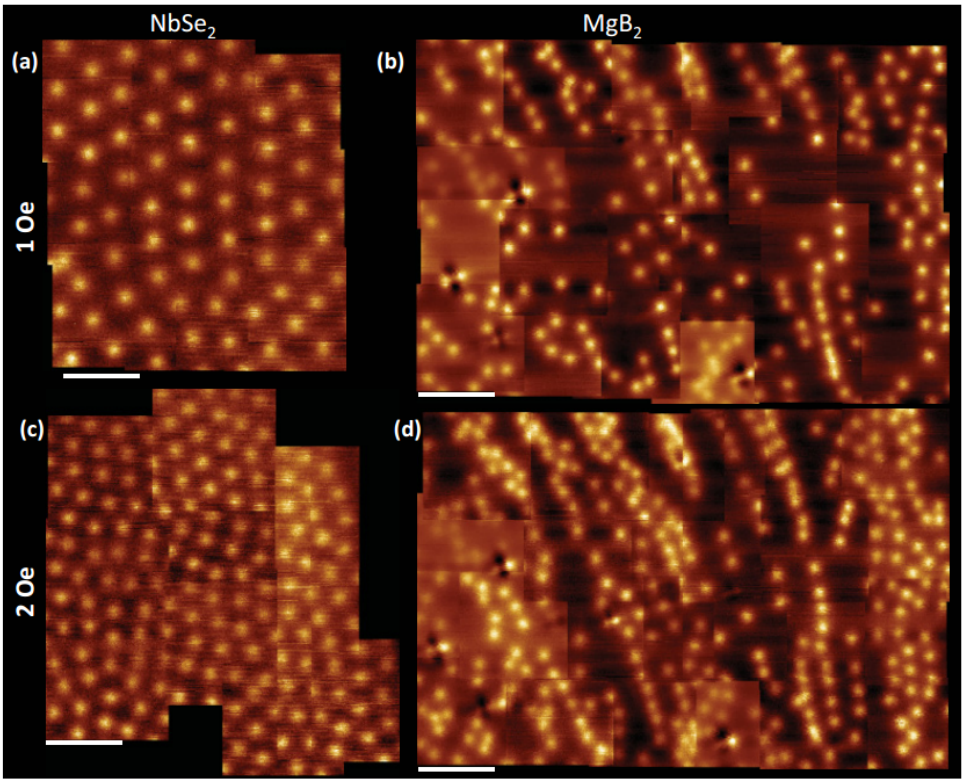

Figure 2.7: Scanning Hall probe microscopy images after performing field cooling (FC) at 1 Oe for the (a) $NbSe_2$ and (b) MgB_2 single crystals; and after doing FC at 2 Oe for (c) $NbSe_2$ and (d) MgB_2 single crystals. Images are taken at 4.2 K. The white bar on each picture corresponds to a length of 10 μm. From Ref. [35].

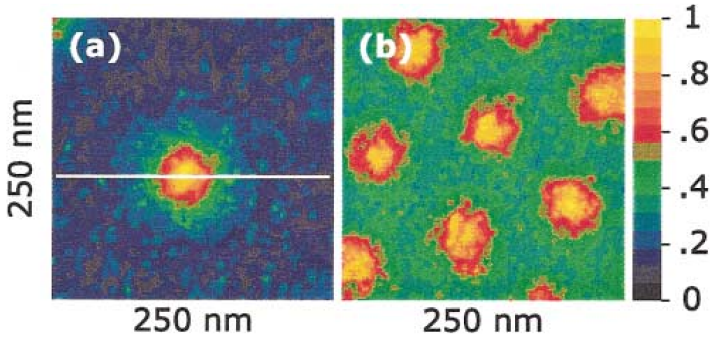

Figure 2.8: The vortices in MgB_2 imaged by Scanning Tunneling microscopy. 250×250 nm^2 spectroscopic images of a single vortex induced by an applied field of 0.05 T (a), and the vortex lattice at 0.2 T (b). From Ref. [42].

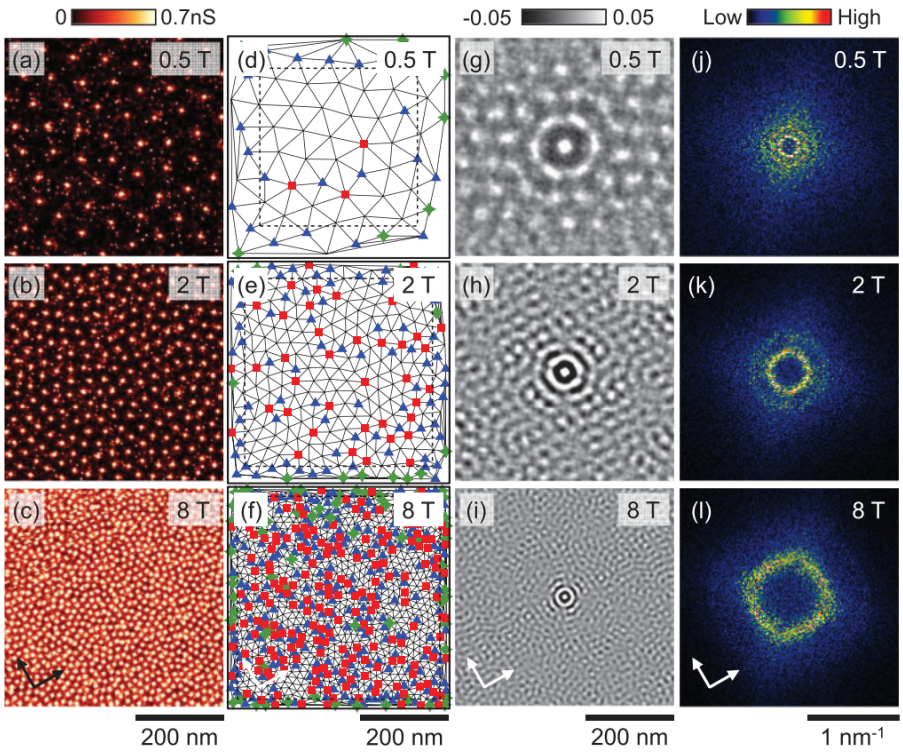

Figure 2.9: The vortices in LiFeAs imaged by Scanning Tunneling microscopy. (a)-(c) Images of vortices at 1.5 K obtained by mapping tunneling conductance at E_F. Arrows denote the nearest Fe-Fe direction. (d)-(f) Delaunay triangulation diagrams obtained from vortex images shown in (a)-(c). Vertices with symbols denote vortices with coordination numbers different from conventional value of 6 (blue triangle, 5; red square, 7; green star, others). (g)-(i) Two-dimensional autocorrelation function calculated from vortex images shown in (a)-(c). (j)-(l) Two-dimensional Fourier transformations from vortex images shown in (a)-(c). From Ref. [43].

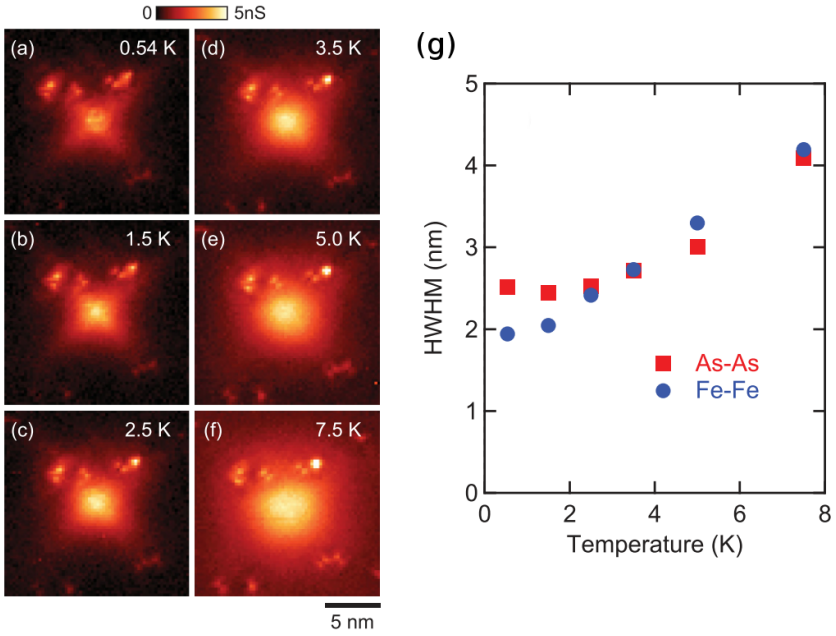

Figure 2.10: (a)-(f) A vortex in LiFeAs imaged at increasing temperatures by Scanning Tunneling microscopy. (g) Temperature dependence of the vortex core size along Fe-Fe and As-As bond directions. Adapted from Ref. [43].

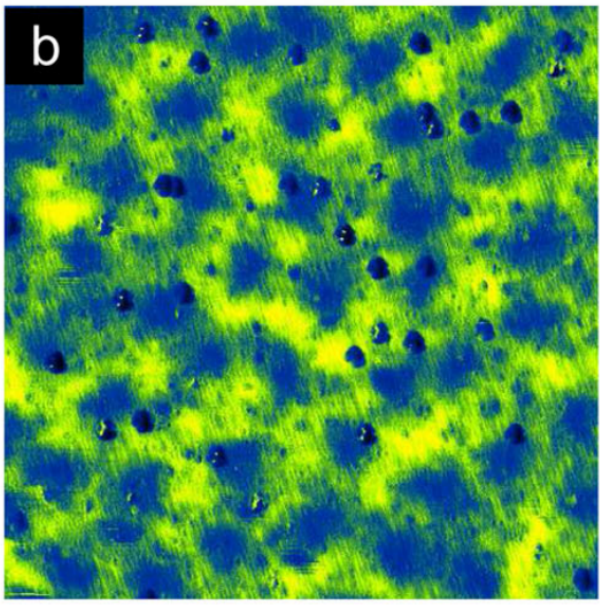

Figure 2.11: Vortices (big dark spots) in $BaFe_{1.8}Co_{0.2}As_2$ imaged by Scanning Tunneling Microscopy at a field of 9 T and temperature $T = 6.15$ K. Smaller sharper spots are impurities. Interestingly, the vortices, while being disordered, are not pinned to the visible impurities. From Ref. [46].

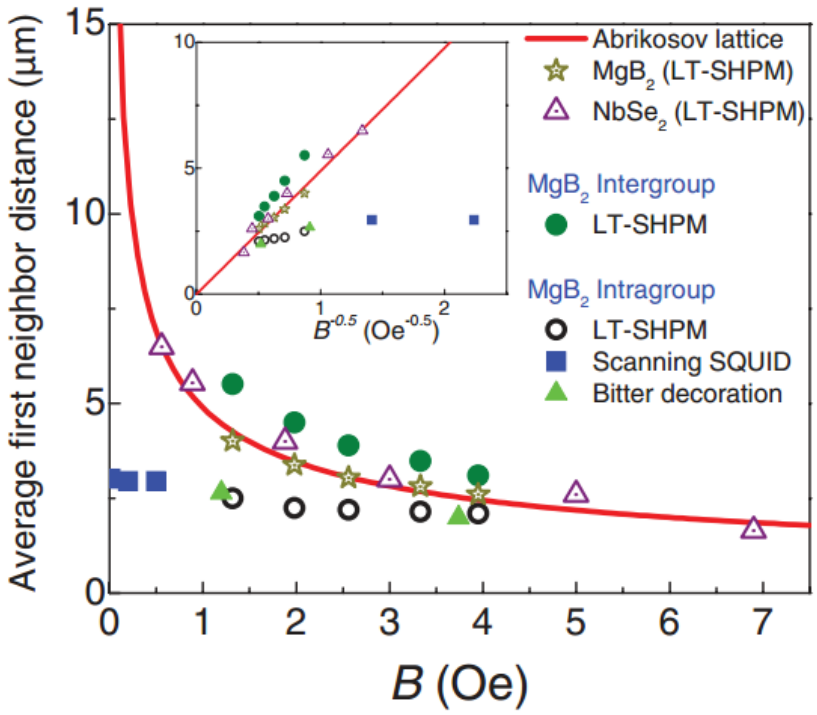

Figure 2.12: Average nearest neighbor distance as a function of B for an $NbSe_2$ single crystal (open triangles), an MgB_2 single crystal (open stars), and for a perfect Abrikosov lattice (solid line). Additionally, the intergroup nearest neighbor distances for an MgB_2 single crystal is shown (full dots) as well as the intragroup nearest neighbor distances for different MgB_2 single crystals; squares, triangles, and open dots correspond to scanning Squid microscopy, Bitter decoration, and to SHPM results, respectively. The inset shows the same data as a function of $1/\sqrt{B}$. From Ref. [35].

ventional superconductor $NbSe_2$ (which follows nicely the expected value $B = (2/\sqrt{3})\Phi_0/d_{vv}^2$ for a perfect Abrikosov lattice) and compares them with different experiments on "type-1.5"-crystals. From this figure one can conclude that behavior qualitatively different from the usual type-2-like homogeneous vortex distribution is expected for very low vortex densities, i.e., fields lower than $\approx$ 3-4 Oe. At higher fields one observes an Abrikosov lattice, as for example in the STM experiment by Eskildsen *et al.* [42] and TEM experiments [36–38]. Most interesting then is to analyze the Bitter decoration data by Vinnikov *et al.* [32], see also Fig. 2.4, who imaged the MgB_2 single crystals both at a higher field 200 Oe, where they see the Abrikosov lattice and at a field at the onset of unconventional vortex interaction at B $\approx$ 4.4

G, where they indeed see much more disorder (still allowing for alternative explanation due to pinning). This suggests that different experiments are not in disagreement, but are rather studying vortex matter in MgB_2 in different regimes - the low field regime below $\approx$ 3-4 Oe where vortices experience mid-range attraction, and the high-field regime above this threshold, where they interact through short-range repulsion. The minimum of the intervortex interaction potential seems to be at about 2.5 μm. This is somewhat puzzling, since it is not obvious from which microscopic scale this originates as it is much more than the estimates of coherence lengths for MgB_2 which are of the order of tens of nanometers, see, e.g., Ref. [1, 42, 47], and of the magnetic field penetration depth which may be around 100 nm [48].

2.4 Theoretical models of two-gap superconductors

2.4.1 Standard two-gap Ginzburg-Landau theory

The standard two-gap Ginzburg-Landau free energy functional contains the single-gap terms for both bands plus a Josephson-like coupling term proportional to the temperature-independent *Josephson coupling* Γ:

$$\begin{aligned} f \;= f_{n0} + \;& \sum_{j=1,2} \alpha_j |\Psi_j|^2 + \frac{1}{2}\beta_j |\Psi_j|^4 + \frac{1}{2m_j}\left|\left(\frac{\hbar}{i}\nabla - \frac{2e}{c}\mathbf{A}\right)\Psi_j\right|^2 \\ & -\Gamma(\Psi_1^*\Psi_2 + \Psi_1\Psi_2^*) + \frac{\mathbf{h}^2}{8\pi}. \end{aligned} \tag{2.1}$$

This form of the Ginzburg-Landau free energy functional can be derived from the microscopic two-gap BCS theory, e.g., following Ref. [49]. Let us now consider the bulk situation without applied magnetic field and close to T_c so that $|\Psi_j|$ are small enough for us to be able to neglect the $|\Psi_j|^4$ terms. Therefore the superconducting free energy density reduces to:

$$f = \alpha_1|\Psi_1|^2 + \alpha_2|\Psi_2|^2 - 2\Gamma|\Psi_1||\Psi_2|\cos(\Delta\phi), \tag{2.2}$$

where $\Delta\phi = \phi_1 - \phi_2$ is the phase difference between the two condensates. Now depending on the sign of the Josephson coupling Γ three situations are possible:

- $\Gamma > 0$, for which the free energy is minimized by adopting $\Delta\phi = 0$,
- $\Gamma < 0$, where the stable situation is $\Delta\phi = \pi$, and finally

- $\Gamma = 0$, that is *decoupled bands*, where the energy is independent of the relative phase of the two condensates.

Notice also that in the first two cases the relative phase is locked and the two-gap superconductor shows $U(1)$ symmetry, while in the last case the symmetry is $U(1) \times U(1)$, a fact that is found to have profound consequences in Chapter 6.

Now, taking aside the special case when $\Gamma = 0$ in which case the gaps have two independent critical temperatures T_{c1} and T_{c2},[1] we may assume without the loss of generality that $\Gamma > 0$ and therefore the phases of two condensates are the same. Then $f = \alpha_1|\Psi_1|^2 + \alpha_2|\Psi_2|^2 - 2\Gamma|\Psi_1||\Psi_2|$ is minimized by solution of the system of two homogeneous equations

$$\alpha_1(T)\Psi_1 - \Gamma\Psi_2 = 0, \tag{2.3}$$
$$-\Gamma\Psi_1 + \alpha_2(T)\Psi_2 = 0. \tag{2.4}$$

By definition the highest temperature at which this system of equations has nontrivial solution is the critical temperature T_c. From elementary algebra we know that this corresponds to the situation when the determinant of the coefficients on the left hand side equals zero, that is,

$$\alpha_1(T_c)\alpha_2(T_c) - \Gamma^2 = 0. \tag{2.5}$$

From this however follows that provided $\Gamma \neq 0$, neither of the α_j can be zero at T_c! This is in dire contrast with the single-gap situation where in order to properly describe the second order phase transition α must be zero at T_c (since it is changing sign there). This means that in the two-gap case α_j's are more appropriately expressed as $\alpha_j = \alpha_j(T_c) + a_1\tau$, with $\tau = (T - T_c)/T_c$ (where only the leading-order temperature dependence has been taken into account similarly to the single-gap case). Now, if we had $|\Psi| \propto \tau^{1/2}$, $\nabla|\Psi| \propto |\Psi|/\xi \propto \tau$ as in the single-gap case, all the terms of the free-energy density would scale as τ^2, with the exception of the terms $\alpha_j(T_c)|\Psi|^2$ and $\Gamma|\Psi_1||\Psi_2|$ which nominally scale just as τ. To treat these two terms on the equal ground as all the others, one has to calculate $|\Psi|$ to the $\tau^{3/2}$-precision. However, in the microscopic derivation of the theory the need for $\tau^{3/2}$ precision in the order parameters was never expected and indeed the higher order terms in the small expansion parameter $\tau = 1 - T/T_c$ are *incomplete*, as was first pointed out in Ref. [2]. We will provide a short explanation of how to calculate $|\Psi|$'s to the $\tau^{3/2}$-precision in Sec. 2.4.3.

[1] In our theoretical discussions we adopt convention $T_{c1} > T_{c2}$, so T_{c2} always refers to the weak-gap critical temperature.

2.4.2 Two-component Ginzburg-Landau equations

To derive the Ginzburg-Landau equations for the two-gap superconductor, we variationally minimize the free energy functional $\mathrm{F} = \int (G_{sH} - G_{nH}) d^3\mathbf{r}$ with respect to the functions Ψ_1^*, Ψ_2^* and $\mathbf{A}$. This leads to one equation for each order parameter:

$$\frac{1}{2m_1}\left(-i\hbar\nabla - \frac{2e}{c}\mathbf{A}\right)^2 \Psi_1 + \alpha_1\Psi_1 + \beta_1|\Psi_1|^2\Psi_1 - \Gamma\Psi_2 = 0, \tag{2.6}$$

$$\frac{1}{2m_2}\left(-i\hbar\nabla - \frac{2e}{c}\mathbf{A}\right)^2 \Psi_2 + \alpha_2\Psi_2 + \beta_2|\Psi_2|^2\Psi_2 - \Gamma\Psi_1 = 0, \tag{2.7}$$

and one equation describing the superconducting current

$$\mathbf{j} = \sum_{j=1,2}\left[-\frac{ie\hbar}{m_j}(\Psi_j^*\nabla\Psi_j - \Psi_j\nabla\Psi_j^*) - \frac{4e^2}{m_j c}|\Psi_j|^2\mathbf{A}\right]. \tag{2.8}$$

The superconducting current relates to the vector potential $\mathbf{A}$ through the Maxwell equation $\mathbf{j} = -\frac{c}{4\pi}\nabla^2\mathbf{A}$ (in the London gauge $\nabla\cdot\mathbf{A} = 0$).

Boundary conditions The boundary conditions are

$$\mathbf{n}\cdot\left(-i\hbar\nabla - \frac{2e}{c}\mathbf{A}\right)\Psi_1\Big|_{\text{boundary}} = 0 \tag{2.9}$$

$$\mathbf{n}\cdot\left(-i\hbar\nabla - \frac{2e}{c}\mathbf{A}\right)\Psi_2\Big|_{\text{boundary}} = 0 \tag{2.10}$$

as appropriate for the superconductor in contact with an insulator (or the vacuum) when no current shall pass perpendicular to the boundary of the sample. In the more general circumstances the boundary conditions would have a general de Gennes form [50]:

$$\mathbf{n}\cdot\left(-i\hbar\nabla - \frac{2e}{c}\mathbf{A}\right)\Psi_1\Big|_{\text{boundary}} = a\Psi_1 + b\Psi_2 \tag{2.11}$$

$$\mathbf{n}\cdot\left(-i\hbar\nabla - \frac{2e}{c}\mathbf{A}\right)\Psi_2\Big|_{\text{boundary}} = c\Psi_1 + d\Psi_2 \tag{2.12}$$

where a, b, c, d are constants depending on the surrounding material.

2.4.3 Extended Ginzburg-Landau (EGL) theory

Substantial effort has been made recently to improve the validity and descriptive power of the two-band Ginzburg-Landau theory by taking care to correctly include the higher order terms by Shanenko *et al.* in Refs. [3] and follow-up papers. As this is important and directly connected to the material presented in this thesis, the summary of these works will be given below.

Ideally, one wants to have a theory of two-gap superconductors which would describe well the multigap features, would be rigorous (mathematically consistent) and if possible simple enough to be amenable to further analytical and numerical work. The standard GL theory [49] has been shown to be mathematically inconsistent, since some terms go beyond the expected $\Delta \propto \tau^{1/2}$ precision to which the theory was originally developed in the single-gap case (there this problem does not arise) [2]. If one just discards the incomplete higher order terms, i.e., in the theory where Δ_j's are evaluated up to $\tau^{1/2}$ order, the order parameters are proportional to each other, $\Delta_1(\mathbf{r}) \propto \Delta_2(\mathbf{r})$. Due to this, the physics described by this "reduced" GL theory is the same as in the single-gap superconductor. The idea of the extended GL theory is to complete the next-to-leading-order $\tau^{3/2}$ terms and exclude any terms of order higher than $\tau^{3/2}$. This plan has been sketched in Ref. [3], and then fully realized in Ref. [51] for single-band and in Ref. [52] for two-band superconductors. Technically one proceeds as usual when deriving the GL theory (see, e.g., Fetter & Walecka textbook (Ref. [53], Sec. 53, p. 466)). First, one expands the self-consistent gap equation in the powers of the order parameter and its spatial gradients to the next-to-leading order. Second, one removes the unwanted terms beyond this precision. The resulting theory in the absence of the applied magnetic field is quite simple, and its predictions for the healing lengths of two order parameters have been analyzed numerically in Ref. [54], see also Chapter 5 of this thesis. The full two-band theory has been used to calculate the gap temperature dependence $\Delta_j(T)$ and the thermodynamic critical field H_c in Ref. [52], showing excellent agreement with the BCS theory. Further work detailing the phase diagram of the two-gap superconductors near the Bogomolnyi point $\kappa \approx 1/\sqrt{2}$ is under way [55].

For the calculations presented in this thesis I only made use of the two-gap extended Ginzburg-Landau theory in the absence of the magnetic field, for which I review the relevant derivations below. The absence of the magnetic field greatly simplifies the situation, because the electronic Green's function calculated to next-to-leading order in τ in the presence of the magnetic field is much more complicated than the one in zero magnetic field.

2.4.4 Single-gap EGL formalism

We start by formulating the Gor'kov equations as a Dyson equation for the Green function $\check{\mathcal{G}}_\omega$ in the Gor'kov-Nambu two by two matrix formalism (see, e.g., textbook by Zagoskin (Ref. [56])):

$$\check{\mathcal{G}}_\omega = \check{\mathcal{G}}^{(0)}_\omega + \check{\mathcal{G}}^{(0)}_\omega \check{\Delta} \check{\mathcal{G}}_\omega, \tag{2.13}$$

where

$$\hbar\omega = \pi k_B T(2n+1) \tag{2.14}$$

are the fermionic Matsubara frequencies.

The matrix (Gor'kov) Green's function is

$$\check{\mathcal{G}}_\omega = \begin{pmatrix} \mathcal{G}_\omega & \mathcal{F}_\omega \\ \tilde{\mathcal{F}}_\omega & \tilde{\mathcal{G}}_\omega \end{pmatrix}, \tag{2.15}$$

while for non-interacting electrons (quantities denoted by superscript (0)) we have

$$\check{\mathcal{G}}^{(0)}_\omega = \begin{pmatrix} \mathcal{G}^{(0)}_\omega & 0 \\ 0 & \tilde{\mathcal{G}}^{(0)}_\omega \end{pmatrix}. \tag{2.16}$$

The matrix gap operator $\check{\Delta}$ is defined as

$$\check{\Delta} = \begin{pmatrix} 0 & \hat{\Delta} \\ \hat{\Delta}^* & 0 \end{pmatrix}, \tag{2.17}$$

where $\langle \mathbf{r}|\hat{\Delta}|\mathbf{r}'\rangle = \delta(\mathbf{r}-\mathbf{r}')\Delta(\mathbf{r}')$ is an s-wave order parameter. The self-consistency equation for the order parameter $\Delta(\mathbf{r})$ reads

$$\Delta(\mathbf{r}) = -g k_B T \sum_\omega \mathcal{F}_\omega(\mathbf{r},\mathbf{r}), \tag{2.18}$$

where g is the coupling constant. The sum over Matsubara frequencies in this equation must be restricted to avoid the ultraviolet divergence.

After we multiply the matrices in Eq. (2.13), we get two Gor'kov equations

$$\mathcal{F}_\omega(\mathbf{r},\mathbf{r}') = \int d^3y \mathcal{G}^{(0)}_\omega(\mathbf{r},\mathbf{y})\Delta(\mathbf{y})\tilde{\mathcal{G}}_\omega(\mathbf{y},\mathbf{r}'), \tag{2.19}$$

and

$$\tilde{\mathcal{G}}_\omega(\mathbf{r},\mathbf{r}') = \tilde{\mathcal{G}}^{(0)}_\omega(\mathbf{r},\mathbf{r}') + \int d^3y \tilde{\mathcal{G}}^{(0)}_\omega(\mathbf{r},\mathbf{y})\Delta^*(\mathbf{y})\mathcal{F}_\omega(\mathbf{y},\mathbf{r}'). \tag{2.20}$$

In the absence of the magnetic field, the $\mathcal{G}_\omega^{(0)}$ is the usual Green's function of the non-interacting electrons

$$\mathcal{G}_\omega^{(0)}(\mathbf{r},\mathbf{y}) = \int \frac{d^3k}{(2\pi)^3} \frac{e^{i\mathbf{k}\cdot(\mathbf{r}-\mathbf{y})}}{i\hbar\omega - \xi_k}, \tag{2.21}$$

where $\xi_k = \hbar^2k^2/2m - \mu$ is the single-particle energy with respect to the chemical potential μ. Furthermore, $\tilde{\mathcal{G}}_\omega(\mathbf{r},\mathbf{y}) = -\mathcal{G}_{-\omega}(\mathbf{y},\mathbf{r})$, for example

$$\tilde{\mathcal{G}}_\omega^{(0)}(\mathbf{r},\mathbf{y}) = \int \frac{d^3k}{(2\pi)^3} \frac{e^{-i\mathbf{k}\cdot(\mathbf{r}-\mathbf{y})}}{i\hbar\omega + \xi_k}. \tag{2.22}$$

Now we need to evaluate the self-consistency equation Eq. (2.18). For this we use Eqs. (2.19) and (2.20) repeatedly to find expression for $\mathcal{F}_\omega(\mathbf{r},\mathbf{r})$ in terms of $\Delta(\mathbf{r})$ and $\mathcal{G}_\omega(\mathbf{r},\mathbf{y})$:

$$\begin{aligned}
\mathcal{F}_\omega(\mathbf{r},\mathbf{r}) &= \int d^3\mathbf{y}\mathcal{G}_\omega^{(0)}(\mathbf{r},\mathbf{y})\Delta(\mathbf{y})\tilde{\mathcal{G}}_\omega(\mathbf{y},\mathbf{r}) \\
&= \int d^3\mathbf{y}\mathcal{G}_\omega^{(0)}(\mathbf{r},\mathbf{y})\Delta(\mathbf{y})\tilde{\mathcal{G}}_\omega^{(0)}(\mathbf{y},\mathbf{r}) \\
&+ \int d^3\mathbf{y}d^3\mathbf{y}_1\mathcal{G}_\omega^{(0)}(\mathbf{r},\mathbf{y})\Delta(\mathbf{y})\tilde{\mathcal{G}}_\omega^{(0)}(\mathbf{y},\mathbf{y}_1)\Delta^*(\mathbf{y}_1)\mathcal{F}_\omega(\mathbf{y}_1,\mathbf{r}) = \dots
\end{aligned}$$

We do this until we have expression for Δ with the desired precision (which in the standard GL was Δ^3, in the extended GL it is Δ^5), and there we cut the expansion by taking $\tilde{\mathcal{G}}_\omega \approx \tilde{\mathcal{G}}_\omega^{(0)}$. Finally one can write:

$$\begin{aligned}
\Delta(\mathbf{r}) &= \int d^3yK_a(\mathbf{r},\mathbf{y})\Delta(\mathbf{y}) \\
&+ \int \prod_{j=1}^{3} d^3y_j K_b(\mathbf{r},\{\mathbf{y}\}_3)\Delta(\mathbf{y}_1)\Delta^*(\mathbf{y}_2)\Delta(\mathbf{y}_3) \\
&+ \int \prod_{j=1}^{5} d^3y_j K_c(\mathbf{r},\{\mathbf{y}\}_5)\Delta(\mathbf{y}_1)\Delta^*(\mathbf{y}_2)\Delta(\mathbf{y}_3)\Delta^*(\mathbf{y}_4)\Delta(\mathbf{y}_5),
\end{aligned} \tag{2.23}$$

where $\{\mathbf{y}\}_n = \{\mathbf{y}_1,\dots,\mathbf{y}_n\}$. The integral kernels are given by:

$$K_a(\mathbf{r},\mathbf{y}) = -gk_BT\sum_\omega \mathcal{G}_\omega^{(0)}(\mathbf{r},\mathbf{y})\tilde{\mathcal{G}}_\omega^{(0)}(\mathbf{y},\mathbf{r}), \tag{2.24}$$

$$K_b(\mathbf{r},\{\mathbf{y}\}_3) = -gk_BT\sum_\omega \mathcal{G}_\omega^{(0)}(\mathbf{r},\mathbf{y}_1)\tilde{\mathcal{G}}_\omega^{(0)}(\mathbf{y}_1,\mathbf{y}_2)\mathcal{G}_\omega^{(0)}(\mathbf{y}_2,\mathbf{y}_3)\tilde{\mathcal{G}}_\omega^{(0)}(\mathbf{y}_3,\mathbf{r}), \tag{2.25}$$

$$\begin{aligned}
K_c(\mathbf{r},\{\mathbf{y}\}_5) = -gk_BT\sum_\omega &\mathcal{G}_\omega^{(0)}(\mathbf{r},\mathbf{y}_1)\tilde{\mathcal{G}}_\omega^{(0)}(\mathbf{y}_1,\mathbf{y}_2)\mathcal{G}_\omega^{(0)}(\mathbf{y}_2,\mathbf{y}_3)\tilde{\mathcal{G}}_\omega^{(0)}(\mathbf{y}_3,\mathbf{y}_4) \\
&\times \mathcal{G}_\omega^{(0)}(\mathbf{y}_4,\mathbf{y}_5)\tilde{\mathcal{G}}_\omega^{(0)}(\mathbf{y}_5,\mathbf{r}).
\end{aligned} \tag{2.26}$$

Then, the nonlinear integral form of the self-consistency equation is transformed into the differential form by introducing the gradient expansion:

$$\Delta(\mathbf{y}_j) = \Delta(\mathbf{r} + \mathbf{z}_j) = \sum_{n=0}^{\infty} \frac{1}{n!} (\mathbf{z}_j \cdot \nabla_{\mathbf{r}})^n \Delta(\mathbf{r}). \tag{2.27}$$

By doing this one may in principle introduce a second expansion parameter $1/l_\Delta$, inverse length scale of the typical order parameter variations, because the relation between the order parameter and its gradient is not known beforehand (see full discussion in Ref. [51]). Fortunately from the standard single-band GL theory it turns out that as one approaches T_c not only the order parameter behaves as $\Delta \propto \tau^{1/2}$, but also its spatial variations occur on the length scale $\xi \propto \tau^{-1/2}$ (henceforth called GL coherence length). Therefore $\nabla\Delta \propto \tau$ and symbolically we can write $\nabla \propto \tau^{1/2}$, meaning the τ-order of each term in the GL expansion can be found by counting one power $\tau^{1/2}$ for each occurence of the order parameter or its gradient.

The coefficients of the partial differential equation governing Δ still have to be calculated by explicitly evaluating integrals in Eq. (2.23) to desired precision. The details of this lengthy calculation go beyond the scope of this thesis and can be found in Ref. [51], here we only quote the results. The first term in Eq. (2.23) evaluates to:

$$\begin{aligned} \int d^3y K_a(\mathbf{r}, \mathbf{y}) \Delta(\mathbf{y}) \approx (1 + gN(0)\tau + gN(0)\frac{\tau^2}{2})\Delta(\mathbf{x}) \qquad (2.28) \\ + \frac{gN(0)}{6}\hbar^2 v_F^2 W_3^2 (1 + 2\tau)\nabla^2\Delta(\mathbf{x}) \\ + \frac{gN(0)}{24}\hbar^4 v_F^4 W_5^4 \nabla^2(\nabla^2\Delta(\mathbf{x})), \qquad (2.29) \end{aligned}$$

where v_F is Fermi velocity, $N(0)$ total density of states at Fermi energy, $W_3^2 = \frac{7\zeta(3)}{8\pi^2 k_B^2 T_c^2}$, and $W_5^4 = \frac{93\zeta(5)}{128\pi^4 k_B^4 T_c^4}$, with $\zeta(\ldots)$ the Riemann zeta-function.

Similarly from the second term of Eq. (2.23) we get:

$$\begin{aligned} &\int \prod_{j=1}^{3} d^3y_j K_b(\mathbf{r}, \{\mathbf{y}\}_3) \Delta(\mathbf{y}_1) \Delta^*(\mathbf{y}_2) \Delta(\mathbf{y}_3) \qquad (2.30) \\ &\approx -gN(0)W_3^2(1 + 2\tau)\Delta|\Delta|^2 \\ &- \frac{5}{36} gN(0)\hbar^2 v_F^2 W_5^4 \left[\nabla^2(\Delta|\Delta|^2) - 2\nabla\Delta \cdot (\Delta^*\nabla\Delta - \Delta\nabla\Delta^*)\right]. \qquad (2.31) \end{aligned}$$

Finally the last term contributes in the order $\tau^{5/2}$ only as:

$$\int \prod_{j=1}^{5} d^3 y_j K_c(\mathbf{r}, \{\mathbf{y}\}_5)\Delta(\mathbf{y}_1)\Delta^*(\mathbf{y}_2)\Delta(\mathbf{y}_3)\Delta^*(\mathbf{y}_4)\Delta(\mathbf{y}_5) \tag{2.32}$$

$$\approx \frac{5}{4} gN(0)W_5^4 \Delta|\Delta|^4. \tag{2.33}$$

In total we have:

$$\begin{aligned}\Delta = &(1 + gN(0)\tau + gN(0)\frac{\tau^2}{2})\Delta + \frac{gN(0)}{6}\hbar^2 v_F^2 W_3^2(1+2\tau)\nabla^2\Delta \\ &+ \frac{gN(0)}{24}\hbar^4 v_F^4 W_5^4 \nabla^2(\nabla^2\Delta) - gN(0)W_3^2(1+2\tau)\Delta|\Delta|^2 \\ &- \frac{5}{36} gN(0)\hbar^2 v_F^2 W_5^4 \left[\nabla^2(\Delta|\Delta|^2) - 2\nabla\Delta\cdot(\Delta^*\nabla\Delta - \Delta\nabla\Delta^*)\right] \\ &+ \frac{5}{4} gN(0)W_5^4\Delta|\Delta|^4,\end{aligned} \tag{2.34}$$

where it is understood that $\Delta = \Delta(\mathbf{x})$, i.e., the gap is spatially dependent. Now, we introduce $\Delta(\mathbf{x}) = \Delta_0(\mathbf{x}) + \Delta_1(\mathbf{x})$, with $\Delta_0(\mathbf{x}) \propto \tau^{1/2}$ and $\Delta_0(\mathbf{x}) \propto \tau^{3/2}$. Then to order $\tau^{1/2}$ Eq. (2.34) gives just the identity $\Delta_0 = \Delta_0$. At the order $\tau^{3/2}$ one gets the GL equation:

$$\tau\Delta_0 + \frac{W_3^2}{6}\hbar^2 v_F^2 \nabla^2(\Delta_0) - W_3^2\Delta_0|\Delta_0|^2 = 0. \tag{2.35}$$

Finally, at order $\tau^{5/2}$ one gets

$$(\tau - 2W_3^2|\Delta_0|^2)\Delta_1 + \frac{W_3^2}{6}\hbar^2 v_F^2\nabla^2(\Delta_1) + \mathcal{F}(\tau, \Delta_0, \Delta_0^*) = 0, \tag{2.36}$$

where

$$\begin{aligned}\mathcal{F}(\tau, \Delta_0, \Delta_0^*) = &-\frac{3}{2}\tau^2\Delta_0 + \frac{W_5^4}{24}\hbar^4 v_F^4 \\ &\times \{\nabla^2(\nabla^2\Delta_0) + 6\Delta_0|\Delta_0|^4 - \frac{10}{3}[\nabla^2(\Delta_0|\Delta_0|^2) \\ &- 2\nabla\Delta_0(\Delta_0^*\nabla\Delta_0 - \Delta_0\nabla\Delta_0^*)]\}.\end{aligned} \tag{2.37}$$

2.4.5 Two-gap EGL formalism

The derivation of the two-gap EGL is very similar to the single-gap case, the only difference comes with the self-consistency equation, which now reads

$\mathbf{\Delta} = \mathbf{gR}$, where $\mathbf{g}$ is a two-by-two matrix of coupling coefficients, and the band components of $\mathbf{R}$ are

$$\begin{aligned} R_\nu = &\int d^3y K_{\nu a}(\mathbf{r},\mathbf{y})\Delta_\nu(\mathbf{y}) \\ &+ \int \prod_{j=1}^{3} d^3y_j K_{\nu b}(\mathbf{r},\{\mathbf{y}\}_3)\Delta_\nu(\mathbf{y}_1)\Delta_\nu^*(\mathbf{y}_2)\Delta_\nu(\mathbf{y}_3) \\ &+ \int \prod_{j=1}^{5} d^3y_j K_{\nu c}(\mathbf{r},\{\mathbf{y}\}_5)\Delta_\nu(\mathbf{y}_1)\Delta_\nu^*(\mathbf{y}_2)\Delta_\nu(\mathbf{y}_3)\Delta_\nu^*(\mathbf{y}_4)\Delta_\nu(\mathbf{y}_5), \end{aligned} \tag{2.38}$$

where the kernels are exactly the same as in the single band case only their definition does not include the coupling constant g (one should take the formulas with $g \equiv 1$). All the Green functions acquire the band index ν, meaning the single-particle energy becomes $\xi_{\nu\mathbf{k}} = \hbar^2k^2/(2m_\nu) - \mu_\nu$. For details of the calculation as well as the extended GL theory for nonzero field one is referred to Refs. [3, 51, 52]. The resulting two-band extended GL equations without the applied field can be found in Chapter 5, where we apply them to calculate the healing lengths of two condensates.

2.4.6 Two-gap BCS

The two-gap BCS theory is useful, because it is simple and valid for all temperatures between $T = 0$ and $T = T_c$. However, similarly as in the single-gap case, it describes only spatially independent situation.

It is straightforward to generalize the single-gap BCS equation Eq. (1.51) to the multigap case:

$$\Delta_i = \frac{1}{\Omega}\sum_{j\mathbf{k}} g_{ij}\frac{\Delta_j}{2E_{j\mathbf{k}}}\tanh\frac{E_{j\mathbf{k}}}{2T}, \tag{2.39}$$

where g_{ij} are the coupling constants. In Eq. (1.51) the interaction was taken in general form $V_{\mathbf{kk}'}$, now we assume it constant within two bands i and j. Similarly we assume that the gap value Δ_i has constant value for any particular band i (full s-wave gap). Therefore for example for the two-gap case we have:

$$\Delta_1 = g_{11}A_1\Delta_1 + g_{12}A_2\Delta_2, \tag{2.40}$$

$$\Delta_2 = g_{21}A_1\Delta_1 + g_{22}A_2\Delta_2, \tag{2.41}$$

where

$$A_i = \frac{1}{\Omega}\sum_{\mathbf{k}}\frac{1}{2E_{i\mathbf{k}}}\tanh\frac{E_{i\mathbf{k}}}{2T}. \tag{2.42}$$

This system of equations is easily solved numerically (e.g, in Matlab) for any values of parameters.

2.4.7 Two-gap BCS for only interband pairing

Let us now consider a special case when we have two superconducting bands with no intraband pairing, but with finite and symmetric interband pairing. This model is relevant for pnictide superconductors, which are characterized by being multiband systems with predominantly interband repulsive pairing interaction. The appropriate coupling matrix $\mathbf{g}$ has diagonal elements $g_{11} = g_{22} = 0$, while the coupling interaction is provided by $g_{12} = g_{21} = g$. We can write the Hamiltonian as follows

$$\hat{H} = \sum_{\mathbf{k},\sigma,j} \xi_{\mathbf{k},j} c^\dagger_{j,\mathbf{k}\sigma} c_{j,\mathbf{k}\sigma} + \frac{g}{\Omega} \sum_{\mathbf{k},\mathbf{k}'} (c^\dagger_{1,\mathbf{k}\uparrow} c^\dagger_{1,-\mathbf{k}\downarrow} c_{2,-\mathbf{k}'\downarrow} c_{2,\mathbf{k}'\uparrow} + \text{h.c.}), \tag{2.43}$$

where $\xi_{\mathbf{k},j} = \epsilon_{\mathbf{k},j} - \mu$ is the electron energy in the band j measured from the chemical potential μ. We then define the expectation value of the anomalous average $b^\dagger_j = \langle c^\dagger_{j,\mathbf{k}\uparrow} c^\dagger_{j,-\mathbf{k}\downarrow} \rangle$, so that the real value becomes $c^\dagger_{j,\mathbf{k}\uparrow} c^\dagger_{j,-\mathbf{k}\downarrow} = b^\dagger_{j\mathbf{k}} + (c^\dagger_{j,\mathbf{k}\uparrow} c^\dagger_{j,-\mathbf{k}\downarrow} - b^\dagger_{j\mathbf{k}})$, where the last term is small. We then express the Hamiltonian up to first order in this correction, while using the shorthand notation $\Delta^\dagger_{3-j} = \frac{g}{\Omega} \sum_{\mathbf{k}} b^\dagger_{j\mathbf{k}}$. This is the definition of $\Delta^\dagger_{3-j}$ rather than $\Delta^\dagger_j$ to be consistent with the full case where all the coupling constants are nonzero. We get

$$\hat{H}_{\text{int}} = \frac{g}{\Omega} \sum_{\mathbf{k}} (\Delta^\dagger_2 c_{2,-\mathbf{k}\downarrow} c_{2,\mathbf{k}\uparrow} + c^\dagger_{1,\mathbf{k}\uparrow} c^\dagger_{1,-\mathbf{k}\downarrow} \Delta_1 + \text{h.c.}) - \frac{2\Delta_1 \Delta_2 \Omega}{g}. \tag{2.44}$$

By introducing $\Psi_{j,\mathbf{k}} = \begin{pmatrix} c_{j,\mathbf{k}\uparrow} & c_{j,-\mathbf{k}\downarrow} \end{pmatrix}$ we can rewrite the Hamiltonian as

$$H = \sum_{j,\mathbf{k}} \Psi_{j,\mathbf{k}} A_{j,\mathbf{k}} \Psi_{j,\mathbf{k}} + \sum_{j,\mathbf{k}} \xi_{j,\mathbf{k}} \mathbf{1} - \frac{2\Delta_1 \Delta_2 \Omega}{g}, \tag{2.45}$$

where

$$A_{j,\mathbf{k}} = \begin{pmatrix} \xi_{j,\mathbf{k}} & \Delta_j \\ \Delta_j & -\xi_{j,\mathbf{k}} \end{pmatrix}. \tag{2.46}$$

The quadratic part has eigenvalues $E_{j\alpha,\mathbf{k}} = (-1)^\alpha \sqrt{\xi^2_{j,\mathbf{k}} + \Delta^2_j}$ with the meaning of energy of the hole-like and particle-like excitations ($\alpha = 1, 2$). These excitations (as before in the single-band case) obey fermionic anticommutation rules; therefore there can be only zero or one particle in any particular

state. This allows us to write the grand thermodynamic potential of the system as

$$F(T,\Omega,\mu) = -T\sum_{j,\mathbf{k},\alpha}\ln(1+e^{-\beta E_{j\alpha,\mathbf{k}}}) - \frac{2\Delta_1\Delta_2\Omega}{g} - \mu N. \tag{2.47}$$

The actual equilibrium gap values are the saddle-point of the free energy function, so we get

$$\frac{\partial F}{\partial \Delta_2} = -\frac{\Delta_1\Omega}{g} - T\sum_{\mathbf{k}} -\frac{e^{-\beta E_{2,\mathbf{k}}}}{1+e^{-\beta E_{2,\mathbf{k}}}}\frac{\Delta_2}{TE_{2,\mathbf{k}}} + \frac{e^{\beta E_{2,\mathbf{k}}}}{1+e^{\beta E_{2,\mathbf{k}}}}\frac{\Delta_2}{TE_{2,\mathbf{k}}} = -\frac{\Delta_1\Omega}{g} - \Delta_2\sum_{\mathbf{k}}\frac{f(-E_{2,\mathbf{k}}) - f(E_{2,\mathbf{k}})}{E_{2,\mathbf{k}}} = 0. \tag{2.48}$$

This can be rewritten using

$$\Pi_j = \frac{1}{\Omega}\sum_{\mathbf{k}}\frac{f(-E_{2,\mathbf{k}}) - f(E_{2,\mathbf{k}})}{E_{2,\mathbf{k}}} \tag{2.49}$$

and we find

$$\Delta_1 = -g\Delta_2\Pi_2, \tag{2.50}$$

$$\Delta_2 = -g\Delta_1\Pi_1, \tag{2.51}$$

and the gap equation is now $\frac{1}{g^2} = \Pi_1\Pi_2$. We see that when $g<0$, Δ_1 and Δ_2 have the same sign, while for $g>0$ they have opposite sign (Π_j are positively definite).

2.4.8 Two-gap Bogoliubov-de Gennes equations

The two-gap (multigap) generalization of the Bogoliubov-de Gennes equations is also straightforward. The Eq. (1.74) only acquires band index:

$$\begin{pmatrix} H_{ei}(\mathbf{r}) + U_i(\mathbf{r}) & \Delta_i(\mathbf{r}) \\ \Delta_i^*(\mathbf{r}) & -H_{ei}^*(\mathbf{r}) - U_i(\mathbf{r}) \end{pmatrix}\begin{pmatrix} u_{in}(\mathbf{r}) \\ v_{in}(\mathbf{r}) \end{pmatrix} = E_{in}\begin{pmatrix} u_{in}(\mathbf{r}) \\ v_{in}(\mathbf{r}) \end{pmatrix}, \tag{2.52}$$

while the self-consistency equation Eq. (1.81) is now summed over different bands

$$\Delta_i(\mathbf{r}) = \sum_{n;j=1,2} g_{ij}u_{jn}(\mathbf{r})v_{jn}^*(\mathbf{r})(1-2f_{FD}^{(jn)}). \tag{2.53}$$

The Bogoliubov-de Gennes approach is valid at all temperatures, but it is still a mean-field approach; some of the beyond mean-field phenomena (fluctuations) were studied, e.g., in Refs. [57, 58].

Chapter 3

Numerical methods

In this chapter I describe different approaches which we have used in this thesis to numerically solve the Ginzburg-Landau equations. The numerical approach used to solve the Bogoliubov-de Gennes equations is described in detail in the PhD thesis of Yajiang Chen [25] and is therefore omitted here. First, the solution of 1D problems using Matlab is described. Next I describe the method used for 2D and 3D problems [59–61], where GL equations are discretized on a regular lattice using the *link variables* [62] for the vector potential and then solved iteratively. In any numerical approach the preliminary step is to introduce some appropriate units reflecting the typical values of the variables and rewrite equations in the dimensionless form. This is necessary because in the CGS units the values of different GL coefficients can vary easily between 10^{-20} and 10^{50} and therefore intermediate results of calculation could exceed the double precision used for the floating-point representation of real numbers in most software/hardware.

3.1 The GL equations in one dimension

We solved the dimensionless form of the (extended) GL equations in one dimension (the normal metal-superconductor interface or the vortex core profile) using MATLAB software. One can use `bvp4c`, which is a generic boundary value problem solver for systems of ordinary differential equations. The standard form of the problem is $\mathbf{y}' = A\mathbf{y}$, where $\mathbf{y}$ is a vector composed of unknown functions and A is a matrix of coefficients, possibly depending on x. Additional unknown functions have to be introduced that represent the first derivatives of the wave functions which we are solving for (because GL equations contain second derivatives rather than only first). The differential equations are supplemented by specifying the boundary values $\mathbf{y}(a)$

and $\mathbf{y}(b)$ and then solved on the interval $[a, b]$. For the vortex problem, one cannot use $r = 0$ as the boundary, because some of the coefficients in the equations are divergent. The equations are then solved starting from some small $r_0 \ll 1$ instead. For the extended GL theory additional problem arises, because after one has solved the first equation for $\Delta_0(\mathbf{r})$ one needs to use it to evaluate the right side of the second EGL equation. However doing so involves computing up to fourth order derivatives, which is numerically very unstable. We therefore used the expression for the second derivative from the first EGL equation and differentiated that term twice to obtain the fourth order term. This stabilized the convergence of our calculation.

3.2 Generic approach to solve GL equations

The Ginzburg-Landau equations are a set of nonlinear partial differential equations that need to be solved self-consistently. We proceed by first calculating the order parameter from the first GL equation with the field equal to the homogeneous applied field. From this order parameter we evaluate the supercurrent using the second GL equation. Then we calculate the change in the vector potential due to this current using the Fourier transform. Finally we use the new magnetic field distribution in the first GL equation and repeat the procedure iteratively until we find a self-consistent solution with required accuracy. In the following paragraphs we describe this process explicitly for the single-gap Ginzburg-Landau theory and then give some comments about the implementation in the two-gap case.

3.2.1 Solving the first GL equation

We use the finite-difference representation of the GL equations, i.e., we solve them on a regular two-dimensional Cartesian space grid (x, y). This is sufficient because all the problems which we solved numerically in this thesis are effectively two-dimensional.[1] We first make the equations dimensionless by introducing dimensional units. We measure the distance in units of the zero-temperature coherence length $\xi(0)$, the temperature in units of the critical temperature T_c, the order parameter Ψ in units of $\Psi_\infty = \sqrt{-\alpha(0)/\beta}$, the vector potential in $A_0 = c\hbar/2e\xi(0)$ and the magnetic field in units of the upper critical field $H_{c2} = c\hbar/2e\xi(0)^2$. Then the two dimensionless GL

[1] The generalization to three-dimensional problems is straightforward and can be found, e.g., in the PhD thesis of Ben Xu [63].

equations (Eqs. (1.13) and (1.14)) become:

$$(-i\nabla - \mathbf{A})^2\Psi = (1-T)\Psi - |\Psi|^2\Psi, \tag{3.1}$$

$$\mathbf{j} = -\kappa^2\nabla^2\mathbf{A} = \frac{1}{2i}(\Psi^*\nabla\Psi - \Psi\nabla\Psi^*) - |\Psi|^2\mathbf{A}, \tag{3.2}$$

where in the second equation we recognized the magnetic field penetration depth

$$\lambda = \sqrt{\frac{m^*c^2}{16\pi e^2\Psi_\infty^2}}, \tag{3.3}$$

and wrote κ instead of ratio λ/ξ as usual.

We solve the first equation iteratively. We know that for any solution of the Ginzburg-Landau equations, the expression $(-i\nabla - \mathbf{A})^2\Psi - (1-T)\Psi + |\Psi|^2\Psi$ will be exactly zero, while it gives a finite value if we are away from the solution. Therefore we can use it to guide the iterative process in this way:

$$\eta(\Psi - \Psi_0) = -\left[(-i\nabla - \mathbf{A})^2\Psi_0 - (1-T)\Psi_0 + |\Psi_0|^2\Psi_0\right], \tag{3.4}$$

where Ψ_0 is the currently found best approximation to the solution of the GL equations, and we are looking for the improved estimate Ψ in the next iteration. It should be noted that the form of Eq. (3.4) mimics the one of the time-dependent single-gap GL theory. η is in our case an arbitrary real coefficient useful to improve the numerical stability of the iterative procedure, in the case of time-dependent GL it would be given by microscopic parameters, see e.g. Refs. [64, 65]. All the terms on the right hand side should in principle be evaluated with the current approximation to the solution Ψ_0, save for the cubic term which requires appropriate linearization, as will be explained below.

In the next step complex link variables $U_\mu^{\mathbf{r}_1,\mathbf{r}_2} = \exp(-i\int_{\mathbf{r}_1}^{\mathbf{r}_2}\mathbf{A}_\mu(\mathbf{r})d\mu)$, $\mu = x, y$ are introduced. We use them to rewrite the terms with the covariant derivative

$$(-i\nabla_\mu - A_\mu)\Psi = -i\frac{1}{U_\mu}\nabla_\mu(U_\mu\Psi), \tag{3.5}$$

$$(-i\nabla_\mu - A_\mu)^2\Psi = -\frac{1}{U_\mu}\nabla_\mu(\nabla_\mu(U_\mu\Psi)). \tag{3.6}$$

We divide our simulation region of size $L_x \times L_y$ into a discrete lattice with spacings $a_x \equiv L_x/M$ and $a_y \equiv L_y/N$, where M (N) are the number of points

in the x (y) direction. We can then write (for example for $\mu = x$)

$$\begin{aligned}(-i\nabla_x - A_x)^2\Psi(x_0,y_0) &= -\frac{1}{U_x}\nabla_x(\nabla_x(U_x\Psi)) \\ &= -\frac{1}{U_x}\nabla_x\left[\frac{U_x^{x_0+1,y_0}\Psi(x_0+1,y_0) - U_x^{x_0,y_0}\Psi(x_0,y_0)}{a_x}\right] \\ &= -\frac{1}{U_x a_x^2}\left[U_x^{x_0+1,y_0}\Psi(x_0+1,y_0) - 2U_x^{x_0,y_0}\Psi(x_0,y_0) + U_x^{x_0-1,y_0}\Psi(x_0-1,y_0)\right] \\ &= -\frac{1}{a_x^2}[U^{Ej}\Psi_E - 2\Psi_j + U^{Wj}\Psi_W].\end{aligned} \tag{3.7}$$

This is written for the lattice point $j = (x_0, y_0)$ and the neighboring lattice points are referred to by the corresponding cardinal direction denoted by its initial: (N)orth, (E)ast, (S)outh, (W)est. We also introduced $U^{Ej} \equiv U_x^{x_0+1,y_0}/U_x^{x_0,y_0} = \exp(-i\int_{(x_0,y_0)}^{(x_0+1,y_0)} A_x(r)dx) \approx \exp(-iA_x a_x)$ and analogous expressions for U^{Wj}, U^{Nj}, U^{Sj} in other directions.

With this discretization the first GL equation becomes:

$$\begin{aligned}\eta(\Psi_j - \Psi_{j0}) = \Big[&\frac{U^{Ej}\Psi_E}{a_x^2} + \frac{U^{Wj}\Psi_W}{a_x^2} + \frac{U^{Nj}\Psi_N}{a_y^2} + \frac{U^{Sj}\Psi_S}{a_y^2} - \frac{2\Psi_j}{a_x^2} - \frac{2\Psi_j}{a_y^2} \\ &+ (1-T)\Psi_j - |\Psi_j|^2\Psi_j\Big].\end{aligned} \tag{3.8}$$

The key numerical trick is to choose terms to associate with the new solution for Ψ and ones to evaluate based on Ψ_0. Moreover, the nonlinear term can be linearized as follows, to facilitate the convergence:

$$\begin{aligned}|\Psi|^2\Psi = \Psi^2\Psi^* &= [\Psi_0 + (\Psi - \Psi_0)]^2[\Psi_0^* + (\Psi^* - \Psi_0^*)] \\ &\approx |\Psi_0|^2\Psi_0 + 2|\Psi_0|^2(\Psi - \Psi_0) + \Psi_0^2(\Psi^* - \Psi_0^*) \\ &= 2|\Psi_0|^2\Psi - 2|\Psi_0|^2\Psi_0 + \Psi_0^2\Psi^*.\end{aligned} \tag{3.9}$$

With our assignment of different terms to Ψ or Ψ_0 and the above expansion of the cubic term, Eq. (3.8) can be rewritten as:

$$\eta(\Psi - \Psi_0) = \tilde{U}\Psi_0 - \frac{4}{a^2}\Psi + (1-T)\Psi - 2|\Psi_0|^2\Psi + 2|\Psi_0|^2\Psi_0 - \Psi_0^2\Psi^*, \tag{3.10}$$

where $\tilde{U}\Psi_0$ is a shorthand notation for the first four terms on the right side of Eq. (3.8), and $a_x = a_y = a$ was taken for simplicity. This choice of terms containing Ψ_0 vs. terms containing Ψ is not unique, but the shown one has demonstrated stability in a vast number of simulations.

We rearrange the first GL equation by conveniently grouping the terms multiplying the Ψ, Ψ^* and constant terms, as:

$$[\eta - (1-T) + 4/a^2 + 2|\Psi_0|^2]\Psi = \tilde{U}\Psi_0 + \eta\Psi_0 + 2\Psi_0|\Psi_0|^2 - \Psi_0^2\Psi^*. \quad (3.11)$$

Equation (3.11) is of the form

$$c\Psi - a + e\Psi^* = 0, \quad (3.12)$$

with

$$c = \eta - (1-T) + 4/a^2 + 2|\Psi_0|^2, \quad (3.13)$$
$$e = \Psi_0^2, \quad (3.14)$$
$$a = \tilde{U}\Psi_0 + \eta\Psi_0 + 2\Psi_0|\Psi_0|^2, \quad (3.15)$$

and solution

$$\Psi = \frac{a^*e - ac^*}{|e|^2 - |c|^2}, \quad (3.16)$$

where right side depends only on Ψ_0. After going through several hundred iterations of the first GL equation in the above form, we use its (approximate) solution Ψ to compute the supercurrent given by

$$j_x = \frac{1}{2}\left[\Psi^*\left(\frac{1}{i}\frac{\partial}{\partial x} - A_x\right)\Psi + \Psi\left(\frac{1}{i}\frac{\partial}{\partial x} - A_x\right)^*\Psi^*\right], \quad (3.17)$$

with the same expression for y component with x replaced by y. These expressions are again easy to express using the link variables:

$$\left(\frac{1}{i}\frac{\partial}{\partial x} - A_x\right)\Psi_j = -i\frac{U_x^{Ej}\Psi_E - \Psi_j}{a_x}, \quad (3.18)$$

and

$$\left(\frac{1}{i}\frac{\partial}{\partial y} - A_y\right)\Psi_j = -i\frac{U_y^{Nj}\Psi_N - \Psi_j}{a_y}. \quad (3.19)$$

Subsequently one uses the Maxwell equation to calculate the new value of the vector potential as explained in the next section and the process is iteratively repeated until convergence is reached.

Periodic boundary conditions In practice it is numerically extremely demanding to find a solution of the Ginzburg-Landau equations for a thin film with very large lateral sizes. We therefore only solve them in some finite region and make our sample "quasi-infinite" by demanding periodic boundary

conditions. Thus the value of any physical (gauge-invariant) variable at the right (upper) end of our grid must be the same as the value of the same variable at the left (lower) end.

The problem arises when we want to use the periodic boundary conditions in the presence of the magnetic field. Specifically, the problem is to correctly treat the vector potential $\mathbf{A}$, which even for the homogeneous magnetic field grows linearly with the distance and thus has necessarily different values at the ends of the grid. Fortunately by using a special gauge transformation this can be accounted for, as explained in Ref. [66]. The boundary conditions then have the form

$$\mathbf{A}(\mathbf{x}+\mathbf{b}_\nu) = \mathbf{A}(\mathbf{x}) + \nabla\chi_\nu(\mathbf{x}), \tag{3.20}$$

$$\Psi(\mathbf{x}+\mathbf{b}_\nu) = \Psi(\mathbf{x}) \exp\left(i\frac{2e}{\hbar c}\chi_\nu(\mathbf{x})\right), \tag{3.21}$$

where $\mathbf{b}_x = (L_x, 0)$ and $\mathbf{b}_y = (0, L_y)$ are lattice vectors, and $\chi_\nu(\mathbf{x})$ are the gauge potentials associated with each $\mathbf{b}_\nu$. This type of boundary conditions is sometimes referred to as *twisted boundary conditions* in the literature, see, e.g., Ref. [67].

From the practical point of view, we use Eq. (3.20) to find the gauge potentials and then use these when evaluating the order parameters with Eq. (3.21) as additional condition. To be specific, let us assume that we use the Landau gauge and the applied field is $\mathbf{B} = (0, 0, B)$. Then we have

$$A_x = 0, \tag{3.22}$$

$$A_y = Bx. \tag{3.23}$$

It follows that the boundary gauge will be

$$\chi_x = BL_x y, \tag{3.24}$$

$$\chi_y = 0. \tag{3.25}$$

Then one needs to change all the expressions involving the link variables going "over the edge" as follows (exemplified on Eq. (3.18)):

$$\left(\frac{1}{i}\frac{\partial}{\partial x} - A_x\right)\Psi_j = -i\frac{U_x^{0j}\Psi_0 \exp(iBL_x y) - \Psi_j}{a_x}, \tag{3.26}$$

i.e., to multiply Ψ_0 by $\exp(i\chi_x)$, if the point "to the east" is out of the lattice.[2] On the other hand, if one runs out of the lattice in the vertical direction, the expression in Eq. (3.19) is only modified to

$$\left(\frac{1}{i}\frac{\partial}{\partial y} - A_y\right)\Psi_j = -i\frac{U_y^{0j}\Psi_0 - \Psi_j}{a_y}, \tag{3.27}$$

[2]The factor $\frac{2e}{\hbar c} = 1/(A_0\xi(0))$ from Eq. (3.21) disappears in our units.

because $\chi_y = 0$.

3.2.2 Solving the second GL equation with periodic boundary conditions

We need to solve the equation $\mathbf{j} = -\kappa^2 \nabla^2 \mathbf{A}$ for the unknown vector potential $\mathbf{A}$. As we will see below, solution of this type of partial differential equation is especially simple in the reciprocal space, i.e., using the Fourier transform. Afterwards we use the inverse Fourier transform to get the real space solution in which we are actually interested.

We shall neglect the variation of the current in the z direction, which is justified, e.g., for very thin films with thickness $d < \lambda, \xi$, but also in the bulk limit. This approximation allows us to use the continuous Fourier transform in the z direction, while in the x and y directions we have to do the expansion into the discrete Fourier series. We chose the exponential Fourier series, because this guaranties to satisfy the periodic boundary conditions in the x and y directions for the vector potential $\forall x, y, z : \mathbf{A}(x + L_x, y, z) = \mathbf{A}(x, y + L_y, z) = \mathbf{A}(x, y, z)$. The $\mathbf{A}$ here is the vector potential which is only due to the magnetic field induced by the superconductor, i.e., does not include the applied field. As before $a_x \equiv L_x/M$, $a_y \equiv L_y/N$ are the numerical grid spacings and finally $A_{mn}(z) \equiv A(ma_x, na_y, z)$. The latter we can express as

$$A_{mn}(z) = \frac{1}{MN} \int_{-\infty}^{\infty} dk \sum_{\alpha=0}^{M-1} \sum_{\beta=0}^{N-1} \hat{A}_{\alpha\beta}(k) e^{-2\pi i z k} e^{-2\pi i \frac{m\alpha}{M}} e^{-2\pi i \frac{n\beta}{N}}. \tag{3.28}$$

Inverse Fourier transform reads:

$$\hat{A}_{\alpha\beta}(k) = \int_{-\infty}^{\infty} dz \sum_{m=0}^{M-1} \sum_{n=0}^{N-1} A_{mn}(z) e^{2\pi i z k} e^{2\pi i \frac{m\alpha}{M}} e^{2\pi i \frac{n\beta}{N}}. \tag{3.29}$$

Taking into account that

$$e^{-2\pi i \frac{m\alpha}{M}} = e^{-2\pi i \frac{m a_x \alpha}{a_x M}} = e^{-2\pi i \frac{x\alpha}{L_x}}, \tag{3.30}$$

it is evident that taking the derivative with respect to x will just pull out a factor $-2\pi i\alpha/L_x$. An analogue expression can be derived also for the derivative with respect to y. Using this we find that the Laplacian of the vector potential $\nabla^2 A \equiv \frac{\partial^2 A}{\partial x^2} + \frac{\partial^2 A}{\partial y^2} + \frac{\partial^2 A}{\partial z^2}$ is equal to

$$\begin{aligned} \nabla^2 A_{mn}(z) = \frac{1}{MN} \int_{-\infty}^{\infty} dk \sum_{\alpha=0}^{M-1} \sum_{\beta=0}^{N-1} \left[-(2\pi k)^2 - (2\pi\alpha/L_x)^2 - (2\pi\beta/L_y)^2 \right] \\ \times \hat{A}_{\alpha\beta}(k) e^{-2\pi i z k} e^{-2\pi i \frac{m\alpha}{M}} e^{-2\pi i \frac{n\beta}{N}}, \end{aligned} \tag{3.31}$$

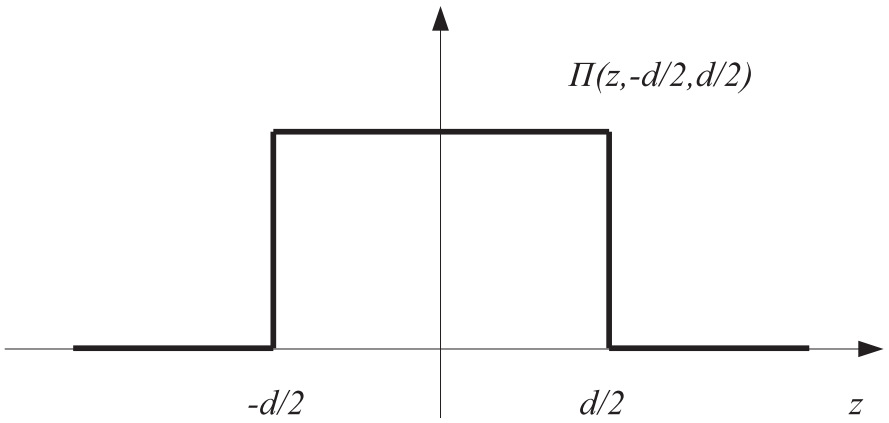

Figure 3.1: The step function $\Pi(z, -d/2, d/2)$ used to define the current distribution in the z-direction.

The current density can be also expressed as a Fourier series

$$j_{mn}(z) = \frac{1}{MN} \int_{-\infty}^{\infty} dk \sum_{\alpha=0}^{M-1} \sum_{\beta=0}^{N-1} \hat{j}_{\alpha\beta}(k) e^{-2\pi i z k} e^{-2\pi i \frac{m\alpha}{M}} e^{-2\pi i \frac{n\beta}{N}}, \tag{3.32}$$

with coefficients

$$\hat{j}_{\alpha\beta}(k) = \int_{-\infty}^{\infty} dz \sum_{m=0}^{M-1} \sum_{n=0}^{N-1} j_{mn}(z) e^{2\pi i z k} e^{2\pi i \frac{m\alpha}{M}} e^{2\pi i \frac{n\beta}{N}}. \tag{3.33}$$

As was already mentioned we assume the uniform current density in the z-direction $j_{mn}(z) = j_{mn}\Pi(z, -d/2, d/2)$, where Π is a steplike function equal to 1 inside the interval $(-d/2, d/2)$, zero outside, see also Fig. 3.1. The Fourier transform of Π function is simply

$$\int_{-\infty}^{\infty} \Pi(z, -d/2, d/2) e^{2\pi i z k} dz = \int_{-d/2}^{d/2} e^{2\pi i z k} dz = \frac{\sin(\pi k d)}{\pi k}. \tag{3.34}$$

This simplifies Eq. (3.33) to

$$\hat{j}_{\alpha\beta}(k) = \hat{j}_{\alpha\beta} \frac{\sin(\pi k d)}{\pi k}. \tag{3.35}$$

We subsequently substitute Eqs. (3.31) and (3.32) into the equation $\mathbf{j} = -\kappa^2 \nabla^2 \mathbf{A}$, to obtain

$$\hat{A}_{\alpha\beta}(k) = \frac{1}{\kappa^2} \frac{\hat{j}_{\alpha\beta}(k)}{(2\pi k)^2 + q_{\alpha\beta}^2}, \tag{3.36}$$

where $q_{\alpha\beta}^2 = (\frac{2\pi\alpha}{L_x})^2 + (\frac{2\pi\beta}{L_y})^2$. Notice that this $q_{\alpha\beta}$ is twice the corresponding variable in the finite sample calculation, where the *sine* Fourier transform is needed (as the vector potential contribution due to superconductor goes to zero at the far boundaries of the simulation, away from the sample).

Having the formula for the vector potential in the reciprocal space $\hat{A}_{\alpha\beta}(k)$ we can Fourier transform it back to the real space using Eq. (3.28):

$$A_{mn}(z) = \frac{1}{MN}\int_{-\infty}^{\infty} dk \sum_{\alpha=0}^{M-1}\sum_{\beta=0}^{N-1} \frac{1}{\kappa^2}\frac{\hat{j}_{\alpha\beta}}{(2\pi k)^2 + q_{\alpha\beta}^2} \times \frac{\sin(\pi k d)}{\pi k} e^{-2\pi i z k} e^{-2\pi i \frac{m\alpha}{M}} e^{-2\pi i \frac{n\beta}{N}}. \tag{3.37}$$

The integral over k,

$$I = \int_{-\infty}^{\infty} \frac{1}{(2\pi k)^2 + q_{\alpha\beta}^2} \frac{\sin(\pi k d)}{\pi k} e^{-2\pi i z k} dk, \tag{3.38}$$

can be done analytically with the result

$$I = \begin{cases} [1 - \cosh(q_{\alpha\beta} z)\exp(-d q_{\alpha\beta}/2)]/q_{\alpha\beta}^2 & z < d/2, \\ \sinh(d q_{\alpha\beta}/2)\exp(-q_{\alpha\beta} z)/q_{\alpha\beta}^2 & z > d/2. \end{cases} \tag{3.39}$$

We are interested mainly in the field behavior in the $z = 0$ plane (special case of $z < d/2$), where $I = [1 - \exp(-d q_{\alpha\beta}/2)]/q_{\alpha\beta}^2$. Finally we have

$$A_{mn}(0) = \frac{1}{MN}\sum_{\alpha=0}^{M-1}\sum_{\beta=0}^{N-1} \frac{\hat{j}_{\alpha\beta}}{\kappa^2 q_{\alpha\beta}^2}[1 - \exp(-d q_{\alpha\beta}/2)] e^{-2\pi i \frac{m\alpha}{M}} e^{-2\pi i \frac{n\beta}{N}}, \tag{3.40}$$

that is we can calculate the vector potential by first Fourier transforming the current density in the xy plane to obtain the set of coefficients $\hat{j}_{\alpha\beta}$, and then by evaluating the Eq. (3.40) which is again doable by Fourier transformation.

3.3 Generalization to two-gap systems

3.3.1 Dimensionless two-gap GL equations

The parameters α_i, β_i etc. of the two-gap GL theory are obtained from the microscopic theory [2]: $\alpha_j = -N(0)n_j\chi_j = -N(0)n_j(\tau - S_j/n_j\eta)$, $\beta_j = N(0)n_j/W^2$, $m_j = 3W^2/N(0)n_j v_j^2$ and $\Gamma = N(0)\lambda_{12}/\eta$, where $\Lambda = \begin{vmatrix} \lambda_{11} & \lambda_{12} \\ \lambda_{21} = \lambda_{12} & \lambda_{22} \end{vmatrix}$ is the coupling matrix with determinant η; n_j ($N(0)$) denotes partial (total) density of states, v_j are the Fermi velocities in the two

bands, and $W^2 = 8\pi^2 T_c^2/7\zeta(3)$. For details on constants S_j we refer to Ref. [2]. We can formally define the coherence lengths $\xi_j = \hbar v_j/(\sqrt{6}W)$ and penetration depths $\lambda_j = \sqrt{3c^2/(16\pi N(0)e^2 n_j v_j^2)}$, as well as the GL parameters $\kappa_j = \lambda_j/\xi_j$ of the two condensates, as if they were independent. The temperature dependence enters the formalism only through the parameters $\alpha_j(T)$.

We chose to express all distances in the formalism in units of ξ_1, which is the zero-temperature coherence length of the first condensate. Correspondingly, we measure the vector potential $\mathbf{A}$ in units of $c\hbar/2e\xi_1$, the magnetic field $\mathbf{H}$ in units of the second critical field of the first band $H_{c2} = c\hbar/2e\xi_1^2$. Both order parameters are measured in the units of $W = \sqrt{8\pi^2 k_B^2 T_c^2/7\zeta(3)} \propto T_c$ which defines our energy scale. All these units are temperature independent.

We then obtain the following dimensionless equations to solve:

$$(-i\nabla - \mathbf{A})^2\Psi_1 - (\chi_1 - |\Psi_1|^2)\Psi_1 - \gamma\Psi_2 = 0, \tag{3.41a}$$

$$(-i\nabla - \mathbf{A})^2\Psi_2 - \alpha(\chi_2 - |\Psi_2|^2)\Psi_2 - \frac{\gamma\kappa_2^2}{\kappa_1^2\alpha}\Psi_1 = 0, \tag{3.41b}$$

$$-\nabla^2\mathbf{A} = \kappa_1^{-2} j_1 + \alpha\kappa_2^{-2} j_2, \tag{3.41c}$$

where $j_j = \Re\left[\Psi_j^*(-i\nabla - \mathbf{A})\Psi_j\right]$, $\alpha = (v_1/v_2)^2$, $\gamma = \Gamma/n_1 N(0)$.

3.3.2 Numerical implementation of two-gap GL equations

The implementation of the two-gap equations is very similar to the single-gap case as the structure of the equations stays the same. The temperature independent units have to be used as we described above, in contrast to the single-gap case where one could hide temperature by using, e.g., $\xi(T)$ as a length unit. In two-gap case however this would cause our length unit to diverge at some temperature T_{cj} below T_c. The discretization scheme remains the same, as well as the use of link variables. The second GL equation has still the form of a Poisson equation and is solved by the Fourier transform in x and y directions and analytically in the z direction, the only difference being that the supercurrent has weighted contributions from both gaps now. For the bilayer system in Chapter 7, we use the Eq. (3.39) (case when $z > d/2$) to calculate the vector potential from the other layer in the middle of the layer under consideration. Due to linearity of the Maxwell equations superposition principle applies and we are indeed allowed to add up the vector potentials

from the supercurrents flowing inside that layer and inside the other layer (for more details, see Chapter 7).

Chapter 4

Conditions for non-monotonic vortex interaction

In this chapter we describe a semi-analytic approach to the standard two-band Ginzburg-Landau theory, which predicts the magnetic behavior of vortices in two-band superconductors. We show that the character of the short-range vortex-vortex interaction is determined by the sign of the normal domain - superconductor interface energy, in analogy with the conventional differentiation between type-I and type-II superconductors. However, we also show that the long-range interaction is determined by a modified Ginzburg-Landau parameter κ^*, different from the standard κ of a bulk superconductor. This opens the possibility for non-monotonic vortex-vortex interaction, which is temperature-dependent, and can be further tuned by alterations of the material on the microscopic scale.

4.1 Introduction

Multigap superconductivity arises when the gap amplitudes on different sheets of the Fermi surface are radically disparate, e.g. due to different dimensionality of the bands for the usual phonon-mediated pairing, as is the case in MgB_2 [68, 69], or due to the repulsive pairing interaction, as it appears to be the case in recently discovered iron-pnictides [70, 71]. The other examples of multigap materials include OsB_2, iron silicides such as $Lu_2Fe_3Si_5$, chalcogenides ($NbSe_2$), but also the conventional superconductors such as Pb when reduced to nanoscale [72, 73].

In a strong magnetic field all superconducting condensates form normal-

metal voids, as an intermediate state before superconductivity is fully destroyed. These normal domains tend to *merge* in type-I superconductors in order to minimize their positive surface energy, whereas in type-II superconductors they have negative surface energy and *split* into quantized vortices. However, in 2005 Babaev and Speight predicted the so-called semi-Meissner state in two-band superconductors [74], the state with localized regions of high and low vortex densities, arising from short-range repulsive while long-range attractive vortex-vortex interaction. This vortex behavior was recently visualized by Moshchalkov *et al.* [1], in the form of stripes and clusters of vortices in a single-crystal MgB_2. Such vortex configurations stemming from the long-range attractive vortex behavior (see also Ref. [15] for review) are clearly very important in the field of superconductivity, but they also present a bridge between solid-state physics and soft condensed matter, where systems with competing interactions are of abiding interest [75, 76].

To date the matter of competing vortex interactions in two-band superconductors has not been conclusively settled although recent years saw a surge of activities in this field. The original prediction in Ref. [74] concerns only the case when one band is type-I and the other type-II, although it is unclear how different types of behavior between bands in k-space (not real space) can be discerned. Ref. [77] demonstrated such vortex behavior in systems where just one band is fully superconducting, and the other superconducts only due to direct coupling. Dao *et al.* found different types of possible vortex-vortex interactions and several resulting exciting vortex configurations, but did not provide a universal criterion to *a priori* determine the type of vortex interaction [78]. Finally some authors expressed scepticism to nonmonotonic vortex interaction; Geyer *et al.* showed that the normal metal/two-gap superconductor surface energy close to T_c depends just on a single Ginzburg-Landau (GL) parameter κ, and thus only either repulsive (type-II) or attractive (type-I) vortex-vortex interaction is possible [79]. This point was later reenforced by Kogan and Schmalian [2].

4.2 Methods and derivations

4.2.1 Two component Ginzburg-Landau formalism

In this chapter we derive criteria for the appearance of non-monotonic interaction of vortices in two-gap systems described by the standard GL model. Our analysis is based on the two-band GL theory, with all coefficients expressed using the microscopic parameters obtained either from theoretical band structure calculations or by fitting the experimental penetration depth

or specific heat data by the so-called γ-model [80]. We begin from the GL energy functional (as explained in Chapter 2), which comprises single-band contributions from both condensates, the coupling term, and the energy of the magnetic field in and around the sample:

$$\begin{aligned}\mathcal{F} &= \sum_{j=1,2} \alpha_j |\Psi_j|^2 + \frac{1}{2}\beta_j |\Psi_j|^4 + \frac{1}{2m_j}\left|\left(\frac{\hbar}{i}\nabla - \frac{2e}{c}\mathbf{A}\right)\Psi_j\right|^2 \\ &\quad -\Gamma(\Psi_1^*\Psi_2 + \Psi_1\Psi_2^*) + \frac{(\mathbf{h}-\mathbf{H})^2}{8\pi}. \end{aligned} \tag{4.1}$$

Here the two Cooper-pair condensates are described by the order parameters Ψ_1 and Ψ_2, $\mathbf{H}$ is the applied magnetic field and $\mathbf{h}$ the net one. The Josephson coupling term provides the 'minimal coupling', well described in literature. The temperature enters the energy expression through $\alpha_{j=1,2}$ [49]. The expansion leading to the GL theory is strictly valid only in the immediate vicinity of the critical temperature T_c, but we use this theory at somewhat lower temperatures as well, arguing that GL theory qualitatively well describes important physics away from T_c (as was demonstrated at many prior instances). Finally, it was shown in Ref. [2], that standard two-band GL theory contains incomplete terms that estimate ψ with precision to $\tau^{3/2}$. The authors reduce the theory by eliminating latter terms, which results in a single coherence length for both order parameters of a two-band superconductor. This is however not a correct physical picture at low temperatures, and two coherence lengths for the two-band superconductors can be recovered even in the GL domain in the extended model of Ref. [3]. Unfortunately, the latter model was at the time presented only in the absence of magnetic field. To be able to capture all the essential physics, at least qualitatively, we based our study on the compromise - the standard GL model. Note however that our further explained semi-analytic approach can be applied to *any improved form* of the energy functional for two-band superconductors.

We calculate the vortex-vortex interaction in a similar fashion to Ref. [74] but within a microscopic framework. The parameters in Eq. (4.1) can then be expressed as: $\alpha_j = -N(0)n_j\chi_j = -N(0)n_j(\tau - S_j/n_j\eta)$, $\beta_j = N(0)n_j/W^2$, $m_j = 3W^2/N(0)n_j v_j^2$ and $\Gamma = N(0)\lambda_{12}/\eta$, where $\Lambda = \begin{vmatrix} \lambda_{11} & \lambda_{12} \\ \lambda_{21}=\lambda_{12} & \lambda_{22} \end{vmatrix}$ is the coupling matrix with determinant η; n_j ($N(0)$) denotes partial (total) density of states, v_j are the Fermi velocities in the two bands, and $W^2 = 8\pi^2 k_B^2 T_c^2/7\zeta(3)$. For details on the constants S_j we refer to Ref. [2]. We formally define the coherence lengths $\xi_j = \hbar v_j/(\sqrt{6}W)$ and penetration depths $\lambda_j = \sqrt{3c^2/(16\pi N(0)e^2 n_j v_j^2)}$, as well as the GL parameters

$\kappa_j = \lambda_j/\xi_j$ of the two condensates, as if they were independent. These are of course just parameters of the model, and are related only indirectly to the resulting penetration depth and the healing lengths of the two order parameters in the two-band material. Notice also that α_1 and α_2 change sign at different temperatures. In particular, close to T_c both α_j are positive but the coupled system is still superconducting. Such situation is already different from the one studied in Ref. [77], where at least one α_j was negative. The Ginzburg-Landau equations minimize the functional from Eq. (4.1), and read (in dimensionless form)

$$(-i\nabla - \mathbf{A})^2\Psi_1 - (\chi_1 - |\Psi_1|^2)\Psi_1 - \gamma\Psi_2 = 0, \tag{4.2a}$$

$$(-i\nabla - \mathbf{A})^2\Psi_2 - \alpha(\chi_2 - |\Psi_2|^2)\Psi_2 - \frac{\gamma\kappa_2^2}{\kappa_1^2\alpha}\Psi_1 = 0, \tag{4.2b}$$

$$-\nabla^2\mathbf{A} = \kappa_1^{-2}\mathbf{j}_1 + \alpha\kappa_2^{-2}\mathbf{j}_2, \tag{4.2c}$$

where $\mathbf{j}_j = \Re\left[\Psi_j^*(-i\nabla - \mathbf{A})\Psi_j\right]$, $\alpha = (v_1/v_2)^2$, $\gamma = \Gamma/n_1N(0)$, both order parameters are scaled to W, distances to ξ_1, and vector potential to $hc/4e\pi\xi_1$.

4.2.2 Long-range vortex interaction

In what follows, we demonstrate the method to determine the asymptotic long-range interaction of vortices, before going into fine details at short vortex-vortex distances. In cylindrical coordinates, considering the ansatz for one circular symmetric vortex $\Psi_j = e^{i\theta}f_j(r)$, and substituting the gauge $\mathbf{A} = a(r)\hat{\theta}/r$, we rewrite Ginzburg-Landau Eqs. (4.2a-c) as

$$\frac{d^2f_1}{dr^2} + \frac{1}{r}\frac{df_1}{dr} - \frac{(a-1)^2}{r^2}f_1 + (\chi_1 - f_1^2)f_1 + \gamma f_2 = 0, \tag{4.3a}$$

$$\frac{d^2f_2}{dr^2} + \frac{1}{r}\frac{df_2}{dr} - \frac{(a-1)^2}{r^2}f_2 + \alpha(\chi_2 - f_2^2)f_2 + \frac{\gamma}{\alpha}\frac{\kappa_2^2}{\kappa_1^2}f_1 = 0, \tag{4.3b}$$

and

$$\frac{d^2a}{dr^2} - \frac{1}{r}\frac{da}{dr} - (a-1)\left(\frac{f_1^2}{\kappa_1^2} + \alpha\frac{f_2^2}{\kappa_2^2}\right) = 0. \tag{4.3c}$$

For $r \to \infty$, a converges to 1 and f_j to a constant w_j. The limit $r \to \infty$ leads to the set of non-linear coupled equations for w_j:

$$(\chi_1 - w_1^2)w_1 + \gamma w_2 = 0, \tag{4.4a}$$

$$\alpha(\chi_2 - w_2^2)w_2 + \frac{\gamma}{\alpha}\frac{\kappa_2^2}{\kappa_1^2}w_1 = 0. \tag{4.4b}$$

These can be decoupled by defining the ratio $\rho = w_1/w_2$, which then obeys the fourth order equation

$$\frac{\gamma}{\alpha^2}\frac{\kappa_2^2}{\kappa_1^2}\rho^4 + \chi_2\rho^3 - \chi_1\rho - \gamma = 0. \tag{4.5}$$

Such an equation has a laborious analytical solution known as Ferrari's method, which will not be presented here, but can be found in Ref. [81]. From Eq. (4.4), one obtains the dependence of the constants w_j on the ratio ρ as

$$w_1 = \sqrt{\frac{\gamma}{\rho} + \chi_1}, \tag{4.6a}$$

$$w_2 = \sqrt{\frac{\gamma}{\alpha^2}\frac{\kappa_2^2}{\kappa_1^2}\rho + \chi_2}. \tag{4.6b}$$

In order to eliminate high order terms for large distances, we must use auxiliary functions that approach zero as $r \to \infty$, namely, $Q(r) = a(r) - 1$ and $\sigma_j(r) = f_j(r) - w_j$. Keeping only first order terms in these functions, Eqs. (4.3) become

$$\frac{d^2\sigma_1}{dr^2} + \frac{1}{r}\frac{d\sigma_1}{dr} + \left(\chi_1 - 3w_1^2\right)\sigma_1 + \gamma\sigma_2 = 0, \tag{4.7a}$$

$$\frac{d^2\sigma_2}{dr^2} + \frac{1}{r}\frac{d\sigma_2}{dr} + \alpha\left(\chi_2 - 3w_2^2\right)\sigma_2 + \frac{\gamma}{\alpha}\frac{\kappa_2^2}{\kappa_1^2}\sigma_1 = 0, \tag{4.7b}$$

and

$$\frac{d^2}{dr^2}\left(\frac{Q}{r}\right) + \frac{1}{r}\frac{d}{dr}\left(\frac{Q}{r}\right) - \left(\frac{\xi_1^2}{\lambda^2} + \frac{1}{r^2}\right)\left(\frac{Q}{r}\right) = 0, \tag{4.7c}$$

where we defined $\lambda^{-2} = (w_1/\lambda_1)^2 + (w_2/\lambda_2)^2$. The solution of Eq. (4.7c) is the Modified Bessel function $Q(r) = \delta_3 r K_1(r\xi_1/\lambda)$. Similarly, if $\gamma = 0$, Eqs. (4.7a) and (4.7b) are decoupled and easily identified as Modified Bessel equations, whose solutions are $\sigma_1(r) = \eta_1 K_0(\sqrt{2\chi_1}r)$ and $\sigma_2(r) = \eta_2 K_0(\sqrt{2\alpha\chi_2}r)$. On the other hand, if $\gamma \neq 0$, the equations for σ_j are still coupled and, in order to decouple them, one must define the operator $\hat{L}_2 = \nabla^2 + \alpha\left(\chi_2 - 3w_2^2\right)$, so that $\hat{L}_2\sigma_2 = -(\gamma\kappa_2^2/\alpha\kappa_1^2)\sigma_1$, and apply it on Eq. (4.7a), obtaining

$$\nabla^2\nabla^2\sigma_1 + C_1\nabla^2\sigma_1 + C_2\sigma_1 = 0. \tag{4.8}$$

Here $C_1 = \left(\chi_1 - 3w_1^2\right) + \alpha\left(\chi_2 - 3w_2^2\right)$ and $C_2 = \alpha\left(\chi_2 - 3w_2^2\right)\left(\chi_1 - 3w_1^2\right) - \gamma^2\kappa_2^2/\alpha\kappa_1^2$. The operator ∇^2 for axially symmetric solutions has eigenfunctions given by Bessel functions $J_0(\beta r)$ and $Y_0(\beta r)$, with eigenvalue $-\beta^2$, or

modified Bessel functions $I_0(\beta r)$ and $K_0(\beta r)$, with eigenvalue β^2. From these four eigenfunctions, only the latter satisfies the condition that σ_j must decay monotonically with r. Substituting $\nabla^2 K_0(\beta r) = \beta^2 K_0(\beta r)$ in Eq. (4.8), one obtains

$$\beta^4 + C_1\beta^2 + C_2 = 0, \tag{4.9}$$

and

$$\sigma_1(r) = \delta_1 \cos(\omega) K_0(\beta_- r) - \delta_2 \sin(\omega) K_0(\beta_+ r), \tag{4.10a}$$

$$\sigma_2(r) = \delta_1 \sin(\omega) K_0(\beta_- r) + \delta_2 \cos(\omega) K_0(\beta_+ r), \tag{4.10b}$$

where

$$\beta_\pm = \sqrt{\frac{-C_1 \pm \sqrt{C_1^2 - 4C_2}}{2}}. \tag{4.10c}$$

Notice that in Eqs. (4.10), each σ_j must contain the Bessel functions for both $\beta_\pm$, in a combination that is conveniently written in the form of a mixing angle ω [77]. In the $\gamma \to 0$ limit, one has $\beta_- \to \sqrt{2\chi_1}$ and $\beta_+ \to \sqrt{2\alpha\chi_2}$. Moreover, substituting Eqs. (4.10) in the differential equation (4.7a), one obtains

$$\tan(\omega) = \frac{\gamma}{\beta_+^2 + (\chi_1 - 3w_1^2)}, \tag{4.11}$$

so that $\gamma \to 0$ leads to $\omega \to 0$ and, consequently, to $\sigma_1(r) \to \eta_1 K_0(\sqrt{2\chi_1} r)$ and $\sigma_2(r) \to \eta_2 K_0(\sqrt{2\alpha\chi_2} r)$, as expected.

The parameters δ_k (η_k) in the expressions for $Q(r)$, $\sigma_1(r)$ and $\sigma_2(r)$ are unknown real constants that can only be determined by fitting numerical solutions for Eqs. (4.3) in analogy to what is done in Ref. [82].

Having the asymptotic form of the order parameters and the vector potential, we now follow the standard procedure [83] for finding the vortex-vortex interaction in the $r \to \infty$ limit, obtaining

$$E_{2B}(\mathsf{r}) = \delta_3^2 K_0\left(\frac{\mathsf{r}}{\lambda}\right) - \delta_1^2 K_0\left(\frac{\beta_- \mathsf{r}}{\xi_1}\right) - \delta_2^2 K_0\left(\frac{\beta_+ \mathsf{r}}{\xi_1}\right), \tag{4.12}$$

where the units are now explicitly shown. Here, we list the consequences of the above asymptotics. i) Comparing Eq. (4.12) to the one-band case [84], where

$$E_{1B}(\mathsf{r}) = \delta_4^2 K_0\left(\mathsf{r}/\lambda_{1B}\right) - \delta_5^2 K_0\left(\sqrt{2}\mathsf{r}/\xi_{1B}\right), \tag{4.13}$$

shows that the lengthscale $\lambda^{-2} = (w_1/\lambda_1)^2 + (w_2/\lambda_2)^2$ is playing the role of an effective penetration depth for the two-band superconductor in accordance with Eq. (60) in Ref. [85], contrary to $\lambda^{-2} = (1/\lambda_1)^2 + (1/\lambda_2)^2$ used in Refs. [74] and [86, 87] which holds only in the (unrealistic) absence of coupling. ii) The parameters δ_k are in general different from each other, but can be

calculated exactly in the Bogomol'nyi point for the two band system as $\delta_1^2 = \delta_2^2 = 2\delta_3^2$. For $\gamma = 0$, the choice of $\xi_1 = \xi_2 = 1$ and $\kappa_1 = \kappa_2 = 1$ in the two-band case is thus analogous to the Bogomol'nyi point $\kappa_{1B} = 1/\sqrt{2}$ for the single band case and, accordingly, the long-range interaction must vanish (and change sign for $\kappa_1 = \kappa_2 < 1$). This directly illustrates that coupling of two (nominally) type-II condensates may lead to a type-I behavior of the coupled system! iii) In Eq. (4.13) for single band superconductors, it is clear that if $\kappa_{1B} = \lambda_{1B}/\xi_{1B} > 1/\sqrt{2}$ ($< 1/\sqrt{2}$), the interaction potential $E_{1B}(\mathsf{r})$ will be repulsive (attractive). For two-band superconductors, Eq. (4.12) shows that the relevant parameters are $\kappa_\pm^* = \frac{\beta_\pm \lambda}{\sqrt{2}\ \xi_1}$, rather than the nominal GL parameters κ_j for each condensate. If either κ_+^* or κ_-^* are below $1/\sqrt{2}$, the long-range vortex interaction is attractive (type-I like). Eqs. (4.4) and (4.10c) provide simple means to evaluate this condition. iv) In the presence of coupling, the long-range behavior of both σ_j depends exponentially on *the smallest* of β_- and β_+. Therefore, in the coupled case, we can define not only a single penetration depth for both bands, but also the order parameters for both condensates exhibit *the same decay* at large distances which implies a joint coherence length $\xi^* = \xi_1/\min(\beta_+, \beta_-)$.

4.2.3 Surface energy and the short-range vortex interaction

The analysis in the previous subsection brings us to the discussion of the real criterion for the attractive/repulsive nature of the vortex interaction. In the single-band case, the changing sign of the normal domain - superconductor surface energy E_S at the Bogomol'nyi point is a correct criterion. However, in the two-band case and for large vortex-vortex distance, the Bogomol'nyi point is determined by a single valued $\kappa^* = \min(\kappa_+^*, \kappa_-^*) = 1/\sqrt{2}$, which is not necessarily where the surface energy of the normal domain (vortex) changes sign!

The sign of the energy of the interfaces between normal-metal domains and the superconductor determines whether merging of those domains is energetically favorable or not (i.e. if the superconductor is type-I or type-II). For the vortices (the smallest possible normal domains) the negative vortex-superconductor surface energy therefore means that the vortices should repel (at least at short distances) in order to avoid the formation of a giant vortex. We here show how to calculate the normal-superconducting interface energy and by that predict the type of the short-range vortex-vortex interaction.

We follow a similar approach to that of Refs. [86, 87], but we take into account the Josephson coupling and the temperature dependence of

the Ginzburg-Landau (GL) parameters, within a microscopic framework. Namely, we consider the interface between normal and superconducting region as the yz-plane at $x = 0$ and calculate the surface energy E_S using the one-dimensional GL functional at the thermodynamic critical field H_c, which reads

$$\begin{aligned} E_S = \int_{-\infty}^{\infty} dx \Big\{ & 2(\Psi_1'^2 + A^2\Psi_1^2) + (2\chi_1 - \Psi_1^2)\Psi_1^2 \\ & + \alpha \frac{\kappa_1^2}{\kappa_2^2} \left[2(\Psi_2'^2 + A^2\Psi_2^2) + \alpha(2\chi_2 - \Psi_2^2)\Psi_2^2 \right] \\ & - 2\gamma\Psi_1\Psi_2 + \left(H_c - \sqrt{2}\kappa_1 A' \right)^2 \Big\}, \end{aligned} \tag{4.14}$$

where the gauge potential is chosen as $\mathbf{A} = (0, A(x), 0)$ and $\Psi_{j=1,2}$ are taken real. The thermodynamic critical field of the coupled system H_c is obtained from the condition that the GL functional in Eq. (4.1) converges to zero for $H = H_c$, leading to

$$H_c^2 = H_{c(1)}^2 w_1^2 (2\chi_1 - w_1^2) + H_{c(2)}^2 w_2^2 (2\chi_2 - w_2^2) + 4\gamma H_{c(1)}^2 w_1 w_2, \tag{4.15}$$

where the formally defined thermodynamic critical field of each condensate is $H_{c(j)} = hc/(4e\sqrt{2}\pi\lambda_j\xi_j) = 2W\sqrt{\pi N(0) n_j}$. We then find Ψ_j and A that minimize E_S by numerically solving the set of Euler-Lagrange equations for the functional in Eq. (4.14), which are exactly the one-dimensional versions of Eqs. (4.2a-c):

$$\Psi_1'' = \frac{A^2}{2}\Psi_1 - \left(\chi_1 - \Psi_1^2\right)\Psi_1 - \gamma\Psi_2, \tag{4.16a}$$

$$\Psi_2'' = \frac{A^2}{2}\Psi_2 - \alpha\left(\chi_2 - \Psi_2^2\right)\Psi_2 - \frac{\gamma\kappa_2^2}{\alpha\kappa_1^2}\Psi_1, \tag{4.16b}$$

$$A'' = \left(\frac{\Psi_1^2}{\kappa_1^2} + \alpha\frac{\Psi_2^2}{\kappa_2^2} \right) A. \tag{4.16c}$$

The boundary conditions in the normal state ($x \to -\infty$) and deep in the superconducting state ($x \to \infty$) are $\psi_j(x \to -\infty) = 0$, $A'(x \to -\infty) = 1$, $\psi_j'(x \to \infty) = 0$ and $A'(x \to \infty) = 0$.

4.2.4 Constrained GL equations for fixed vortices

We supplement our argumentation by numerically obtained vortex-vortex interaction potentials (in a similar fashion as in Ref. [88]). Since the problem

of two vortices does not have circular symmetry, we now consider the fixed-vortex ansatz in Cartesian coordinates $\Psi_j = e^{i\ell_1\theta_1}e^{i\ell_2\theta_2}f_j(x,y)$, describing two fixed vortices with winding numbers ℓ_1 and ℓ_2, where $e^{i\ell_k\theta_k}$ is written in Cartesian coordinates as

$$e^{i\ell_k\theta_k} = \left(\frac{x_k + iy_k}{x_k - iy_k}\right)^{\ell_k/2}, \tag{4.17}$$

and $\mathbf{r}_k = (x_k, y_k, 0)$ is the in-plane position vector with origin at the center of the vortex k. For the case of two vortices separated by a distance d, we take $\mathbf{r}_1 = (x - d/2, y, 0)$ and $\mathbf{r}_2 = (x + d/2, y, 0)$. With this ansatz, the Euler-Lagrange equations for the energy functional in Eq. (4.1) read (see also Ref. [98])

$$\nabla^2 f_1 - \left[\overline{X}^2 + \overline{Y}^2 + 2(A_x\overline{Y} - A_y\overline{X}) + \mathbf{A}^2\right] f_1 + (\chi_1 - f_1^2)f_1 + \gamma f_2 = 0, \tag{4.18a}$$

$$\nabla^2 f_2 - \left[\overline{X}^2 + \overline{Y}^2 + 2(A_x\overline{Y} - A_y\overline{X}) + \mathbf{A}^2\right] f_2 + \alpha\left(\chi_2 - f_2^2\right) f_2 + \frac{\gamma\kappa_2^2}{\alpha\kappa_1^2} f_1 = 0, \tag{4.18b}$$

and

$$\nabla \times \nabla \times \mathbf{A} = -\left[\mathbf{A} - \frac{\ell_1\hat{\theta}_1}{r_1} - \frac{\ell_2\hat{\theta}_2}{r_2}\right]\left(\frac{f_1^2}{\kappa_1^2} + \alpha\frac{f_2^2}{\kappa_2^2}\right), \tag{4.18c}$$

where

$$\overline{X} = \frac{\ell_1 x_1}{r_1^2} + \frac{\ell_2 x_2}{r_2^2}, \qquad \overline{Y} = \frac{\ell_1 y_1}{r_1^2} + \frac{\ell_2 y_2}{r_2^2},$$

and the angular unit vectors around each vortex are written as

$$\widehat{\theta_k} = (-y_k/r_k, x_k/r_k, 0). \tag{4.19}$$

In the following we consider only the case $\ell_1 = \ell_2 = 1$, i.e., the most usual single flux quantum composite vortex.

Eqs. (4.18a-c) are thus the GL equations for the two fixed vortices, and we solve them numerically by a relaxation method. The obtained order parameter and vector potential are then substituted back in the energy functional, yielding the energy $E(d)$ for the vortex pair at distance d. Repeating this procedure for different vortex-vortex separation, we obtain the interaction potential $\Delta E = E(d) - E(0)$ between vortices in the two-gap superconductor, as shown in Fig. 4.1(b-d).

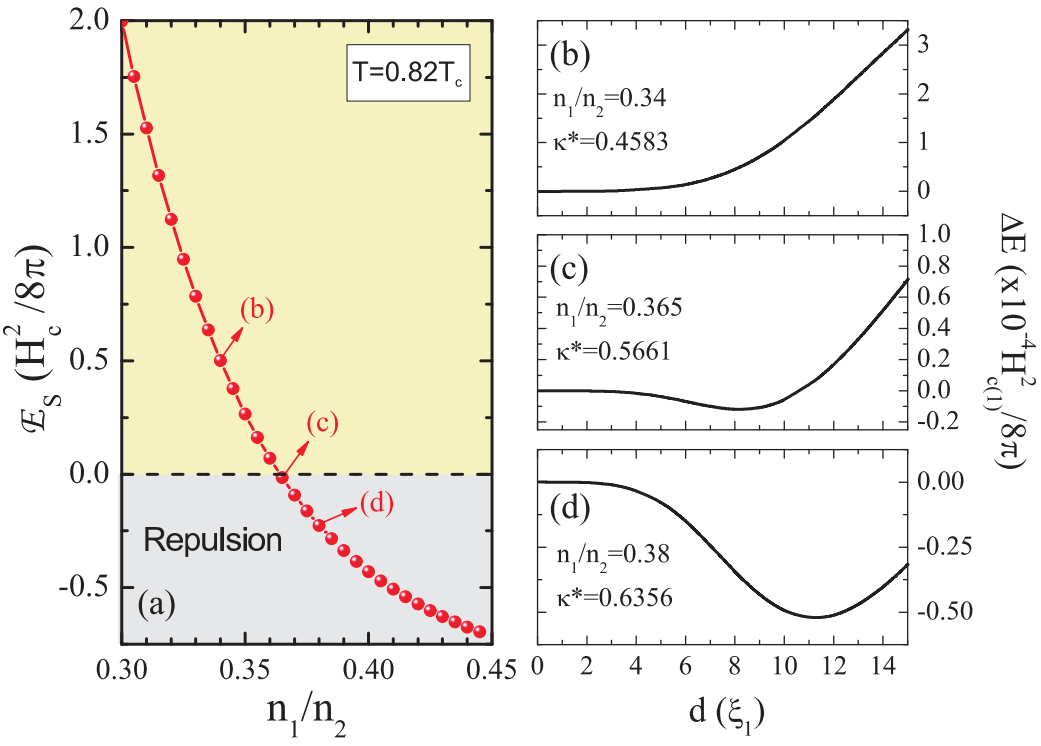

Figure 4.1: The normal domain - superconductor surface energy E_S as a function of the ratio of the density of states in the two bands (a) and the corresponding vortex-vortex interaction energies (b-d) for indicated parameters. The short-range interaction force changes sign when the surface energy changes sign.

4.3 Results and discussion

We now apply the techniques described in the previous sections to calculate (i) the asymptotic long-range GL parameter κ^*, (ii) the normal domain - superconductor surface energy E_S, and (iii) the full vortex-vortex potential (using the constrained GL equations (4.18)(a-c)).

As a first example, Fig. 4.1 shows the surface energy E_S and the numerically obtained vortex-vortex interaction potentials for a set of parameters corresponding (arguably) to MgB_2: $\kappa_1 = 3.71$ and $\xi_1/\xi_2 = v_1/v_2 = 0.255$ are taken from Ref. [1], the coupling matrix is obtained from Ref. [89], the temperature is fixed at $T = 0.82T_c$, while we vary the density of states in the two bands. We note that in all considered cases $\kappa^* < 1/\sqrt{2}$ and the long-range interaction is always attractive, whereas short-range interaction changes to repulsive *exactly when the surface energy E_S changes sign* with increasing

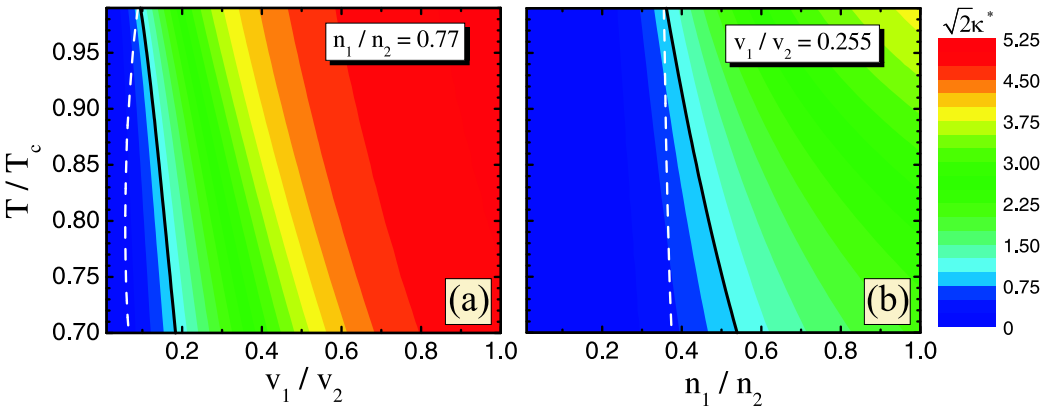

Figure 4.2: The long-range interaction phase diagram for a MgB_2 crystal, at different temperatures and for varied values of the ratio between (a) the Fermi velocities, and (b) the partial density of states, of the two bands. In each panel, the black line separates the regions of long-range attraction and long-range repulsion (left to right). The white lines indicate where E_S changes sign and the short-range interaction changes from attractive to repulsive (left to right).

n_1/n_2. **To conclude, the long-range vortex-vortex interaction is determined by κ^* with respect to $1/\sqrt{2}$, while the short-range behavior is determined by the sign of the surface energy** E_S. This also proves insufficient the initial premise in Ref. [1] that if the system has $\lambda/\xi_1 > 1/\sqrt{2}$ and $\lambda/\xi_2 < 1/\sqrt{2}$, the vortex interaction should be long-range attractive and short-range repulsive. The actual behavior is far more complex, and can be *exactly* determined as explained above.

Recent calculations have shown that as $T \to T_c$, only type-I or type-II vortex behavior can be observed [79]. Indeed, by analyzing κ^* and the sign of E_S at $T \to T_c$ as explained above, we always found the same type of interaction in either long- or short-range limit. However, for T immediately below T_c the sign change of E_S and the transition from $\kappa^* > 1/\sqrt{2}$ to $\kappa^* < 1/\sqrt{2}$ occur for different sets of parameters, opening up the parameter space for observation of the non-monotonic vortex interaction. This is shown in Fig. 4.2, where we plot κ^* as a function of temperature and also the ratios between the Fermi velocities (Fig. 4.2(a)) and the partial density of states of each condensate (Fig. 4.2(b)). The black line in Fig. 4.2 denotes $\kappa^* = 1/\sqrt{2}$ and the white line indicates where $E_S = 0$. At $T = T_c$ these lines coincide, in agreement with Ref. [79], but as T decreases, the lines separate, bordering the region where the system exhibits short-range repulsion ($E_S < 0$) and long-range attraction ($\kappa^* < 1/\sqrt{2}$), i.e., non-monotonic vortex interaction. This

finding further creates a new possibility of *tuning the magnetic interactions* in two-band superconductors *by changing temperature*. For example, for the parameters of MgB_2 given in Ref. [1] (Fig. 4.2(a) for $v_1/v_2 = 0.255$), we find that non-monotonic vortex interactions occur only for $T \lesssim 0.49\ T_c$,[1] whereas pure type-II behavior is expected at higher temperatures. The experiment in Ref. [1] was done at $T \approx 0.1\ T_c$, and could thus be repeated at higher temperatures to verify our prediction.

In Fig. 4.3(a) a similar phase diagram is constructed for recently discovered, and for many reasons exciting, pnictides. In particular, we show the results for LiFeAs, using the parameters given in Ref. [71], except for the fact that λ_{12} in the Λ matrix must be taken negative due to the $s_\pm$ pairing. For this material, we extract $\kappa_1 = 2.4$, $n_1/n_2 = 1.384$ and $v_1/v_2 = 0.722$. Interestingly enough, as $\kappa_2 = \kappa_1\sqrt{n_1 v_1^2/n_2 v_2^2}$, we note that both nominal GL parameters of the bands are larger than $1/\sqrt{2}$ if $\sqrt{n_1 v_1^2/n_2 v_2^2} \gtrsim 0.295$. Therefore, it can be once more verified that in a large portion of the parameter space where both bands are convincingly type-II, the coupled system exhibits type-I behavior. In Fig. 4.3(b), we show that for $T = 0.9\ T_c$, the $E_S = 0$ (white) and $\kappa^* = 1/\sqrt{2}$ (black) curves coincide for small n_1/n_2 and large v_1/v_2. This behavior persists even at lower temperatures, as shown in Fig. 4.3(c). However, in the opposite case (large n_1/n_2 and small v_1/v_2), the curves separate, forming a region of non-monotonic vortex interaction in the phase diagram which grows larger as temperature decreases (see Fig. 4.3(d)). This broad temperature range for the observation of partial vortex attraction is important experimentally, to discriminate the non-monotonic vortex interactions from irregular vortex lattices formed due to intrinsic defects in the material [90, 91] (with latter being dominant only at temperatures where the vortex core and the defects are similar in size, unless defects are of magnetic nature).

4.4 Conclusions

In conclusion, we have demonstrated the semi-analytic method to relatively easily determine the nature of vortex-vortex interaction in two-band superconductors. This is of significant theoretical and experimental importance, as Figs. 4.2, 4.3 sketch just two examples of many possibilities attainable by two-band hybridization. Note that a plethora of transitions, even reentrant behaviors, can be found as a function of the microscopic parameters,

[1] This temperature is far out of the Ginzburg-Landau domain, but is taken as an example. Our prediction can also be made at a higher temperature, but for microscopic parameters that do not correspond to any known material at the moment.

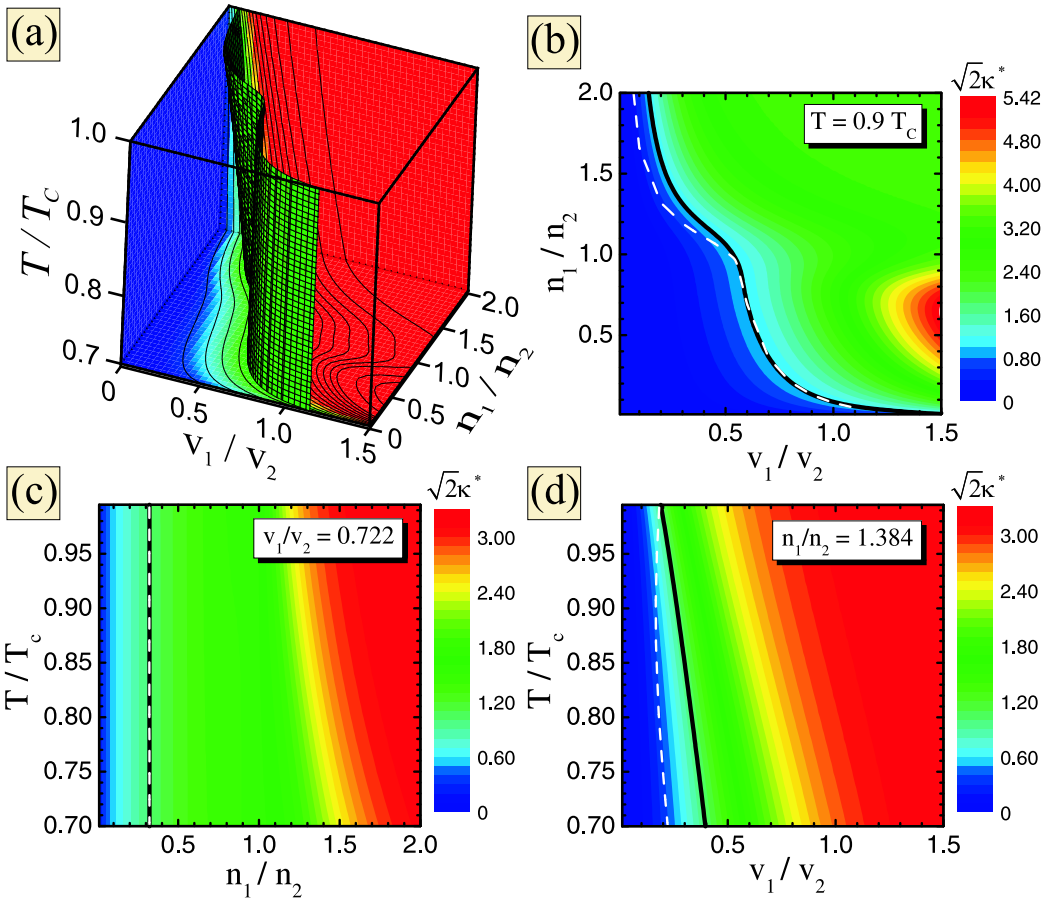

Figure 4.3: (a) The long-range vortex interaction $(v_1/v_2, n_1/n_2, T)$ phase diagram for LiFeAs, for other parameters taken from Ref. [71]. The shown isosurface corresponds to $\kappa^* = 1/\sqrt{2}$ and the change of the long-range vortex-vortex interaction. (b-d) 2D cuts of (a) in the $T = 0.9\ T_c$, $v_1/v_2 = 0.722$, and $n_1/n_2 = 1.384$ planes, respectively. Black (white) lines correspond to $\kappa^* = 1/\sqrt{2}$ ($E_S = 0$).

which can be tuned experimentally (to some extent) by e.g. carrier injection [92]. Finally, with appropriate modifications of the initial energy functional our approach can also provide insight in similar situations encountered in nanoscale superconducting films, tailor-made two-component superconducting hybrids, and dirty two-band compounds.

Related publication

- A. Chaves, L. Komendová, M. V. Milošević, J. S. Andrade, Jr., G. A. Farias, and F. M. Peeters: *Conditions for nonmonotonic vortex interaction in two-band superconductors*, Phys. Rev. B **83**, 214523 (2011).

Chapter 5

Order-parameter length scales in the extended GL theory

Using the Ginzburg-Landau theory extended to the next-to-leading order we determine numerically the healing lengths of the two order parameters at the two-gap superconductor/normal metal interface. We demonstrate on several examples that those can be different even in the strict domain of applicability of the Ginzburg-Landau theory. This justifies the use of this theory to describe relevant physics of two-gap superconductors, distinguishing them from their single-gap counterparts. Afterwards, we turn to the study of the vortex profiles in two-gap superconductors using the extended Ginzburg-Landau theory. We compare the behavior expected from the standard Ginzburg-Landau theory with the extended GL approach, and find qualitative agreement in the case of LiFeAs.

5.1 Introduction

Over the past half-century, the Ginzburg-Landau (GL) theory [4] has proven to be a very helpful tool in studies of superconductivity, but also other systems in and out of condensed matter physics. By its construction, the formalism is only justified near the critical temperature T_c, but it typically produces qualitatively correct results even far below T_c. Recently an exception was found to this unwritten rule, when it was shown that the standard formulation of the GL theory is insufficient for adequate description of two-band (or multiband) superconductors, because it predicts the same spatial variation of the condensates in all bands [2] (within its range of applicability,

i.e., very close to T_c). This renders it unable to connect to the theoretical results obtained by using Usadel [93, 94] or Eilenberger [95] equations in the broader temperature range, which unambiguously show presence of two separate length scales for two gaps. Experimentally, the evidence for different coherence lengths in σ and π bands of MgB_2 was previously found by direct vortex imaging [42], μSR imaging of the supercarrier density [47], and in pronounced features in the flux-flow resistivity [96] as a function of the applied magnetic field.

In order to capture the important physics of different length scales, one needs to extend the GL formalism as realized in Ref. [3], where the two order parameters are calculated up to order $\tau^{3/2}$ in the small deviation from the critical temperature $\tau = 1 - T/T_c$, instead of the standard $\tau^{1/2}$ as used in Ref. [2]. In the latter article, the authors mention that the extra terms in the next-to-leading order are by construction small corrections, not significant enough to alter the *single* coherence length controlling the spatial distribution of *both* condensates. First, we argue that the effects of higher-order corrections can be significant since the above argument about small corrections applies only to the order parameter - not necessarily to its spatial profile i.e. healing lengths and other physical quantities. Second, we argue that any (even small) difference between the characteristic length scales of two condensates is of fundamental importance, since it may lead to other novel phenomena related to the competition of length scales. Note that here we do not enter the recent debate about sufficient discrepancy of length scales and/or relation between them to provide 'type-1.5' superconductivity [1, 97, 98]. Instead, we complement that discussion, by exactly quantifying the difference in length scales in the domain of the extended GL theory.

The fact that the difference of characteristic length scales of two Cooper pair condensates exists even in the strict Ginzburg-Landau domain is of great practical importance, since the calculations based on the Ginzburg-Landau theory are typically far less computationally demanding than the calculations based on full microscopic theories (Bogoliubov-de Gennes, Gor'kov, Usadel or Eilenberger equations). In microscopic formalisms, one usually has to make clever approximations and make compromises in the calculation procedure. As a consequence, even though these approaches are valid in the whole temperature range from absolute zero to T_c, they are limited to the simple systems such as a single vortex or other highly symmetric or effectively one-dimensional cases. On the contrary, the Ginzburg-Landau equations have a much simpler structure and therefore allow for studying of highly non-trivial situations such as vortex lattice statics and dynamics, current driven systems, interaction with pinning, and fluxonic devices. Since the above is well established in the standard GL formalism, we emphasize here that the calculations

become only a fraction more complicated in the extended Ginzburg-Landau formalism. While it does contain more equations (for the order parameters to the leading, and next-to-leading order), the coupling of those equations is realized through the coefficients and not the calculated variables - contrary to the standard set of two-band GL equations [98–100].

Finally, the present study and its conclusions are relevant not only to bulk multiband materials, but also to nanoscale superconductors, e.g., single-crystalline metallic nanofilms [101–105], and also pancake-shaped superfluid Fermi gases in optical traps [106], where the multiband structure appears due to quantum confinement. The key mechanism there is the formation of discrete single-particle energy levels for the motion in the strongly-confined direction (while motion is quasi-free in the other directions).

5.2 Theoretical formalism

Following Ref. [3], we evaluate the order parameters Δ_j up to order $\tau^{3/2}$ by taking $\Delta_j(\mathbf{x}) = \Delta_j^{(0)}(\mathbf{x}) + \Delta_j^{(1)}(\mathbf{x})$, where $\Delta_j^{(0)}(\mathbf{x}) \propto \tau^{1/2}$ and $\Delta_j^{(1)}(\mathbf{x}) \propto \tau^{3/2}$, with $j = 1, 2$ indexing two coupled condensates in a two-band superconductor. Let us consider two complex order parameters at zero magnetic field. By the procedure described in detail in Ref. [3] we obtain in leading order

$$\alpha\Delta_j^{(0)} + \beta_j\Delta_j^{(0)}|\Delta_j^{(0)}|^2 - K\nabla^2\Delta_j^{(0)} = 0. \tag{5.1}$$

In the next-to-leading order we have

$$\alpha\Delta_j^{(1)} + 2\beta_j|\Delta_j^{(0)}|^2\Delta_j^{(1)} + \beta_j(\Delta_j^{(0)})^2\Delta_j^{*(1)} - K\nabla^2\Delta_j^{(1)} = F(\Delta_j^{(0)}) + F_j(\Delta_j^{(0)}), \tag{5.2}$$

where

$$F(\Psi) = \sigma\Psi + S\nabla^2\Psi + Y\nabla^2(\nabla^2\Psi), \tag{5.3}$$

and

$$F_j(\Psi) = \rho_j|\Psi|^2\Psi + \chi_j|\Psi|^4\Psi + \frac{U_j}{5}[2\Psi|\nabla\Psi|^2 + 3\Psi^*(\nabla\Psi)^2 + \Psi^2\nabla^2\Psi^* + 4|\Psi|^2\nabla^2\Psi] + V_j\nabla^2(\Psi|\Psi|^2) + \frac{Z_j}{3}\left[2|\Psi|^2\nabla^2\Psi + \Psi^2\nabla^2\Psi^*\right]. \tag{5.4}$$

The formal definitions of the coefficients α, β_j, K, σ, S, Y, ρ_j, χ_j, U_j, V_j and Z_j are given in Ref. [3] and their explicit form we give below. Parameters

entering the zeroth order are

$$\alpha = -\frac{N(0)\tau}{\lambda_{12}}(A_2 n_1 + A_1 n_2), \tag{5.5}$$

$$\beta_1 = \frac{N(0)W_3^2}{\lambda_{12}^3}(A_2 n_1 \lambda_{12}^2 + n_2 A_1^3), \tag{5.6}$$

$$K = \frac{\hbar^2 N(0)W_3^2}{6\lambda_{12}}(A_2 n_1 v_1^2 + A_1 n_2 v_2^2), \tag{5.7}$$

while parameters entering the first order are

$$\sigma = \frac{N(0)\tau^2}{2\lambda_{12}}[A_2 n_1 + A_1 n_2 - 2\eta n_1 n_2], \tag{5.8}$$

$$\rho_1 = -\frac{N(0)W_3^2\tau}{\lambda_{12}^3}[2n_1\lambda_{12}^2 A_2 + 2n_2 A_1^3 - \eta n_1 n_2(3A_1^2 + \lambda_{12}^2)], \tag{5.9}$$

$$\chi_1 = \frac{N(0)}{\lambda_{12}^5}(n_2 W_5^4 A_1^5 - 3\eta n_1 n_2 \lambda_{12}^2 W_3^4 A_1^2 + W_5^4 A_2 \lambda_{12}^4 n_1), \tag{5.10}$$

$$S = \frac{\hbar^2 N(0)W_3^2\tau}{6\lambda_{12}}[2n_1 v_1^2 A_2 + 2n_2 v_2^2 A_1 - \eta n_1 n_2(v_1^2 + v_2^2)], \tag{5.11}$$

$$Y = \frac{\hbar^4 N(0)}{180\lambda_{12}}[6W_5^4(A_2 n_1 v_1^4 + A_1 n_2 v_2^4) - 5\eta n_1 n_2 v_1^2 v_2^2 W_3^4], \tag{5.12}$$

$$V_1 = \frac{\eta\hbar^2 N(0) n_1 n_2 W_3^4}{6\lambda_{12}} v_2^2, \tag{5.13}$$

$$Z_1 = \frac{\eta\hbar^2 N(0) W_3^4 n_1 n_2}{2\lambda_{12}^3} A_1^2 v_1^2, \tag{5.14}$$

$$U_1 = -\frac{5\hbar^2 N(0) W_5^4}{9\lambda_{12}^3}(n_1 v_1^2 \lambda_{12}^2 A_2 + n_2 v_2^2 A_1^3), \tag{5.15}$$

with $A_1 = \lambda_{22} - \eta n_1 A$ and $A_2 = \lambda_{11} - \eta n_2 A$. Here $A = \ln(2e^{\Gamma}\hbar\omega_D/\pi T_c)$, with Euler constant $\Gamma = 0.577$, and η denotes the determinant of the interaction matrix $\lambda_{ij} = N(0)g_{ij}$, with g_{ij} the coupling constant, $N(0)$ the total density of states (DOS) and $n_j N(0)$ the band-dependent DOS. In addition, the coefficients feature Fermi velocities v_j of both bands, $W_3^2 = 7\zeta(3)/(8\pi^2 k_B^2 T_c^2)$, and $W_5^4 = 93\zeta(5)/(128\pi^4 k_B^4 T_c^4)$, with $\zeta(\ldots)$ the Riemann zeta-function. The coefficients β_2, ρ_2, χ_2, V_2, Z_2 and U_2 are obtained by exchanging the indices 1 and 2 throughout the respective formulas.

Since Eq. (5.1) is completely equivalent to the single-gap GL equation and the bands share the same critical temperature T_c, we have either *both* bands normal or *both* bands superconducting. In the first case, Eq. (5.2) allows only $\Delta_j^{(1)} = 0$ as a solution and thus superconductivity cannot be restored by

corrections in the extended GL model. In the following we will consider that both bands are superconducting and their bulk amplitudes $W_j = \sqrt{-\alpha/\beta_j}$ are real. We rescale the equations using $\Delta_j^{(k)} = W_j \tilde{\Delta}_j^{(k)}$ and $x = \xi\tilde{x}$, where $\xi = \sqrt{-K/\alpha}$ is the unit of length common for both condensates, and obtain (tildes omitted)

$$\Delta_j^{(0)} - [\Delta_j^{(0)}]^3 + \nabla^2 \Delta_j^{(0)} = 0, \tag{5.16a}$$

$$\Delta_j^{(1)}(1 - 3[\Delta_j^{(0)}]^2) + \nabla^2 \Delta_j^{(1)} = \frac{F(\Delta_j^{(0)}) + F_j(\Delta_j^{(0)})}{\alpha W_j}. \tag{5.16b}$$

The first equation is the same for both bands, while the second one differs through the terms on the right hand side. This is exactly the cause for the emergence of two different characteristic lengths in the two bands. From Eq. (5.16) it is also directly apparent why this does not happen in the order parameters of order $\tau^{1/2}$, i.e., in Eq. (5.16a), but only in the higher order considerations as in Eq. (5.16b). To evaluate the coefficients entering Eq. (5.16) one needs in principle to specify the coupling constants λ_{11}, λ_{22} and λ_{12}, the partial density of states in one band, e.g., n_1, (since $n_1 + n_2 = 1$ this determines n_2 as well), and the ratio of the Fermi velocities v_1/v_2. All other parameters enter units of scaling, and therefore have no impact on any physical effects.

5.3 The Ginzburg-Landau domain

Before discussing the numerical results of Eqs. (5.16), it is very important to get a feeling about the relevant values of τ, i.e., *the domain of applicability* of the extended GL model. First of all, our analysis shows that $\tau\Delta_j^{(0)} \sim \Delta_j^{(1)}$. Then, by construction, $\Delta_j^{(0)} > \Delta_j^{(1)}$ and the trivial inequality $\tau < 1$ holds. However, this is a necessary but not sufficient condition justifying Eqs. (5.16), as one also needs to keep in mind the justification for the use of the gradient expansion in the derivation of Eqs. (5.16). This expansion requires the GL coherence length ξ to be larger than the band-dependent correlation length $\zeta_j = \hbar v_j/(2\pi T)$ that controls the spatial variations of the relevant kernels in the integral expansion of the anomalous (Gor'kov) Green function in powers of the band-dependent order parameters (in the clean limit), i.e.,

$$\zeta_1, \zeta_2 < \xi. \tag{5.17}$$

It is important to note here that for a two-band superconductor ζ_j is not necessarily close to the band-dependent generalization of the Pippard length, i.e., $\hbar v_j/(\pi\Delta_j)|_{T=0}$, often used as an estimate of the coherence lengths of two

bands [1, 2]. Using definitions of α, K and β_j, we obtain from Eq. (5.17) the following estimate for the GL domain $\tau \lesssim \tau^*$ with

$$\frac{\tau^*}{(1-\tau^*)^2} = 1 + \frac{v_1^2/v_2^2 - 1}{1 + n_2\mathcal{A}_1/(n_1\mathcal{A}_2)} \quad (v_1 < v_2). \tag{5.18}$$

If $v_1 \geq v_2$, the replacement $1 \leftrightarrow 2$ should be made. Equation (5.18) shows that the extent of the Ginzburg-Landau domain for specific multigap superconductor depends on its material parameters, as was first pointed out in Ref. [94]. Equation (5.18) is most sensitive to the ratio of the Fermi velocities v_1/v_2. In particular, when $v_1/v_2 = 1$, the above inequality simply implies $\tau \lesssim 0.38$, i.e., the same as in the one-band case, regardless of the particular values of the other parameters, i.e., n_2/n_1 and $\mathcal{A}_2/\mathcal{A}_1$ (where $\mathcal{A}_2/\mathcal{A}_1 = [\Delta_1^{(0)}/\Delta_2^{(0)}]^2$). For $n_1 \approx n_2$ and $\mathcal{A}_1 \approx \mathcal{A}_2$, we typically obtain $0.27 < \tau^* < 0.38$, thus the temperature domain of GL theory is still very large. The GL domain shrinks significantly only when the ratio $n_2\mathcal{A}_1/(n_1\mathcal{A}_2)$ acquires either extremely large or very small values, which, e.g., can occur when the two energy gaps differ more than an order of magnitude and at the same time v_1 is very different from v_2. For example, for the magnesium diboride parameters (as elaborated further below) one finds from Eq. (5.18) $\tau^* = 0.08 - 0.32$ depending on the relevant ratio of the Fermi velocities, i.e., on the direction considered, because σ band of magnesium diboride is highly anisotropic. The threshold temperature for the applicability of the GL theory (τ^*) for a broader range of parameters (i.e., other materials) is plotted in Fig. 5.1. Additionally, we demand that bulk solutions satisfy $|\Delta_j^{(1)}| \ll \Delta_j^{(0)}$, i.e., the 'correction' must be smaller than the main part of the wave function.

5.4 Different length scales in selected multigap materials

To evaluate and compare the spatial distribution of the two order parameters in a two-band superconductor, we study the simple case of a superconductor/normal metal (S/N) interface in the absence of any applied magnetic field. It then suffices to consider the one-dimensional version of Eqs. (5.16), along the x-axis perpendicular to the S/N interface, with both gaps taken to be real. The appropriate boundary conditions are $\Delta_j^{(k=0,1)}(x=0) = 0$, and $\nabla\Delta_j^{(k)}(x \to \infty) = 0$, where thus $x = 0$ lies at the interface, with superconductivity fully suppressed there. The second boundary condition ensures unperturbed two-gap superconductivity away from the S/N interface. In Fig.

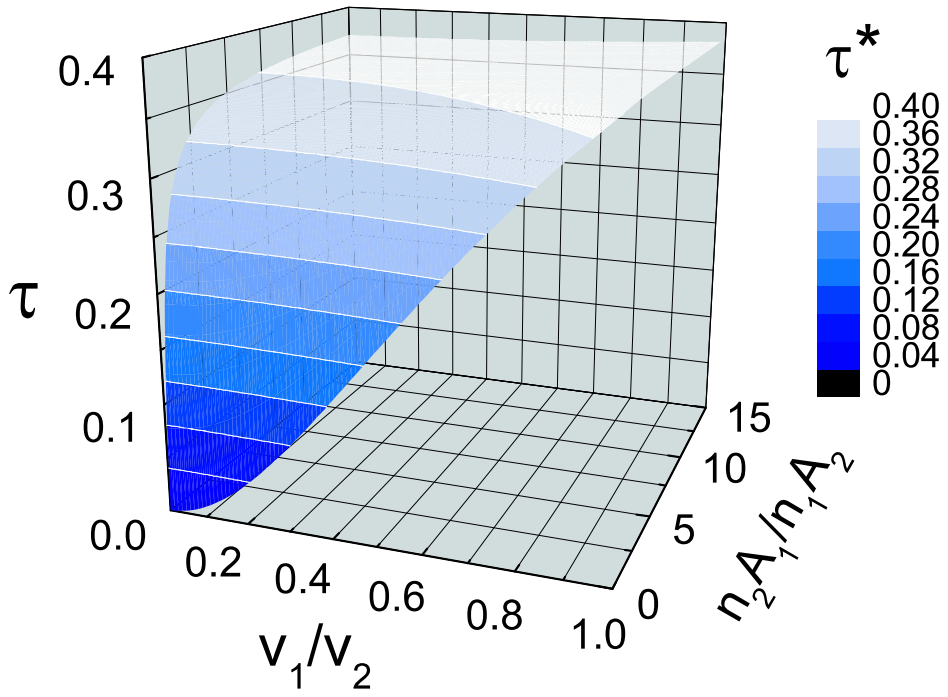

Figure 5.1: The estimated temperature range $\tau < \tau^*$ of the validity of the GL theory based on Eq. (5.18). The gradient expansion made in the derivation of the GL equations (both standard and extended) is fully justified below the plotted 3D-surface.

5.2(a) we show the results for $\Delta_j(x)$ in MgB_2 (normalized to bulk values, at temperature $T = 0.95T_c$, and with other parameters taken from Refs. [1] and [89]), obtained within standard [98], extended [3], and reduced [2] GL formalism. In the case of MgB_2, the extended GL model clearly gives two length scales for two order parameters $\Delta_{j=1,2}$, *smaller* than those obtained in the standard GL theory (with incomplete higher-order terms).

For correct comparison one must define a measure for the spatial variations of Δ_j. From the numerical solution of Eq. (5.16a) we found that at the characteristic distance ξ the single-gap-like order parameter $\Delta_j^{(0)}$ increases from zero to 0.6089 of its bulk value Δ_{j0}. Therefore we define the *healing lengths* ξ_j for the two condensates in a two-gap superconductor using the criterion $\Delta_j(\xi_j) \equiv 0.6089\Delta_{j0}$, as depicted in Fig. 5.2(b). The difference between the characteristic length scales in two bands is clear already from their definition in Fig. 5.2(b), but we emphasize this point in Figs. 5.2(c,d), where the ratio of the healing lengths of the two order parameters is plotted as a function of temperature [Fig. 5.2(c)] and ratio of Fermi velocities v_1/v_2 [Fig. 5.2(d)]. At the lowest temperature shown in (c), $T = 0.92T_c$, the disparity between the healing lengths is already over 25%, and the difference increases as the ratio of the Fermi velocities is taken smaller [see (d)].

In the analysis of the above phenomenon we noticed that only the coefficient S (Eq. (5.11)) in front of the term $\nabla^2\Delta_j^{(0)}$ in $F(\Delta_j^{(0)})$ depends both on τ and v_1/v_2. We can rewrite it as follows:

$$S = \frac{\hbar^2 N(0) W_3^2 \tau}{6\lambda_{12}} \sum_{j=1,2} v_j^2 (2n_j\lambda_{jj} - \eta n_1 n_2 (1 + 2\mathcal{A})). \tag{5.19}$$

Due to this special form, for particular values of n_j and λ_{ij} the term in brackets can be positive for one band, but negative for the other. In such a case it is possible to change the sign of S term by varying the ratio of the Fermi velocities v_1/v_2 around its threshold value

$$\left(\frac{v_1}{v_2}\right)^* = \left(-\frac{2n_2\lambda_{22} - \eta n_1 n_2(1+2\mathcal{A})}{2n_1\lambda_{11} - \eta n_1 n_2(1+2\mathcal{A})}\right)^{1/2}, \tag{5.20}$$

which equals 0.46 for the parameters of Fig. 5.2. Therefore, two cases with v_1/v_2 significantly larger and smaller than 0.46 will show very different behavior with respect to the disparity of the healing lengths of the two condensates, as is visible in Fig. 5.2(d). For $v_1/v_2 \approx 0.46$, the term with coefficient S has no influence and other terms determine the spatial behavior of the order parameters.

Besides the difference in the healing lengths of the two condensates, the extended GL model provides insight also in a more accurate temperature

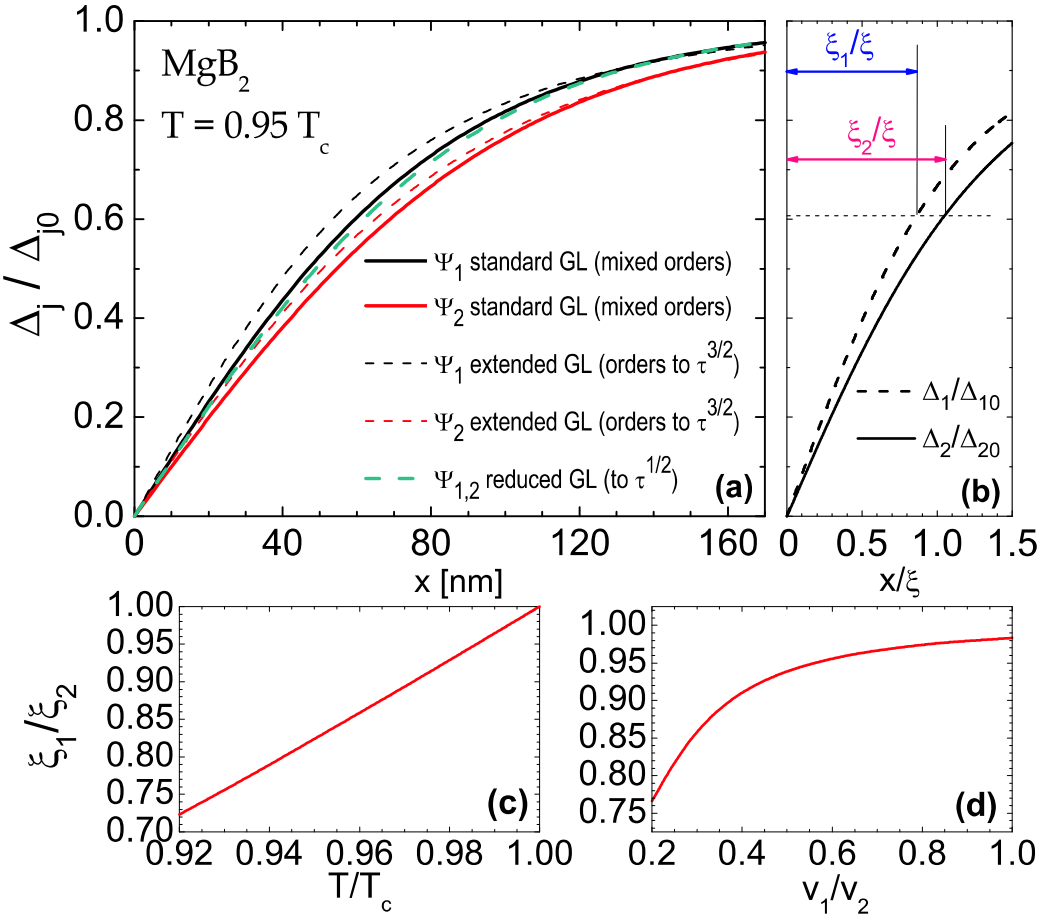

Figure 5.2: (a) The spatial profile of the order parameters at the S/N interface at $T = 0.95T_c$, for microscopic parameters of MgB_2 ($\xi_1/\xi_2 = v_1/v_2 = 0.255$ [1]; $\lambda_{11} = 1.88, \lambda_{22} = 0.5, \lambda_{12} = 0.21$, $n_1 = 0.43$ [89]), compared in three versions of the two-band GL theory. The ratio of the healing lengths of the two coupled condensates ξ_1/ξ_2 calculated in extended GL theory [with $\xi_{1,2}$ determined as illustrated in (b)] is shown in (c) as a function of temperature for fixed $v_1/v_2 = 0.255$, and in (d) as a function of the ratio v_1/v_2 at $T = 0.95T_c$.

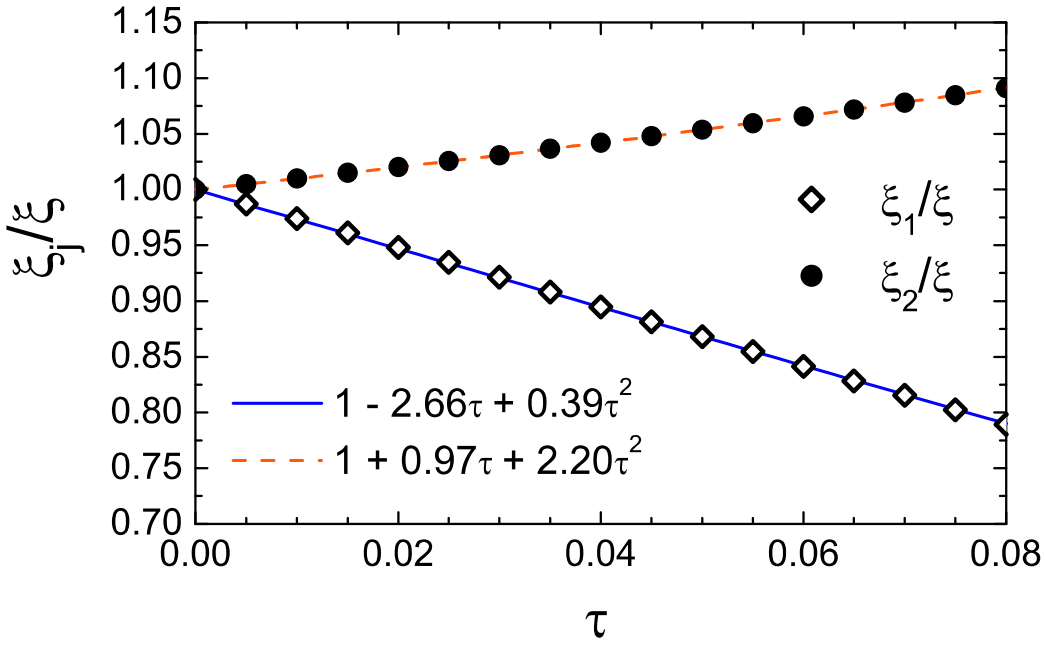

Figure 5.3: The healing lengths of the two order parameters in MgB_2 [Fig. 5.2(a)] scaled to the standard GL length scale ξ as a function of temperature. The lines show the fitting functions of the data.

dependence of the order parameters. Namely, standard GL theory leaves one with simply $\Delta \propto \tau^{1/2}$, which is shown in Fig. 5.3 to be clearly inadequate for our calculations. Specifically, in Fig. 5.3 we show two healing lengths as a function of temperature, both already normalized to the temperature-dependent length $\xi \propto \tau^{-1/2}$. It is directly obvious that we are left with a non-constant value, and we fitted the general temperature-dependence of the residue to a quadratic form $\xi_j/\xi = 1 + A\tau + B\tau^2$, as shown in Fig. 5.3.[1]

In what follows, we extend our analysis to materials other than MgB_2. We first address the recently discovered iron-pnictides, more specifically LiFeAs [107]. Interestingly enough, several existing experimental works on this material provide us with *radically different* microscopic parameters obtained from the fit of the superfluid density data in the self-consistent γ-model [71, 80] and from two-band fitting of the upper critical field [108, 109]. In Fig. 5.4(a), we show the GL-calculated ratio of the healing lengths of two bands in LiFeAs, for the parameters taken from latter two references. Although different, both curves in Fig. 5.4 clearly show a discrepancy between the healing lengths,

[1] Accurate fitting of our data requires a quadratic function, although the terms of order $\mathcal{O}(\tau^2)$ are not included in the extended GL theory. Therefore the obtained coefficient B should be taken with reservations.

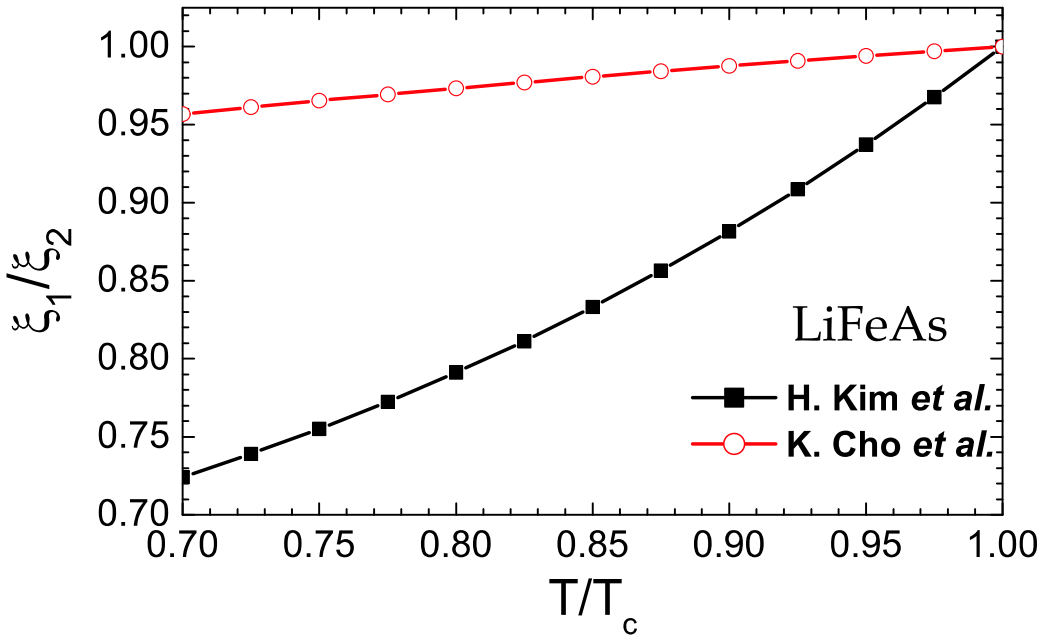

Figure 5.4: The temperature dependence of the ratio of the healing lengths ξ_1/ξ_2 in LiFeAs, for parameters from Ref. [71] and Ref. [108].

up to 20% at temperatures above $0.8T_c$.

Specific bulk superconductors are not the only possible multiband system. As already mentioned in introduction, other interesting examples are single-crystalline superconducting nanofilms and quasi-1D/2D optically trapped fermionic condensates. An advantage of such multiband systems is that the band Fermi velocities can be widely tailored here by simply changing the quantum-confinement dimensions (through a change in the energetic positions of the discrete levels, see details in Ref. [101]). In particular, the Pb(111) nanofilms with thickness four and five monolayers (ML) are two-band superconductors due to the presence of only two perpendicular single-electron levels below the Fermi energy [104]. In this case, the ratio of the band Fermi velocities can be estimated on the basis of the available tunneling data in Ref. [104], i.e., the energetic positions of single-electron levels. This results in $v_1/v_2 \approx 3$ or $v_1/v_2 \approx 2.5$ for 4 ML and 5 ML, respectively (when assuming the parabolic band approximation for each band with the same band mass). In addition, we have the constraint $\lambda_{11} = \lambda_{22} = 1.5\lambda_{12}$, the ratio between the interband and intraband coupling which is typical for the film geometry [110, 111]. The thickness-dependent T_c can then be taken to adjust λ_{11}, which is expected to be close to its bulk value 0.39. For the band-dependent dimensionless DOS it is reasonable to take $n_1 = n_2$, which

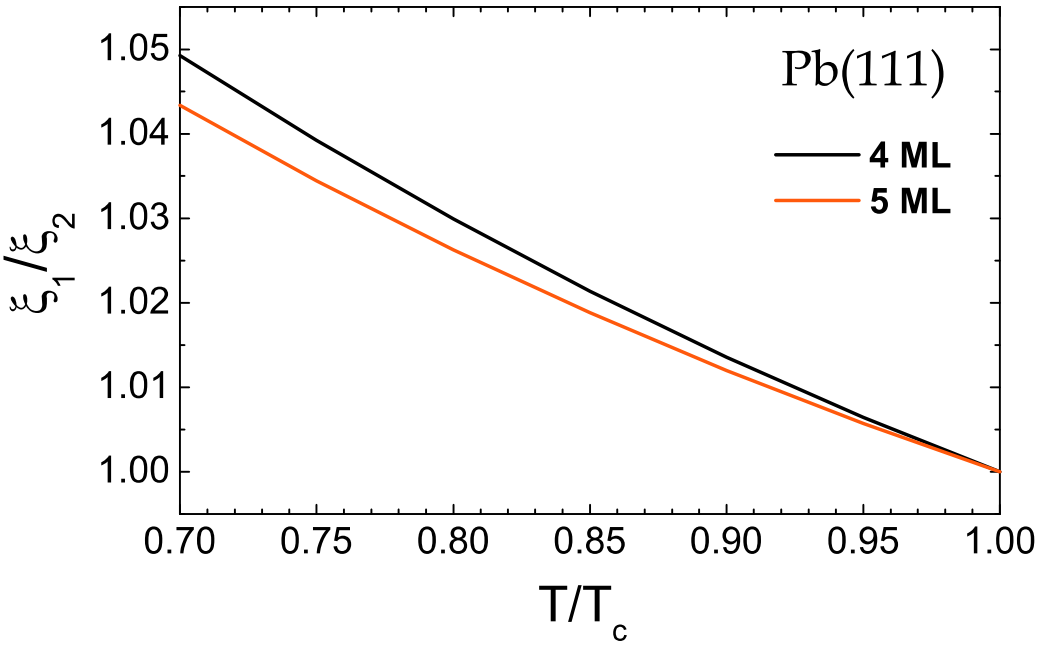

Figure 5.5: The temperature dependence of the ratio of the healing lengths ξ_1/ξ_2 in 4 and 5 monolayers thick Pb(111) nanofilms.

follows from the well-known expression for the two-dimensional DOS. We inserted such estimated parameters in the extended GL formalism, and again obtained a non-zero difference between the spatial scales of the two order parameters ($\sim 5\%$), as shown in Fig. 5.5. Here, contrary to the case of MgB_2, both healing lengths decrease with respect to the standard GL ξ, and therefore the ratio ξ_1/ξ_2 is smaller than in MgB_2. However, since in quantum confined systems, either nanofilms or pancake fermionic condensates, the exact position of the bands with respect to the Fermi level (and therefore the v_1/v_2 ratio) can be tuned the discrepancy between the corresponding healing lengths can be further enlarged.

5.5 Vortex profiles in the extended GL theory

We next apply the extended Ginzburg-Landau (EGL) formalism to study a single vortex, i.e., a point singularity around which the phases of order parameters change by $2\pi n$ where n is an integer number. We rewrite Eqs. (5.1) and (5.2) in the cylindrical coordinates, so that the nabla operator

becomes

$$\nabla = \hat{\rho}\frac{\partial}{\partial\rho} + \frac{1}{\rho}\hat{\phi}\frac{\partial}{\partial\phi} + \hat{z}\frac{\partial}{\partial z}, \tag{5.21}$$

where ρ is the radial coordinate and ϕ the radial angle in the cylindric coordinates and $\hat{\rho}$, $\hat{\phi}$ and $\hat{z}$ are the usual unit vectors. It follows that Laplace operator is

$$\nabla^2 = \frac{\partial^2 u}{\partial\rho^2} + \frac{1}{\rho}\frac{\partial u}{\partial\rho} + \frac{1}{\rho^2}\frac{\partial^2 u}{\partial\phi^2} + \frac{\partial^2 u}{\partial z^2}. \tag{5.22}$$

We use the ansatz for composite vortex with the winding number n, namely

$$\Delta_j^{(0)}(\rho,\phi,z) = \Psi_j(\rho)e^{in\phi}, \tag{5.23a}$$

$$\Delta_j^{(1)}(\rho,\phi,z) = g_j(\rho)e^{in\phi}. \tag{5.23b}$$

Finally we scale the distance to $\xi = \sqrt{-K/\alpha}$ and the gap functions $\Delta_j^{(k=0,1)}$ to $W_j = \sqrt{-\alpha/\beta_j}$, i.e., the equilibrium value of $\Delta_j^{(0)}$. Equation (5.1) then gives

$$\frac{\partial^2\Psi_j}{\partial\rho^2} + \frac{1}{\rho}\frac{\partial\Psi_j}{\partial\rho} - \frac{n^2}{\rho^2}\Psi_j = \Psi_j^3 - \Psi_j. \tag{5.24}$$

Similarly, from Eq. (5.2) we get for the correction g_j

$$\frac{\partial^2 g_j}{\partial\rho^2} + \frac{1}{\rho}\frac{\partial g_j}{\partial\rho} - \frac{n^2}{\rho^2}g_j = (3\Psi_j^2 - 1)g_j + \tilde{F} + \tilde{F}_j, \tag{5.25}$$

where

$$\tilde{F} = \frac{\sigma}{\alpha}\Psi_j - \frac{S}{K}(\Psi_j^3 - \Psi_j) + \frac{\alpha Y}{K^2}\left[6\Psi_j\left(\frac{\partial\Psi_j}{\partial\rho}\right)^2 + (3\Psi_j^2 - 1)\left(\frac{\partial^2\Psi_j}{\partial\rho^2} + \frac{1}{\rho}\frac{\partial\Psi_j}{\partial\rho}\right) - \frac{n^2}{\rho^2}(\Psi_j^3 - \Psi_j)\right], \tag{5.26}$$

and

$$\tilde{F}_j = \frac{\rho_j W_j^2}{\alpha}\Psi_j^3 + \frac{\chi_j W_j^4}{\alpha}\Psi_j^5 + \frac{Z_j W_j^2}{K}(\Psi_j^3 - \Psi_j^5) - \frac{U_j W_j^2}{K}\left[\Psi_j\left(\frac{\partial\Psi_j}{\partial\rho}\right)^2 - \frac{6n^2\Psi_j^3}{5\rho^2} + \Psi_j^2\frac{\partial^2\Psi_j}{\partial\rho^2} + \frac{\Psi_j^2}{\rho}\frac{\partial\Psi_j}{\partial\rho}\right] - \frac{V_j W_j^2}{K}\left[6\Psi_j\left(\frac{\partial\Psi_j}{\partial\rho}\right)^2 + 3\Psi_j^2\frac{\partial^2\Psi_j}{\partial\rho^2} + \frac{3\Psi_j^2}{\rho}\frac{\partial\Psi_j}{\partial\rho} - \frac{n^2\Psi_j^3}{\rho^2}\right]. \tag{5.27}$$

In derivation of the above expressions for $\tilde{F}$ and $\tilde{F}_j$ we already made use of Eq. (5.24) to avoid calculating high order derivatives of Ψ_j in later numerical evaluations. The appropriate boundary conditions for the vortex are $\Delta_j^{(k)}(\rho \to 0) \to 0$ and $\partial_\rho \Delta_j^{(k)}(\rho \to \infty) \to 0$, i.e., the amplitude of each condensate disappears in the centre of the vortex and rises to its (constant) equilibrium value far from it.

Extended GL analysis of LiFeAs In what follows, we focus on a particular iron pnictide superconductor, LiFeAs. The intention is to compare the characteristic features of the extended GL results with the analysis within the standard GL theory from Chapter 4. To facilitate this comparison, the plots are made in the same parameter ranges as in Chapter 4. This occasionally means going beyond the GL validity region, as determined by Eq. (5.18). Where this is the case, we indicate the border of the GL validity region directly in the plot by a dashed line. The results shown were calculated for a single $n = 1$ vortex using the parameters appropriate for LiFeAs. Specifically, we used the coupling constants $\lambda_{11} = 0.63$, $\lambda_{22} = 0.642$, $\lambda_{12} = -0.061$ [71] (λ_{12} taken negative to get the $s_\pm$ gap symmetry), Debye temperature $T_D = 240$ K, density of states $N(0) = 2.7 \times 10^{34}$ states/erg/cm^3 (determined from $N(0)$ value from Ref. [112] using the cell volume at $T = 6.5$ K from Ref. [113]) and $v_1 = 3 \times 10^7$ cm/s (estimate based on Ref. [29]). Data from Ref. [71] also allow one to determine $n_1/n_2 = 1.384$ and $v_1/v_2 = 0.722$.

In Fig. 5.6(a) we show the calculated ratio of healing lengths ξ_1/ξ_2 as a function of the ratio of Fermi velocities and the ratio of partial densities of states of two bands. Most importantly, the region with great disparity of the healing lengths matches very well with the expected position of the nonmonotonic intervortex interaction in the standard GL theory, as displayed in Fig. 4.3.

Note that the information about the magnetic field and thus about the penetration depth is absent in the used EGL formalism.[2] Despite that, it is possible to estimate λ using formula

$$\frac{1}{\lambda^2} \approx \sum_{j=1,2} \frac{16\pi N(0) e^2 n_j v_j^2}{3c^2 W^2} \left(\Delta_j^{(0)} + \Delta_j^{(1)}\right)^2, \tag{5.28}$$

where $W = \sqrt{8\pi^2 T_c^2 / 7\zeta(3)}$ is a convenient energy unit. This formula coincides with Eq. (43) from Ref. [2] for the case when $\Delta_j^{(1)}$ is set to zero.

In Fig. 5.6(b) we show the (estimate of) magnetic penetration depth λ divided by the length unit ξ to get some information about the expected value

[2]The complete EGL formalism only became available after completion of this study.

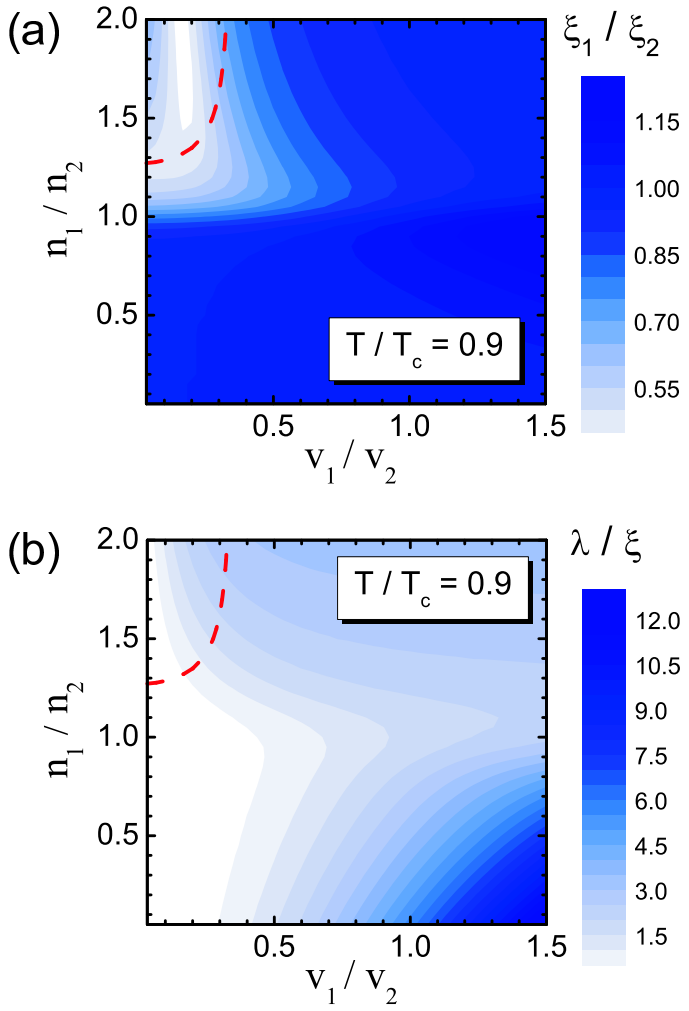

Figure 5.6: (a) The ratio of the healing lengths ξ_1/ξ_2 for LiFeAs as a function of ratios n_1/n_2 and v_1/v_2 at fixed temperature $T = 0.9T_c$. (b) The estimate of ratio λ/ξ for the same situation. The dashed red line shows the boundary of the strict validity region of the GL theory. The corresponding results obtained in the standard two-gap GL theory can be found in Fig. 4.3(b).

of the GL parameter κ, i.e., about preference for type-I or type-II behavior. Since the region with the great disparity of the coherence lengths in low v_1/v_2 and high n_1/n_2 sector of Fig. 5.6(a) overlaps with the region with low λ/ξ values, we conclude that this indeed could support the competition between the type-I and type-II behavior. Similar conclusions hold for the Fig. 5.7, which shows the ratios ξ_1/ξ_2 and λ/ξ as a function of temperature and v_1/v_2 for fixed partial densities of states $n_1/n_2 = 1.384$. Unfortunately, in this case the most interesting portion of the parameter space is well below the expected validity region of the GL theory.

In Fig. 5.8 similar diagrams are constructed as a function of temperature and n_1/n_2 for fixed $v_1/v_2 = 0.722$. Here, according to the extended GL results the disparity of the healing lengths is expected to be quite large in the dome around $n_1/n_2 \approx 1.1$ at lower temperatures. However, the ratio λ/ξ stays firmly in type-II values, its minimum value being 1.03. Surprisingly, the type-I region for low n_1/n_2 from the standard GL theory is not reproduced. This discrepancy is due to the different calculational procedure employed in Chapter 4 and Ref. [98], where the nominal GL parameter κ_1 has been fixed for the first band and the ratio n_1/n_2 was only considered to affect the properties of the second band. When both κ_1 and κ_2 are allowed to change, the type-II region for low n_1/n_2 ratio is present also in the standard GL calculation, consistently with the results in this section.

5.6 Conclusions

To summarize, we demonstrated on examples of several relevant superconducting materials that characteristic length scales of coupled condensates in two-band or multiband samples are in general *different* from each other in the domain of the extended Ginzburg-Landau (EGL) theory. Although we do not show it explicitly, we mention here again that the extended model is not more complicated than its standard predecessor - it does contain more equations, but the coupling of those equations is realized in a computationally-friendly manner. This makes EGL model an excellent tool for further studies of two-band systems, where one expects a plethora of novel physical effects emerging from the competition of different characteristic length scales.

Further, we have calculated the vortex core profiles in the extended Ginzburg-Landau theory for two gap superconductors. We compared the predictions of the standard and extended GL theory for LiFeAs, and found a good qualitative agreement. In particular, we identified the regions with great disparity between the coherence lengths and at the same time the ratio $\lambda/\xi \approx 1$, which are of special interest because the competition between

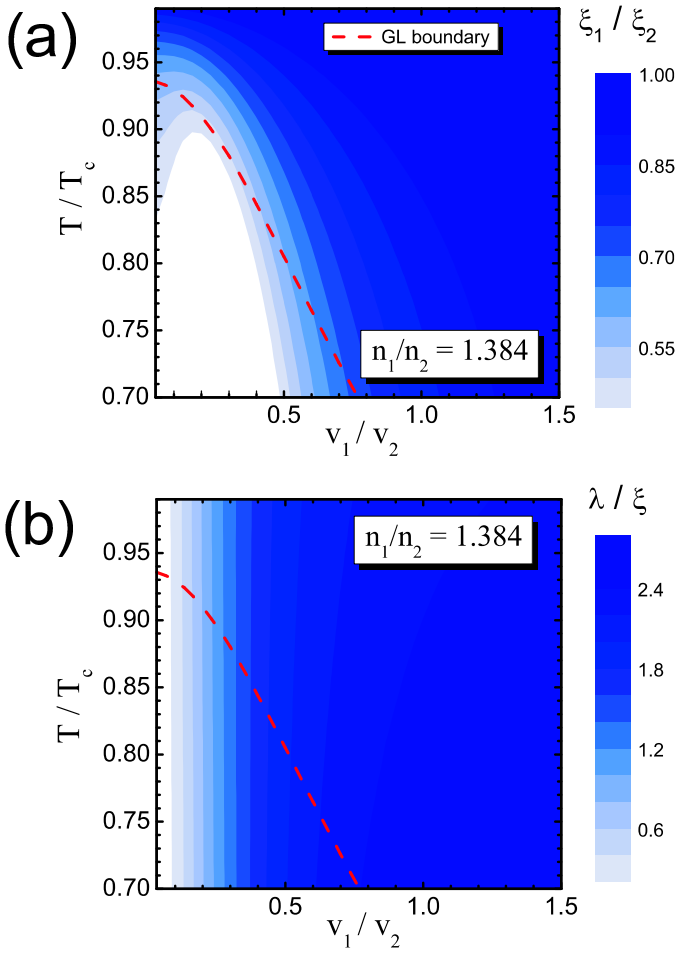

Figure 5.7: (a) The ratio of the healing lengths ξ_1/ξ_2 for LiFeAs as a function of temperature T/T_c and v_1/v_2 ratio at fixed $n_1/n_2 = 1.384$. Minimal value of ξ_1/ξ_2 inside the GL validity region is about 0.5. (b) The estimate of ratio λ/ξ for the same situation. The dashed red line shows the boundary of the GL validity region. The corresponding results obtained in the standard two-gap GL theory can be found in Fig. 4.3(d).

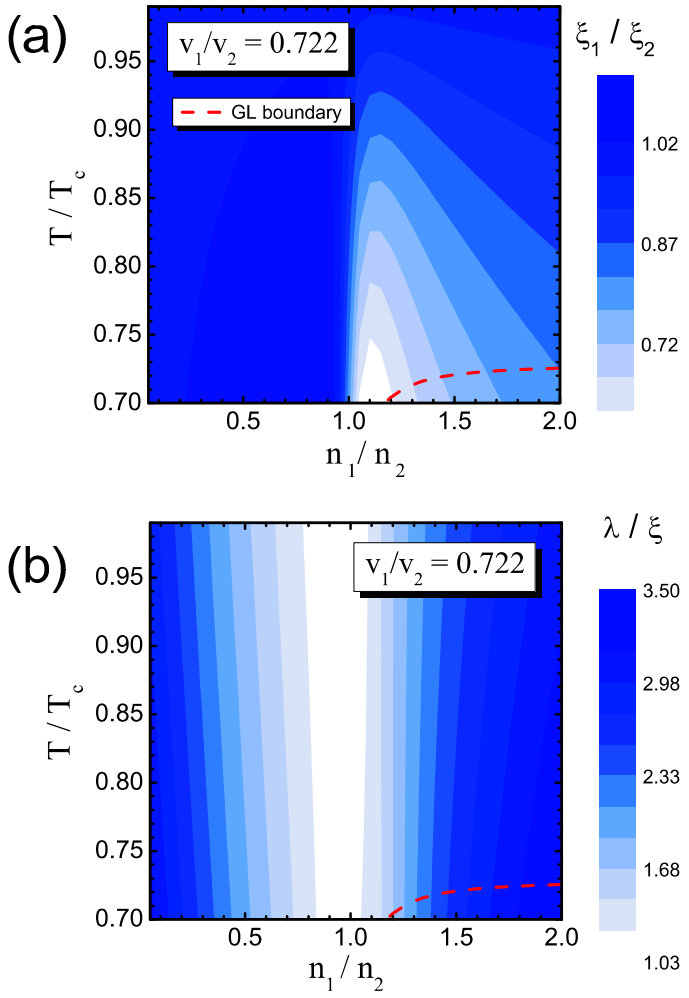

Figure 5.8: (a) The ratio of the healing lengths ξ_1/ξ_2 for LiFeAs as a function of temperature T/T_c and n_1/n_2 ratio at fixed $v_1/v_2 = 0.722$. (b) The estimate of ratio λ/ξ for the same situation. Most importantly, the ratio λ/ξ is always larger than 1 in the displayed region, thus preferring type-II-like behavior. The dashed red line shows the boundary of the GL validity region. The corresponding results obtained in the standard two-gap GL theory can be found in Fig. 4.3(c).

type-I and type-II behavior might occur there. These results are reasonably well matched by the standard GL theory.

Related publications

- L. Komendová, M. V. Milošević, A. A. Shanenko, and F. M. Peeters: *Different length scales for order parameters in two-gap superconductors: Extended Ginzburg-Landau theory*, Phys. Rev. B **84**, 064522 (2011).
- L. Komendová, A. A. Shanenko, M. V. Milošević, and F. M. Peeters: *The healing lengths in two-band superconductors in extended Ginzburg-Landau theory*, Physica C **479**, 126 (2012).

Chapter 6

Hidden criticality deep in the superconducting state

We show that two-band superconductors harbor hidden criticality deep in the superconducting state, stemming from the critical temperature of the weaker band taken as an independent system. For sufficiently small interband coupling γ the coherence length of the weaker band exhibits a remarkable deviation from the conventional monotonic increase with temperature, namely, a pronounced peak close to the hidden critical point. The magnitude of the peak scales as $\propto \gamma^{-\mu}$, with the Landau critical exponent $\mu = 1/3$, the same as found for the mean-field critical behavior with respect to the source field in ferromagnets and ferroelectrics. Here reported hidden criticality of multiband superconductors can be experimentally observed by, e.g., imaging of the variations of the vortex core in a broader temperature range. Similar effects are expected for the superconducting multilayers.

6.1 Introduction

Critical phenomena [114] constitute one of the most important aspects of the physics of complex systems. The classical scenario of both thermal and quantum criticality involves the ordered phase induced by a breakdown of a basic symmetry and the disordered phase appearing due to the restoration of this symmetry. These two phases are separated by a critical point, i.e., a second-order phase transition accompanied by critical phenomena, e.g., the Curie point, the superconducting-to-normal state transition, the metal-insulator transition, etc., (see, e.g., [114, 115]). However, possible realizations of the

critical behavior are not restricted to this standard picture. The present chapter reports a fascinating example when in addition to the standard critical behavior, the system is affected by *hidden criticality deep in the ordered phase*. This is the case of a two-band superconductor [116] (for recent activity see, e.g., [1–3, 15, 49, 54, 74, 77, 78, 86, 87, 95, 98, 100, 117–123]) where the interband coupling measures the proximity to the hidden critical point and plays the role of the source field governing the hidden criticality.

The family of multiband superconducting materials is characterized by the presence of multiple sheets of the Fermi surface (bands). In this case the superconducting properties are controlled by a set of different band condensates [116]. Because of the presence of a nonzero interband coupling, such condensates are not independent. As a result, a band order parameter, i.e., the measure of the condensate in a given band, is not simply proportional to the Cooper-pair amplitude in this band but involves a sum over all band pairing amplitudes, each multiplied by a specific coefficient, i.e., the coupling constant $g_{ij} = g_{ji}$. In a two-band superconductor, when pairing of electrons between bands is negligible (e.g., due to symmetry reasons), the order parameter $\Delta_i(\mathbf{x})$ reads

$$\Delta_i(\mathbf{x}) = \sum_{j=1,2} g_{ij} \langle \hat{\psi}_{j\uparrow}(\mathbf{x}) \hat{\psi}_{j\downarrow}(\mathbf{x}) \rangle, \tag{6.1}$$

where i, j enumerate the two bands, and $\langle \hat{\psi}_{j\uparrow}(\mathbf{x}) \hat{\psi}_{j\downarrow}(\mathbf{x}) \rangle$ is the band-dependent Cooper-pair amplitude (anomalous average of the field operators with the spin projection up and down for the singlet s-wave pairing). The system described by Eq. (6.1) has a unique critical temperature T_c for any nonzero interband coupling g_{12}. However, when $g_{12} = 0$, one deals theoretically with two independent superconducting condensates with two different critical temperatures T_{c1} (for the stronger band) and T_{c2} (for the weaker band), and the basic symmetry changes from U(1) to U(1) × U(1). Here the question arises whether or not the behavior of the more realistic, *weakly* coupled system is affected by the proximity of decoupled bands.

6.2 Analytical results

The initial step in our study is to get analytical information about a two-gap system with weakly coupled components. With this in mind, we examine Eq. (6.1) at $T = T_{c2}$ by developing a Ginzburg-Landau (GL) type of approach for $g_{12} \to 0$. Actually, instead of g_{12} it is more convenient to deal with the dimensionless parameter $\gamma = \lambda_{12}/(\lambda_{11}\lambda_{22})$, where $\lambda_{ij} = g_{ij}N(0)$, and $N(0)$ is the total density of states at the Fermi energy, i.e., $N(0) = \sum_i N_i(0)$.

The GL approach invokes an expansion in powers of the order parameter and its spatial derivatives. Such an expansion for the Cooper-pair amplitude (anomalous Green's function) in a two-band superconductor reads [2, 3, 49]

$$\frac{\langle\hat{\psi}_{i\uparrow}(\mathbf{x})\hat{\psi}_{i\downarrow}(\mathbf{x})\rangle}{N(0)} = \alpha_i\Delta_i - \beta_i\Delta_i|\Delta_i|^2 + \mathcal{K}_i\mathbf{D}^2\Delta_i + \ldots, \tag{6.2}$$

with the gauge-invariant gradient $\mathbf{D} = \boldsymbol{\nabla} - \frac{2ie}{\hbar c}\mathbf{A}$ and the parameters (in the clean limit)

$$\alpha_i = n_i \ln\Big(\frac{2e^{\Gamma}\hbar\omega_c}{\pi T}\Big),\ \beta_i = n_i\frac{7\zeta(3)}{8\pi^2T^2},\ \mathcal{K}_i = \frac{\beta_i}{6}\hbar^2v_i^2. \tag{6.3}$$

Here $\hbar\omega_c$ is the cut-off energy, $\zeta(x)$ is the Riemann zeta-function, $\Gamma = 0.577$ is the Euler constant, $n_i = N_i(0)/N(0)$, and v_i is the band-dependent Fermi velocity. Note however that at $T = T_{c2}$ the expansion given by Eq. (6.2) holds only for the weaker band in the limit $\gamma \to 0$, while it is inappropriate for the stronger band where the order parameter does not vanish in this limit. Nevertheless, Eq. (6.2) provides plenty of information about the weaker band. Using Eq. (6.1) and invoking the expansion of Eq. (6.2) for the weaker band, we find [1] the following γGL equation for Δ_2 at $T = T_{c2}$:

$$\beta_2\Delta_2|\Delta_2|^2 - \mathcal{K}_2\mathbf{D}^2\Delta_2 - \gamma\Delta_{1,\gamma\to0} = 0, \tag{6.4}$$

with $\Delta_{1,\gamma\to0}$ being the order parameter of the strong band in the limit $\gamma \to 0$, and β_2 and $\mathcal{K}_2$ given by Eq. (6.3) at $T = T_{c2}$. We stress that Eq. (6.4) is exact for Δ_2 in the leading order in γ at $T = T_{c2}$. Note that due to $T = T_{c2}$ there is no linear term in Δ_2 in Eq. (6.4), in contrast to the ordinary GL theory. Despite the absence of the linear term in Δ_2, a stable solution to Eq. (6.4) exists due to the presence of the source term $\gamma\Delta_{1,\gamma\to0}$, which reflects the Josephson-like coupling between the bands. This solution can be obtained only after solving the proper formalism for the stronger band at $\gamma = 0$. Nevertheless, qualitative information about Δ_2 as a function of γ can be found from a general analysis of Eq. (6.4). In the simplest case of a spatially uniform system we obtain for $\gamma \to 0$ and $T = T_{c2}$

$$\Delta_2 = \Big(\frac{\gamma\Delta_{1,\gamma\to0}}{\beta_2}\Big)^{1/3},\ \frac{\partial\Delta_2}{\partial\gamma} = \frac{\gamma^{-2/3}}{3}\Big(\frac{\Delta_{1,\gamma\to0}}{\beta_2}\Big)^{1/3}. \tag{6.5}$$

Based on Eq. (6.5) and assuming a similar general dependence of Δ_2 on γ, we can analyze the solution of Eq. (6.4) in the presence of a spatially nonuniform condensate. We find for $\gamma \to 0$ and $T = T_{c2}$

$$\Delta_2 \propto \gamma^{1/3},\ \ \frac{\partial\Delta_2}{\partial\gamma} \propto \gamma^{-2/3},\ \ \xi_2 \propto \gamma^{-1/3}, \tag{6.6}$$

[1] See also the Appendix to this chapter.

where ξ_i denotes the band-dependent healing (coherence) length and the asymptotic behavior for ξ_2 is found from $\nabla^2\Delta_2 \propto \xi_2^{-2}\Delta_2 \propto \gamma$. Equations (6.5) and (6.6) therefore reveal the critical behavior (see, e.g., Ref. [114]) of the order parameter in the weaker band $\propto \gamma^{1/\delta}$, the corresponding susceptibility $\propto \gamma^{1/\delta-1}$ and the healing length (proportional to the correlation radius of fluctuations r_c) $\propto \gamma^{-\mu}$, with the Landau mean-field critical exponents $\delta = 3$ and $\mu = \frac{1}{3}$. As seen, the interband coupling γ can be interpreted as a source field governing the hidden criticality in two-band superconductors [2]. This is analogous to the source fields in criticality of e.g. ferromagnets (magnetic field) or ferroelectrics (electric field), where the same Landau exponents are found within the mean field. Here we note that λ_{12} is not easily tunable in two-band superconductors, which is different as compared to the source field in ferromagnets and ferroelectrics. However, the coexistence of two weakly coupled order parameters was also achieved in layered mesoscopic rings [124], where the interlayer coupling can be varied by changing the distance between two participating layers. The physics of the coherent phenomena in such a two-layer system is essentially the same as in two-band superconductors [124, 125].

Equation (6.2) enables us to further examine the dependence of Δ_2 on γ for $T > T_{c2}$. When $\gamma \to 0$ and $T_{c2} < T < T_{c1}$ we find (for bulk, see the Appendix to this chapter)

$$\Delta_2 = \gamma\Delta_{1,\gamma\to 0}\Big[n_2 \ln(T/T_{c2})\Big]^{-1}, \tag{6.7}$$

where T_{c1} is the critical temperature of the stronger band for $\gamma = 0$. The behavior of Δ_2 changes dramatically as compared to Eq. (6.5). The hidden critical point manifests here in the fact that the factor $\Big[n_2 \ln(T/T_{c2})\Big]^{-1}$ diverges when $T \to T_{c2}$.[3] We should note the existence of another (analogous) hidden criticality at T_{c1}, which is the reason why Eq. (6.7) is not valid for $T = T_{c1}$. However, for $\gamma \to 0$ this point is in close vicinity to the overall critical temperature T_c and, as a result, it is always strongly overshadowed by the usual critical behavior close to T_c.

[2] When keeping the direct analogy to, e.g., ferromagnet materials or ferroelectrics, the product $\gamma\Delta_{1,\gamma\to 0}$ must be viewed as the source field. Then, as $\Delta_{1,\gamma\to 0}$ does not depend on γ (we keep the intraband couplings constant), it is possible to treat γ as a source field measured in units of $\Delta_{1,\gamma\to 0}$.

[3] Note that similar arguments do not hold for $T < T_{c2}$ because $\Delta_{2,\gamma\to 0}$ is nonzero in this case, and the expansion given by Eq. (6.2) is no longer valid. However, it is reasonable to expect that $\Delta_2 - \Delta_{2,\gamma\to 0}$ is linear in γ for $\gamma \to 0$ with a slope that increases when approaching T_{c2}. See also the Appendix to this chapter.

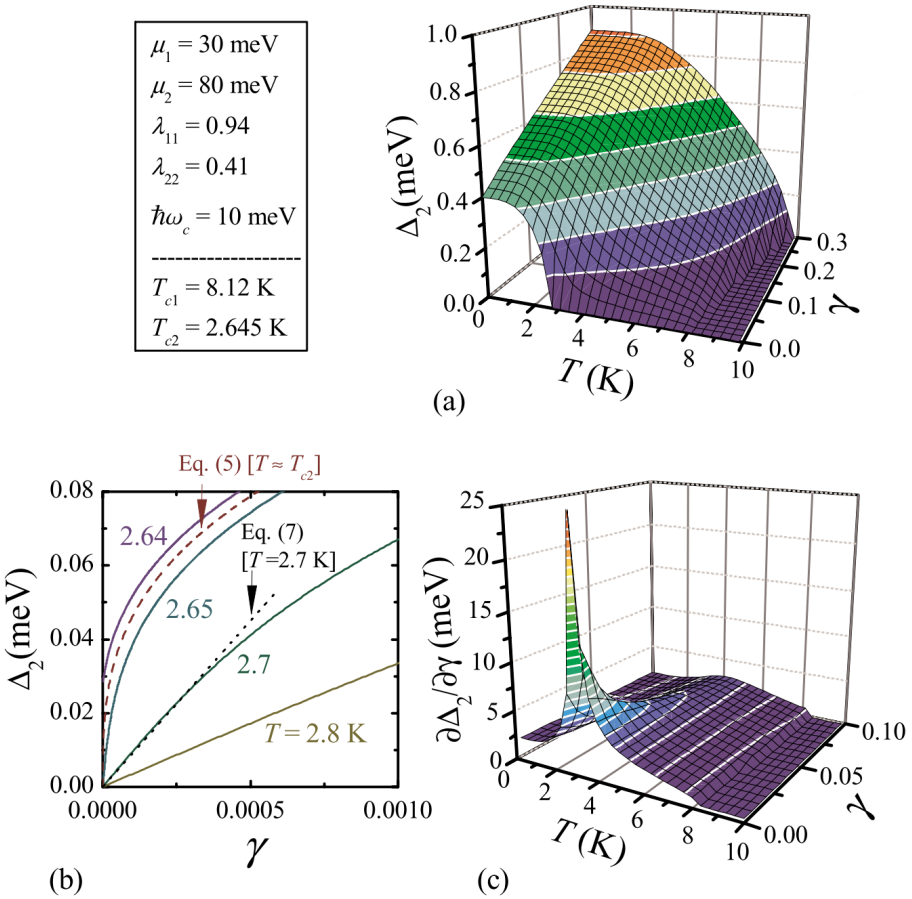

Figure 6.1: (a) The weaker-band order parameter Δ_2 versus the temperature T and the interband coupling γ as calculated from the BdG equations for bulk. (b) Δ_2 as function of γ for temperatures $T = 2.64$, 2.65, 2.7 and 2.8 K from the BdG equations (solid curves); the dashed curve shows the results of Eq. (6.5) for Δ_2 at $T \approx T_{c2}$; the dotted curve is the dependence given by Eq. (6.7) at $T = 2.7$ K. (c) The γ-susceptibility $\frac{\partial \Delta_2}{\partial \gamma}$ as a function of T and γ, that diverges at the critical point $(T, \gamma) = (T_{c2}, 0)$.

6.3 Numerical results

In what follows, we perform a full numerical study within a microscopic formalism, in a broader range of temperatures and interband couplings. In addition, we need to confirm the above analytical results since Eq. (6.2) assumes the validity of the gradient expansion - which is only correct when the corresponding healing length goes to infinity when $\gamma \to 0$. In other words, the important limitation of our γGL-analysis is that we first assumed $\xi_2 \to \infty$ ($\gamma \to 0$) in order to subsequently obtain the diverging behavior of ξ_2 with the critical exponent μ, which may be misleading.

As an appropriate theoretical formalism, we choose the Bogoliubov-de Gennes (BdG) equations [12]. We emphasize that the standard two-band GL formalism cannot be used for our purpose, being well justified only near T_c. In the present case, the BdG equations read

$$\begin{pmatrix} T_i(\mathbf{x}) & \Delta_i(\mathbf{x}) \\ \Delta_i^*(\mathbf{x}) & -T_i^*(\mathbf{x}) \end{pmatrix} \begin{pmatrix} u_{i\nu}(\mathbf{x}) \\ v_{i\nu}(\mathbf{x}) \end{pmatrix} = E_{i\nu} \begin{pmatrix} u_{i\nu}(\mathbf{x}) \\ v_{i\nu}(\mathbf{x}) \end{pmatrix}, \tag{6.8}$$

where $u_{i\nu}(\mathbf{x})$, $v_{i\nu}(\mathbf{x})$ and $E_{i\nu}$ are the particle-like and hole-like wave functions and the quasiparticle energy, with the subscript i enumerating the band and ν the set of relevant quantum numbers. The single-electron energy reads $T_i(\mathbf{x}) = -\frac{\hbar^2}{2m_i}\mathbf{D}^2 - \mu_i$, with m_i the band mass (set to the free electron mass) and μ_i the chemical potential measured from the lower edge of the corresponding band. Formally, the BdG equations for different band order parameters look decoupled but, in fact, they are connected through Eq. (6.1) taken with

$$\langle \hat{\psi}_{i\uparrow}(\mathbf{x})\hat{\psi}_{i\downarrow}(\mathbf{x})\rangle = \sum_{\nu} u_{i\nu}(\mathbf{x})v_{i\nu}^*(\mathbf{x})\big[1 - 2f(E_{i\nu})\big], \tag{6.9}$$

where $f(E_{i\nu})$ is the Fermi distribution of quasiparticles. Inserting Eq. (6.9) into Eq. (6.1), one needs to remedy the ultraviolet divergence: though the product $u_{i\nu}(\mathbf{x})v_{i\nu}^*(\mathbf{x})$ vanishes for large energies, its decay is not sufficiently fast to provide convergence of the sum over the relevant quantum numbers given by Eq. (6.9). Following the standard cut-off procedure as implemented in other papers on two-band superconductors [2, 49, 116]), the cut-off energy $\hbar\omega_c$ is used.

We first investigate a numerical solution of Eqs. (6.8) and (6.9) for a bulk superconductor for small γ. Figure 6.1 shows calculated results for the weaker band in a bulk superconductor, for the set of parameters given in the figure. Note that this particular choice of the parameters is not decisive for our conclusions - similar results are found for μ_i up to $\sim 10\,\mathrm{eV}$, typical of metals.

Our choice of $\mu_i \sim 10\,\text{meV}$ is justified by recent angle-resolved photoemission experiments (ARPES) on $FeSe_xTe_{1-x}$, which revealed the presence of multiple bands with extremely small Fermi energies ($\sim 5\,\text{meV}$) [126].

Figure 6.1(a) shows that the increase in Δ_2 with γ becomes faster as T approaches $T_{c2} \approx 2.645\,\text{K}$, which supports our expectations. Δ_2 versus γ in the uniform system is plotted in Fig. 6.1(b) for selected temperatures, where a comparison is made with our analytical results, Eqs. (6.5) and (6.7). As seen, for $T > T_{c2}$ and $\gamma \to 0$ the weaker-band order parameter Δ_2 is indeed a linear function of γ. However, when T approaches T_{c2}, this linear dependence is replaced by $\propto \gamma^{1/3}$, as confirmed by the very good agreement between the numerically obtained curves for $T = 2.64$ and $2.65\,\text{K}$ and the analytic curve for $T \approx T_{c2}$ in Fig. 6.1(b). At $T = T_{c2}$ the critical behavior of Δ_2 as a function of γ leads to a diverging γ-susceptibility, as shown numerically in Fig. 6.1(c). Because of the well-known interrelation between the susceptibility and the coherence length, one expects that ξ_2 is also a divergent function of γ at $T = T_{c2}$. However, to study this feature and check the scaling $\xi_2 \propto \gamma^{-1/3}$ found in the γGL model, we need to abandon the uniform case and study a spatially varying two-band condensate.

We chose to investigate the single-vortex solution in a superconducting cylinder (with radius $R = 300\,\text{nm}$) by numerically solving Eq. (6.8), and extract the band-dependent healing lengths ξ_i from the size of the vortex core. When numerically studying a single-vortex solution in the cylinder, we follow a procedure similar to that of Ref. [127]. We neglect the screening of the magnetic field, which is justified for extreme type-II superconductors. The spatial variation of the order parameters in two bands $\Delta_i(\rho)$ are shown around a vortex in Fig. 6.2(a) in units of their bulk zero-temperature values $\Delta_{i,\text{bulk}}$, for $\gamma = 0.0002$ and $T = 0$. We defined the healing lengths by $\Delta_i(\rho = \xi_i) = 0.8\Delta_{i,\text{bulk}}$, i.e., $\xi_1 = 14\,\text{nm}$ and $\xi_2 = 74\,\text{nm}$ for this particular case [4]. Figure 6.2(b) shows the temperature dependence of ξ_2 for different γ as extracted from our numerical results. We point out our main finding: the existence of a clear peak in ξ_2 at temperatures close to T_{c2}. Its peak value increases with decreasing γ and almost ideally follows the scaling $\gamma^{-1/3}$ found within the γGL model. For sufficiently small interband couplings, ξ_2 approaches its independent-band limit shown by the dashed curve

[4] Our choice of the threshold $\Delta_i = 0.8\Delta_{i,\text{bulk}}$ for the definition of ξ_i is not essential for our conclusions. For example, when choosing $\Delta_i(\rho = \xi_i) = 0.9\Delta_{i,\text{bulk}}$, we find $\xi_1 = 22\,\text{nm}$ and $\xi_2 = 116\,\text{nm}$, i.e. ξ_i is simply rescaled by a factor of 1.56-1.57. Note that the Friedel-like oscillations (see, e.g., Ref. [128]) of Δ_1 and Δ_2 inside the vortex core [see Fig. 6.2(a)] may cause more disperse values of the rescaling factor when decreasing the threshold down to $0.5\Delta_{i,\text{bulk}}$. However, such oscillations are rapidly washed out at higher temperatures, see, e.g., [128].

Material	λ_{11}	λ_{22}	λ_{12}	$T_{c1}(K)$	$T_{c2}(K)$	$T^*(K)$	$T_c(K)$	γ	Ref.
MgB_2	1.88	0.5	0.21	38	3.9	14	39	0.22	[89]
OsB_2	0.39	0.29	0.0084	2.1	1.2	1.5	2.1	0.074	[129–131]
LiFeAs	0.63	0.642	0.061	17.7	6.7	(14)	18	0.15	[132]
V_3Si	0.566	0.472	0.0074	16.4	8.1	9	16.5	0.03	[133]
$FeSe_{1-x}$	0.482	0.39	0.001	8.3	3.1	3.2	8.3	0.005	[134]

Table 6.1: The coupling constants, calculated nominal critical temperatures T_{c1} and T_{c2} of the separate bands, the approximate crossover temperature T^*, the critical temperature T_c and the interband coupling γ for selected two-gap materials. The coupling constants are taken from the references in the last column of the table.

in Fig. 6.2(b). The peak in $\xi_2(T)$ also marks the temperature range where the most pronounced difference is found between the two healing lengths in the two bands [shown in Fig. 6.2(c) for $\gamma < 0.2$]. When approaching T_c, the difference between the spatial profiles of the band-dependent condensates disappears, i.e., $\xi_2/\xi_1 \to 1$, in agreement with Refs. [2, 3]. The present study shows that the effect of the hidden criticality on the vortex core is very pronounced for $T_{c2} < 0.8T_c$. At higher temperatures the peak in ξ_2 is overshadowed by the usual critical behavior around T_c, unless the coupling γ is extremely weak.

As seen in Figs. 6.2(b,c), with increasing coupling γ the temperature where ξ_2 peaks, labeled T^*, increases while the peak itself decreases (for the chosen parameters, the peak is washed out for $\gamma > 0.2$). Regarding the maximal peak magnitude, it is limited by the taken sample radius ($0.3\,\mu$m). The largest value of ξ_2 in Fig. 6.2(b) is well below this limit and finite size effects do not alter our conclusions. It is interesting that T^* can be evaluated without a time-consuming numerical study of the vortex solution, being very close to the temperature at which $\partial^2\Delta_2/\partial T^2 = 0$ for a bulk superconductor. This is illustrated in Fig. 6.2(d) for $\gamma = 0.02$, where the inflection point of $\Delta_2(T)$ at $T = 0.33\ T_c$ matches well with $T^* = 0.31\ T_c$ found from the peak position in panel (b). In either case, T^* should be seen as the crossover temperature between the two regimes: lower temperatures - where Δ_2 is governed by the properties of the weaker band (for sufficiently small γ), and higher temperatures - where Δ_2 is controlled by the tunneling from the stronger band.

Finally, we briefly discuss available two-gap materials from the point of view of the hidden criticality. Based on the coupling constants available from Refs. [89, 129–134], we estimate the dimensionless coupling strength

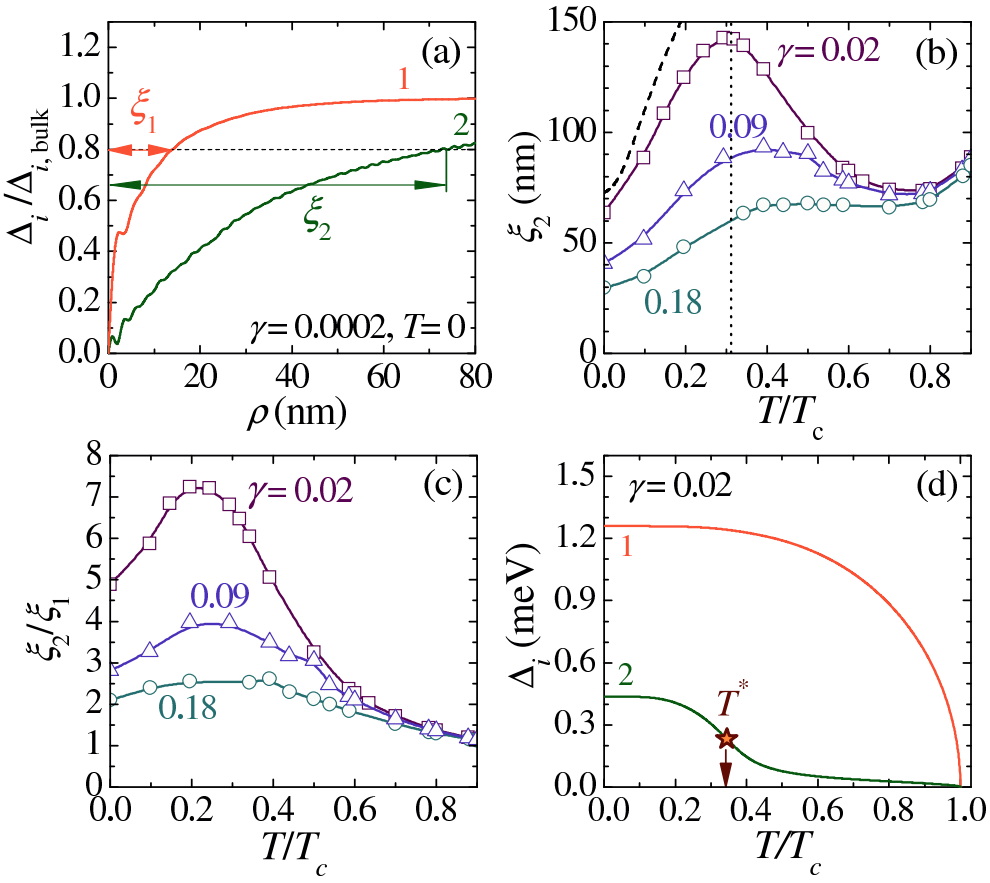

Figure 6.2: (a) $\Delta_i(\rho)$ in the vortex core as calculated for $T = 0$ and $\gamma = 0.0002$ and the definition of the healing lengths ξ_i. (b) The numerically extracted healing length of the weaker band ξ_2 as a function of T/T_c for different γ. The dashed curve represents ξ_2 in the independent-band limit $\gamma \to 0$, and the dotted line marks $T_{c2} = 2.645\,\mathrm{K}$ (for comparison, they are shown versus T/T_c with T_c calculated for $\gamma = 0.02$). (c) The ratio of the healing lengths ξ_2/ξ_1 versus temperature. (d) The bandgaps versus temperature and the definition of the crossover temperature T^* (where ξ_2 peaks) extracted from the condition $\frac{\partial^2 \Delta_2}{\partial T^2} = 0$.

γ for various two-gap superconductors in Table 6.1 [5]. According to our calculations the best candidates to observe the effects associated with the hidden criticality seem to be V_3Si and $FeSe_{1-x}$ due to their particularly low values of coupling γ and low T^* and T_{c2} in comparison with the bulk T_c. This is supported by the experimentally observed anomalies close to T^* in these two materials, see Refs. [133, 134].

6.4 Conclusions

In summary, we demonstrated that the properties of a two-band superconductor are affected by *two critical points*. In addition to the ordinary critical temperature T_c, there exists a hidden critical point - at the critical temperature of the weaker band in the absence of coupling. Interband coupling γ controls the proximity to this hidden critical point and governs the criticality similarly to an external magnetic field for ferromagnetic materials or an external electric field for ferroelectric systems. For weak coupling, the weaker-band healing length exhibits an atypical temperature dependence, with the *well pronounced peak* close to the hidden critical point. This gives rise to a large disparity of healing lengths of the two condensates in this temperature region.[6] Such a competition of length scales in a single material can lead to significant new physics, and may be closely related to the recently observed exotic behavior of vortex matter [1, 15, 74, 77, 78, 86, 87, 95, 98, 100, 117–121]. Direct measurement of the weaker-band coherence length can be realized experimentally, as was demonstrated for π band in MgB_2 [42]. We suggest that more experimental work should be done on recent multiband materials close to their hidden critical point, where evidence for criticality can be found through unusual thermal properties [135], resurgence of fluctuations deep in the superconducting state or anomalous cusps in superfluid density as a function of temperature [133, 134]. Further experimental advancements are facilitated by direct similarities of two-band superconductors with superconducting bilayers, where the atypical temperature behavior of

[5] The crossover temperature T^* for MgB_2, OsB_2 and LiFeAs was estimated in a simplified model with two-spherical Fermi surfaces, taking into account realistic values of ratios of Fermi velocities and densities of states but otherwise neglecting subtle properties of the band structure. $\Delta_2(T)$ for LiFeAs is a concave function of temperature at all temperatures therefore the value of T^* is not defined. However, its second derivative narrowly approaches zero at 14 K, a value quoted in Table 6.1. The T^* for V_3Si and $FeSe_{1-x}$ is obtained from the weak gap profiles in Refs. [133, 134] respectively.

[6] Note that for the parameters chosen for our calculation the coherence lengths are indeed very different, however the material is nevertheless deep in the type-II regime, since one can estimate $\kappa_1 \approx 46$ and $\kappa_2 \approx 13.5$.

the coherence length can be observed as a function of an alterable interlayer coupling. Some signatures of such behavior are already visible in Ref. [124].

6.5 Appendix

6.5.1 Derivation of the γGL equation (Eq. (6.4))

It is convenient to recast the self-consistency equation Eq. (6.1) for a two-band superconductor in the form

$$\begin{pmatrix} \Delta_1(\mathbf{x}) \\ \Delta_2(\mathbf{x}) \end{pmatrix} = \begin{pmatrix} \lambda_{11} & \lambda_{12} \\ \lambda_{21}=\lambda_{12} & \lambda_{22} \end{pmatrix} \begin{pmatrix} R_1[\Delta_1(\mathbf{x})] \\ R_2[\Delta_2(\mathbf{x})] \end{pmatrix}, \tag{6.10}$$

where $R_i[\Delta_i(\mathbf{x})]$ is a functional of $\Delta_i(\mathbf{x})$ related to the anomalous Green function as [see Eq. (6.2)]

$$R_i[\Delta_i(\mathbf{x})] = \frac{\langle \hat{\psi}_{i\uparrow}(\mathbf{x})\hat{\psi}_{i\downarrow}(\mathbf{x})\rangle}{N(0)} \tag{6.11}$$

and $\lambda_{ij} = \lambda_{ji} = N(0)g_{ij}$, with $N(0)$ the total density of states. Then, Eq. (6.10) can further be rearranged as

$$\begin{pmatrix} R_1[\Delta_1(\mathbf{x})] \\ R_2[\Delta_2(\mathbf{x})] \end{pmatrix} = \frac{1}{\eta} \begin{pmatrix} \lambda_{22} & -\lambda_{12} \\ -\lambda_{12} & \lambda_{11} \end{pmatrix} \begin{pmatrix} \Delta_1(\mathbf{x}) \\ \Delta_2(\mathbf{x}) \end{pmatrix}, \tag{6.12}$$

with $\eta = \lambda_{11}\lambda_{22} - \lambda_{12}^2$. Based on Eq. (6.2) and Eq. (6.12) given above, one finds

$$\Big(\frac{\lambda_{11}}{\eta} - \alpha_2\Big)\Delta_2 + \beta_2\Delta_2|\Delta_2|^2 - \mathcal{K}_2\mathbf{D}^2\Delta_2 - \frac{\lambda_{12}}{\eta}\Delta_1 = 0, \tag{6.13}$$

where α_2, β_2 and $\mathcal{K}_2$ are defined in Eq. (6.3). Now, assuming that

$$T = T_{c2} = \frac{2e^{\Gamma}}{\pi}\hbar\omega_c\, e^{-1/(n_2\lambda_{22})},$$

with $n_i = N_i(0)/N(0)$ the partial density of states, and keeping only the terms linear in λ_{12}, Eq. (6.13) yields

$$\beta_2\Delta_2|\Delta_2|^2 - \mathcal{K}_2\mathbf{D}^2\Delta_2 - \frac{\lambda_{12}}{\lambda_{11}\lambda_{22}}\Delta_{1,\lambda_{12}\to 0} = 0, \tag{6.14}$$

with β_2 and $\mathcal{K}_2$ taken at $T = T_{c2}$, which is the γGL equation [$\gamma = \lambda_{12}/(\lambda_{11}\lambda_{22})$] given by Eq. (6.4).

6.5.2 Derivation of Eq. (6.7)

Let us again consider Eq. (6.13) but now for $T_{c2} < T < T_{c1}$ and *in the homogeneous case*. In this temperature domain $\Delta_2 \to 0$ for $\lambda_{12} \to 0$ and $\Delta_{1,\lambda_{12}\to 0} \neq 0$. From Eq. (6.13) we have

$$\Big[\frac{\lambda_{11}}{\eta} - n_2 \ln\Big(\frac{2e^{\Gamma}\hbar\omega_c}{\pi T}\Big)\Big]\Delta_2 + n_2\frac{7\zeta(3)}{8\pi^2 T^2}\Delta_2|\Delta_2|^2 = \frac{\lambda_{12}}{\eta}\Delta_1. \tag{6.15}$$

Note that the expansion given by Eq. (6.2) and therefore also Eq. (6.13) given above is not justified for *a spatially nonuniform solution* at $T_{c2} < T < T_{c1}$ because the coherence length ξ_2 associated with a spatial variation of the condensate in a weaker band does not diverge as λ_{12} goes to zero. In other words, one cannot invoke the gradient expansion in the Gor'kov derivation of Eq. (6.2). However, for homogeneous case Eq. (6.2) is simply an expansion in powers of the order parameter Δ_2 and, so, is fully correct. Keeping only terms linear in λ_{12}, from Eq. (6.15) one finds

$$n_2 \ln(T/T_{c2})\Delta_2 = \frac{\lambda_{12}}{\lambda_{11}\lambda_{22}}\Delta_{1,\lambda_{12}\to 0}, \tag{6.16}$$

which is Eq. (6.7).

We remark that at first sight Eq. (6.16) prescribes that Δ_2 is infinite when $T \to T_{c2}$ and $\lambda_{12} = \text{const}$. This is not true because the validity of the expansion in powers of λ_{12} given in Eq. (6.16) requires that $\lambda_{12} \lesssim \lambda_{12}^{(\mathrm{lim})}(T)$, and $\lambda_{12}^{(\mathrm{lim})}(T) \to 0$ for $T \to T_{c2}$. Hence, λ_{12} can not be considered as constant when using Eq. (6.16) for $T \to T_{c2}$. In particular, during the derivation of Eq. (6.16) we first assumed that

$$\frac{\lambda_{11}}{\eta} - n_2 \ln\Big(\frac{2e^{\Gamma}\hbar\omega_c}{\pi T}\Big) = n_2 \ln\big(T/T_{c2}\big) + \frac{\lambda_{12}^2}{\lambda_{11}\lambda_{22}^2} + \mathcal{O}(\lambda_{12}^4) \tag{6.17}$$

and, then, we ignored contributions of the order λ_{12}^2 and higher. However, when the first and second terms in the right-hand-side of Eq. (6.17) become of the same order of magnitude, then the contributions $\propto \lambda_{12}^2$ can not be neglected any more. This makes it possible to estimate $\lambda_{12}^{(\mathrm{lim})}(T)$ as

$$\lambda_{12}^{(\mathrm{lim})}(T) \sim \lambda_{22}\Big[\lambda_{11} n_2 \ln\big(T/T_{c2}\big)\Big]^{1/2}, \tag{6.18}$$

which proves that $\lambda_{12}^{(\mathrm{lim})}(T) \to 0$ when $T \to T_{c2}$. Notice that Eq. (6.16) does not hold for $T \geq T_{c1}$, where $\Delta_{1,\lambda_{12}\to 0} = 0$. Formally, it gives $\Delta_2 = 0$ which means that Δ_2 is no longer linear in λ_{12} for small interband couplings.

This is directly related to the fact that $T = T_{c1}$ is one more hidden critical point for the system of interest, however it is now associated with a stronger band. As pointed out in Sec. 6.2, the hidden criticality associated with T_{c1} is overshadowed by the usual critical behavior around T_c.

Related publication

- L. Komendová, Yajiang Chen, A. A. Shanenko, M. V. Milošević, and F. M. Peeters: *Two-band superconductors: Hidden criticality deep in the superconducting state*, Phys. Rev. Lett. **108**, 207002 (2012).

Chapter 7

Soft vortex matter in a type-I/type-II bilayer

Magnetic flux patterns are known to strongly differ in the intermediate state of type-I and type-II superconductors. Using a type-I/type-II bilayer we demonstrate hybridization of these flux phases into a plethora of unique new ones. Owing to a complicated multibody interaction between individual fluxoids, many different intriguing patterns are possible under applied magnetic field, such as few-vortex clusters, vortex chains, mazes, or labyrinthal structures resembling the phenomena readily encountered in soft-matter physics. However, in our system the patterns are tunable by sample parameters, magnetic field, current and temperature, which reveals transitions from short-range clustering to long-range ordered phases such as parallel chains, gels, glasses, and crystalline vortex lattices, or phases where lamellar type-I flux domains in one layer serve as a bedding potential for type-II vortices in the other, configurations clearly beyond the soft-matter analogy.

7.1 Introduction

Soft-matter physics deals with systems as different as colloids, polymers, gels, glasses, liquid crystals, and others, where one common feature is their self-organization into very rich mesoscopic phases [136]. To model this behavior, one often uses a pairwise interparticle interaction possessing several length scales and/or mixture of attraction and repulsion [137–144]. Such interaction potential, as a function of the particle density, indeed leads to the formation of clusters, particle chains, labyrinthal gel-like structures, and (almost) reg-

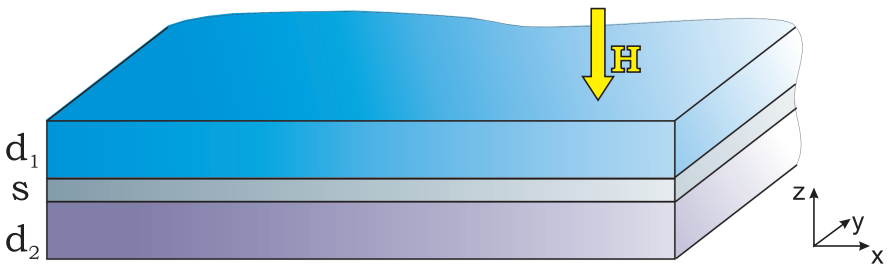

Figure 7.1: The oblique view of the considered bilayer sample. The two superconducting layers are separated by an ultrathin oxide/insulating layer. The magnetic field is applied in the direction perpendicular to the layers (along the z axis).

ular lattices. This in turn questions the known analogy between charged colloids and vortices in superconductors, since the latter typically repel and form a triangular (Abrikosov) lattice. On the other hand, type-I superconductors are known to exhibit lamellar and labyrinthal flux patterns, which lose distinction of individual vortices but resemble the soft-matter structures in their macroscopic shape [8, 145, 146].

With this in mind, we here investigate magnetic flux patterns in a coupled bilayer of two superconducting films - one type-I and one type-II - under perpendicular magnetic field (see Fig. 7.1), in an attempt to reveal unique vortex phases. In addition to the crystalline vortex lattice, one now envisages vortex flocculation, gelation, and glassy phases, some similar to vortex matter encountered in high-temperature [147], multiband [1, 34, 35], and other unconventional superconducting [148] and superfluid systems [149]. The film geometry is chosen for an easy realization in experiment, but also in order to have asymptotic long-range $1/r$ repulsion between vortices [150], similar to the electrostatic Coulomb interaction in charged colloids. We will show that the complexity of the obtained patterns stems from the changes in the short- and midrange interaction between vortices, whose relative strength depends on the parameters of the layers, especially their coherence length ξ and penetration depth λ, but also their thicknesses, electronic coupling between them, and chosen temperature with respect to their individual critical temperatures.

7.2 Theoretical formalism

Most of earlier works on vortex structures and their dynamics employed molecular dynamics with pairwise vortex interactions. This is truly valid

only for vortices in extreme type-II superconductors, where vortex cores are pointlike small. However, overlapping vortex cores do not interact pairwise, and the interaction potentials are highly nontrivial [88, 151]. This turns out to be even more complex for our bilayer system, where vortices are extended objects with different size of the core in two layers. We therefore opt for full numerical simulation within the Ginzburg-Landau (GL) theory, supplemented by the Lawrence-Doniach (LD) coupling between the layers [19, 152–155]. The appropriate free energy functional then consists of the individual contributions from each layer, the LD coupling term, and the energy of the magnetic field in and around the sample:

$$\mathcal{F} = \sum_{j=1,2} d_j \int \left[\alpha_j |\Psi_j|^2 + \frac{1}{2}\beta_j |\Psi_j|^4 + \frac{1}{2m_j} \left| \left(\frac{\hbar}{i}\nabla - \frac{2e}{c}\mathbf{A} \right) \Psi_j \right|^2 \right] dS$$
$$+ s \int \eta |p\Psi_2 - \Psi_1|^2 dS + \int \frac{(\mathbf{h}-\mathbf{H})^2}{8\pi} dV. \tag{7.1}$$

Here Cooper-pair condensates in the two layers are indexed by $j = 1, 2$ and described by the order parameters $\Psi_j(\mathbf{r})$, assumed to be uniform over the layer thickness d_j. $\mathbf{H}$ is the applied magnetic field and $\mathbf{h} = \text{curl } \mathbf{A}$ is the field including the magnetic response of the layers. The coefficients $\alpha_j(T) = -\alpha_{j0}(1 - T/T_{cj})$ are temperature dependent (where T_{cj} are the critical temperatures of the individual layers) and connected with the nominal coherence lengths of the layers $\xi_j(T) = \hbar/|2m_j\alpha_j(T)|^{1/2} = \xi_{j0}/\sqrt{1 - T/T_{cj}}$, where m_j denotes Cooper-pair masses in the layers. The LD coupling coefficient is $\eta = \hbar^2/(2m_\perp s^2)$, where $m_\perp$ is the effective Cooper pair mass for tunneling between the layers and s is the vertical distance between the layers (see Fig. 7.1). The phase factor $p = \exp(-i\frac{2e}{\hbar c}\int_0^s A_z dz)$ ensures the gauge invariance.

In what follows, we work in the London gauge $\nabla \cdot \mathbf{A} = 0$; therefore the Maxwell equation is just

$$-\nabla^2 \mathbf{A} = \frac{4\pi}{c}\mathbf{j}. \tag{7.2}$$

Further we make approximation $A_z = 0$, so that the phase factor p in the LD coupling term is unity (a similar model was also employed in Ref. [124]). Since $A_z = 0$, Eq. (7.2) implies also $j_z = 0$. On the other hand, in the full model the current between the layers is

$$j_z = \frac{ie\hbar}{m_\perp s}\left[\psi_1^* p \psi_2 - p^* \psi_2^* \psi_1\right]$$
$$= \frac{2e\hbar}{m_\perp s}|\psi_1||\psi_2| \sin(\varphi_1 - \varphi_2), \tag{7.3}$$

where we used $p = 1$ and $\psi_j = |\psi_j|e^{i\varphi_j}$. The current between the layers j_z can be neglected if it is much smaller than the currents within the superconducting layers

$$\mathbf{j}_j = -\frac{ie\hbar}{m_j}(\Psi_j^*\nabla\Psi_j - \Psi_j\nabla\Psi_j^*) - \frac{4e^2}{m_j c}|\Psi_j^2|\mathbf{A}. \tag{7.4}$$

which leads to the condition

$$\frac{m_j}{m_\perp}\frac{\xi_j(T)}{s}\sin(\phi_1 - \phi_2) \ll 1, \tag{7.5}$$

if we assume that the amplitudes of the wave functions in two layers are not too different from each other. Assuming $A_z = 0$ is thus well justified for $m_\perp \gg m_j$ or very distant layers $s \gg \xi_j(T)$, i.e., in the case of very weakly coupled layers, but also in the opposite case $m_\perp \approx m_j$ where the phases of the two order parameters are almost the same, so that the term $\sin(\phi_1 - \phi_2)$ vanishes. Therefore, for the parameters of the sample chosen in the present work j_z is always much smaller than the current within the superconducting layers and one can safely neglect it.

The variational minimization of the functional (7.1) (with $p = 1$) with respect to Ψ_j^* leads to the GLLD equations

$$\frac{1}{2m_1}\left(\frac{\hbar}{i}\nabla - \frac{2e}{c}\mathbf{A}\right)^2\Psi_1 + \tilde{\alpha}_1\Psi_1 + \beta_1|\Psi_1|^2\Psi_1 - \eta\frac{s}{d_1}\Psi_2 = 0, \tag{7.6a}$$

$$\frac{1}{2m_2}\left(\frac{\hbar}{i}\nabla - \frac{2e}{c}\mathbf{A}\right)^2\Psi_2 + \tilde{\alpha}_2\Psi_2 + \beta_2|\Psi_2|^2\Psi_2 - \eta\frac{s}{d_2}\Psi_1 = 0, \tag{7.6b}$$

where $\tilde{\alpha}_j = \alpha_j + \eta s/d_j$. We solve this system of equations numerically, self-consistently with the equations for the supercurrent density per unit volume in each layer given by Eq. (7.4). Note that the supercurrents only flow inside the respective layers and therefore are spatially separated. Substituting Eq. (7.4) into Eq. (7.2) with $\mathbf{j} = \mathbf{j}_1 + \mathbf{j}_2$ provides the total 3D vector potential $\mathbf{A}$, which we calculated in the middle of each layer and used iteratively in respective Eqs. (7.6a) and (7.6b) to compute Ψ_1 and Ψ_2 (for details of the procedure, see Ref. [61]).

We performed the numerical simulations on a rectangular region, with aspect ratio $2 : \sqrt{3}$ and periodic boundary conditions. We chose the parameter values close to a clean Nb film as the type-II layer (with GL parameter $\kappa_1 = 1.03$, $T_{c1} = 9.2$ K) and Sn as the type-I layer ($\kappa_2 = 0.15$, $T_{c2} = 3.7$ K). The lowest considered temperature was 1 K, which was necessary to be deep in the superconducting state of the type-I layer. Zero-temperature coherence

length of the type-II layer (ξ_{10}) was then taken as unit of distance in all calculations, while ξ_{20} was swept between 2 and 10 ξ_{10}. Since this variation had only minor qualitative influence on the observed vortex structures, we fixed the parameter $\zeta = (\xi_{10}/\xi_{20})^2$ to 0.2, for computational convenience. Order parameters were scaled to $\Psi_{j0} = \sqrt{-\alpha_j(0)/\beta_j}$, and magnetic field to $B_0 = \Phi_0/(2\pi\xi_{10}^2)$, where Φ_0 is the flux quantum.

7.3 Phase diagram as a function of applied magnetic field and coupling between the layers

In Fig. 7.2, we show the key result of this chapter, the vortex phase diagram of the described bilayer at $T = 1$ K as a function of the applied magnetic field and the effective mass in the spacer layer, which controls the strength of the coupling between the superconducting layers. The field is expressed through the number of vortices in the simulation region. We revealed a series of nonuniform vortex phases, with phase transitions between them indicated by dashed curves in the diagram. In what follows, we discuss these transitions by showing exemplary vortex configurations.

Figure 7.3 shows obtained vortex configurations for very strongly coupled layers ($m_\perp = 5m_1$). At low fields we observe a quasihomogeneous distribution of vortices, indicative of long-range repulsion between them, reminiscent of Wigner glass in soft-matter physics (see, e.g., Ref. [142]). However, with increasing field, after reaching some threshold vortex density, vortex dimers, short individual chains, and then long-ordered parallel chains are formed, in complete analogy to what was seen in Ref. [137] (reproduced here in Fig. 7.4) for particle systems with purely repulsive interactions but two governing length scales [i.e., a potential with very strong repulsion at short range ("hard core"), flattening at midrange ("soft core"), and then abruptly weaker repulsion at long range]. The half-distance between the parallel vortex chains in Fig. 7.3(c) then gives an estimate of the "soft core". As the vortex density is further increased, the chains interconnect into a glassy disordered structure, and finally form the crystalline (Abrikosov) lattice. The intervortex distance at the latter glass-solid transition then provides an estimate of the "hard core" of the repulsive vortex interaction. In Fig. 7.5, we reduced the coupling between the layers with a factor 2 as compared to Fig. 7.3 (i. e., we increased $m_\perp$ to $10m_1$). The found vortex configurations are very different, starting at low fields from small clusters of 2-4 vortices, combined with short chains. With further increase of the magnetic field the

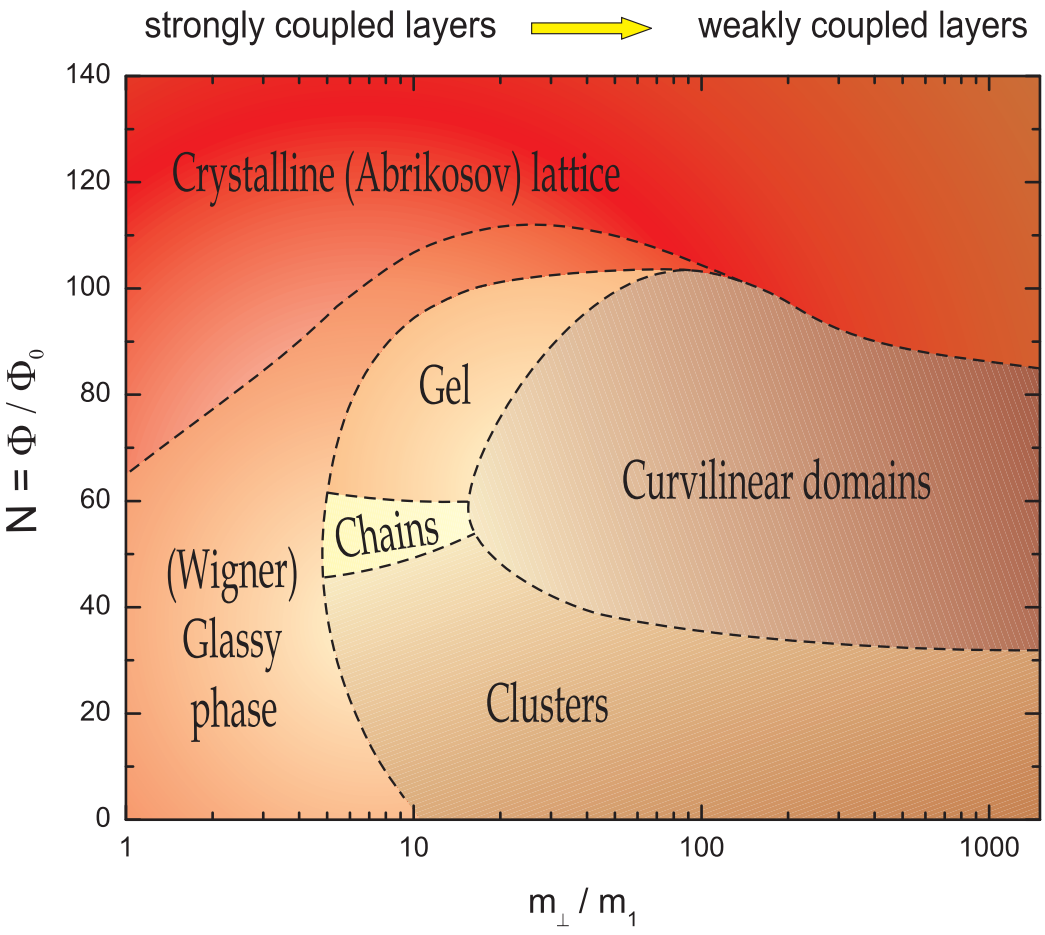

Figure 7.2: The equilibrium phase diagram of a Nb/Sn bilayer calculated at $T = 1$ K, for both layers $5\xi_{10}$ thick and spacer layer of $0.05\xi_{10}$ in between, as a function of the applied field (expressed through the number of flux quanta N in the simulation region $55 \times 47.6\ \xi_{10}^2$) and effective mass $m_\perp$ of the Cooper pairs in the spacer layer. When other parameters are fixed, the electronic coupling between the superconducting layers is inversely proportional to $m_\perp$.

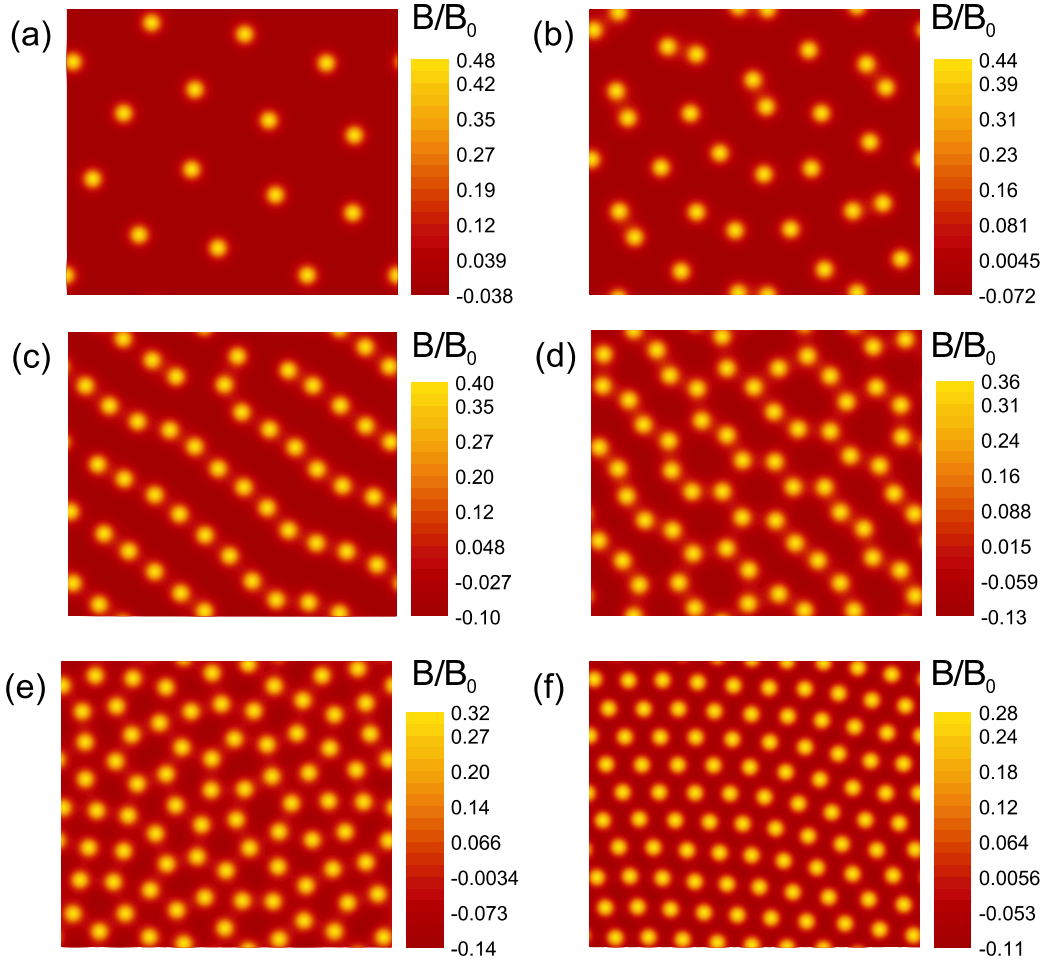

Figure 7.3: *Very strongly coupled layers.* Vortex structure shown via normalized magnetic field profile in the type-II layer (identical vortex structure is found in the type-I layer), corresponding to Fig. 7.2 for $m_\perp = 5m_1$. In panels (a)-(f) there are 16, 32, 48, 64, 80, and 96 vortices in the simulation region, respectively.

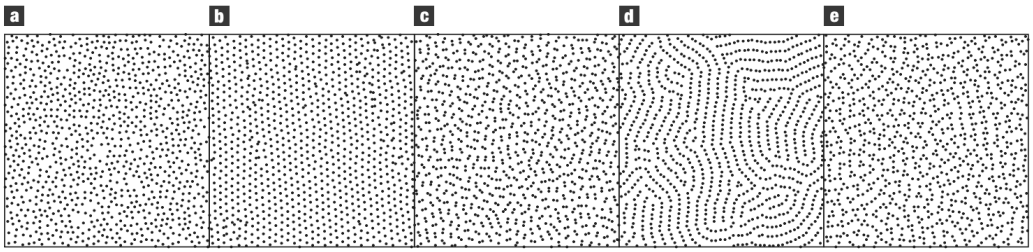

Figure 7.4: Molecular dynamics results from Ref. [137] for particles interacting purely repulsively with two characteristic length scales. Each particle has an inpenetrable hard core of radius σ_0 and a soft shoulder with energy ε between σ_0 and $\sigma_1 = 2.5\sigma_0$. Beyond the distance σ_1 the particles do not interact. Shown are structures at temperature $T = 0.1\varepsilon/k_B$ (NVT simulation) at densities (a) $\rho = 0.1\sigma_0^{-2}$, (b) $0.15\sigma_0^{-2}$, (c) $0.227\sigma_0^{-2}$, (d) $0.291\sigma_0^{-2}$, (e) $0.38\sigma_0^{-2}$. Filled circles represent the hard core of each particle.

chains establish long-range order, then curve, recombine, and finally interconnect into a low-density network filling the entire simulation region. Such a network, that spans the volume of the medium while at low particle density, is typical for **gels**. This gel-like structure is retained in Fig. 7.5 until the newly added vortices fill all the voids in the gel and form a disordered (glassy) lattice, similarly to the case of Fig. 7.3, followed by crystallization at high vortex density.

In Fig. 7.6, the states are shown for $m_\perp = 15m_1$, which is still a relatively strong coupling. For low fields tiny clusters are formed, which then give way to prolonged chains, gel states, and finally a (quasi-)crystalline lattice for 128 vortices in the simulation box (not shown). One can see that $m_\perp = 15m_1$ lies on the crossover of stability regions of spatial structures with lateral extent one and two vortices, i.e., at the transition from chains to curvilinear domains in Fig. 7.2. In Fig. 7.7, the electronic coupling between superconducting layers is further decreased ($m_\perp = 20m_1$), and the qualitative trend of Fig. 7.6 is maintained. With increasing field, a transition from a solution of clusters to short-range mazes and then long-range gel is found, followed by crystallization of the vortex lattice. However, the superconducting type-I behavior of the type-I layer becomes more apparent, as vortices become less distinct from each other, and occupy increasingly wider domains. This is more clearly demonstrated in Fig. 7.8, where we gradually increased the coupling between the layers for a fixed number of vortices in the simulation. Notice that the lateral extent of the vortex stripes varies from just one vortex for strong coupling, to four vortices for weak coupling. This behavior is reminiscent of the colloidal structures studied in Ref. [138] (reproduced also here

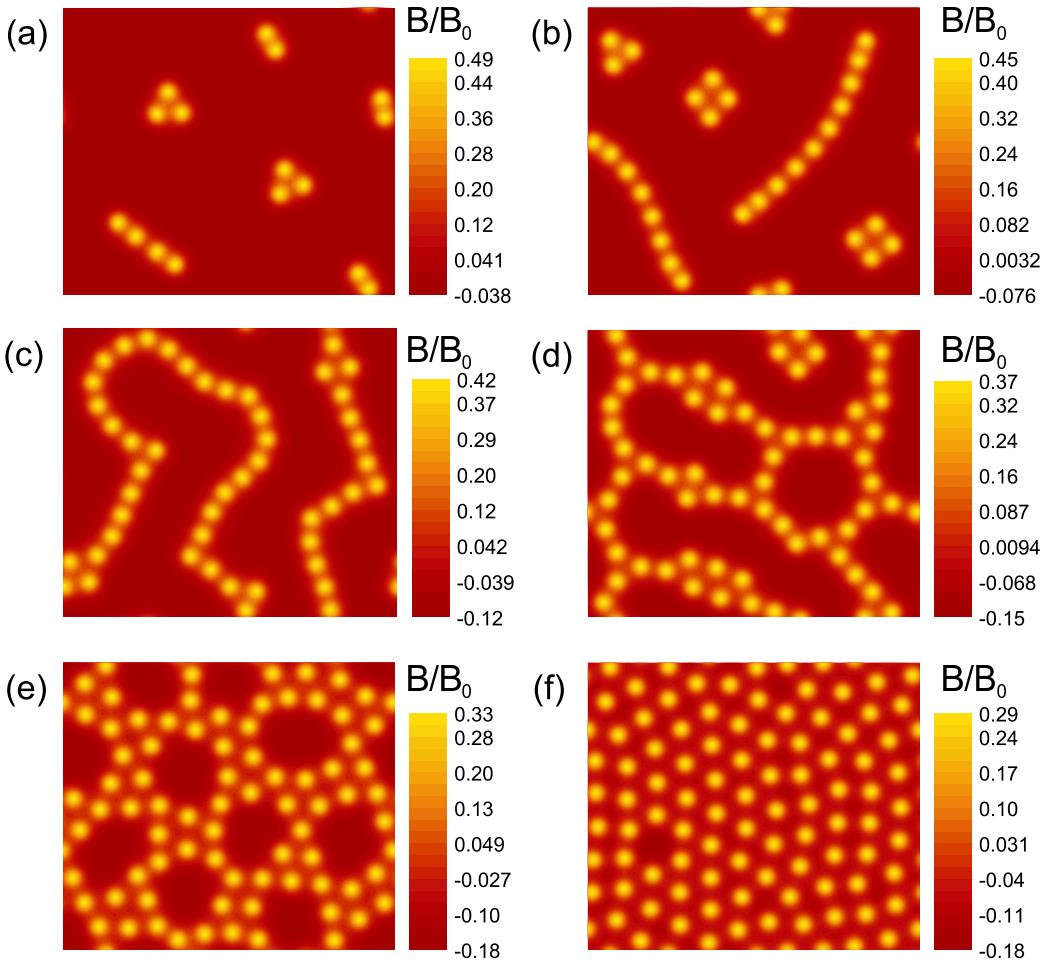

Figure 7.5: *Strongly coupled layers.* Same as Fig. 7.3, but for twice weaker coupling between the layers; i.e., $m_\perp = 10m_1$. In panels (a)-(e) there are 16, 32, 48, 64, 80, and 96 vortices in the simulation region, respectively.

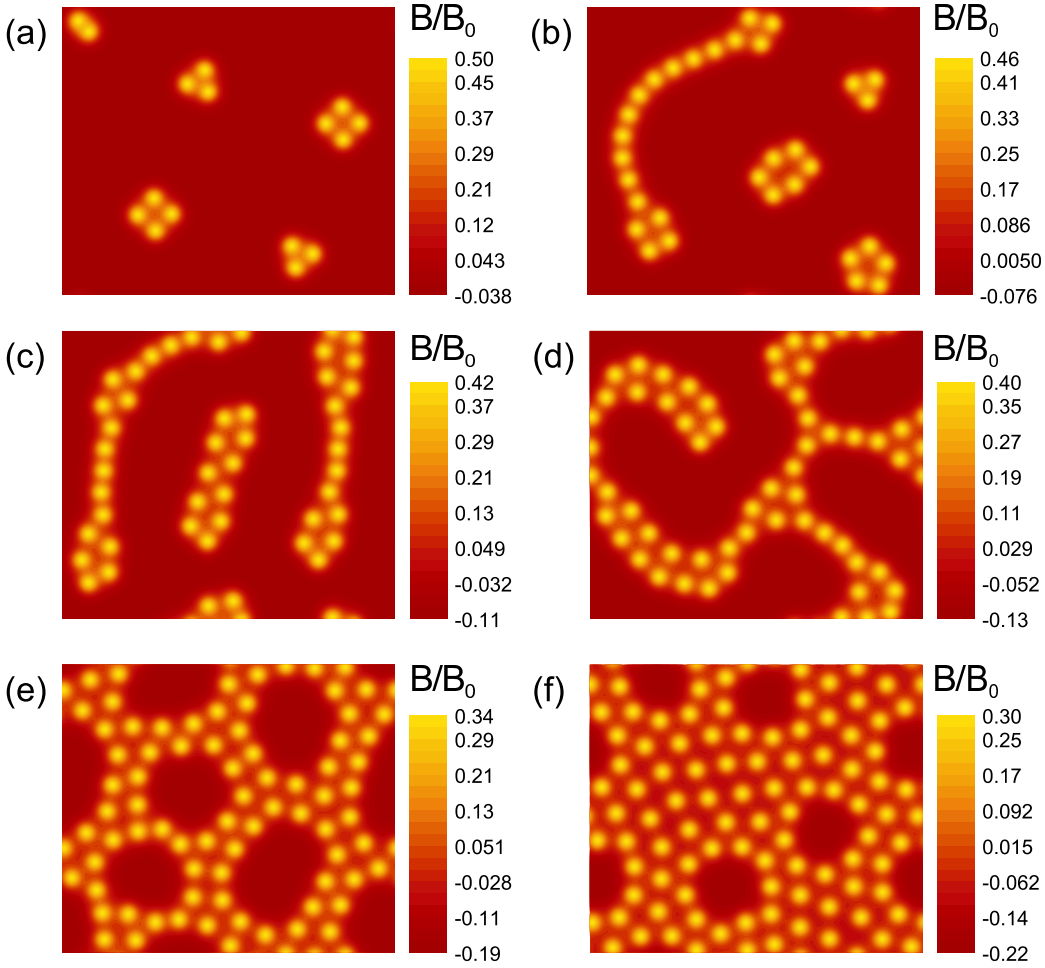

Figure 7.6: Evolution of the states with applied magnetic flux, at coupling $m_\perp/m_1 = 15$ (c.f. Fig. 7.2). The spatial profile of the magnetic field is shown for (a)-(f) 16, 32, 48, 56, 80, and 96 vortices, respectively. In this sequence of images, we sample the found phases in the busiest region of the phase diagram shown in Fig. 7.2. Transitions between clusters and chains, to mazes and gel are shown.

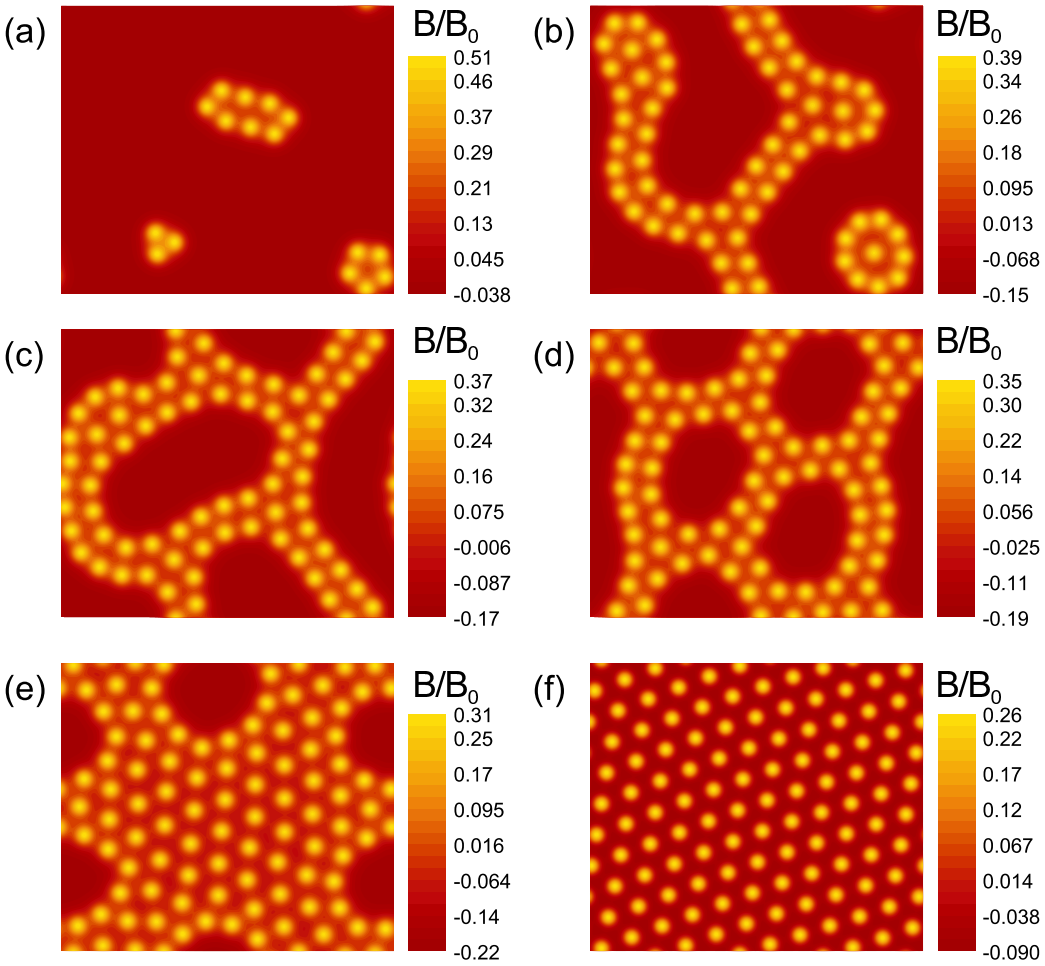

Figure 7.7: *Intermediately strongly coupled layers.* Same as Figs. 7.3-7.6 but for further weakened coupling between layers, i.e., for $m_\perp = 20m_1$. In panels (a)-(f) there are 16, 64, 72, 80, 96, and 112 vortices in the simulation region, respectively.

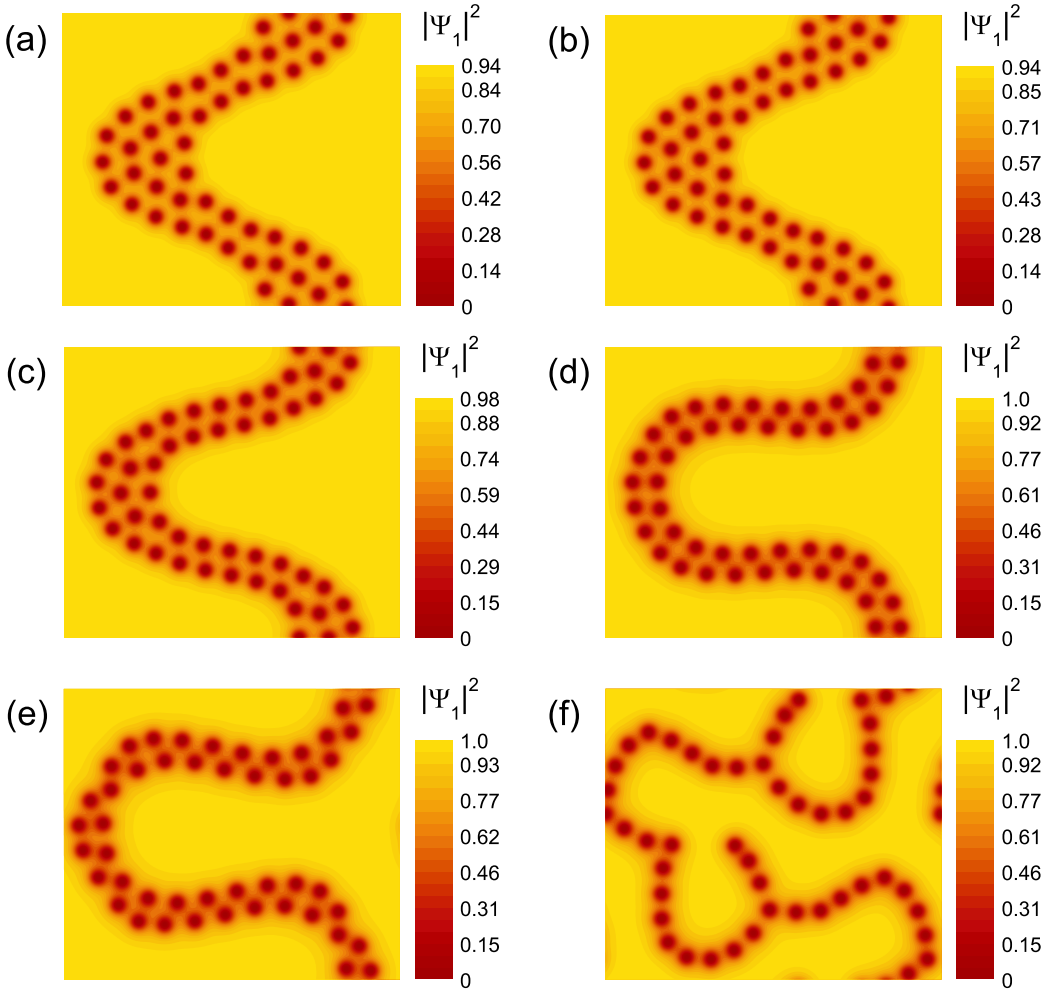

Figure 7.8: The evolution of the vortex structure with decreasing $m_\perp$, i. e., with increasing strength of the electronic coupling between the layers, for 48 vortices in the simulation region. In panels (a)-(f), the normalized Cooper-pair density in the type-II layer is shown for $m_\perp/m_1 = 160$, 120, 60, 30, 20, and 10, respectively.

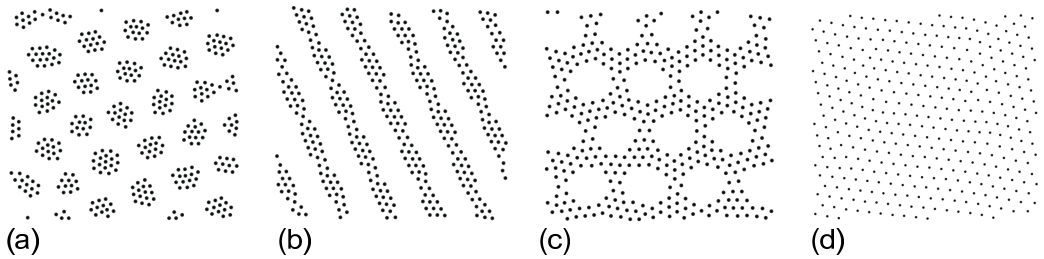

Figure 7.9: Molecular dynamics results from Ref. [138] for particles interacting through an interaction potential $V(R_{ij}) = 1/R_{ij} - Be^{-\kappa R_{ij}}$, taken with $\kappa = 1$ and $B = 2$. R_{ij} is the distance between two particles. Shown are structures obtained by simulated annealing of 380 particles to $T = 0$ at densities (a) $\rho = 0.27$, (b) 0.28, (c) 0.46, respectively (d) 0.6. The densities are given in number of particles per unit area. Different densities are achieved by changing the size of the simulation region. Please consult the original reference [138] for details and more states.

in Fig. 7.9), where particles interacted via Coulomb-like repulsion combined with a midrange attraction, and where the widening of the stripe phases was directly linked to the increasing strength and range of the attractive part of the interaction.

For even smaller values of interlayer coupling one can no longer rely on a two-body vortex-vortex interaction, since the type-I layer exhibits laminar domains, and the notion of individual vortices is completely lost. In Fig. 7.10 we depict the changes in vortex patterns in a broad range of $m_\perp$ values, where formation of type-I domains is visible for $m_\perp > 20m_1$. Those domains act as potential wells for vortices in the type-II layer, as exemplified in Fig. 7.11, which shows states for $m_\perp = 1000m_1$. Because of this, the structural phase transitions become different from the $m_\perp < 20m_1$ cases. This is clearly seen in the change of curvature of the sol-gel and the gel-glass transition lines in Fig. 7.2. With decreasing coupling, due to the easier formation of type-I domains, vortices in the type-II layer connect into mazes at lower densities. On the other hand, they also crystallize at lower densities than for strong coupling, which is due to the practically destroyed superconductivity in the type-I layer at such a large magnetic field. The formation of domains in the type-I layer as a trapping potential for vortices is interesting because of their sensitivity to applied in-plane magnetic field [156], or current [157]. Therefore one can easily manipulate externally the domain structure in the type-I layer (e.g., straighten/relax the domains), and thereby dynamically change and restore the vortex patterns in the type-II layer, similarly to the controllability achieved in the superconductor-ferromagnet bilayers [158, 159].

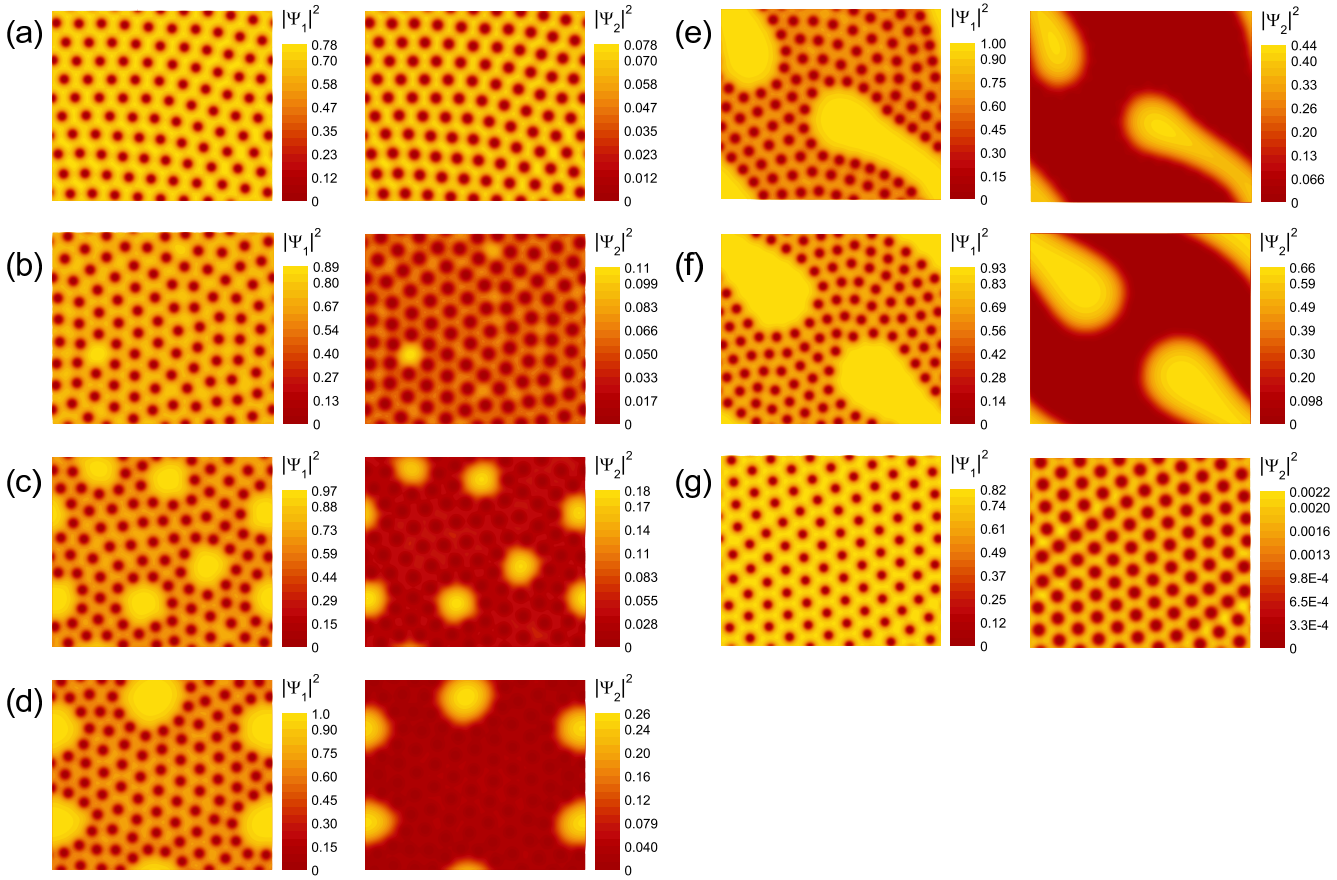

Figure 7.10: Evolution of the vortex states with decreasing coupling, at fixed magnetic flux (96 vortices; c.f. Fig. 7.2). The spatial profile of $|\Psi_1|^2$ and $|\Psi_2|^2$ is shown. Calculated for $m_\perp/m_1 =$ (a) 5, (b) 10, (c) 15, (d) 20, (e) 40, (f) 200, and (g) 300.

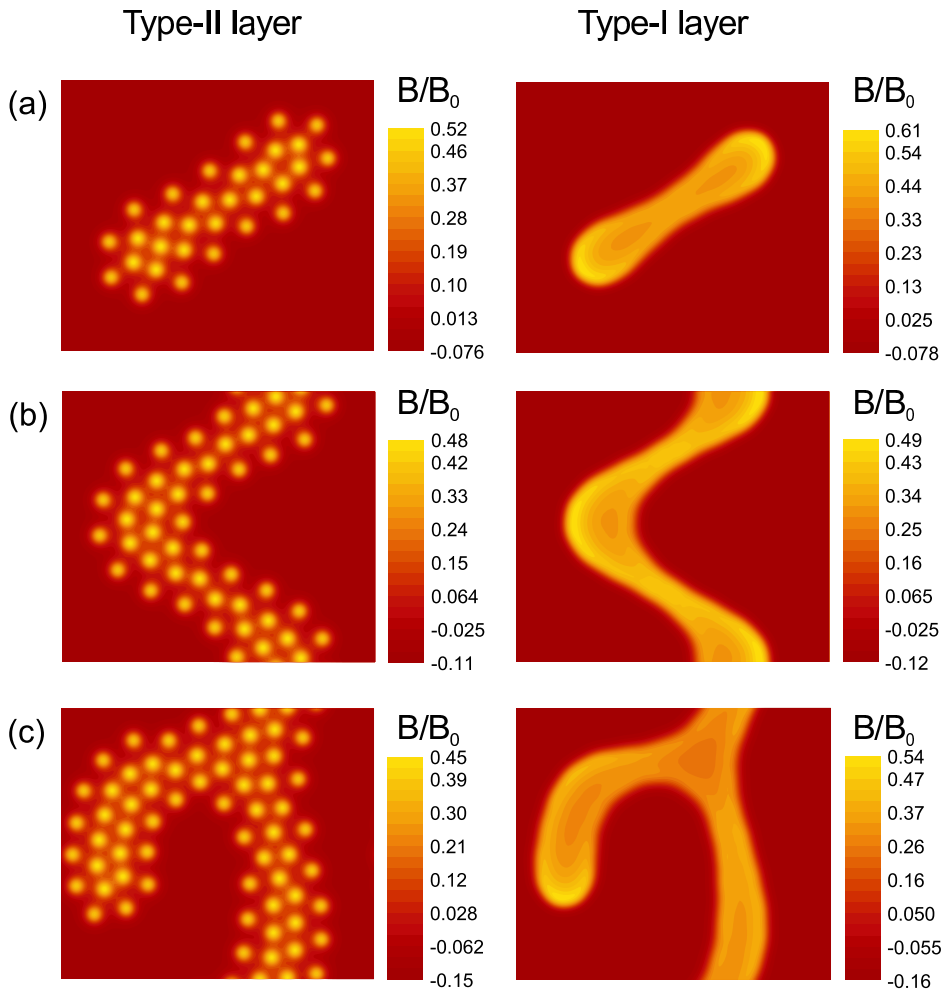

Figure 7.11: *Weakly coupled layers.* Flux patterns shown in the type-II layer (left) and the type-I layer (right), corresponding to Fig. 7.2 for $m_\perp = 1000m_1$. In panels (a)-(c) there are 32, 48, and 64 flux quanta in the simulation region, respectively.

7.4 Radial distribution functions of observed configurations

In this section we present the radial distribution functions $g(r)$ of different vortex phases observed in the superconducting type-I/type-II bilayer, which can in some cases serve to distinguish particular vortex configurations in, e.g., small-angle neutron scattering (SANS) measurements.

The radial distribution function $g(r)$ characterizes the particle distribution. It gives clear signatures of the crystalline order and can be also experimentally determined, e.g., by neutron scattering. It is defined as

$$g(r) = \frac{1}{N}\frac{\rho(r)}{\rho}, \tag{7.7}$$

where $\rho(r)$ is the density of particles at some distance r from the origin, while $\rho = N/A$, with N the total number of particles and A the total area, is the average density. The density $\rho(r)$ is in practice computed from the histogram of all distances between the pairs of particles, where the number of particles N_i in each bin $[r_i - dr/2; r_i + dr/2]$ is divided by the area corresponding to that bin $A_i = \pi\left[(r_i + dr/2)^2 - (r_i - dr/2)^2\right]$. Note that each pair counts for two particles. Taking this into account, we calculated $g(r)$ using the formula

$$g(r) = \frac{2N_i}{N\rho\pi\left[(r_i + dr/2)^2 - (r_i - dr/2)^2\right]}. \tag{7.8}$$

In Figs. 7.12 and 7.13 we show the radial distribution function for the states displayed in Figs. 7.3 and 7.7, respectively. In each case we use the total number of bins equal to half of the total number of vortices. The distance between any two vortices is determined as the distance to the nearest periodic image. In order not to account the interaction of vortex with its own periodic image, we only show $g(r)$ for r up to 23 ξ_{10}, i.e., approximately half of the shorter side of our simulation region.

The $g(r)$ functions for smaller densities, i.e., for 16 and 32 vortices in the simulation region, are too coarse to be useful; however in the radial distribution functions for our simulations for larger applied magnetic fields we can see important signatures of the order. For example in Fig. 7.13 in panels (e) and (f) for 96 respectively 112 vortices, one can see that the second peak splits into two, which is a well-known effect due to the formation of the regular triangular (Abrikosov) lattice (in the first case with holes of the Meissner state still present). One can also see in Fig. 7.12 that the chain phase for $m_\perp/m_1 = 5$ and intermediate densities (48 and 64 vortices) can be distinguished by having the second peak of $g(r)$ higher than the first

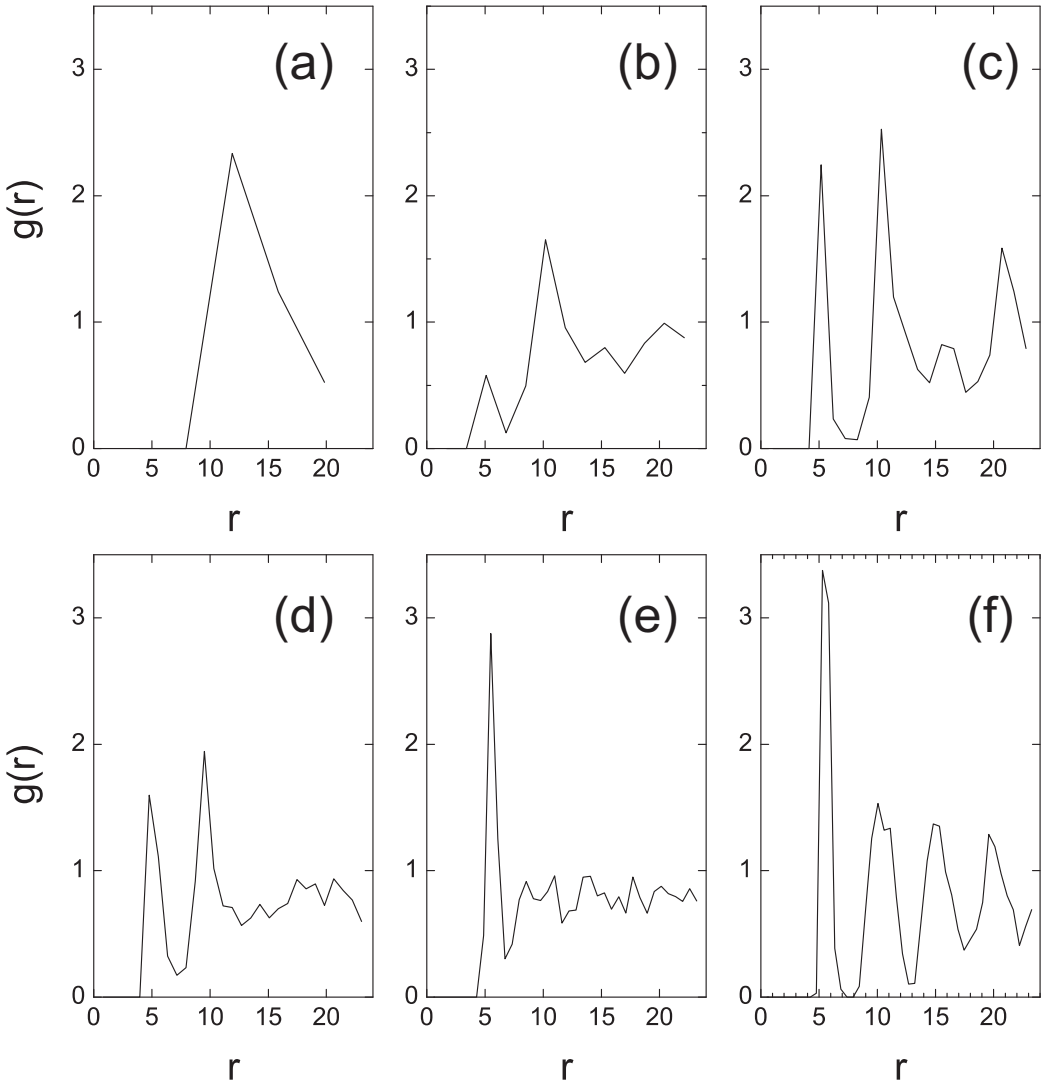

Figure 7.12: The radial distribution function $g(r)$ for $m_\perp = 5m_1$. Panels (a)-(f) correspond to states with 16, 32, 48, 64, 80 and 96 vortices in the simulation region, respectively.

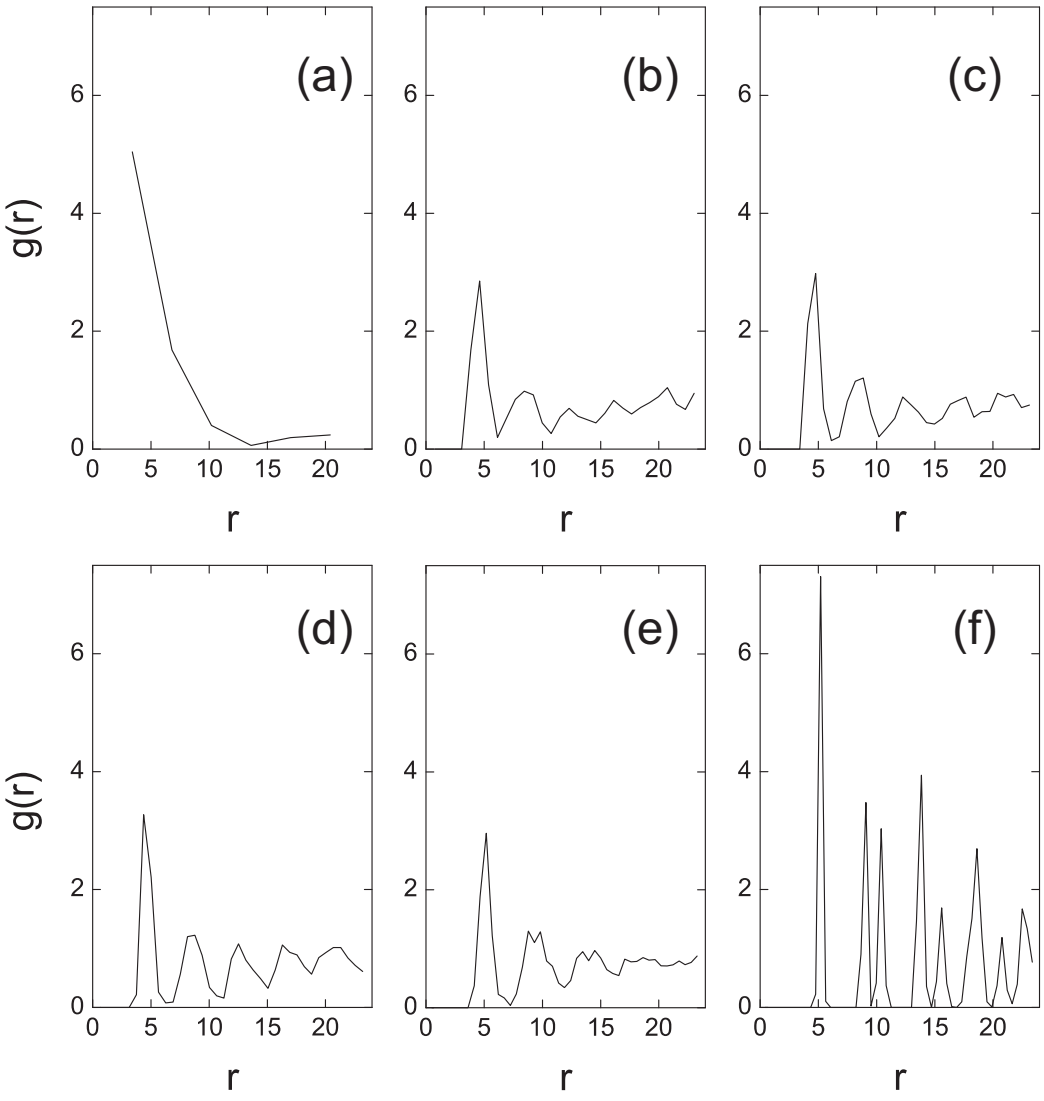

Figure 7.13: The radial distribution function $g(r)$ for $m_\perp = 20m_1$. Panels (a)-(f) correspond to states with 16, 64, 72, 80, 96, and 112 vortices in the simulation region, respectively.

one. Similar signature was also observed in Ref. [137], but there it was found for the structure factor $S(k)$, i.e., in the k space. This signature disappears when a gel state is formed.

7.5 Phase transitions of soft vortex matter with increasing/decreasing temperature

Another degree of controllability of the flux patterns in our system is provided by temperature, due to the different critical temperatures T_{cj} of the layers. For the considered parameters, elevated temperature will swiftly deplete superconductivity in the type-I layer, and will also interconnect the flux patterns in that layer due to the increasing coherence length. Both these features will influence the observed vortex configurations in the type-II layer. Hence, one is able to control and monitor the phase transitions of soft vortex matter in our bilayer system simply by changing temperature. We illustrate this in Fig. 7.14, where we start from a rather disordered gel-like state from Fig. 7.5(d) and gradually increase temperature. After a transition to a honeycomb (or fishing net) structure at $T = 1.25$ K, a transition to a glassy phase was found at 1.8 K, followed by crystallization into the Abrikosov lattice at 2.1 K (where the magnetic influence of the type-I layer became negligible). It is therefore interesting to note that contrary to most natural structures, including soft matter, the vortex configurations in our system become *more ordered* with increasing temperatures. Similarly, in Fig. 7.15 one can see how increasing the temperature transforms the chain state of Fig. 7.8(f) to the gel phase.

To gain insight into the nature of the phase transitions between different spatial arrangements of vortices, we show one particular example calculated for 16 vortices, thickness of the coupling layer $s = 2\xi_{10}$ and effective mass for tunneling of the Cooper pairs between the layers $m_\perp = 40m_1$. We found that for these parameters the stable phase at low temperature is small vortex clusters. These for intermediate temperatures coalesce into a single stripe which at higher temperature spreads over the entire simulation region and interconnects with adjacent stripes into the Abrikosov lattice. However, we found that there is considerable hysteretic behavior, since Fig. 7.16 shows the transition from several clusters to a stripe between 3.1 K and 3.15 K with increasing temperature, while on cooling (Fig. 7.17) the stripe is stable down to a much lower temperature of 0.85 K. In order to characterize this phase transition, we calculate the free energy and heat capacity. The free energy

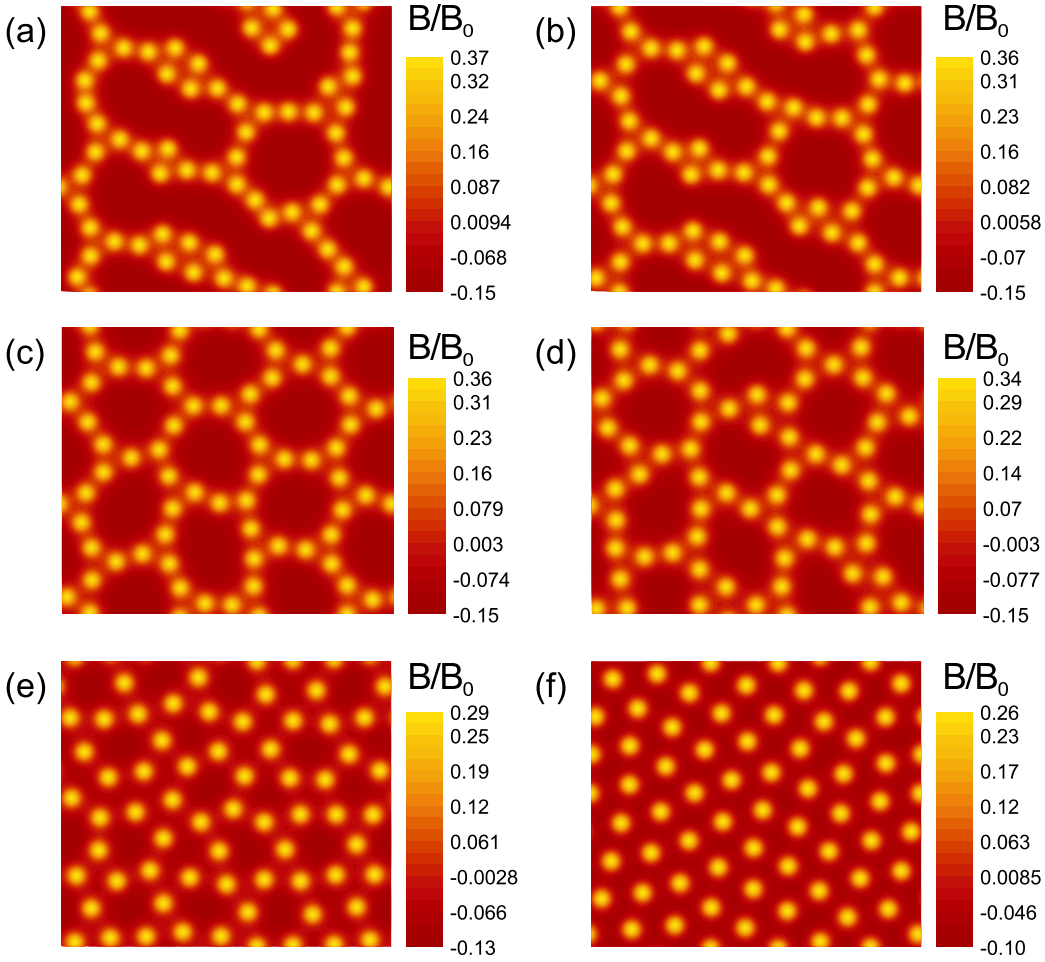

Figure 7.14: The evolution of the gel-like phase of Fig. 7.5(d) with increasing temperature. The vortex structure in the type-II layer is shown for (a) $T = 1$ K (original state) and the field-heated states (b) $T = 1.1$ K, (c) 1.25 K, (d) 1.45 K, (e) 1.85 K, and (f) 2.2 K.

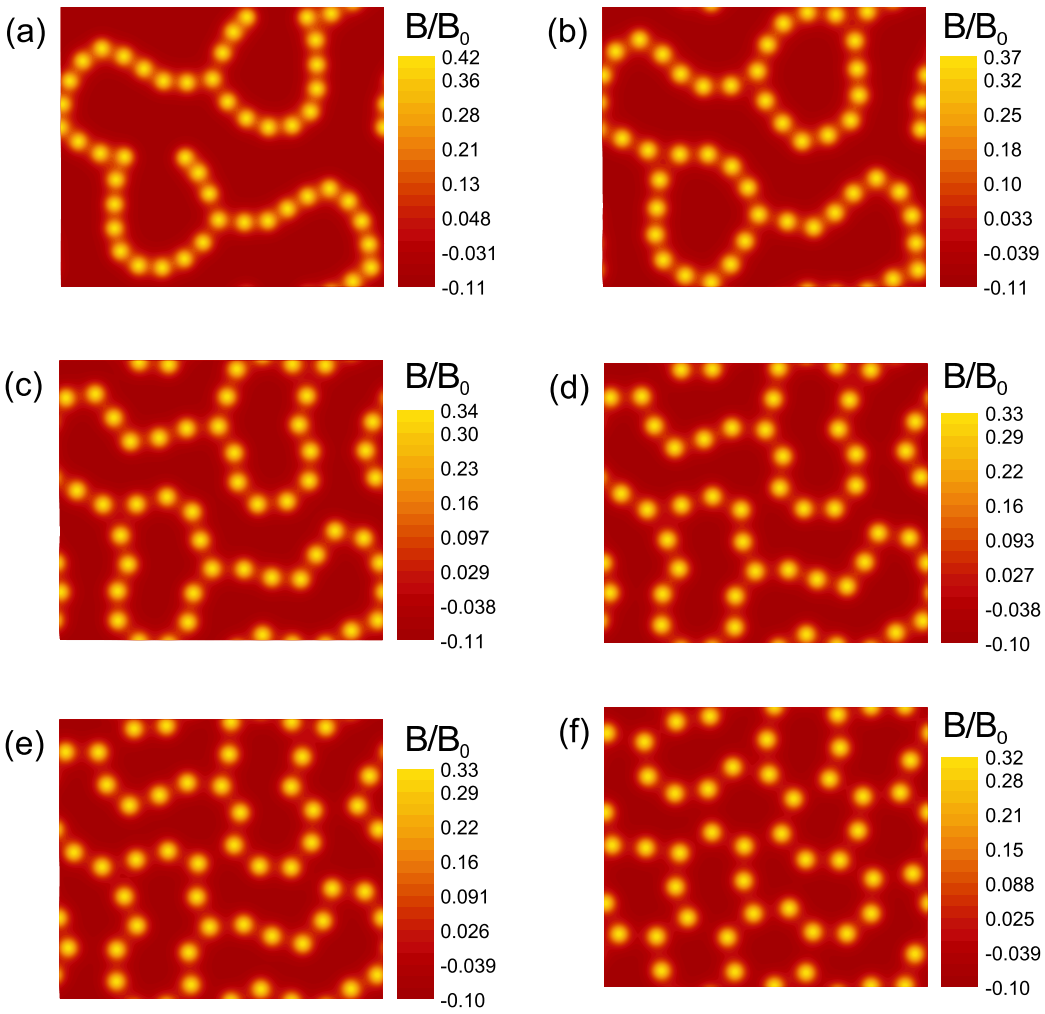

Figure 7.15: Evolution of the state shown in Fig. 7.8(f), with increasing temperature. The spatial profile of the magnetic field is shown. In this sequence of images, we show the transition from the chain phase to the gel phase by gradual increase of temperature. (a)-(f) $T = 1$ K, 1.5 K, 1.75 K, 1.85 K, 1.9 K, and 2 K.

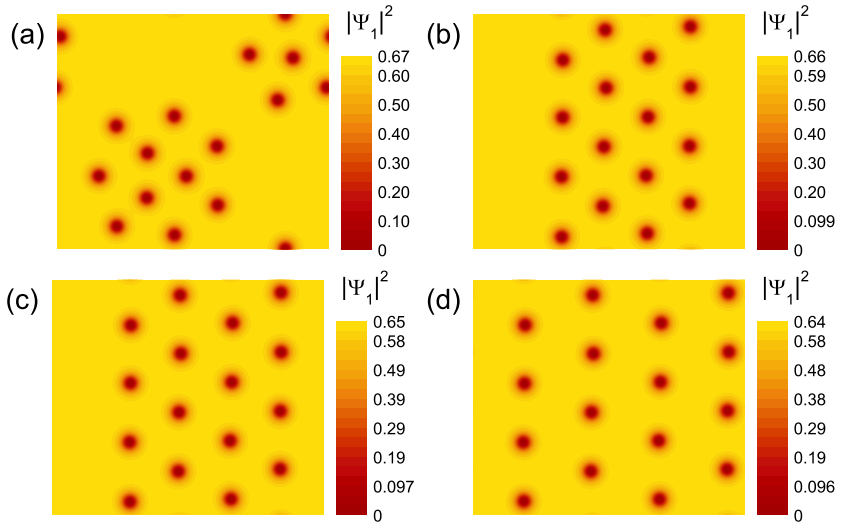

Figure 7.16: The transition from the cluster phase through stripe phase to the Abrikosov lattice *on heating*, shown as Cooper-pair density plots in the type-II layer at (a) $T = 3.1$ K (clusters), (b) $T = 3.15$ K, (c) $T = 3.25$ K (stripe), and (d) $T = 3.3$ K (Abrikosov lattice).

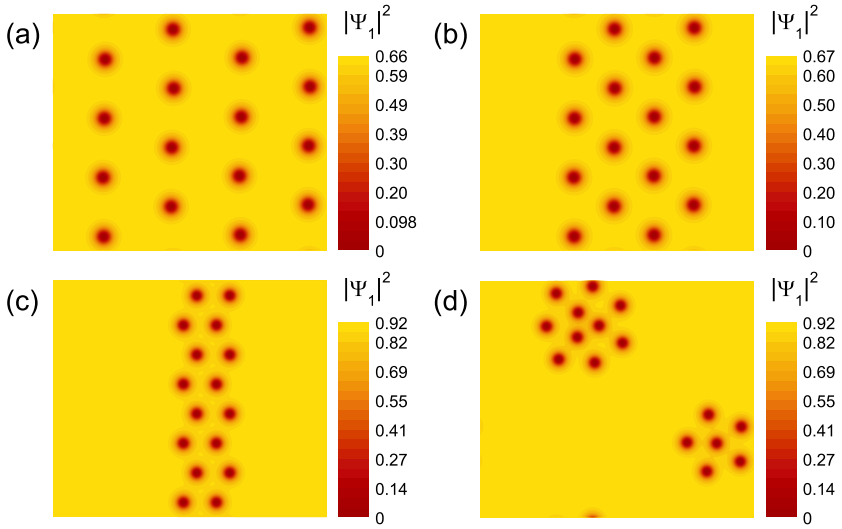

Figure 7.17: The transition from the Abrikosov lattice through stripe phase to the cluster phase *on cooling*, shown as Cooper-pair density plots in the type-II layer at (a) $T = 3.15$ K (Abrikosov lattice), (b) $T = 3.1$ K, (c) $T = 0.85$ K (stripe), and (d) $T = 0.84$ K (clusters).

is given by Eq. (7.1) which in dimensionless form reads

$$\begin{aligned}\frac{\mathcal{F}}{\mathcal{F}_0} &= d_1 \int \left[-\chi_1|\Psi_1|^2 + \frac{1}{2}|\Psi_1|^4 + |(-i\nabla - \mathbf{A})\,\Psi_1|^2\right] dS \\ &+ C_1 d_2 \int \left[-\chi_2|\Psi_2|^2 + \frac{1}{2}|\Psi_2|^4 + \frac{1}{\zeta}\,|(-i\nabla - \mathbf{A})\,\Psi_2|^2\right] dS \\ &+ C_2 \int |\Psi_1 - C_3\Psi_2|^2 dS + \kappa_1^2 \int (\mathbf{A} - \mathbf{A}_0)\cdot\mathbf{j} dV, \end{aligned} \tag{7.9}$$

where $\mathcal{F}_0 = \xi_{10}^3 \alpha_{10}^2/\beta_1 = \Phi_0^2/(32\pi^3\kappa_1^2\xi_{10})$ is our unit of energy ($\mathcal{F}_0 \approx 1.07 \times 10^{-18}$ J for Niobium with $\xi_{10} = 38$ nm), $\chi_j = 1 - T/T_{cj}$, $\mathbf{A}_0$ is the vector potential of the applied field, $\mathbf{j}$ the supercurrent, and $C_1 = \zeta^2 \frac{\kappa_1^2}{\kappa_2^2}$, $C_2 = \frac{m_1}{s m_\perp}$ and $C_3 = \frac{\kappa_1}{\kappa_2}\sqrt{\zeta \frac{m_2}{m_1}}$.

In Fig. 7.18(a) we show the specific heat capacity vs. temperature, computed as $c_v = -\frac{T}{V}\frac{\partial^2 \mathcal{F}}{\partial T^2}$. We convert the specific heat capacity from the units of $\mathcal{F}_0/(V\mathrm{K})$ (free energy per volume per kelvin) to its equivalent SI value which is in our case $6.2 \times 10^{-7}\mathrm{J}\cdot\mathrm{K}^{-1}\cdot\mathrm{cm}^{-3}$ (using volume of the simulation region $V = 31416\ \xi_{10}^3 \approx 1.72 \times 10^{-12}$ cm^3). The most pronounced feature in the specific heat capacity curve is a jump Δc_v of approximately 109 nJ $\cdot$ K$^{-1}\cdot$ cm^{-3}, where on heating the transition from small clusters to a single stripe is immediately followed by the rapid transition of the type-I layer through its own T_c to only proximity-induced superconductivity. After that transition the vortices occupy the entire sample evenly, forming an Abrikosov lattice. Therefore we can associate the onset of the attraction between vortices directly with the onset of superconductivity in the type-I layer. This implies that for considered parameters the type-I layer must be below its own critical temperature in order to observe any unusual clustering of vortices.

On cooling the heat capacity shows a similar jump, but associated only with the transition from Abrikosov lattice to the stripe phase. The subsequent transition at 0.85 K corresponds to the rearrangement of the vortices from the stripe into clusters, it is of first order, and associated with latent heat $L \approx 150\ \mu\mathrm{J}\cdot\mathrm{cm}^{-3}$. The described features in the heat capacity are ideal for observing the phase transitions of soft vortex matter by calorimetry, similarly to what is proposed for detection of flux phases inside the 3D samples and distinction of giant vortex to multivortex transitions in Refs. [160, 161]. The experimental realization of the required high-precision calorimetry is feasible, and has already been reported in Ref. [162].

In Fig. 7.18(b) we then show the difference in the free energies $\mathcal{F}_c - \mathcal{F}_h$ between the states found on cooling and heating, respectively. The sign of this quantity determines which of the possible states is energetically favorable

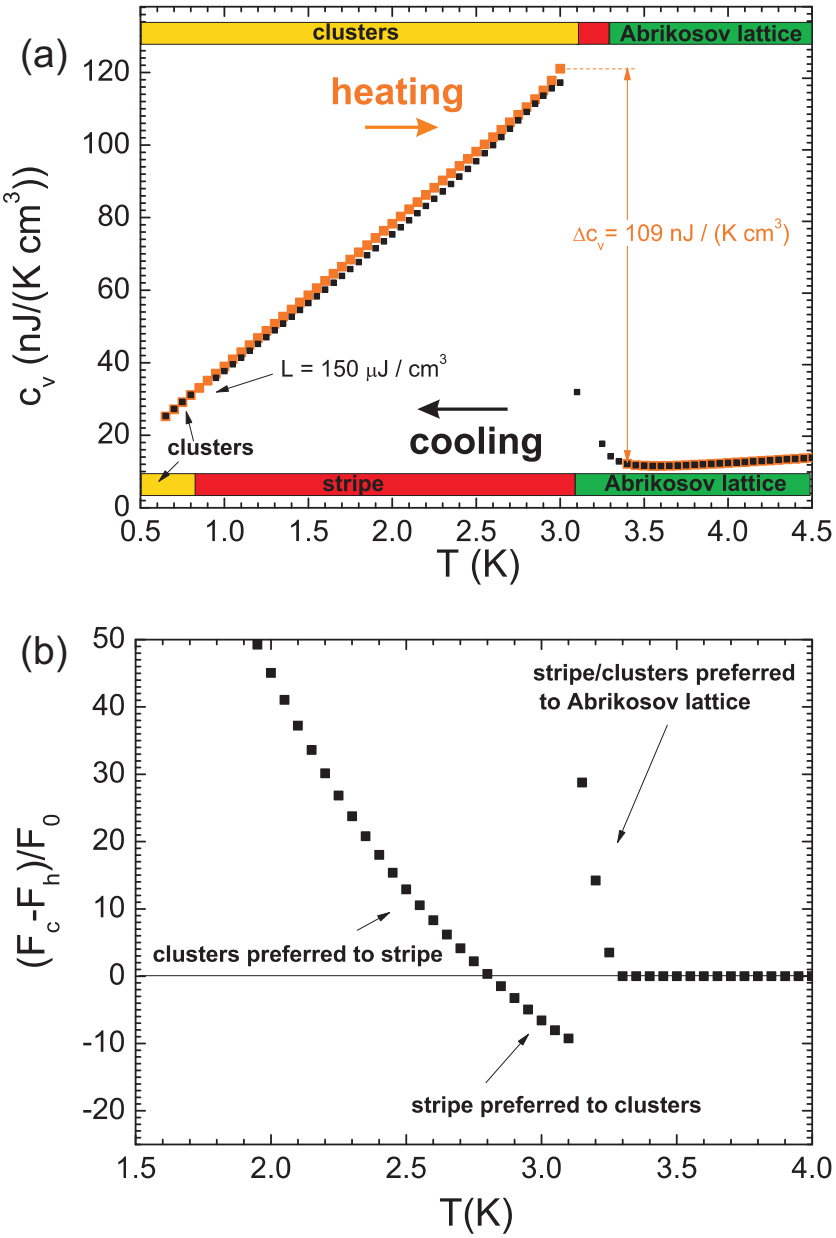

Figure 7.18: (a) The hysteretic behavior between the cluster phase, the stripe phase, and the Abrikosov lattice, shown via calculated heat capacity c_v on heating and cooling. The top (bottom) banner labels the states found on heating (cooling). The major difference is that on heating the stripes are only found in a narrow temperature region close to $T = 3.1$ K, while on cooling they are stable down to 0.85 K. (b) The difference in the free energy $\mathcal{F}$ between the states found on cooling ($\mathcal{F}_c$) and on heating ($\mathcal{F}_h$).

and details the energy cost of the metastable states. For example, one can directly see from Fig. 7.18(b) that the transition between the stripe and clusters in the equilibrium should occur at $T \approx 2.8$ K.

7.6 Conclusions

We presented novel and rich vortex phases and phase transitions in a type-I/type-II superconducting bilayer, resembling known phenomena in soft-matter physics. The solution-gel-glass-crystal transitions of vortex matter can be induced in our system by an external magnetic field, current, or temperature, but can be also engineered by a proper choice of the constituent materials, thinning the type-I layer to effective type-II behavior, or changing the spacer material to influence the coupling strength. The proposed superconducting system is in many ways peculiar and different from any soft-matter system, but similarities arise from the competing interactions with different length scales, present in both systems. Our superconducting system is controllable, relatively easy to fabricate, and allows for convenient vortex imaging or detection of transitions between phases using neutron scattering or calorimetric measurements. Moreover, this system opens a further research direction, leaning upon the early discovery of Giaver that it is possible to make a dc transformer by using applied current in one superconductor to drag vortices through another and induce voltage there [163–165]. The inability to *ad hoc* predict what would happen to soft vortex matter phases in that case, as well as the links to related studies of Coulomb drag in semiconductor heterostructures [166, 167] and bilayer graphene [168], makes our system a very interesting testbed for a plethora of new phenomena.

Related publication

- L. Komendová, M. V. Milošević, and F. M. Peeters: *Soft vortex matter in a type-I/type-II superconducting bilayer*, Phys. Rev. B **88**, 094515 (2013).

Chapter 8

Summary

Two-gap and multi-gap superconductivity is at the forefront of current research thanks to the recently discovered materials such as magnesium diboride (MgB_2) and dozens of new iron-based superconductors. In these materials one can talk about several coexisting and coupled condensates. Those give rise to novel competing and collective phenomena unattainable in conventional one-gap superconductors. Arguably the most direct testbed for those phenomena is the vortex matter. In that respect, particularly motivating for this thesis was the paper of Moshchalkov *et al.* [1] on "Type-1.5" superconductivity which has shown unusual behavior of the vortex matter in the prototypical two-gap superconductor MgB_2.

In the introductory chapters of this thesis, I first reviewed the phenomenology of conventional single-gap superconductors and the theoretical approaches used to describe them (London theory, Ginzburg-Landau theory, BCS theory and Bogoliubov-de Gennes equations) in **Chapter 1**. I turned to two-gap superconductivity in **Chapter 2**, to first discuss in depth the available data from various direct vortex imaging experiments, confronting the sometimes observed unusual clustering and stripe phases with the more commonly observed Abrikosov lattices. Subsequently I reviewed the theories of two-gap superconductors, i.e., the two-gap cousins of the previously named single-gap theories, but also the recently developed Extended Ginzburg-Landau theory (which we used later in Chapter 5). In **Chapter 3** I described the basic numerical approaches that I have used to solve the two-gap Ginzburg-Landau equations in their different flavors. In particular I discussed the solution of the 1D Extended GL equations using Matlab and the solution of the two-gap Ginzburg-Landau theory in periodic systems using the method of finite differences.

In the rest of this thesis I described the results of our investigations in various superconducting systems with two components. Motivated by the

"type-1.5" vortex structures, we first studied the vortex states and interaction of vortices within the "standard" two-gap GL theory. We found previously unquantified conditions for nonmonotonic intervortex interaction. We established that the character of the short-range interaction is determined by the sign of the surface energy of the normal metal-superconductor interface. Meanwhile, essentially independently, the long-range vortex profile asymptotics enabled us to define new effective GL parameter κ^* which determines the long-range interaction. Note that for the single-band superconductors the two criteria are practically equivalent except for very tiny region close to $\kappa = 1/\sqrt{2}$. We determined for several known multigap materials how likely they are to exhibit the nonmonotonic interaction between vortices (leading to the formation of vortex clusters). These results were discussed in **Chapter 4**.

About the time we were finishing this work several related papers appeared on the Arxiv, two of which from the Ames lab in USA. The main point was that once there is a finite Josephson coupling between the gaps so that the gaps have a common T_c, the material can only have a single coherence length and therefore single κ, which would prohibit the appearance of the long-range vortex attraction. These arguments are however valid only at T_c. Shanenko *et al.* [3] were able to show that if one derives the GL equations to the next-to-leading order, one obtains a difference in the characteristic lengths of the two condensates immediately below T_c (later on a complete theory was derived, the aforementioned Extended Ginzburg-Landau theory (EGL)). After the first proof-of-concept paper was published, I calculated numerically the healing lengths of the two condensates using this theory and have shown that their difference can be more than 20% for realistic material parameters even, e.g., at $0.9T_c$. This was important to convince the scientific community that the corrections are not negligible, even though they are of subleading order. We calculated the healing lengths not only for bulk materials, but also for nanoscale lead (Pb) as an example where multiband structure is due to confinement, and for LiFeAs, where I compared the results of the standard two-band GL theory (early one, which mixes orders of expansion in the small parameter $\tau = 1 - T/T_c$) and the results of the theory correct to the next-to-leading order. These studies were discussed in detail in **Chapter 5**.

Next, we wanted to compare my results in these various GL-type theories with the microscopic theory, so we set up the calculation for a single vortex in the two-gap Bogoliubov-de Gennes formalism. We found something much more dramatic and originally unexpected and that is a peak in the temperature dependence of the weak-gap coherence length in case when the gaps are very weakly coupled. This is actually a consequence of the bare T_c of the weak gap, which is for nonzero coupling no longer the point where the

superconductivity in the weak gap completely disappears, however it still has measurable effects. We named this *hidden critical point*, because it will never be an actual critical point of any real two-band superconductor due to the finite coupling, but nevertheless it is a true critical point in the sense that one can define a parameter measuring the proximity to it (namely the Josephson coupling γ, but taken only in the leading order in the interband coupling constant λ_{12}) and furthermore it definitely has manifestations in measurable quantities close to T_{c2}. At the hidden critical point, one gets power laws with critical exponents for various thermodynamic properties, and may even construct a complete analytical theory at T_{c2} to first order in γ. These findings are discussed in every detail in **Chapter 6**.

Last but not least, in **Chapter 7** we reverted our attention again to vortex matter in two gap samples, this time by studying the artificial analogue of a two-gap system - a type-I/type-II bilayer. Although no strict analogy can be made between the two systems, the vortex matter in a bilayer has proven to be an exciting study object, comprising structures as rich as parallel chains, gels, glasses, and crystalline vortex lattices, or phases where lamellar type-I flux domains in one layer trap the type-II vortices in the other. These vortex structures are very similar to the ones commonly observed in soft-matter systems. The similarity stems from the similar form of the interaction potentials comprising several length scales and/or mixture of attraction and repulsion. To enable easier identification of these novel vortex states in the experiments we calculated their radial distribution functions. We also followed in detail the phase transition between the vortex clusters through the stripe phase to the Abrikosov lattice on increasing the temperature and the opposite sequence of states on cooling. We found a considerable hysteresis, where the stripe phase on cooling survives to much lower temperature and only then rearranges in clusters in a first order phase transition. The associated latent heat and also the specific heat jump associated with the onset of vortex attraction, when the type-I layer switches to bulk as opposed to proximity induced superconductivity, should be experimentally observable by high-precision calorimetry.

8.1 Outlook & future directions

The topic of multigap superconductivity is still at the stage where we have considerable voids in our understanding, and therefore every further research and systematic analysis can reveal a new surprise. In this spirit, I name a few of the possible future directions related to this thesis:

- Multigap type-I superconductivity, which is largely unexplored and

may be relevant to low-T_c two-gap superconductors, such as OsB_2;

- (Fractional) vortices in bilayers and multilayers, and to calculate interaction potential between vortices in a superconducting bilayer such as the one studied in Chapter 7;

- Magnetic properties of multilayers with large number of alternating layers of two superconducting compounds (such samples are relatively easy to fabricate);

- Vortex matter in multigap superconductors with artificial pinning centra, where it should be possible to take advantage of different healing lengths of two condensates and therefore their different interaction with the same pinning potential may be exploited for fluxonic applications;

- Numerical implementation of two-gap Extended Ginzburg-Landau model with magnetic field, to fully characterize the intermediate state of (mesoscopic) two-gap superconductors;

- Behavior of newly found vortex states (clusters, chains, gel) present in the two-gap superconductors and/or bilayers when current is applied through the sample, in search of the new flux flow and other new resistive regimes;

- Signatures of the hidden criticality (the remnants of the weak-gap bare critical temperature) in the thermodynamic properties and studies of the emerging fluctuations phenomena in two-gap superconductors, deep in the superconducting state;

- Development of the GL theory for two-band superconductors valid at all temperatures in analogy to what was recently achieved in Ref. [169] for two-band superfluid Fermi gases.

Chapter 9

Samenvatting

Twee-kloof en multi-kloof supergeleiding staat aan de spits van het huidige onderzoek dankzij de recent ontdekte materialen zoals magnesium diboride (MgB_2) en tientallen nieuwe ijzer gebaseerde supergeleiders. In deze materialen kan men spreken van een aantal naast elkaar bestaande en gekoppelde condensaten. Deze leiden tot nieuwe concurrerende en collectieve fenomenen, onbereikbaar in conventionele één-kloof supergeleiders. Misschien wel de meest directe testomgeving voor die verschijnselen is vortex materie. In dat opzicht bijzonder motiverend voor dit proefschrift, was het artikel van Moshchalkov *et al.* [1] over "Type-1.5"-supergeleiding, dat ongewoon gedrag van de vortex materie heeft aangetoond in de prototypische twee-kloof supergeleider MgB_2.

In de inleidende hoofdstukken van dit proefschrift behandel ik eerst de fenomenologie van conventionele één-kloof supergeleiders en de theoretische benaderingen die worden gebruikt om hen te beschrijven (London theorie, Ginzburg-Landau theorie, BCS theorie en Bogoliubov-de Gennes vergelijkingen komen aan bod) in **Hoofdstuk 1**. In **Hoofdstuk 2** beschrijf ik twee-kloof supergeleiding. Eerst bespreek ik grondig de beschikbare gegevens uit verschillende directe vortex beeldvormingsexperimenten: ik confronteer de soms waargenomen, ongebruikelijke clustering en streepfases met de vaker waargenomen Abrikosov roosters. Vervolgens behandel ik de theorieën van twee-kloof supergeleiders (de twee-kloof varianten van de eerder genoemde één-kloof theorieën), maar ook de recent ontwikkelde Uitgebreide Ginzburg-Landau theorie (Extended Ginzburg-Landau theory (EGL)) die we later in Hoofdstuk 5 gebruiken. In **Hoofdstuk 3** beschrijf ik de numerieke benaderingen die ik gebruikt heb om de twee-kloof Ginzburg-Landau vergelijkingen in hun verschillende variaties op te lossen. Met name behandel ik de oplossing van de 1D Uitgebreide GL vergelijkingen in Matlab en de oplossing van de twee-kloof Ginzburg-Landau theorie in periodieke systemen met de eindige-

differentiemethode.

In de rest van dit proefschrift beschrijf ik de resultaten van mijn onderzoek in diverse supergeleidende systemen met twee componenten. Gemotiveerd door de "type-1.5" vortex structuren, bestuderen we eerst de vortextoestanden en interactie van vortices binnen de "standaard" twee-kloof GL theorie. We hebben de eerder niet gekwantificeerde voorwaarden voor niet-monotone intervortex interactie gevonden. Wij hebben namelijk vastgesteld dat het karakter van de korte afstands interactie wordt bepaald door het teken van de oppervlakte-energie van het metaal-supergeleider grensvlak. Aan de andere kant, het lange afstands vortex profiel laat ons toe een nieuwe effectieve GL parameter κ^* te definiëren die de lange afstands interactie bepaalt. Merk op dat voor de één-kloof supergeleiders de twee criteria nagenoeg gelijk zijn, behalve voor een zeer kleine gebied dicht bij $\kappa = 1/\sqrt{2}$. We bepaalden voor verschillende bekende multikloof materialen hoe groot de kans is dat ze de niet-monotone interactie tussen vortices (die tot de vorming van vortex-clusters leidt) vertonen. Deze resultaten worden besproken in **Hoofdstuk 4**.

Tijdens de afronding van dit werk, verschenen diverse, gerelateerde artikels op het arXiv, waarvan twee uit het Ames laboratorium in de VS. Hun belangrijkste conclusie was dat zodra er een eindige Josephson koppeling tussen de kloven is, zodat ze een gemeenschappelijke T_c hebben, het materiaal slechts een enkele coherentielengte en dus een enkele κ kan hebben, dus lange afstands vortex attractie zou onmogelijk zijn. Deze argumenten zijn echter alleen geldig exact op T_c. Shanenko *et al.* [3] konden aantonen dat in de op-een-na-grootste orde men een verschil krijgt in de karakteristieke lengten van de twee condensaten juist onder T_c (later werd een volledige theorie afgeleid, de voornoemde Uitgebreide Ginzburg-Landau theorie). Ik heb de herstellengtes van de twee condensaten met behulp van deze theorie numeriek berekend. Het verschil tussen de lengtes kan meer dan 20% worden voor realistische materiaal parameters, ook dichtbij de kritische temperatuur. Dit resultaat was belangrijk om de wetenschappelijke gemeenschap ervan te overtuigen dat de correcties niet verwaarloosbaar zijn, ook al zijn ze niet van leidende orde. We berekenden de herstellengtes niet alleen voor grote supergeleidende structuren, maar ook voor nanoschaal lood (Pb) als voorbeeld waar een multiband structuur ontstaat door opsluiting. Daarnaast vergelijk ik de resultaten van de standaard twee-kloof GL theorie (een vroegere versie die termen in verschillende orders in de kleine parameter $\tau = 1 - T/T_c$ bevat) en de resultaten van de theorie juist in de op-een-na-grootste orde voor LiFeAs. Deze studies worden in detail besproken in **Hoofdstuk 5**.

Vervolgens wilden we onze resultaten vergelijken in deze verschillende GL-achtige theorieën met de microscopische theorie, dus begonnen we de berekening voor een vortex in het twee-kloof Bogoliubov-de Gennes formalisme. We

hebben iets oorspronkelijk onverwacht gevonden: een piek in de temperatuursafhankelijkheid van de zwakke kloof coherentielengte in het geval wanneer de kloven zeer zwak gekoppeld zijn. Dit is eigenlijk een gevolg van de intrinsieke T_c van de zwakke kloof. Zonder koppeling is T_{c2} het punt waar de supergeleiding in de zwakke kloof volledig verdwijnt, maar met eindige koppeling zijn er nog steeds meetbare effecten. We noemden $(\gamma = 0, T = T_{c2})$ het *verborgen kritisch punt*, omdat het nooit een echt kritisch punt van een echte twee-kloof supergeleider kan zijn vanwege de eindige koppeling. Op het verborgen kritisch punt zijn verschillende thermodynamische grootheden de machtsverbanden in γ. Bovendien hebben we daar zelfs een complete analytische theorie tot eerste orde in γ geconstrueerd. De voornaamste conclusie is dat de coherentielengte daar divergeert. Deze bevindingen worden besproken in detail in **Hoofdstuk 6**.

Ten slotte, in **Hoofdstuk 7** vestigen we onze aandacht opnieuw op vortex materie in twee-kloof supergeleiders, dit keer door het bestuderen van het kunstmatige equivalent van een twee-kloof-systeem - een type-I/type-II - bilaag. Hoewel er geen strikte analogie kan worden gemaakt tussen de twee systemen, heeft de vortex materie in een bilaag zich bewezen als een spannend studieobject. Het bezit vele nieuwe structuren zoals parallelle kettingen, gels, glasachtige structuren, en Abrikosov vortex roosters, of fasen waarbij lamellaire type-I flux domeinen een val maken voor het type-II-vortices in de andere laag. Deze vortex structuren zijn zeer vergelijkbaar met die vaak waargenomen in zachte materie systemen. De overeenkomst komt voort uit de soortgelijke vorm van de interactie potentiaal tussen relevante "deeltjes" in de beide gevallen, met meerdere lengteschalen en/of een mengsel van aantrekking en afstoting. Om deze nieuwe vortextoestanden in experimenten beter te kunnen herkennen, hebben we hun radiale distributie functies berekend. Ook hebben we de faseovergang tussen de vortex clusters doorheen de streep-fase naar de Abrikosov rooster bij het verhogen van de temperatuur en de omgekeerde volgorde van fasen bij afkoeling opgevolgd. We vonden een grote hysterese, de streepfase bij afkoelen overleeft bij veel lagere temperatuur en herschikt dan pas in clusters in een eerste orde faseovergang. De bijbehorende latente- en soortelijke warmte sprong geassocieerd met het ontstaan van de vortex aantrekking (wanneer het type-I laag zijn eigen supegeleiding krijgt in tegenstelling tot de geïnduceerde supergeleiding door koppeling aan het type-II laag) zou experimenteel kunnen worden geobserveerd door hoge precisie calorimetrie.

9.1 Toekomstperspectieven

Het onderwerp van multi-kloof supergeleiding is nog steeds in het stadium waar men aanzienlijke gaten in kennis heeft, en daarom kan elk verder onderzoek en systematische analyse een nieuwe verrassing onthullen. Daarom noem ik hier een paar van de mogelijke toekomstige onderzoeksvragen met betrekking tot dit proefschrift:

- Multikloof type-I supergeleiding, die grotendeels onbekend is en voor lage-T_c twee-kloof supergeleiders, zoals OsB_2, relevant zou kunnen zijn;
- (Fractionele) vortices in bilagen en multilagen, en de interactie tussen de vortices te berekenen in een supergeleidende bilaag zoals die in Hoofdstuk 7;
- Magnetische eigenschappen van multilagen met een groot aantal afwisselende lagen van twee supergeleiders (dat type van structuren is relatief eenvoudig om te produceren);
- Vortex materie in multikloof supergeleiders met kunstmatige pinningcentra, om te antwoorden op de vraag of het mogelijk is gebruik te maken van verschillende herstellengtes van twee condensaten en dus hun verschillende interacties met dezelfde pinning potentieel te benutten bvb. voor toepassingen in fluxonica;
- Numerieke implementatie van het twee-kloof Uitgebreide Ginzburg-Landau model met een magnetisch veld, om de intermediaire toestand van (mesoscopische) twee-kloof supergeleiders volledig te karakteriseren;
- Gedrag van nieuwe vortextoestanden (clusters, ketens, gel) aanwezig in de twee-kloof supergeleiders en/of bilagen wanneer er een stroom vloeit door de structuur, op zoek naar de nieuwe flux-flow en andere resistieve regimes;
- Onderzoek naar de mogelijke signalen van de verborgen criticaliteit (de restanten van de zwakke-kloof eigen kritische temperatuur) in de thermodynamische eigenschappen en studies van de opkomende schommelingen in de twee-kloof supergeleiders, diep in de supergeleidende toestand;
- Ontwikkeling van de GL theorie voor twee-kloof supergeleiders geldig bij alle temperaturen in analogie met wat onlangs werd bereikt in Ref. [169] voor twee-kloof superfluïde Fermi gassen.

Curriculum vitae

Name:	**Lucia Komendová**
Born:	6 September 1985, Nová Baňa, Slovakia
Contact:	Groenenborgerlaan 171 (U209)
	2020, Antwerpen
	Belgium
E-mail:	Lucia.Komendova@gmail.com

Education

2009-2013: PhD in Physics, University of Antwerp, Belgium
2007-2009: Master in Solid State Physics, Comenius University, Slovakia
2004-2007: Bachelor in Physics, Comenius University, Slovakia

Research Interests

Condensed Matter Theory, New materials, Superconductivity, Vortices, Ginzburg-Landau theory, Microscopic models

Computer skills

Operating systems:	Windows, Linux
Office:	Word, Excel, PowerPoint
Programming (basic):	Fortran, Java, Python
Mathematical software:	MATLAB, Mathematica
Webdesign:	HTML, CSS

Languages

Slovak (native), English, Dutch, French

Publications

Journal Articles

1. L. Komendová, M. V. Milošević, and F. M. Peeters, *Soft vortex matter in a type-I/type-II superconducting bilayer*, Phys. Rev. B **88**, 094515 (2013).

2. L. Komendová, Yajiang Chen, A. A. Shanenko, M. V. Milošević and F. M. Peeters, *Two-band superconductors: Hidden criticality deep in the superconducting state*, Phys. Rev. Lett. **108**, 207002 (2012).

3. L. Komendová, M. V. Milošević, A. A. Shanenko, and F. M. Peeters, *Different length scales for order parameters in two-gap superconductors: Extended Ginzburg-Landau theory*, Phys. Rev. B **84**, 064522 (2011).

4. A. Chaves, L. Komendová, M. V. Milošević, J. S. Andrade, Jr., G. A. Farias, and F. M. Peeters, *Conditions for nonmonotonic vortex interaction in two-band superconductors*, Phys. Rev. B **83**, 214523 (2011).

5. L. Komendová and R. Hlubina, *Density of states in a split superconducting vortex*, Phys. Rev. B **81**, 012505 (2010).

Proceedings

- L. Komendová, A. A. Shanenko, M. V. Milošević and F. M. Peeters, *The healing lengths in two-band superconductors in extended Ginzburg-Landau theory*, Physica C **479**, 126 (2012).

Research stay

1 September 2012 - 31 October 2012
With Dr. Lara Benfatto at the Condensed Matter Theory group, University La Sapienza in Rome, the accommodation provided by the grant of Academia Belgica in Rome.

Professional service

Referee for Physical Review B and Physical Review Letters (since 2011) and for International Journal of Modern Physics B (since 2012).

Bibliography

[1] V. V. Moshchalkov, M. Menghini, T. Nishio, Q. H. Chen, A. V. Silhanek, V. H. Dao, L. F. Chibotaru, N. D. Zhigadlo, and J. Karpinski, Phys. Rev. Lett. **102**, 117001 (2009).

[2] V. G. Kogan and J. Schmalian, Phys. Rev. B **83**, 054515 (2011).

[3] A. A. Shanenko, M. V. Milošević, F. M. Peeters, and A. V. Vagov, Phys. Rev. Lett. **106**, 047005 (2011).

[4] V. L. Ginzburg and L. D. Landau, Sov. Phys. JETP **20**, 1064 (1950).

[5] J. Bardeen, L. N. Cooper, and J. R. Schrieffer, Phys. Rev. **108**, 1175 (1957).

[6] L. P. Gor'kov, Zh. Eksperim. i Teor. Fiz. **36**, 1918 (1959) [Soviet Phys. - JETP **9**, 1364 (1959)].

[7] A. A. Abrikosov, Zh. Eksperim. i Teor. Fiz. **32**, 1442 (1957) [Soviet Phys. - JETP **5**, 1174 (1957)].

[8] R. Prozorov, Phys. Rev. Lett. **98**, 257001 (2007).

[9] J. G. Bednorz and K. A. Müller, Z. Phys. **B64**, 189 (1986).

[10] *An accidental discovery breathes new life into superconductivity research!*, JST Breakthrough Report, Vol. 7. Retrieved from `http://www.jst.go.jp/EN/research/bt07_en.html` on 8 February 2013.

[11] M. Tinkham, *Introduction to Superconductivity*, 2nd edition (Dover publications, New York, 1996).

[12] P. G. de Gennes, *Superconductivity of Metals and Alloys* (Benjamin, New York, 1966).

[13] J. C. Osborn, and A. T. Dorsey, Phys. Rev. B **50**, 15961 (1994).

[14] J. Auer and H. Ullmaier, Phys. Rev. B **7**, 136 (1973).

[15] E. H. Brandt and M. P. Das, J. Supercond. Nov. Magn. **24**, 57 (2011).

[16] Huebener, R. P., *Magnetic flux structures in superconductors: extended reprint of a classic text* (Vol. 6., Springer, 2001).

[17] E. B. Bogomolnyi, Sov. J. Nucl. Phys. **24**, 449-454 (1976).

[18] P. Miranović and K. Machida, Phys. Rev. B **67**, 092506 (2003).

[19] W. Lawrence and S. Doniach, in Proceedings of the Twelfth International Conference on Low Temperature Physics, edited by Eizo Kanda (Academic Press of Japan, Kyoto, 1971), p. 361.

[20] J. E. Hirsch, Physica Scripta **84**, 045705 (2011), also on arXiv:1108.3835.

[21] Piers Coleman, *Introduction to Many Body Physics*, version from 11 April 2013, accessible online at `http://www.physics.rutgers.edu/~coleman/620/mbody/pdf/bkx.pdf`.

[22] Carsten Timm, *Theory of Superconductivity*, version from 6 February 2012, accessible online at `http://www.physik.tu-dresden.de/~timm/personal/teaching/thsup_w11/Theory_of_Superconductivity.pdf`.

[23] A. Gurevich, Phys. Rev. B **82**, 184504 (2010).

[24] T. Mizushima, M. Takahashi, and K. Machida, arXiv:1305.3678.

[25] Yajiang Chen, PhD thesis (2012), accessible online through `www.cmt.uantwerpen.be`.

[26] N. B. Kopnin, *Theory of Superconductivity*, (2010), accessible online at `http://ltl.tkk.fi/wiki/images/8/8f/TheorySC10.pdf`.

[27] H. J. Choi, D. Roundy, H. Sun , M. L. Cohen, and S. G. Louie, Nature, **418**, 758-760 (2002).

[28] Hai-Hu Wen and Shiliang Li, Annu. Rev. Condens. Matter Phys. **2**, 121 (2011).

[29] H. Nakamura, M. Machida, T. Koyama, and N. Hamada, J. Phys. Soc. Jpn. **78**, 123712 (2009).

[30] D. V. Evtushinsky, A. A. Kordyuk, V. B. Zabolotnyy, D. S. Inosov, T. K. Kim, B. Büchner, Huiqian Luo, Zhaosheng Wang, Hai-Hu Wen, Guoli Sun, Chengtian Lin, and S. V. Borisenko, J. Phys. Soc. Jpn. **80**, 023710 (2011).

[31] S. J. Bending, Advances in Physics **48**, 449 (1999).

[32] L. Ya. Vinnikov, J. Karpinski, S. M. Kazakov, and J. Jun, J. Anderegg, S. L. Budko, and P. C. Canfield, Phys. Rev. B **67**, 092512 (2003).

[33] D. Vasyukov, Y. Anahory, L. Embon, D. Halbertal, J. Cuppens, L. Neeman, A. Finkler, Y. Segev, Y. Myasoedov, M. L. Rappaport, M. E. Huber, and E. Zeldov, Nature Nanotechnology (2013), doi:10.1038/nnano.2013.169

[34] T. Nishio, Vu Hung Dao, Q. Chen, L. F. Chibotaru, K. Kadowaki, and V. V. Moshchalkov, Phys. Rev. B **81**, 020506(R) (2010).

[35] J. Gutierrez, B. Raes, A. V. Silhanek, L. J. Li, N. D. Zhigadlo, J. Karpinski, J. Tempere, and V. V. Moshchalkov, Phys. Rev. B **85**, 094511 (2012).

[36] J.C. Loudon, C.J. Bowell, N.D. Zhigadlo, J. Karpinski, P.A. Midgley, Physica C: Superconductivity **474**, 18 (2012).

[37] J.C. Loudon, C.J. Bowell, N.D. Zhigadlo, J. Karpinski, P.A. Midgley, Phys. Rev. B **87**, 144515 (2013).

[38] M. J. G. Cottet, M. Cantoni, B. Mansart, D. T. L. Alexander, C. Hébert, N. D. Zhigadlo, J. Karpinski, and F. Carbone, Phys. Rev. B **88**, 014505 (2013).

[39] Ø. Fischer, M. Kugler, I. Maggio-Aprile, C. Berthod and C. Renner, Rev. Mod. Phys. **79**, 353 (2007).

[40] J. E. Hoffman, Rep. Prog. Phys. **74**, 124513 (2011).

[41] Can-Li Song, J. E. Hoffman, Current Opinion in Solid State and Materials Science **17**, 39 (2013).

[42] M. R. Eskildsen, M. Kugler, S. Tanaka, J. Jun, S. M. Kazakov, J. Karpinski, and . Fischer, Phys. Rev. Lett. **89**, 187003 (2002).

[43] T. Hanaguri, K. Kitagawa, K. Matsubayashi, Y. Mazaki, Y. Uwatoko,and H. Takagi, Phys. Rev. B **85**, 214505 (2012).

[44] Can-Li Song, Yi Yin, Martin Zech, Tess Williams, Michael M. Yee, Gen-Fu Chen, Jian-Lin Luo, Nan-Lin Wang, E. W. Hudson, and Jennifer E. Hoffman, Phys. Rev. B **87**, 214519 (2013).

[45] Lei Shan, Yong-Lei Wang, Bing Shen, Bin Zeng, Yan Huang, Ang Li, Da Wang, Huan Yang, Cong Ren, Qiang-Hua Wang, Shuheng H. Pan, and Hai-Hu Wen, Nature Physics **7**, 325 (2011).

[46] Yi Yin, M. Zech, T. L. Williams, X. F. Wang, G. Wu, X. H. Chen, and J. E. Hoffman, Phys. Rev. Lett. **102**, 097002 (2009).

[47] S. Serventi, G. Allodi, R. De Renzi, G. Guidi, L. Romanò, P. Manfrinetti, A. Palenzona, Ch. Niedermayer, A. Amato, and Ch. Baines, Phys. Rev. Lett. **93**, 217003 (2004).

[48] A. A. Golubov, A. Brinkman, O. V. Dolgov, J. Kortus, and O. Jepsen, Phys. Rev. B **66**, 054524 (2002).

[49] M. E. Zhitomirsky and V. H. Dao, Phys. Rev. B **69**, 054508 (2004).

[50] I. N. Askerzade, Physica C 397 (2003) 99-111.

[51] A. V. Vagov, A. A. Shanenko, M. V. Milošević, V. M. Axt, and F. M. Peeters, Phys. Rev. B **85**, 014502 (2012).

[52] A. Vagov, A. A. Shanenko, M. V. Milošević, V. M. Axt, and F. M. Peeters, Phys. Rev. B **86**, 144514 (2012).

[53] A. L. Fetter, J. D. Walecka, *Quantum theory of many-particle systems*, McGraw-Hill, New York (1971).

[54] L. Komendová, M. V. Milošević, A. A. Shanenko, and F. M. Peeters, Phys. Rev. B **84**, 064522 (2011).

[55] A. Vagov, A. A. Shanenko, M. V. Milošević, V. M. Axt, V. M. Vinokur, and F. M. Peeters, arxiv:1311.5624.

[56] A. M. Zagoskin, *Quantum Theory of Many-Body Systems: Techniques and Applications*, Springer-Verlag, New York (1998).

[57] L. Fanfarillo, L. Benfatto, S. Caprara, C. Castellani, and M. Grilli, Phys. Rev. B **79**, 172508 (2009).

[58] A. E. Koshelev, A. A. Varlamov, and V. M. Vinokur, Phys. Rev. B **72**, 064523 (2005).

[59] V. A. Schweigert and F. M. Peeters, Phys. Rev. B **57**, 13817 (1998).

[60] V. A. Schweigert and F. M. Peeters, Phys. Rev. Lett. **81**, 2783 (1998).

[61] M. V. Milošević, R. Geurts, Physica C **470**, 791 (2010).

[62] Ryuzo Kato, Yoshihisa Enomoto, Sadamichi Maekawa, Phys. Rev. B **47**, 8016 (1993).

[63] Ben Xu, PhD thesis (2011), accessible online through `www.cmt.uantwerpen.be`.

[64] E. Abrahams and T. Tsuneto, Phys. Rev. **152**, 416 (1966).

[65] V. L. Ostrovski, arXiv:1208.1677.

[66] M. M. Doria, J. E. Gubernatis, D. Rainer, Phys. Rev. B, **39**, 13 (1989).

[67] C. T. Sachrajda, G. Villadoro, Physics Letters B **609**, 73 (2005).

[68] F. Bouquet, R. A. Fisher, N. E. Phillips, D. G. Hinks, and J. D. Jorgensen, Phys. Rev. Lett. **87**, 047001 (2001).

[69] P. Szabó, P. Samuely, J. Kačmarčík, T. Klein, J. Marcus, D. Fruchart, S. Miraglia, C. Marcenat, and A. G. M. Jansen, Phys. Rev. Lett. **87**, 137005 (2001).

[70] M. L. Teague, G. K. Drayna, G. P. Lockhart, P. Cheng, B. Shen, H.-H. Wen, and N.-C. Yeh, Phys. Rev. Lett. **106**, 087004 (2011).

[71] H. Kim, M. A. Tanatar, Y. J. Song, Y. S. Kwon, and R. Prozorov, Phys. Rev. B **83**, 100502(R) (2011).

[72] D. Eom, S. Qin, M.-Y. Chou, and C. K. Shih, Phys. Rev. Lett. **96**, 027005 (2006).

[73] A. A. Shanenko, M. D. Croitoru, A. Vagov, and F. M. Peeters, Phys. Rev. B **82**, 104524 (2010).

[74] E. Babaev and M. Speight, Phys. Rev. B **72**, 180502 (2005).

[75] M. Seul and D. Andelman, Science **267**, 476 (1995).

[76] C. J. Olson Reichhardt, C. Reichhardt, and A. R. Bishop, Phys. Rev. Lett. **92**, 016801 (2004).

[77] E. Babaev, J. Carlström, and M. Speight, Phys. Rev. Lett. **105**, 067003 (2010).

[78] V. H. Dao, L. F. Chibotaru, T. Nishio, and V. V. Moshchalkov, Phys. Rev. B **83**, 020503 (2011).

[79] J. Geyer, R. M. Fernandes, V. G. Kogan, and J. Schmalian, Phys. Rev. B **82**, 104521 (2010).

[80] V. G. Kogan, C. Martin, and R. Prozorov, Phys. Rev. B **80**, 014507 (2009).

[81] M. Abramowitz and I. A. Stegun, *Handbook of Mathematical Functions with Formulas, Graphs, and Mathematical Tables*, pp. 17-18, New York - Dover, 1972.

[82] L. Kramer, Phys. Rev. B **3**, 3821 (1971).

[83] J. M. Speight, Phys. Rev. D **55**, 3830 (1997).

[84] F. Mohamed, M. Troyer, G. Blatter, and I. Luk'yanchuk, Phys. Rev. B **65**, 224504 (2002).

[85] A. Gurevich, Physica C **456**, 160-169 (2007).

[86] J.-P. Wang, Phys. Lett. A **374**, 58 (2009).

[87] J.-P. Wang, Phys. Rev. B **82**, 132505 (2010).

[88] A. Chaves, F. M. Peeters, G. A. Farias, and M. V. Milošević, Phys. Rev. B **83**, 054516 (2011).

[89] A. A. Golubov, J. Kortus, O. V. Dolgov, O. Jepsen, Y. Kong, O. K. Andersen, B. J. Gibson, K. Ahn, and R. K. Kremer, J. Phys. Cond. Matt. **14**, 1353 (2002).

[90] M. R. Eskildsen, L. Ya. Vinnikov, T. D. Blasius, I. S. Veshchunov, T. M. Artemova, J. M. Densmore, C. D. Dewhurst, N. Ni, A. Kreyssig, S. L. Bud'ko, P. C. Canfield, and A. I. Goldman, Phys. Rev. B **79**, 100501(R) (2009).

[91] L. Ya. Vinnikov, T. M. Artemova, I. S. Veshchunova, N. D. Zhigadlo, J. Karpinski, P. Popovich, D. L. Sund, C. T. Lind, and A. V. Boris, JETP Lett. **90**, 299 (2009).

[92] Y. Koval, X. Jin, C. Bergmann, Y. Simsek, L. Özyüzer, Paul Müller, Huabing Wang, G. Behr, and B. Büchner, Appl. Phys. Lett. **96**, 082507 (2010).

[93] A. E. Koshelev and A. A. Golubov, Phys. Rev. Lett. **90**, 177002 (2003).

[94] A. E. Koshelev and A. A. Golubov, Phys. Rev. Lett. **92**, 107008 (2004).

[95] M. Silaev and E. Babaev, Phys. Rev. B **84**, 094515 (2011).

[96] A. Shibata, M. Matsumoto, K. Izawa, Y. Matsuda, S. Lee and S. Tajima, Phys. Rev. B **68**, 060501(R) (2003).

[97] E. Babaev and M. Silaev, Phys. Rev. B **86**, 016501 (2012); V. G. Kogan and J. Schmalian, Phys. Rev. B **86**, 016502 (2012).

[98] A. Chaves, L. Komendová, M. V. Milošević, J. S. Andrade, Jr., G. A. Farias, and F. M. Peeters, Phys. Rev. B **83**, 214523 (2011).

[99] M. E. Zhitomirsky and V.-H. Dao, Phys. Rev. B **69**, 054508 (2004).

[100] R. Geurts, M. V. Milošević, and F. M. Peeters, Phys. Rev. B **81**, 214514 (2010).

[101] A. A. Shanenko, M. D. Croitoru, A. Vagov and F.M. Peeters, Phys. Rev. B **82**, 104524 (2010).

[102] Y. Guo, Y.-F. Zhang, X.-Y. Bao, T. Z. Han, Z. Tang, L. X. Zhang, W. G. Zhu, E. G. Wang, Q. Niu, Z. Q. Qiu, J. F. Jia, Z. X. Zhao, and Q. K. Xue, Science **306**, 1915 (2004).

[103] D. Eom, S. Qin, M. Y. Chou and C. K. Shih, Phys. Rev. Lett. **96**, 027005 (2006).

[104] S. Qin, J. Kim, Q. Niu, C.-K. Shih, Science **324**, 1314 (2009).

[105] T. Zhang, P. Cheng, W.-J. Li, Y. J. Sun, G. Wang, X. G. Zhu, K. He, L. L. Wang, X. C. Ma, X. Chen, Y. Y. Wang, Y. Liu, H. Q. Lin, J. F. Jia, and Q. K. Xue, Nature Phys. **6**, 104 (2010).

[106] P. Dyke, E. D. Kuhnle, S. Whitlock, H. Hu, M. Mark, S. Hoinka, M. Lingham, P. Hannaford and C. J. Vale, Phys. Rev. Lett. **106**, 105304 (2011).

[107] X. C. Wang, Q. Q. Liu, Y. X. Lv, W. B. Gao, L. X. Yang, R. C. Yu, F.Y.Li, C.Q. Jin, Solid State Commun. **148**, 538 (2008).

[108] K. Cho, H. Kim, M. A. Tanatar, Y. J. Song, Y. S. Kwon, W. A. Coniglio, C. C. Agosta, A. Gurevich and R. Prozorov, Phys. Rev. B **83**, 060502(R) (2011).

[109] A. Gurevich, Phys. Rev. B **82**, 184504 (2010).

[110] C. J. Thompson and J. M. Blatt, Phys. Lett. **5**, 6 (1963).

[111] E. H. Hwang, S. Das Sarma and M. A. Stroscio, Phys. Rev. B **61**, 8659 (2000).

[112] I.A. Nekrasov, Z. V. Pchelkina, and M. V. Sadovskii, JETP Letters **88**, 543 (2008).

[113] M. J. Pitcher, D. R. Parker, P. Adamson, S. J. C. Herkelrath, A. T. Boothroyd, R. M. Ibberson, M. Brunellid and S. J. Clarke, Chem. Commun., 5918 (2008).

[114] L. D. Landau and E. M. Lifshitz, *Course of Theoretical Physics*, vol. 5 (Butterworth-Heinemann, Oxford, 1980).

[115] A. Z. Patashinskii and V. L. Pokrovskii, *Fluctuation theory of phase transitions* (Pergamon, Oxford, 1979).

[116] H. Suhl, B. T. Matthias, and L. R. Walker, Phys. Rev. Lett. **3**, 552 (1959); V. A. Moskalenko, Fiz. Met. Metalloved. **8**, 503 (1959) [Phys. Met. Metallogr. **8**, 25 (1959)].

[117] M. N. Chernodub and A. S. Nedelin, Phys. Rev. D **81**, 125022 (2010).

[118] Shi-Zeng Lin and Xiao Hu, Phys. Rev. B **84**, 214505 (2011).

[119] M. A. Silaev, Phys. Rev. B **83**, 144519 (2011).

[120] P. J. Pereira, L. F. Chibotaru, and V. V. Moshchalkov, Phys. Rev. B **84**, 144504 (2011).

[121] J. Berger and M. V. Milošević, Phys. Rev. B **84**, 214515 (2011).

[122] G. Litak, T. Ord, K. Rago and A. Vargunin, arXiv:1112.5661, Acta Physica Polonica (2012) in press.

[123] M. Silaev and E. Babaev, Phys. Rev. B **85**, 134514 (2012).

[124] H. Bluhm, N. C. Koshnick, M. E. Huber, and K. A. Moler, Phys. Rev. Lett. **97**, 237002 (2006).

[125] A. De Col, V. B. Geshkenbein, and G. Blatter, Phys. Rev. Lett. **94**, 097001 (2005).

[126] Y. Lubashevsky, E. Lahoud, K. Chashka, D. Podolsky, and A. Kanigel, arXiv:1107.1487.

[127] F. Gygi and M. Schlüter, Phys. Rev. B **43**, 7609 (1991).

[128] N. Hayashi, T. Isoshima, M. Ichioka, and K. Machida, Phys. Rev. Lett. **80**, 2921 (1998).

[129] Y. Singh, A. Niazi, M. D. Vannette, R. Prozorov, and D. C. Johnston, Phys. Rev. B **76**, 214510 (2007).

[130] Y. Singh, C. Martin, S. L. Bud'ko, A. Ellern, R. Prozorov, and D. C. Johnston, Phys. Rev. B **82**, 144532 (2010).

[131] Y. Singh and R. Prozorov, private communication.

[132] H. Kim, M. A. Tanatar, Y. J. Song, Y. S. Kwon and R. Prozorov, Phys. Rev. B **83**, 100502(R) (2011).

[133] Yu. A. Nefyodov, A. M. Shuvaev, and M. R. Trunin, Europhys. Lett. **72**, 638 (2005).

[134] R. Khasanov, M. Bendele, A. Amato, K. Conder, H. Keller, H.-H. Klauss, H. Luetkens, and E. Pomjakushina, Phys. Rev. Lett. **104**, 087004 (2010).

[135] P. Popovich, A. V. Boris, O. V. Dolgov, A. A. Golubov, D. L. Sun, C. T. Lin, R. K. Kremer, and B. Keimer, Phys. Rev. Lett. **105**, 027003 (2010).

[136] R. A. L. Jones, *Soft Condensed Matter* (Oxford University Press, Oxford, 2002).

[137] G. Malescio and G. Pellicane, Nature Materials **2**, 97 (2003).

[138] C. J. Olson Reichhardt, C. Reichhardt, and A. R. Bishop, Phys. Rev. E **82**, 041502 (2010).

[139] H. J. Zhao, V. R. Misko, and F. M. Peeters, New J. Phys. **14**, 063032 (2012).

[140] P. J. Camp, Phys. Rev. E **68**, 061506 (2003).

[141] J. C. Fernandez Toledano, F. Sciortino, and E. Zaccarelli, Soft Matter **5**, 2390 (2009).

[142] C. L. Klix, C. P. Royall, and H. Tanaka, Phys. Rev. Lett. **104**, 165702 (2010).

[143] N. Osterman, D. Babič, I. Poberaj, J. Dobnikar, and P. Ziherl, Phys. Rev. Lett. **99**, 248301 (2007).

[144] J. Dobnikar, J. Fornleitner, and G. Kahl, J. Phys.: Condens. Matter **20**, 494220 (2008).

[145] R. Prozorov, A. F. Fidler, J. R. Hoberg, and P. C. Canfield, Nature Physics **4**, 327 (2008).

[146] G. R. Berdiyorov, A. D. Hernandez, and F. M. Peeters, Phys. Rev. Lett. **103**, 267002 (2009).

[147] G. Blatter, M. V. Feigel'man, V. B. Geshkenbein, A. I. Larkin and V. M. Vinokur, Rev. Mod. Phys. **66**, 1125 (1994).

[148] M. Sigrist and K. Ueda, Rev. Mod. Phys. **63**, 239 (1991).

[149] V. B. Eltsov, R. Blaauwgeers, N. B. Kopnin, M. Krusius, J. J. Ruohio, R. Schanen, and E. V. Thuneberg, Phys. Rev. Lett. **88**, 065301 (2002).

[150] E. H. Brandt, Phys. Rev B **79**, 134526 (2009).

[151] J. Carlström, J. Garaud, and E. Babaev, Phys. Rev. B **84**, 134515 (2011).

[152] R. A. Klemm, A. Luther, and M. R. Beasley, Phys. Rev. B **12**, 877 (1975).

[153] L. N. Bulaevskii and I. D. Vagner, Phys. Rev. B **43**, 8694 (1991).

[154] S. J. Chapman, Q. Du and M. D. Gunzburger, SIAM J. Appl. Math. **55**, 156 (1995).

[155] M. J. Graf, D. Rainer, and J. A. Sauls, Phys. Rev. B **47**, 12089 (1993).

[156] M. Menghini and R. J. Wijngaarden, Phys. Rev. B **72**, 172503 (2005).

[157] J. R. Hoberg and R. Prozorov, Phys. Rev. B **78**, 104511 (2008).

[158] V. Vlasko-Vlasov, A. Buzdin, A. Melnikov, U. Welp, D. Rosenmann, L. Uspenskaya, V. Fratello, and W. Kwok, Phys. Rev. B **85**, 064505 (2012)

[159] V. Vlasko-Vlasov, U. Welp, G. Karapetrov, V. Novosad, D. Rosenmann, M. Iavarone, A. Belkin, and W.-K. Kwok, Phys. Rev. B **77**, 134518 (2008).

[160] Ben Xu, M. V. Milošević, and F. M. Peeters, Phys. Rev. B **81**, 064501 (2010).

[161] Ben Xu, M. V. Milošević, Shi-Hsin Lin, F. M. Peeters, and B. Jankó, Phys. Rev. Lett. **107**, 057002 (2011).

[162] O. Bourgeois, S. E. Skipetrov, F. Ong, and J. Chaussy, Phys. Rev. Lett. **94**, 057007 (2005).

[163] Ivar Giaver, Phys. Rev. Lett. **15**, 825 (1965).

[164] R. Deltour and M. Tinkham, Phys. Rev. **174**, 478 (1968).

[165] J. W. Ekin, B. Serin, and J. R. Clem, Phys. Rev. B **9**, 912 (1974).

[166] P. M. Solomon, P. J. Price, D. J. Frank, and D. C. La Tulipe, Phys. Rev. Lett. **63**, 2508 (1989).

[167] T. J. Gramila, J. P. Eisenstein, A. H. MacDonald, L. N. Pfeiffer, and K. W. West, Phys. Rev. Lett. **66**, 1216 (1991).

[168] R. V. Gorbachev, A. K. Geim, M. I. Katsnelson, K. S. Novoselov, T. Tudorovskiy, I. V. Grigorieva, A. H. MacDonald, S. V. Morozov, K. Watanabe, T. Taniguchi, and L. A. Ponomarenko, Nature Phys. **8**, 896 (2012).

[169] S. N. Klimin, J. Tempère, and J. T. Devreese, arXiv:1309.1421v1 (2013).